

## **Durham E-Theses**

# Electron Microscopy and Density Functional Theory Investigations of Degenerate Boron Doped Silicon

#### DHAMOTHARAN, KAVIYADHARSHINI

#### How to cite:

DHAMOTHARAN, KAVIYADHARSHINI (2025) Electron Microscopy and Density Functional Theory Investigations of Degenerate Boron Doped Silicon, Durham theses, Durham University. Available at Durham E-Theses Online: http://etheses.dur.ac.uk/16333/

#### Use policy

The full-text may be used and/or reproduced, and given to third parties in any format or medium, without prior permission or charge, for personal research or study, educational, or not-for-profit purposes provided that:

- a full bibliographic reference is made to the original source
- a link is made to the metadata record in Durham E-Theses
- the full-text is not changed in any way

The full-text must not be sold in any format or medium without the formal permission of the copyright holders.

Please consult the full Durham E-Theses policy for further details.

# Electron Microscopy and Density Functional Theory Investigations of Degenerate Boron Doped Silicon

## Kaviyadharshini Dhamotharan

A thesis presented for the degree of Doctor of Philosophy



Condensed Matter Physics

Durham University

United Kingdom

July 2025

# Electron Microscopy and Density Functional Theory Investigations of Degenerate Boron Doped Silicon Kaviyadharshini Dhamotharan

Abstract: This thesis investigates the impact of degenerate boron doping on vibrational and scattering properties of crystalline silicon using a combined approach involving electron microscopy, multislice simulations, and density functional theory (DFT). Momentumresolved and momentum-integrated electron energy loss spectroscopy measurements revealed broad, high-energy optical phonon modes centred around 132 meV, features absent in intrinsic silicon. DFT simulations attributed these signatures to localised vibrational modes arising from neutral interstitial boron clusters, particularly compact configurations such as  $3B_i^0$  (confi 1 and 2), which produced non-dispersive modes in agreement with experimental data. Selected area diffraction patterns (SADPs), supported by multislice simulations, were used to probe diffuse scattering behaviour in doped silicon. At low scattering angles, enhanced Kikuchi lines and increased background intensity were observed without Bragg peak broadening, consistent with localised strain from boron incorporation. Simulations confirmed that both substitutional and interstitial defects contributed to this behaviour. At high scattering angles, an anomalous increase in diffuse intensity was observed in doped silicon. This enhancement, absent in frozen phonon simulations, was attributed to boron-induced localised phonon modes. Cryogenic experiments confirmed this interpretation. The final study provides a foundational step in bridging theoretical and experimental thermal diffuse scattering (TDS). First-order TDS profiles computed from DFT were fitted to experimental data, and empirical corrections using Gaussian and exponential models significantly improved agreement. These findings demonstrate the feasibility of integrating phonon theory with experimental electron scattering in doped silicon.

Supervisor: Prof.B.G.Mendis

## **Declaration**

The work in this thesis is based on research carried out in the Department of Physics, Durham University, United Kingdom. No part of this thesis has been submitted elsewhere for any other degree or qualification and it is all my own work unless referenced to the contrary in the text.

## Copyright © 2025 by Kaviyadharshini Dhamotharan.

"The copyright of this thesis rests with the author. No quotations from it should be published without the author's prior written consent and information derived from it should be acknowledged.".

# **Acknowledgements**

First and foremost, I would like to express my deepest gratitude to my supervisor Prof. Budhika G. Mendis. His guidance, support, and patience have been invaluable throughout this research journey. No matter what questions or uncertainties I faced, I could always approach him without hesitation. His door was always open, and I was able to clarify my doubts and seek advice whenever needed. I cannot imagine a better supervisor, and I consider myself truly fortunate to have had the opportunity to work under his mentorship.

I am also profoundly grateful to my family. My parents and my two sisters have been a constant source of strength, encouragement, and unconditional love. Without their support, I would not have reached this stage in my academic journey. Their belief in me carried me through the most difficult times.

To Tepi, thank you for being by my side when I needed it most. Your presence brought comfort, safety, and strength during some of the most testing times. One of the reasons I could feel at home in Durham, far from my own family, was because of the unwavering support and companionship you offered.

To my friends whom I met in Durham- Urmi, Oli, Roy, and Lizzie - I cannot thank you enough for the joy, and warmth you brought into my life. You reminded me that alongside the work, it's the people who make the experience truly meaningful.

To my friends back in India, thank you for your love and encouragement across the

distance. Despite being far away, your support meant everything to me and helped me stay motivated.

I would also like to sincerely thank Prof. Quentin Ramasse and Dr. Shihao Wang for their help with the STEM-EELS measurements, and Prof. Guillaume Zoppi for his support with the SIMS measurements. I am especially grateful to Prof. Stewart Clark, whose expert advice and guidance were vital in navigating the DFT simulations.

I am thankful to the NOS Scholarship for providing the funding that made this PhD possible.

Finally, to everyone I met in Durham who contributed to my happiness, learning, and growth, thank you.

# **Contents**

| De       | eclara         | ation   |   | 11 |  |
|----------|----------------|---------|---|----|--|
| Li       | ist of Figures |         |   |    |  |
| Li       | st of          | Tables  | S   | XX |  |
| 1        | The            | sis ove | erview  | 1  |  |
|          | 1.1            | Motiv   | ation   | 1  |  |
|          | 1.2            | Aim o   | f this thesis   | 5  |  |
| <b>2</b> | Intr           | oducti  | ion   | 9  |  |
|          | 2.1            | Crysta  | al structure  | 10 |  |
|          |                | 2.1.1   | Primitive lattice                                     | 10 |  |
|          |                | 2.1.2   | Some important crystal lattices                       | 11 |  |
|          |                | 2.1.3   | Crystal planes, crystal Directions and Miller indices | 12 |  |
|          |                | 2.1.4   | Reciprocal lattice                                    | 14 |  |
|          |                | 2.1.5   | Brillouin zone  | 15 |  |
|          | 2.2            | Electr  | onic band structure                                   | 16 |  |
|          | 2.3            | Phono   | on band structure                                     | 18 |  |
|          |                | 2.3.1   | Harmonic model  | 19 |  |
|          | 2.4            | Defect  | s due to doping                                       | 22 |  |

|   |     | 2.4.1   | Point defects                             | 24 |
|---|-----|---------|---|----|
|   |     | 2.4.2   | Lattice distortion                        | 25 |
|   |     | 2.4.3   | Local vibrational modes                   | 27 |
|   | 2.5 | Point   | defects due to boron doping in silicon    | 29 |
|   | 2.6 | Summ    | ary                                       | 31 |
| 3 | Sca | ttering | g Theory                                  | 32 |
|   | 3.1 | Scatte  | ering from ideal single crystals          | 32 |
|   |     | 3.1.1   | Bragg diffraction                         | 34 |
|   |     | 3.1.2   | Atomic scattering factor                  | 36 |
|   |     | 3.1.3   | Structure factor and Bragg intensities    | 38 |
|   |     | 3.1.4   | Thermal diffuse scattering                | 40 |
|   | 3.2 | Diffus  | e scattering from point defects           | 43 |
|   |     | 3.2.1   | Huang diffuse scattering                  | 46 |
|   | 3.3 | Summ    | ary                                       | 47 |
| 4 | Exp | erime   | ntal Techniques                           | 48 |
|   | 4.1 | Transı  | mission electron microscopy               | 48 |
|   |     | 4.1.1   | TEM instrumentation                       | 50 |
|   |     | 4.1.2   | Aberrations                               | 53 |
|   |     | 4.1.3   | The modes of operation                    | 54 |
|   |     | 4.1.4   | Scanning transmission electron microscopy | 57 |
|   |     | 4.1.5   | Electron energy loss spectroscopy         | 63 |
|   | 4.2 | Rama    | n spectroscopy                            | 67 |
|   |     | 4.2.1   | Theory                                    | 68 |
|   |     | 4.2.2   | Instrumentation                           | 69 |
|   | 4.3 | Focuse  | ed ion beam                               | 71 |
|   |     | 4.3.1   | Instrumentation                           | 72 |
|   |     | 4.3.2   | Modes of operation                        | 75 |

|   | 4.4  | Second   | dary ion mass spectroscopy                                      | 76   |
|---|------|----------|---|------|
|   |      | 4.4.1    | Instrumentation   | 77   |
|   |      | 4.4.2    | Modes of operation  | 78   |
|   | 4.5  | Hall n   | neasurements  | 79   |
|   |      | 4.5.1    | Principle   | 79   |
|   |      | 4.5.2    | Hall measurement setup  | 79   |
|   | 4.6  | Summ     | ary   | 82   |
| 5 | Sim  | ıulatioı | n Techniques  | 83   |
|   | 5.1  | Densit   | by functional theory  | 83   |
|   |      | 5.1.1    | Kohn-Sham equations   | 85   |
|   |      | 5.1.2    | The exchange-correlation functional                             | 88   |
|   |      | 5.1.3    | Pseudopotentials  | 89   |
|   |      | 5.1.4    | Phonon calculations - Finite displacement method                | 91   |
|   | 5.2  | Multis   | slice   | 93   |
|   |      | 5.2.1    | Multislice simulation- Static atoms                             | 93   |
|   |      | 5.2.2    | Multislice simulation - Frozen phonon                           | 96   |
|   | 5.3  | Summ     | ary   | 98   |
| 6 | Infl | uence    | of Boron Defects on the Vibrational Properties of Silicon       | 99   |
|   | 6.1  | Prelin   | ninary characterisation of boron                                |      |
|   |      | doped    | Si sample   | 99   |
|   |      | 6.1.1    | Hall Measurements   | 100  |
|   |      | 6.1.2    | SIMS  | 100  |
|   |      | 6.1.3    | Raman spectroscopy  | 102  |
|   | 6.2  | Exper    | imental EELS measurements of phonon modes in boron doped silico | n104 |
|   |      | 6.2.1    | Momentum-resolved EELS spectra                                  | 104  |
|   |      | 6.2.2    | Momentum integrated EELS spectra                                | 108  |
|   | 6.3  | Simula   | ation of phonon modes for boron defects in silicon              | 117  |

| Bi | Bibliography 185 |         |   |     |
|----|------------------|---------|---|-----|
| 9  | Out              | look    |   | 181 |
|    |                  | 8.1.3   | Conclusion  | 180 |
|    |                  | 8.1.2   | TDS Intensity analysis at cryogenic temperature                     | 173 |
|    |                  | 8.1.1   | TDS intensity analysis at room temperature                          | 166 |
|    | 8.1              | Theore  | etical background   | 162 |
|    | Diff             | use Sc  | attering (TDS) in Silicon   | 162 |
| 8  | Con              | nparat  | ive Analysis of Experimental and Theoretical Thermal                |     |
|    | 7.4              | Conclu  | asion   | 161 |
|    |                  | 7.3.2   | Radial intensity analysis   | 156 |
|    |                  | 7.3.1   | Cryogenic temperature calibration using EELS                        | 154 |
|    | 7.3              | Effects | s of temperature on diffuse scattering                              | 153 |
|    |                  |         | tering angles   | 150 |
|    |                  | 7.2.2   | The role of boron concentration in diffuse scattering at high scat- |     |
|    |                  |         | tering angles   | 135 |
|    |                  | 7.2.1   | The role of boron concentration in diffuse scattering at low scat-  |     |
|    | 7.2              | Effects | s of strain due to boron doping in silicon at room temperature      | 134 |
|    | 7.1              | SAED    | techniques and indexing DPs   | 132 |
| 7  | Diff             | use sca | attering analysis: Elemental vs. Boron-Doped Silicon                | 132 |
|    | 6.4              | Conclu  | ısion   | 130 |
|    |                  | 6.3.4   | Phonon modes  | 127 |
|    |                  | 6.3.3   | Defect formation energies   | 124 |
|    |                  | 6.3.2   | Structural configurations of boron defects in silicon               | 120 |
|    |                  | 6.3.1   | Convergence tests   | 117 |

# **List of Figures**

| 1.1 | The increase in transistors count on a given IC by year for several manufac-                                     |    |
|-----|--|----|
|     | turers[12]   | 2  |
| 1.2 | Image of Si containing 50 nm B-Si layers as viewed along $\langle 110 \rangle$ zone axis.                        |    |
|     | Threading dislocation segments are also visible under the following ima-   |    |
|     | ging conditions: (a) bright field (BF), and (b) high angle annular dark field                                    |    |
|     | (HAADF) [40]   | 6  |
| 1.3 | Experimental TDS images of Si for (a) [111] and (b) [100] zone axes, along                                       |    |
|     | with theoretical first-order TDS calculations for (c) [111] and (d) [100] [45].                                  | 8  |
| 2.1 | Some important unit cells characterising crystalline solids.(a) The simple                                       |    |
|     | cubic (SC) unit cell, (b) the body centered cubic (BCC) unit cell, (c) the face-                                 |    |
|     | centred cubic (FCC) unit cell, (d) diamond cubic unit cell, (e) zincblende                                       |    |
|     | unit cell [58]   | 12 |
| 2.2 | Miller indices for some significant planes and directions in a cubic crystal. (a)                                |    |
|     | (100) plane, (b) (110) plane, (c) (111) plane, (d) family of $\langle 100 \rangle$ directions,                   |    |
|     | and (e) [111] direction [60]   | 13 |
| 2.3 | Depiction of the first Brillouin zone for the face-centered cubic lattice (FCC)                                  |    |
|     | with lattice constant ${\bf a}$ . Several high-symmetry points are highlighted: $\Gamma=$                        |    |
|     | $(0, 0, 0), X = \frac{2\pi}{a}(1, 0, 0), L = \frac{2\pi}{a}(0.5, 0.5, 0.5), W = \frac{2\pi}{a}(1, 0.5, 0)$ [67]. | 16 |

| 2.4  | Schematic diagram of the energy bands for tetravalent semiconductors such                                |    |
|------|--|----|
|      | as silicon (Si), and germanium (Ge) in relation to atomic spacing [72]                                   | 17 |
| 2.5  | The energy band structures of (a) silicon and (b) gallium arsenide exhibit an                            |    |
|      | indirect and direct band gap, respectively (band structures generated using                              |    |
|      | CASTEP code [75])  | 18 |
| 2.6  | Phonon dispersion curves in diamond and zinc-blende structured semicon-                                  |    |
|      | ductors along high-symmetry points. (a) Gallium arsenide (GaAs), (b) Dia-                                |    |
|      | mond (C) (Phonon structures generated using CASTEP code [75])  | 19 |
| 2.7  | Schematic silicon crystal lattice with (a) pentavalent impurity atom ( $n$ -                             |    |
|      | type), (b) trivalent impurity atom ( $p$ -type) [88]   | 23 |
| 2.8  | Schematic representation of the Fermi energy $E_f$ of (a) an $n$ -type and, (b)                          |    |
|      | a p-type semiconductor at 0 K. In (a), $E_D$ denotes the donor energy levels,                            |    |
|      | and in (b), $E_A$ represents the acceptor energy levels [89]   | 23 |
| 2.9  | Schematic diagram of the lattice distortion due to single point defect in                                |    |
|      | the host crystal lattice. (a) crystal lattice before the lattice relaxation, (b)                         |    |
|      | distorted crystal lattice after the lattice relaxation [100]   | 26 |
| 2.10 | The dependency of the electrical resistivity of silicon at 300 K temperature                             |    |
|      | on the p type (boron) doping concentration [107]   | 30 |
| 2.11 | Electron mobility of silicon as a function of boron acceptor doping concen-                              |    |
|      | trations at 300 K temperature [108]  | 31 |
| 3.1  | Illustration of Bragg's diffraction (a) and the Ewald sphere construction (b).                           |    |
|      | In (a), the incident and diffracted beams are shown, with wave vectors $\mathbf{k}_{\text{in}}$          |    |
|      | and $\mathbf{k}_{\text{out}}$ at the Bragg angle $\theta_B$ , while the interplanar spacing is denoted   |    |
|      | by $d_{hkl}$ . In (b), the Ewald sphere construction illustrates the relationship                        |    |
|      | between the incident wave vector $\mathbf{k}_{in}$ , diffracted wave vector $\mathbf{k}_{out}$ , and the |    |
|      | reciprocal lattice point $G$ , with the sphere radius equal to $\frac{1}{\lambda}$ , showing the         |    |
|      | geometric condition for diffraction [120]  | 35 |
|      | 0  | 50 |

| 3.2 | Graph of the atomic scattering factor $f(\mathbf{Q})$ for carbon (C), silicon (Si),               |    |
|-----|---|----|
|     | germanium (Ge), and gold (Au), computed using the empirical expression n                          |    |
|     | Equation 3.11. The graph displays the atomic scattering factor as a function                      |    |
|     | of scattering vector magnitude $Q$ for each element, showcasing the variations                    |    |
|     | in scattering properties among the different materials [130]                                      | 38 |
| 3.3 | Isointensity curves for an isotropic point defect in Cu for different reflections.                |    |
|     | a) [100] reflection (dotted curve, isotropic approximation); (b)curve in (001)                    |    |
|     | plane for a [110] reflection; (c) curve in $(1\overline{1}0)$ plane for a [111] reflection [148]. | 47 |
| 4.1 | (a) Tungsten hairpin filament of a thermionic emitter, (b) The energy-level                       |    |
|     | diagram of thermionic emission, the symbol E denotes the energy required                          |    |
|     | to transfer an electron from the lowest energy state within the metal to the                      |    |
|     | vacuum, (c) Tungsten field emission gun, (d) Energy-level diagram of field                        |    |
|     | emission, d denotes the potential barrier width [171]   | 51 |
| 4.2 | A schematic diagram of an electron microscope. The electron beam is illus-                        |    |
|     | trated in blue, while gray brackets indicate the lenses. Black bars represent                     |    |
|     | the apertures, and a red arrow signifies the specimen and its (intermedi-                         |    |
|     | ate) images. The trajectories of scattered electrons are shown in orange and                      |    |
|     | green [172]   | 52 |
| 4.3 | Schematic representation of (a) spherical aberration $(C_s)$ and (b) chromatic                    |    |
|     | aberration $(C_c)$ in an electron lens. $d_s$ and $d_c$ are the minimum diameters                 |    |
|     | for spherical and chromatic aberrated electron beams, respectively [171]                          | 54 |
| 4.4 | This diagram represents the optical paths and operational modes in a trans-                       |    |
|     | mission electron microscope (TEM). (a) diffraction mode, and (b) imaging                          |    |
|     | mode [168]  | 55 |

| 4.5  | Ray diagrams of imaging modes in a transmission electron microscope (TEM).    |    |
|------|---|----|
|      | (a) Bright-field (BF) mode, where the objective aperture selects the un-      |    |
|      | scattered (direct) beam. (b) Dark-field (DF) mode, with the objective aper-   |    |
|      | ture selecting a diffracted beam. (c) Centred DF imaging with a tilted        |    |
|      | incident beam [168]   | 56 |
| 4.6  | Electron optics in a scanning transmission electron microscope (STEM),        |    |
|      | showing the trajectory of electron beams as they pass through optical com-    |    |
|      | ponents such as condenser, objective, projector lenses and apertures. The     |    |
|      | diagram also shows the array of detectors used to capture transmitted elec-   |    |
|      | tron signals [179]  | 58 |
| 4.7  | Schematic of STEM detection geometry showing different detectors used for     |    |
|      | various angular ranges of scattered electrons[168]                            | 59 |
| 4.8  | Diagram of magnetic multipoles used for spherical aberration correction       |    |
|      | shows the top view of poles with alternating polarities [179]                 | 60 |
| 4.9  | A diagram of the trajectories of axial rays in the x and y directions through |    |
|      | the QO aberration corrector (with z along the optic axis) [180]               | 61 |
| 4.10 | Schematic cross section of alpha shaped monochromator of STEM column [182].   |    |
|      |   | 62 |
| 4.11 | Schematic of an electron energy loss spectroscopy (EELS) system illustrat-    |    |
|      | ing the dispersion of electrons through a magnetic prism, analogous to the    |    |
|      | dispersion of white light through a glass prism, with the formation of a      |    |
|      | spectrum in the dispersion plane [168]  | 65 |
| 4.12 | Example of an EELS spectrum highlighting key features, including the zero-    |    |
|      | loss peak, plasmon peak, and energy loss edges associated with specific ele-  |    |
|      | ments [168]   | 67 |
| 4.13 | Energy level diagrams illustrating Rayleigh, Stokes, and Anti-Stokes Raman    |    |
|      | scattering [193]  | 69 |
|      |   |    |

| 4.14 | Optical diagram of a Raman spectroscopy system. The setup includes a laser                         |    |
|------|--|----|
|      | source, spatial filters ( $D_1$ and $D_1$ ), beam splitter, microscope objective for               |    |
|      | focusing the beam on the sample, holographic filter, and a rotating grating                        |    |
|      | spectrometer for spectral analysis. The removable mirror allows the beam                           |    |
|      | to be directed to the eyepiece for visualisation or to the detector for Raman                      |    |
|      | signal acquisition[120]  | 70 |
| 4.15 | A schematic of the arrangement of an ion beam column, electron beam                                |    |
|      | column, Omniprobe needle, and Pt needle with respect to the sample in a                            |    |
|      | dual-beam system [200]   | 72 |
| 4.16 | A ray diagram detailing the key components of a FIB system, including the                          |    |
|      | suppressor, extractor, beam defining aperture, lenses, quadrupole, and the                         |    |
|      | sample [200]   | 73 |
| 4.17 | (a) Ion milled trenches adjacent to the platinum coated region, (b) attached                       |    |
|      | omniprobe with the platinum deposition, (c) lifting the sample out using                           |    |
|      | omniprobe, (d) the lamella near a TEM grid before attaching. (e) the lemalla                       |    |
|      | before coarse thinning, and (f) the final polished lemalla. $\dots$                                | 75 |
| 4.18 | Illustration of three modes of FIB: (a) imaging via secondary ions and elec-                       |    |
|      | trons, (b) milling by sputtering material, and (c) deposition using a Pt needle.                   | 76 |
| 4.19 | Schematic of ion-solid interactions in SIMS [205]  | 77 |
| 4.20 | Schematic diagram of the Hall effect measurement setup. A rectangular sil-                         |    |
|      | icon sample (dimensions: L × W × t) is placed in a perpendicular magnetic                          |    |
|      | field $(\mathbf{B}_z)$ , with a constant current $(\mathbf{I}_x)$ applied along its length. Due to |    |
|      | the Lorentz force, charge carriers are deflected, creating a transverse Hall                       |    |
|      | voltage $(V_H)$ across the width of the sample [210, 212]  | 81 |
| 5.1  | Schematic illustration of the self-consistent cycle for solving the Kohn–Sham                      |    |
|      | equations [219]  | 87 |

| 0.2 | Schematic inustration of the screened nuclear potential (solid lines) and                   |      |
|-----|---|------|
|     | pseudopotential (dashed lines), along with their corresponding wavefunc-                    |      |
|     | tions [222]   | 90   |
| 5.3 | Schematic of the multislice method, where the incident electron wavefunction                |      |
|     | is sequentially propagated through multiple slices of the projected crystal                 |      |
|     | potential. The diffraction intensity distribution is obtained by taking the                 |      |
|     | squared modulus of the Fourier-transformed exit wavefunction                                | 96   |
| 6.1 | Hall measurements of boron-doped silicon conducted across a temperature                     |      |
|     | range of 10 K to 320 K to determine the hole concentration                                  | 100  |
| 6.2 | Secondary Ion Mass Spectrometry (SIMS) profiling of boron-doped silicon                     |      |
|     | showing the signal from boron ( $^{11}$ B) and silicon ( $^{29}$ Si) isotopes               | 102  |
| 6.3 | Raman spectrum of elemental silicon (Si), low boron-doped silicon (Low-B-Si),               |      |
|     | and heavily (degenerate) boron-doped silicon (High-B-Si)                                    | 103  |
| 6.4 | (a) Diffraction pattern of degenerately boron-doped silicon oriented along                  |      |
|     | the [100] zone axis, with the selected $\Gamma$ -X- $\Gamma$ path defined by the slot aper- |      |
|     | ture (red rectangle) connecting the 000 and 004 reflections. (b) Momentum-                  |      |
|     | resolved EELS of degenerately boron-doped silicon showing the energy–momen                  | ntum |
|     | (ω-q) dispersion along the Γ-X-Γ direction  | 105  |
| 6.5 | (a) Momentum-resolved EELS dispersion measurements of phonons in de-                        |      |
|     | generate boron doped silicon. (b) Phonon dispersion curves of Si along                      |      |
|     | $\Gamma$ -X- $\Gamma$ , showing the transverse acoustic (TA), longitudinal acoustic (LA),   |      |
|     | transverse optical (TO), and longitudinal optical (LO) phonon branches                      | 106  |
| 6.6 | Parent spectrum, extracted from a narrow $q$ -range close to the direct beam                |      |
|     | (box region in Figure 6.5(a)), with background fit (inset) using power law                  |      |
|     | to isolate the phonon signal  | 107  |
| 6.7 | Gaussian fit of the high-energy optical modes associated with boron                         | 108  |
| 6.8 | Savitzky–Golay (S-G) filtered off-axis EELS spectrum for High-B-Si                          | 110  |

| 6.9  | Off-axis smoothed spectrum and the extracted inelastic signal plotted to-                                   |     |
|------|---|-----|
|      | gether for (a) Si, and (b) High-B-Si  | 111 |
| 6.10 | On-axis smoothed spectrum and the extracted inelastic signal plotted to-                                    |     |
|      | gether for (a) Si, and (b) High-B-Si  | 112 |
| 6.11 | Background subtracted off-axis EELS intensity for (a) Si, and (b) High-B-Si                                 |     |
|      | plotted alongside the background fit and the normalised smoothed spectrum.                                  | 113 |
| 6.12 | Background subtracted on-axis EELS intensity for (a) Si, and (b) High-B-Si                                  |     |
|      | plotted alongside the background fit and the normalised smoothed spectrum.                                  | 113 |
| 6.13 | Comparison of background subtracted signal of Si and High-B-Si for (a)                                      |     |
|      | off-axis, and (b) on-axis EELS collection geometries  | 114 |
| 6.14 | Difference spectrum obtained by subtracting the signal of Si from that of                                   |     |
|      | High-B-Si for both (a) off-axis, and (b) on-axis EELS spectra. The difference                               |     |
|      | spectrum is modelled by least squares fitting two Gaussian functions. The                                   |     |
|      | sum of the Gaussians is overlaid to evaluate the goodness of fit and the                                    |     |
|      | extent to which the Gaussian model captures the spectral features   | 116 |
| 6.15 | Variation of the total energy of a 64-atom silicon supercell containing a single                            |     |
|      | boron acceptor as a function of the plane-wave cutoff energy  | 119 |
| 6.16 | Variation of the total energy of a 64-atom silicon supercell containing a single                            |     |
|      | boron acceptor as a function of the $k\text{-point}$ grid density   | 120 |
| 6.17 | Structural configurations of, (a) a single boron acceptor $(B^-)$ , (b) two nearest-                        |     |
|      | neighbour ionised boron acceptors $(2B^-)$ , $(c)$ a neutral boron interstitial                             |     |
|      | $(\mathbf{B}_i^0)$ , and (d) two boron interstitials cluster $(2\mathbf{B}_i^0)$ , boron defects in silicon |     |
|      | as viewed along [001]. Red and blue atoms represent boron and silicon                                       |     |
|      | atoms, respectively   | 122 |

| 6.18 | Structural configurations of boron defects in silicon as viewed along [001].                     |     |
|------|--|-----|
|      | (a) The boron interstitial cluster $(2B_i^0)$ with two neutral boron atoms in                    |     |
|      | interstitial sites.<br>(b) Boron interstitial cluster (3B $^0_i$ - confi 1) with three neut-     |     |
|      | ral boron atoms illustrates a tightly bound trio of interstitials. (c) Boron                     |     |
|      | interstitial cluster (3 $\mathbf{B}_{i}^{0}$ - confi 2) shows three neutral boron atoms arranged |     |
|      | in a linear fashion, forming a less compact structure. (d) Boron interstitial                    |     |
|      | cluster $(3B_i^0$ - confi 3) shows a linear arrangement with alternating boron                   |     |
|      | interstitial atoms and empty interstitial spaces   | 123 |
| 6.19 | Silicon supercell containing an octahedrally shaped $6\mathrm{B}_i^0$ interstitial cluster,      |     |
|      | viewed along the [111] crystallographic direction. (a) Initial configuration                     |     |
|      | of the cluster before geometry optimisation. (b) Relaxed configuration after                     |     |
|      | geometry optimisation, showing the local distortion and strain induced in                        |     |
|      | the surrounding silicon lattice  | 127 |
| 6.20 | Phonon dispersion curves of a single boron acceptor defect in an 8-atom                          |     |
|      | silicon cell along the $\Gamma \to X$ direction. The phonon branches are folded due              |     |
|      | to the larger cell size  | 128 |
| 7.1  | Indexing of the electron diffraction pattern from boron doped Si along $[\bar{1}11]$ .           | 133 |
| 7.2  | STEM HAADF images of (a) Si, and (b) High-B-Si   | 135 |
| 7.3  | Selected Area Electron Diffraction Patterns (SADPs) of silicon (Si) and                          |     |
|      | heavily boron-doped silicon (High-B-Si). (a) [100] zone axis SADP of Si,                         |     |
|      | (b) [100] zone axis SADP of High-B-Si  | 136 |
| 7.4  | Selected Area Electron Diffraction Patterns (SADPs) of silicon (Si) and                          |     |
|      | heavily boron-doped silicon (High-B-Si). (a) [110] zone axis SADP of Si,                         |     |
|      | and (b) [110] zone axis SADP of High-B-Si  | 137 |

| 7.5  | Selected Area Electron Diffraction Patterns (SADPs) of silicon (Si) and                  |     |
|------|--|-----|
|      | heavily boron-doped silicon (High-B-Si). (a) [100] zone axis SADP of Si,                 |     |
|      | (b) [100] zone axis SADP of High-B-Si, (c) [110] zone axis SADP of Si,                   |     |
|      | and (d) [110] zone axis SADP of High-B-Si. The SADPs are displayed in a                  |     |
|      | logarithmic intensity scale  | 138 |
| 7.6  | Intensity profiles comparison of symmetrical diffraction spots for elemental             |     |
|      | silicon (Si) and heavily boron-doped silicon (High-B-Si) along the (a) [100]             |     |
|      | and (b) [110] zone axes  | 141 |
| 7.7  | Gaussian fit of the diffraction peaks for silicon (Si) and boron-doped silicon           |     |
|      | (H-B-Si) from the $02\bar{2}$ diffraction spot for a) the [100] zone axis of silicon and |     |
|      | b) the [100] zone axis of boron-doped silicon, and from the 002 diffraction              |     |
|      | spot for c) the [110] zone axis of silicon and d) the [110] zone axis of boron-          |     |
|      | doped silicon  | 142 |
| 7.8  | Projection view of the interstitial boron cluster system (High-B-Si-int) along           |     |
|      | the (a) [100], and (b) [110] zone axes. The red atoms represent silicon, and             |     |
|      | the blue atoms represent boron   | 145 |
| 7.9  | Simulated SADPs for (a) Si, (b) High-B-Si-int, and (c) High-B-Si-acc along               |     |
|      | the [100] zone axis, all displayed on a logarithmic intensity scale. Panel               |     |
|      | (d) shows the corresponding radial intensity profiles extracted from each                |     |
|      | pattern, plotted on a logarithmic scale.   | 146 |
| 7.10 | Simulated SADPs for (a) Si, (b) High-B-Si-int, and (c) High-B-Si-acc along               |     |
|      | the [110] zone axis, all displayed on a logarithmic intensity scale. Panel               |     |
|      | (d) shows the corresponding radial intensity profiles extracted from each                |     |
|      | pattern, plotted on a logarithmic scale  | 147 |
| 7.11 | Magnitude of silicon atomic displacements as a function of distance from the             |     |
|      | boron site for a a) single acceptor boron configuration (High-B-Si-acc), and             |     |
|      | (b) single interstitial boron configuration (High-B-Si-single-int)                       | 149 |
|      |  |     |

| 7.12 | Comparison of radial intensity profiles for Si and High-B-Si along the [100]                    |     |
|------|---|-----|
|      | axis  | 150 |
| 7.13 | Comparison of radial intensity profiles for Si and High-B-Si along [110] zone                   |     |
|      | axis  | 151 |
| 7.14 | Comparison of radial intensity profiles for Si, High-B-Si-acc, and High-B-                      |     |
|      | Si-int, calculated along (a) the $[100]$ and (b) the $[110]$ zone axes The                      |     |
|      | intensity profiles were extracted from frozen phonon multislice simulations.                    | 152 |
| 7.15 | Comparison of background-subtracted EELS spectra of the fifth plasmon                           |     |
|      | peak of Al at room temperature (25 °C) and cryogenic temperature (–176 °C                       | 156 |
| 7.16 | Radial intensity profiles extracted from SADPs acquired along the $[100]$ zone                  |     |
|      | axis for Si and High-B-Si at room temperature and cryogenic temperatures.                       | 157 |
| 7.17 | Simulated SADPs for (a) Si, (b) High-B-Si-acc, and (c) High-B-Si-int at                         |     |
|      | $-152~^{\circ}\mathrm{C},$ displayed on a logarithmic intensity scale, with corresponding high- |     |
|      | angle radial intensity profiles comparison shown in (d)   | 158 |
| 7.18 | Simulated SADPs for (a) High-B-Si-acc, and (b) High-B-Si-int at 0K, dis-                        |     |
|      | played on a logarithmic intensity scale   | 160 |
| 8.1  | Phonon dispersion curves of silicon along $\Gamma$ - $K$  | 163 |
| 8.2  | SADP of silicon acquired along the $[100]$ zone axis at room temperature                        | 167 |
| 8.3  | (a) Comparison of the theoretical first-order TDS intensity and mean exper-                     |     |
|      | imental TDS intensity as a function of scattering vector magnitude $Q$ with                     |     |
|      | error bars of $\sigma$ , and (b) Residuals between experimental and first-order TDS             |     |
|      | intensities   | 168 |
| 8.4  | (a) Comparison of the optimised theoretical first-order TDS intensity and                       |     |
|      | mean experimental TDS intensity (Equation 8.8) as a function of scatter-                        |     |
|      | ing vector magnitude $Q$ with error bars of $\sigma$ , and (b) Residuals between                |     |
|      | experimental and first-order TDS intensities  | 171 |

| 0.0  | a) Comparison of the experimental 1D5 intensity with the optimised model             |     |
|------|--|-----|
|      | (Equation 8.10) incorporating a scaled theoretical TDS curve and an ex-              |     |
|      | ponential background of the form $\exp(-bQ^2)$ , and b) Residuals between            |     |
|      | experimental and first-order TDS intensities   | 173 |
| 8.6  | Comparison of the theoretical first-order TDS intensities computed at 300K           |     |
|      | and 123K   | 174 |
| 8.7  | Comparison of the experimental intensities computed at 300K and 123K. $$ .           | 175 |
| 8.8  | a) Comparison of the theoretical first-order TDS intensity and mean ex-              |     |
|      | perimental TDS intensity as a function of scattering vector magnitude $Q$            |     |
|      | with error bars of $\sigma$ at 123 K, and b) Residuals between experimental and      |     |
|      | first-order TDS intensities  | 176 |
| 8.9  | (a) Comparison of the optimised theoretical first-order TDS intensity (Equa-         |     |
|      | tion 8.8) and mean experimental TDS intensity as a function of scattering            |     |
|      | vector magnitude $Q$ with error bars of $\sigma$ at 123 K, and (b) Residuals between |     |
|      | experimental and first-order TDS intensities   | 178 |
| 8.10 | (a) Comparison of the optimised theoretical first-order TDS intensity (Equa-         |     |
|      | tion 8.10) and mean experimental TDS intensity as a function of scattering           |     |
|      | vector magnitude $Q$ with error bars of $\sigma$ at 123 K, and (b) Residuals between |     |
|      | experimental and first-order TDS intensities   | 179 |

# **List of Tables**

| 6.1 | Formation energies of boron point defect configurations in silicon. Numbers  |     |
|-----|--|-----|
|     | within brackets denote the formation energy per atom                         | 126 |
| 6.2 | Vibrational wavenumbers of boron point defect configurations in silicon. The |     |
|     | defect phonon modes for a $B^-$ acceptor are triply degenerate               | 130 |

## Thesis overview

## 1.1 Motivation

Semiconductor materials are necessary for modern electronics based technologies, forming the backbone of numerous devices that have transformed our lives, communication, and computing. Their applications stretch over a variety of electronic devices, including diodes[1], transistors [2], integrated circuits (ICs) [3], light-emitting diodes (LEDs) [4], solar cells, and sensors [5]. Semiconductors were first observed by Michael Faraday in 1833 [6], although their practical applications began with the invention of the first metal-semiconductor junction device [7]. Since silicon (Si) emerged as the material with most favourable properties in the 1930s [8], the semiconductor industry's advancements were rapid which led to an entirely new field in solid state electronics [9].

These advancements in electronics were significantly accelerated by the introduction of the Metal-Oxide-Semiconductor-Field-Effect-Transistor (MOSFET) in 1960 [10]. Today, the majority of semiconductor devices manufactured heavily depend on silicon in their construction. During the final decades of the 20th century, there was a rapid production of integrated circuits, where numerous transistors were etched into a single device. Initially, such a device may have contained a fewer separate semiconductor devices. However, today, these circuits contain billions of transistors. This has lead to a wide-spread adoption of technologies such as cell phones, GPS devices, laptops, tablets, and

our global communications infrastructure [11]. Figure 1.1 shows how the number of transistors in a single integrated circuit increased over time, described by Moore's Law which is an empirical law coming from economics[12].

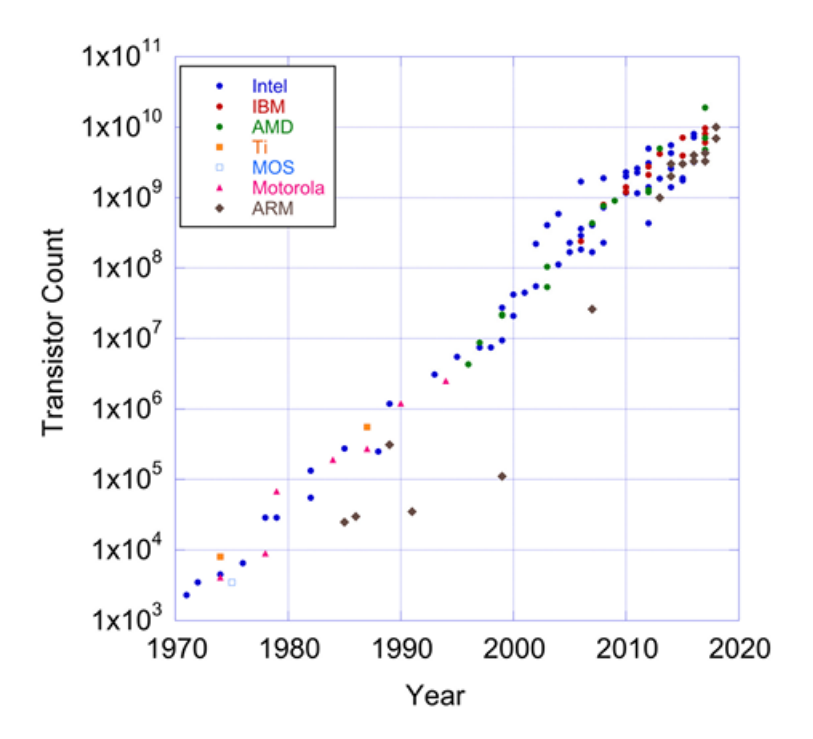


Figure 1.1: The increase in transistors count on a given IC by year for several manufacturers[12].

The presence of defects in semiconductors can significantly impact device performance as scaling increases. Understanding the physics of defects is essential in exploring the physical properties of semiconductor materials. These include zero-dimensional defects, i.e, point defects, one-dimensional (linear) defects such as dislocations, two-dimensional (planar) defects encompassing external and internal surfaces, and three-dimensional (volume) defects like point defect clusters, voids, and precipitates [13]. This thesis exclusively examines point defects and clusters. Point defects in crystals can be intrinsic (native defects, such as vacancy and interstitial) which involve atoms of the host crystal, or extrinsic which involves intentional and unintentional 'impurity' atoms [14, 15].

The performance of semiconductor devices is highly dependent on the concentration

of both native defects and intentionally introduced impurities within the lattice structure. Point defects influence the optical, electrical, and mechanical characteristics of the host semiconductor materials. They introduce electronic levels into the energy bandgap of the semiconductors [16]. Point defects also introduces localised vibrational modes that might affect the material's thermal conductivity [17, 18]. Other significant effects include:

- 1) Point defects serve as scattering centres for electrons and holes travelling through the crystal, which decreases charge carriers mobility. Additionally, they can create deep-level traps within the bandgap, impacting the semiconductor's conductivity [19–21].
- 2) Point defects introduce localised states which can influence the spin-photon interaction in devices designed to store and transfer quantum information, playing essential roles in applications such as quantum computing, sensing, and networking [22].
- 3) The change in yield strength due to a point defect is attributed to the alteration of the crystal's stress state. This occurs because the point defect induces stress concentrations in its vicinity, thereby affecting the material's overall strength [23].

Extensive research has to be conducted to characterise, and either eliminate these defects or effectively manage their behaviour. A variety of experimental as well as simulation techniques have been developed to acquire detailed information about these defects properties. This thesis explores two such methods.

Electron microscopy, including transmission electron microscopy (TEM) and scanning transmission electron microscopy (STEM), is a powerful tool for characterising point defects in semiconductors. One of the primary advantages of electron microscopy over X-ray and neutron diffraction methods is its spatial resolution [24]. Electron microscopes can achieve atomic-scale resolution, allowing for the direct observation of individual defects [25].

X-ray diffraction and neutron scattering, while valuable for certain types of structural analysis, have limitations when it comes to defect analysis. X-ray diffraction provides

information about the overall crystal structure and can detect changes in lattice parameters caused by defects [26, 27]. However, X-ray diffraction typically lacks the spatial resolution needed to observe individual point defects or defect clusters [24, 28]. X-rays interact with a large volume of the sample, which means that fine details about local defects are often averaged out [29]. Additionally, X-ray techniques are less effective for studying light elements due to weaker scattering [30], such as boron in silicon, which is a primary focus of this thesis.

Additionally, X-rays interact entirely with the electronic cloud surrounding the atomic nucleus, with negligible scattering by the nucleus itself. This interaction leads to a phase mismatch for scattering from individual electrons at higher scattering angles, resulting in an intensity reduction described by the conventional X-ray form factor. The form factor decreases with larger scattering vectors  $\mathbf{k}$ , making X-ray diffraction less effective for detecting point defects compared to electron microscopy, as the form factor is even more pronounced since scattering from the nucleus is higher due to a nuclear scattering contribution [31].

Neutron scattering, although sensitive to lighter elements [32], is less effective for defect detection due to its isotropic scattering amplitude [33], which arises from interactions with the atomic nucleus rather than the electron cloud. Therefore, neutron scattering is not suitable for detailed defect analysis compared to electron microscopy. Additionally, neutron experiments typically involve sample volumes much larger than X-rays, which further limits their effectiveness in observing defects at the atomic scale.

First-principles calculations offer powerful tools for exploring the properties of defects in semiconductors and insulators. Advanced techniques such as density functional theory (DFT) [34] allow for quantitative predictions of electronic and atomic structures, as well as optical properties [35]. Comparing these predictions with experimental results from techniques such as STEM helps identifying the nature and local structure of the defect and evaluate the suitability of materials for device applications.

DFT is a quantum mechanical method used to investigate the electronic structure of many-body systems at the atomic scale. By solving the Kohn-Sham equations [36], DFT enables the calculation of electronic density, which in turn allows for the derivation of various material properties [37]. One of the significant advantages of DFT in the context of defect analysis is its ability to provide insights into the vibrational properties of materials, which are directly affected by the presence of point defects. Defects lead to local vibrational modes (LVMs), whose frequencies and polarisations reveal information about the chemical nature of the involved atoms and their bonding environment [38]. The vibrational properties, phonon dispersion spectra, reflect how atoms oscillate around their equilibrium positions and are sensitive to changes induced by defects [39]. These changes can be quantitatively assessed using DFT, which helps in understanding how defects affect material performance.

## 1.2 Aim of this thesis

The aim of this thesis is to investigate the effects of degenerate boron doping in silicon through a comprehensive approach combining experimental electron microscopy techniques and advanced simulations, including multislice simulations for electron scattering and density functional theory (DFT) calculations of phonon properties using CASTEP.

Boron is a p-type dopant in silicon and is widely used in the semiconductor industry. It also shows anomalous behaviour, which motivates its study in this thesis. The primary objective is motivated by previous observations reported by Perovic *et al.*, who noticed an unexpectedly strong high-angle annular dark-field (HAADF) contrast, as in Figure 1.2, in degenerate boron-doped silicon (B-Si) compared to pure silicon (Si), despite the lower atomic number of boron [40].

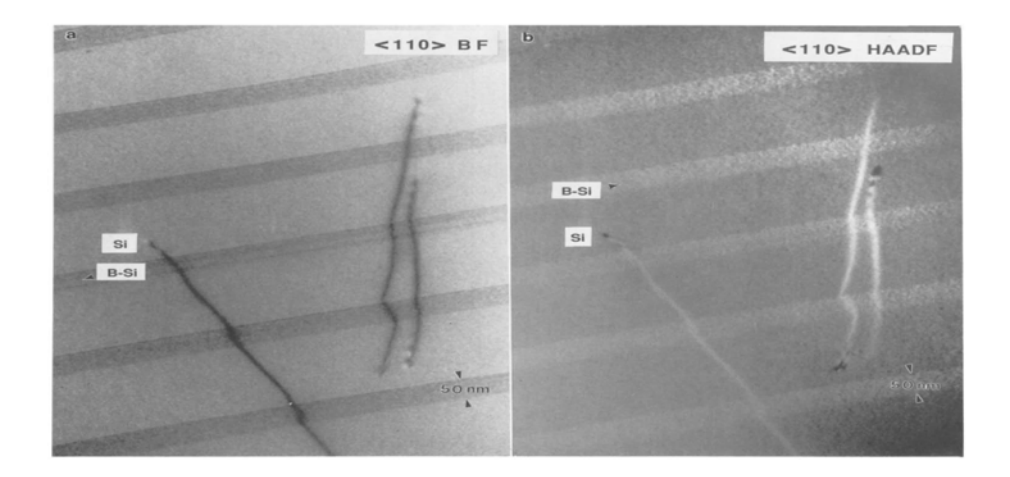


Figure 1.2: Image of Si containing 50 nm B-Si layers as viewed along  $\langle 110 \rangle$  zone axis. Threading dislocation segments are also visible under the following imaging conditions: (a) bright field (BF), and (b) high angle annular dark field (HAADF) [40].

Two potential explanations for this anomalous contrast are considered: first, static atomic displacements of silicon atoms from their equilibrium lattice sites adjacent to substitutional boron atoms, which may result in so-called "Huang" contrast; and second, the introduction of boron leading to local vibrational modes above the optical mode frequency of 16 THz, thereby modifying high angle thermal diffuse scattering (TDS).

To address these aspects, this thesis employs transmission electron microscopy (TEM) in selected area diffraction pattern (SADP) mode at both room and cryogenic (liquid nitrogen) temperatures to analyse the strain fields around boron atoms in silicon and their effect on high-angle scattering. Additionally, multislice simulations are performed to further understand how strain from boron doping influences high-angle scattering.

Recent advancements in aberration-corrected scanning transmission electron microscopy (STEM), combined with improvements in spectrometers and monochromators, have led to STEM systems capable of achieving atomic resolution with electron energy loss spectroscopy (EELS) at energy resolutions around 5 meV [41]. One of the main applications of EELS in this context is the study of phonon lattice vibrations, which typically occur within the range of a few meV to 1 eV, especially at large scattering

angles (10 -1000 mrad) [42-44]. This thesis also utilises aberration corrected STEM with monochromated EELS to directly measure the vibrational frequencies of boron-doped silicon. This experimental data is complemented by density functional theory (DFT) calculations to validate and interpret the observed vibrational frequencies. Specifically, we conduct DFT-based vibrational studies using the CASTEP software to calculate the phonon dispersion curves of boron doped silicon. The theoretical phonon dispersion curves obtained from these DFT calculations will be compared against STEM EELS experimental data to assess the accuracy and reliability of the theoretical models.

Furthermore, this thesis aims to bridge the gap between experimental and theoretical approaches in understanding phonon dynamics in silicon by developing and implementing a novel methodology for extracting phonon dispersion curves from electron diffraction patterns of elemental silicon, and to rigorously compare these experimental results with theoretical phonon dispersion curves derived from first order thermal diffuse scattering intensity.

This part of the work was stimulated by similar measurements on silicon using X-ray diffraction by Xu and Chiang, where they used experimental X-ray TDS diffraction patterns (Figures 1.3a and 1.3b), in combination with a theoretical Born-von Karman model (Figures 1.3c and 1.3d) to determine phonon frequencies in silicon. By fitting the experimental TDS data to the theoretical TDS calculations, they successfully extracted accurate phonon dispersion relations, which describe the variation of phonon frequencies with respect to the momentum in the crystal [45]. Extension of this method to electron diffraction provides additional benefits over X-rays, such as an improvement in the spatial resolution and less demand on the sample quality, i.e. polycrystalline samples can be used instead of single crystals, provided the grain size is large enough for acquiring a SADP of a single grain.

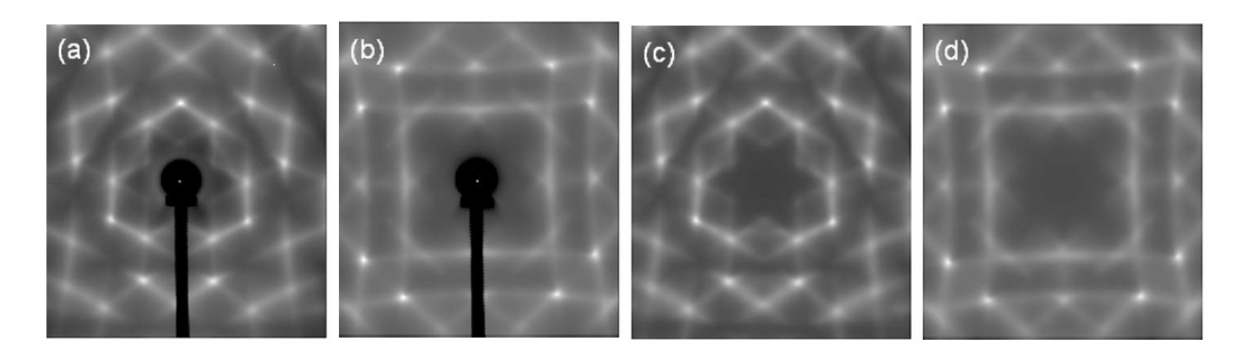


Figure 1.3: Experimental TDS images of Si for (a) [111] and (b) [100] zone axes, along with theoretical first-order TDS calculations for (c) [111] and (d) [100] [45].

# Introduction

Since most modern information processing and electronic devices depends critically on the purity and perfection of semiconductor materials, it is important to investigate the fundamental physics behind their crystallinity, including impurities and defects. Therefore, the intention of this chapter is to review and summarise the importance of semiconductors, their crystal structures, their electronic and vibrational properties and to explore how their lattice structures are impacted by doping, leading to defects and changes in their structural and vibrational properties.

There are certain substances that are neither good conductors (e.g. metals) nor insulators (e.g. glass). A substance which has a crystalline structure and contains very few free, conduction electrons at room temperature is called a semiconductor. More precisely semiconductors are materials whose energy band gap ( $E_g$ ) is typically between 0 eV and 3 eV [46]. There are a few exceptions to this definition, such as diamond and gallium nitride (GaN), whose energy band gaps are about 5.5 eV and 3.5 eV, respectively. While silicon stands as the most widely used semiconductors, numerous others exist beyond it, e.g. naturally occurring minerals such as zincblende (ZnS) [47]. Semiconductors are found in a wide array of chemical compositions with a large variety of crystal structures. They can be elemental semiconductors, such as Si, compounds such as antimony selenide (Sb<sub>2</sub>Se<sub>3</sub>) or organic compounds, e.g. polyacetylene (CH)<sub>n</sub> [48, 49]. Semiconductors can be classified into two categories; intrinsic semiconductors where

the concentration of electrons and holes are equal, and extrinsic semiconductors which contain added impurities through a process called doping [50], discussed in detail in section 2.4.

One of the main reason why semiconductors plays a vital role in electronic applications is that their conductivity can be manipulated by factors such as temperature, illumination, and minute amount of impurity atoms [51]. Electrical conductivity ( $\sigma$ ) of a material is determined by two factors: the concentration of free carriers available to conduct current and their mobility:

$$\sigma = q[\mu_n(T)n(T) + \mu_p(T)p(T)]. \tag{2.1}$$

where q is the magnitude of the electron charge,  $\mu_n$  and  $\mu_p$  refer to the mobilities of the electrons and holes, and n and p refer to the number density of electrons and holes, respectively. In a semiconductor, both mobility and carrier concentration are temperature (T) dependent, and there are a variety of possible temperature dependencies for conductivity [52]. As some useful properties of semiconductors, such as conductivity and sensitivity to strain, can easily be influenced by the crystal structure, it is crucial to understand the specific arrangement and periodicity of atoms in semiconductors in order to investigate these useful properties [53].

## 2.1 Crystal structure

#### 2.1.1 Primitive lattice

An ideal crystalline solid is represented by atoms or group of atoms called a 'basis' that repeat regularly throughout the material, as if they were connected to an underlying set of points with corresponding periodicity. These points in space are not physical entities but rather an analytical construct derived from studying the geometric arrangement of the crystal. The collection of these mathematical points where the basis is attached is referred to as the 'lattice' [54]. In three dimensions, the lattice can be defined in terms

of three translational vectors denoted by  $\mathbf{a}_1$ ,  $\mathbf{a}_2$  and  $\mathbf{a}_3$  from symmetry. One then can express a vector  $\mathbf{R}$  connecting any two lattice points in a crystal as

$$\mathbf{R} = u\mathbf{a}_1 + v\mathbf{a}_2 + w\mathbf{a}_3,\tag{2.2}$$

where, u, v and w are arbitrary integers. The complete set of such vectors is called a Bravais lattice, and the generated lattice will have translational symmetry. Hence, the crystal looks the same when viewed from the point  $\mathbf{r}$  as well as every point  $\mathbf{r}'$  if  $\mathbf{r}' = \mathbf{r} + \mathbf{R}$  [46]. The primitive cell of a lattice represents the smallest volume that, when translated through the entire Bravais lattice, it fills all the space through periodic repetition [55].

## 2.1.2 Some important crystal lattices

There exists 14 types of Bravais lattices. For metals and semiconductors the atoms in a lattice tend to arrange themselves in close-packed structures. The most basic close-packed structures exhibit either cubic or hexagonal symmetry. Cubic crystals are more symmetrical than other crystal structures and their symmetry is easier to visualise directly. Figures 2.1a, 2.1b and 2.1c shows the simple cubic (SC), body-centred cubic (BCC), and face-centred cubic (FCC) structures. The SC unit cell has lattice points only at the cube corners and is not therefore common. The BCC unit cell has lattice points at the cube corners and an additional lattice point at the centre of the cube, while the FCC unit cell has additional lattice points at the centre of each cube face [56]. In both diamond and zincblende crystal structures the basis consists of two atoms, shown in Figures 2.1d and 2.1e. The two atoms are separated by a  $\frac{1}{4}$ [111] vector. The only difference is that the basis in the diamond structure (Figure 2.1d) consists of two silicon atoms, while in zincblende (Figure 2.1e) the two atoms are zinc and sulfur [57].

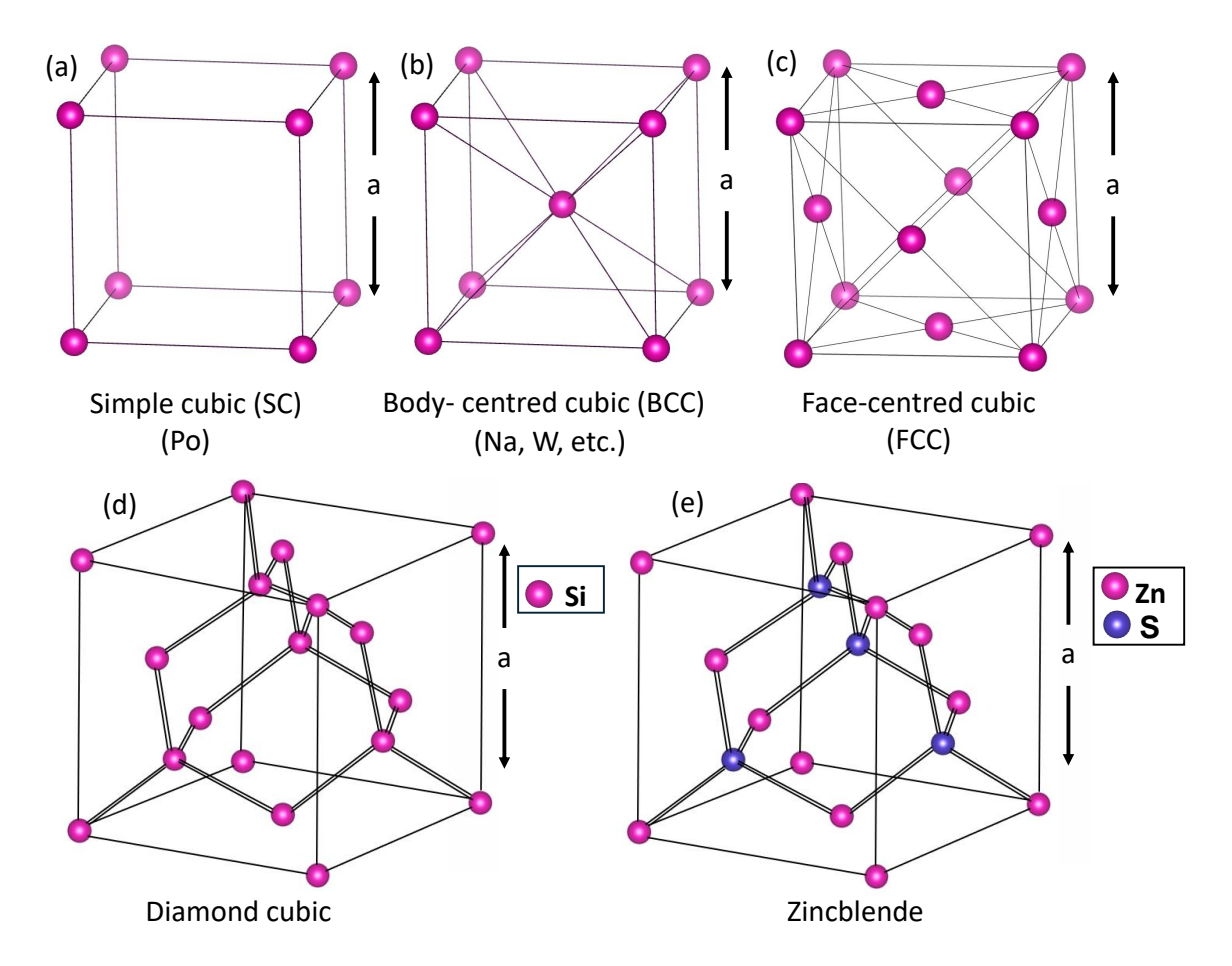


Figure 2.1: Some important unit cells characterising crystalline solids.(a) The simple cubic (SC) unit cell, (b) the body centered cubic (BCC) unit cell, (c) the face-centred cubic (FCC) unit cell, (d) diamond cubic unit cell, (e) zincblende unit cell [58].

## 2.1.3 Crystal planes, crystal Directions and Miller indices

Since many physical properties are dependent on the plane and the direction in the crystal lattice [59], it is important to define a particular lattice direction and plane. A convenient method of defining crystal directions and planes in a crystal is to use Miller indices. The figure 2.2 below shows Miller indices for some significant planes and directions.

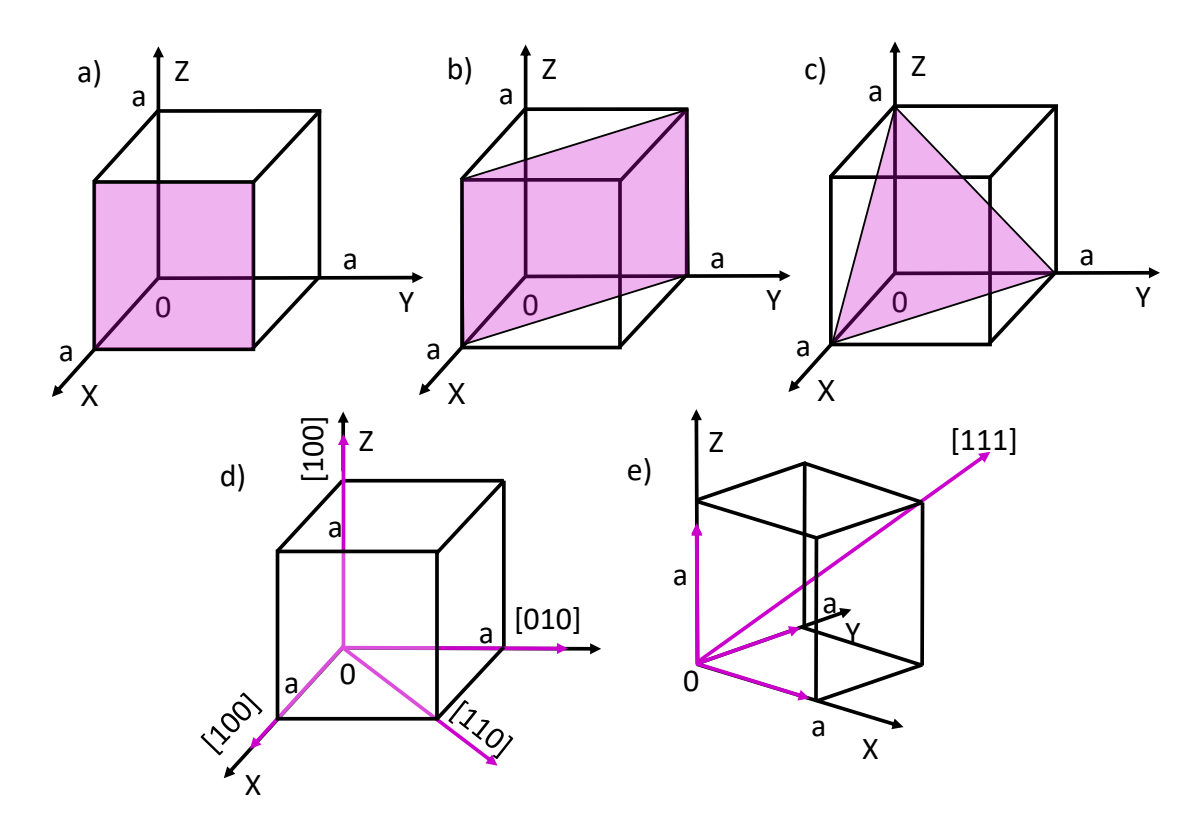


Figure 2.2: Miller indices for some significant planes and directions in a cubic crystal. (a) (100) plane, (b) (110) plane, (c) (111) plane, (d) family of  $\langle 100 \rangle$  directions, and (e) [111] direction [60].

For a given crystal plane, the corresponding Miller indices can be determined by finding the intercepts on each of the  $\mathbf{a}_1$ ,  $\mathbf{a}_2$ ,  $\mathbf{a}_3$  axes, and then taking the reciprocal of these intercepts. Three integers h, k and l are assigned to the plane, such that their ratios correspond to the ratios of the reciprocal intercepts [61]. The three integers h, k and l are called the Miller indices, and the lattice is expressed in reciprocal space using these integers. The integers enclosed in a round brackets (hkl) denotes the planes in a crystal, and square brackets [uvw] denotes specific directions in a crystal. If a plane intersects an axis on the negative side of the origin, its corresponding index is negative, denoted by placing a minus sign above the index, e.g.  $(h\overline{k}l)$ . The indices [uvw] of a direction in a lattice is represented by a set of three integers that maintain the same ratio as the components of a vector in that direction. These vector components, as in Equation 2.2, are expressed as multiples of the basis vectors, and the integers are reduced to their smallest values while preserving their proportional relationship [60].

Since many planes and directions in a lattice are equivalent due to symmetry, the indices of such equivalent planes and directions are collectively denoted by curly brackets and angle brackets (Figure 2.2d), respectively, e.g.  $\{hkl\}$  and  $\langle uvw \rangle$  [62].

## 2.1.4 Reciprocal lattice

Because of the periodicity of the real crystal lattice, a function in real space can be expressed as a Fourier series in terms of the reciprocal space translation vector  $\mathbf{G}$ . The set of reciprocal lattice basis vectors  $\mathbf{a}_1^*$ ,  $\mathbf{a}_2^*$  and  $\mathbf{a}_3^*$  are related to the direct lattice vectors  $\mathbf{a}_1$ ,  $\mathbf{a}_2$  and  $\mathbf{a}_3$  by

$$\mathbf{a}_{i}^{*} = 2\pi \frac{\mathbf{a}_{j} \times \mathbf{a}_{k}}{\mathbf{a}_{1} \cdot (\mathbf{a}_{2} \times \mathbf{a}_{3})}.$$
(2.3)

where i, j, and k represent a cyclic permutation of the three indices 1, 2, and 3 and  $\mathbf{a}_1 \cdot (\mathbf{a}_2 \times \mathbf{a}_3)$  is the volume of the primitive cell [63]. By defining the reciprocal lattice vectors in this manner, it imposes the condition that  $\mathbf{a}_i \cdot \mathbf{a}_j^* = 2\pi \delta_{ij}$ , where  $\delta_{ij}$  is the Kronecker delta symbol. The general reciprocal lattice vector  $\mathbf{G}$  is then given by

$$\mathbf{G} = h\mathbf{a}_1^* + k\mathbf{a}_2^* + l\mathbf{a}_3^*. \tag{2.4}$$

A significant characteristic of the Bravais lattice and reciprocal lattice vectors is that they satisfy:

$$\mathbf{G} \cdot \mathbf{R} = 2\pi \mathbf{I}.\tag{2.5}$$

Where, I is an integer. The primary advantage of the reciprocal lattice is its ability in describing functions that exhibit the periodicity of the lattice. Hence, it can be expressed as plane waves with the periodicity of the Bravais lattice [57]:

$$e^{i\mathbf{G}\cdot(\mathbf{r}+\mathbf{R})} = e^{i\mathbf{G}\cdot\mathbf{r}}e^{i\mathbf{G}\cdot\mathbf{R}} = e^{i\mathbf{G}\cdot\mathbf{r}}.$$
 (2.6)

The reciprocal lattice vectors have dimensions of inverse length, meaning they are not present in the typical real space but rather in what is known as **k**-space, where '**k**' represents the wave vector with inverse length dimensions. As the momentum of a particle is expressed as  $\hbar \mathbf{k}$ , this space is also called as momentum space ( $\hbar$  is the reduced Planck's constant) [52].

#### 2.1.5 Brillouin zone

The primitive cell of a reciprocal lattice can be represented by a Wigner-Seitz (WS) cell by drawing perpendicular planes that bisect the lines connecting the origin to all the nearest neighbour lattice points. The irreducible WS cell in  $\mathbf{k}$  space consisting of all points  $\mathbf{k}$  is referred to as the first Brillouin zone [64]. The construction of the Brillouin zone is very convenient for describing many crystal properties, such as electronic structures and phonon structures of crystals [62]. In the Brillouin zone, several points hold special significance and are assigned individual symbols using abbreviations derived from group theory, such as  $\Gamma$ , L, K, X, etc. [65].

For a face centred cubic crystal,  $\Delta$  represents a direction, such as [100], intersecting the zone boundary at X, situated in the midpoint of a square face (Figure 2.3),  $\Lambda$  represents the [111] direction, perpendicular to the close-packed planes of the face-centered structure, and intersects the midpoints of the hexagonal faces of the zone at L. [110] direction denoted by  $\Sigma$ , meeting the boundary at K, positioned in the midpoint of an edge shared by two hexagons [66]. Among these, the most crucial point is where  $\mathbf{k} = 0$ , which is the centre of the first Brillouin zone, this particular location in  $\mathbf{k}$ -space is referred to as the  $\Gamma$  point [65]. Figure 2.3 shows the first Brillouin zone with high-symmetry points labeled for a face-centered cubic lattice [67]. In this case, the Brillouin zone is a truncated octahedron. For certain Bravais lattices, the Brillouin zone exhibits a distinct shape. However, for some Bravais lattices, the shape of the Brillouin zone can vary, depending on the axial ratios and inter-axial angles of the lattice [68].

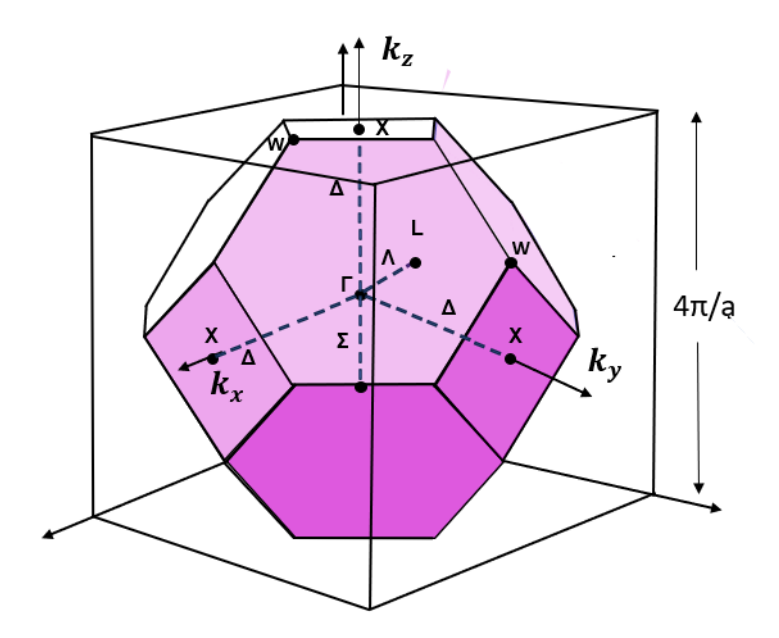


Figure 2.3: Depiction of the first Brillouin zone for the face-centered cubic lattice (FCC) with lattice constant **a**. Several high-symmetry points are highlighted:  $\Gamma = (0, 0, 0)$ ,  $X = \frac{2\pi}{a}(1, 0, 0)$ ,  $L = \frac{2\pi}{a}(0.5, 0.5, 0.5)$ ,  $W = \frac{2\pi}{a}(1, 0.5, 0)$  [67].

## 2.2 Electronic band structure

The behaviour of electrons within semiconductors can be described by solving the Schrödinger equation appropriate to the crystal's structure. These solutions, which are the collection of electron energies, yield the electronic band structure of the electrons, and can be determined using techniques like tight binding, pseudopotential, orthogonalised plane wave, and perturbative methods. When analysing band structure, the complexity reduces significantly when dealing with crystalline materials as electrons encounter a periodic potential due to the repeating structure of those materials [69]. In a perfect crystalline lattice, due to the translation symmetry, the potential energy  $V(\mathbf{r})$  of a crystal lattice satisfies  $V(\mathbf{r} + \mathbf{R}) = V(\mathbf{r})$ . Since the potential is periodic, the electron wavefunction  $\Psi_{\mathbf{k},n}(\mathbf{r})$  can be written as the product of a periodic function  $u_{\mathbf{k},n}(\mathbf{r})$  and a plane wave  $e^{i\mathbf{k}\cdot\mathbf{r}}$  [70], which is a Bloch function of the form,

$$\Psi_{\mathbf{k},n}(\mathbf{r}) = e^{i\mathbf{k}\cdot\mathbf{r}} u_{\mathbf{k},n}(\mathbf{r}). \tag{2.7}$$

where  $u_{\mathbf{k},n}(\mathbf{r}) = u_{\mathbf{k},n}(\mathbf{r}+\mathbf{R})$  has the same periodicity as the potential and is a function of  $\mathbf{k}$ . For every value of the wave vector  $\mathbf{k}$ , there exists an infinite set of eigenfunctions with varying u, labeled by n [64]. Given that a real macroscopic crystal is effectively 'infinite' with approximately  $10^{23}$  atoms or molecules, the set of  $\mathbf{k}$  values densely populates  $\mathbf{k}$  space. Consequently, the energy levels of a crystal can be confined to the first Brillouin zone, accounting for the translation symmetry of the crystal [71]. By solving the Schrödinger equation using Bloch wave functions, the eigenvalues  $E_n(\mathbf{k})$ , which is a continuous function of  $\mathbf{k}$  can be obtained. A plot of the eigenvalues  $E_n(\mathbf{k})$  versus the wave vector  $\mathbf{k}$  is known as the electronic band structure. Since the electron energies of a crystal are continuous, they are represented by energy bands whose widths are determined by the the overlap of the Bloch wavefunctions within the crystal [67]. Forbidden energy band gaps are also formed where no electrons are allowed. Figure 2.4 shows a schematic of the energy bands for tetravalent elements such as silicon (Si), and germanium (Ge) in relation to atomic spacing.

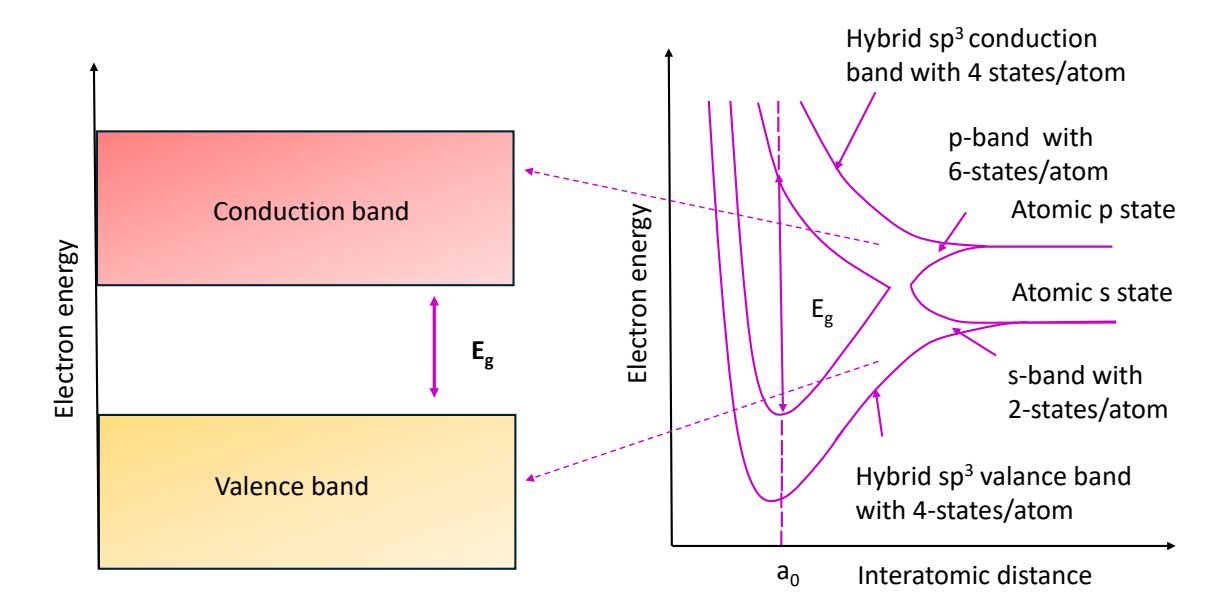


Figure 2.4: Schematic diagram of the energy bands for tetravalent semiconductors such as silicon (Si), and germanium (Ge) in relation to atomic spacing [72].

At absolute zero temperature, electrons occupy an energy band from the lowest energy level upwards. The highest occupied energy band is referred to as the valence band (VB), which is completely filled in a semiconductor at absolute zero temperature. The

subsequent available energy band is termed the conduction band (CB). The energy difference between the highest energy level of the valence band and the lowest energy level of the conduction band, determining whether a material behaves as a semiconductor or an insulator, is defined as the energy band gap  $(E_g)$  [73]. When the lowest energy point of the conduction band matches the highest energy point of the valence band in **k**-space, it is a direct-gap semiconductor (Figure 2.5b). Otherwise, it is an indirect-gap semiconductor (Figure 2.5a) [74].

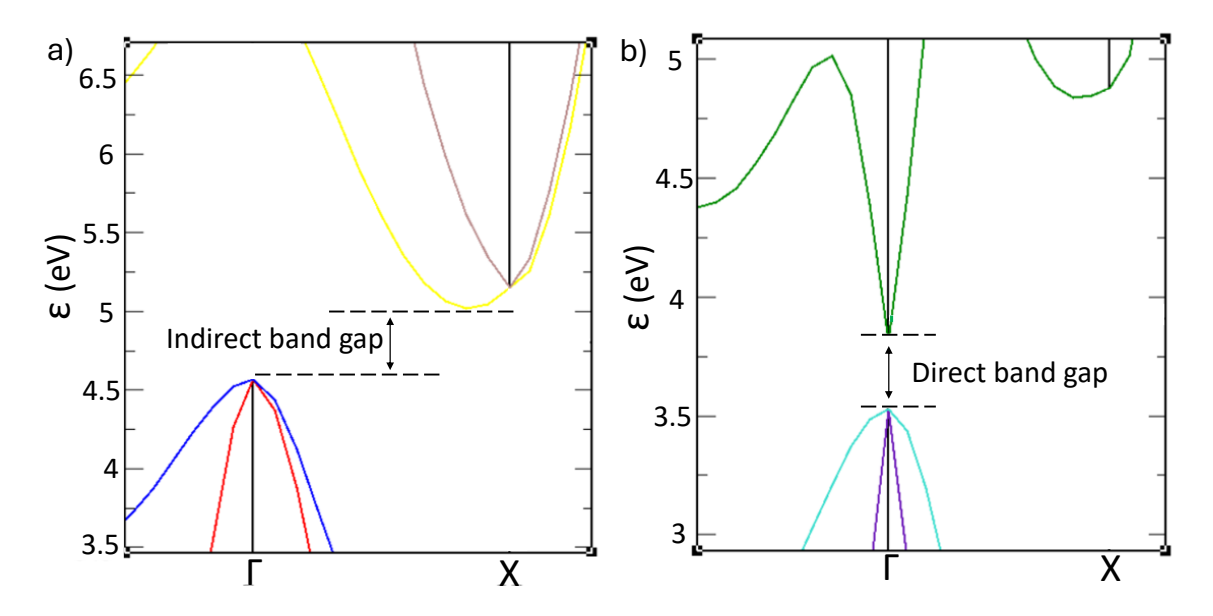


Figure 2.5: The energy band structures of (a) silicon and (b) gallium arsenide exhibit an indirect and direct band gap, respectively (band structures generated using CASTEP code [75]).

## 2.3 Phonon band structure

At finite temperatures, atoms within a crystalline lattice are not static but undergo thermal vibrations around their equilibrium positions. Due to the crystal symmetries, these vibrations inside a solid can be analysed as collective modes of ion motion known as phonons. These modes correspond to collective excitations, which, similar to electronic states, can be excited by heating the solid. Phonons are considered bosons due to their ability to exist at the same quantum state without a limit [76]. Each phonon

carries an energy  $E = \hbar \omega$ , where  $\omega$  represents the angular frequency of the oscillation, and  $\hbar$  denotes the reduced Planck constant [77].

Since the dynamics of atoms within a crystal lattice are interconnected, their interactions are governed by equations of motion. The phonon frequencies obtained are termed as the normal modes of the lattice, where the relationship between frequencies and reciprocal lattice vectors is expressed through the dispersion relation, shown in Figure 2.6, denoted as  $\omega(\mathbf{k})$  [46].

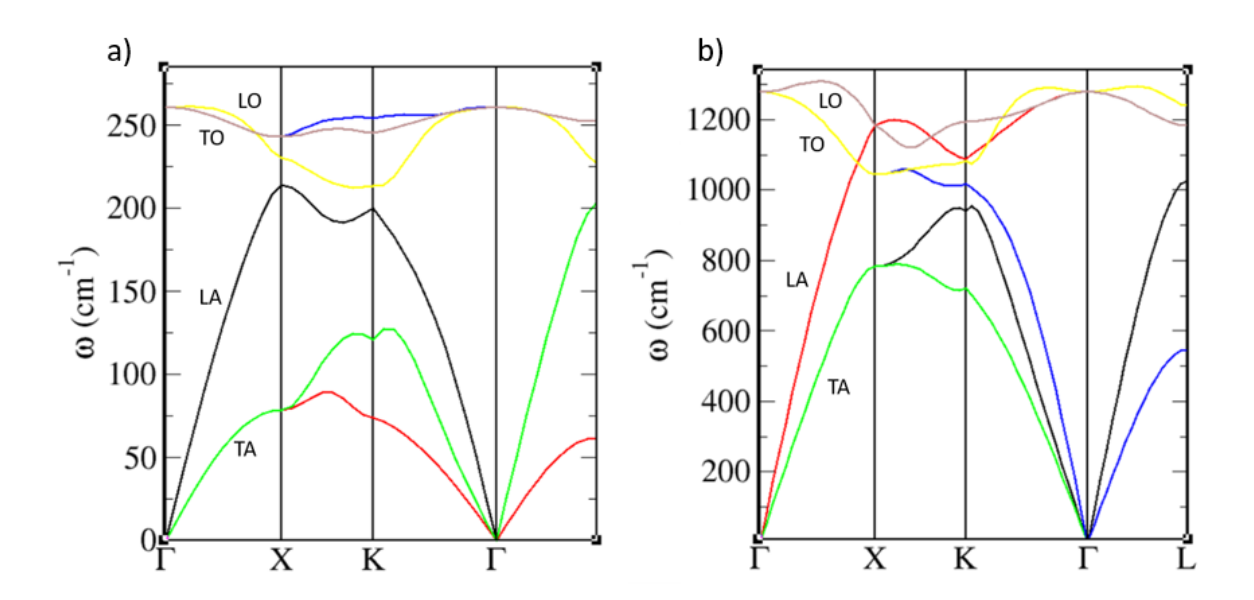


Figure 2.6: Phonon dispersion curves in diamond and zinc-blende structured semiconductors along high-symmetry points. (a) Gallium arsenide (GaAs), (b) Diamond (C) (Phonon structures generated using CASTEP code [75]).

#### 2.3.1 Harmonic model

The behaviour of phonon waves can be predicted using the harmonic oscillator model, assuming that all the atoms inside a crystal lattice are connected by massless electronic springs [78]. Under the Born-Oppenheimer approximation, the motion of the nuclei is considered to be independent of the electrons as the electrons are assumed to follow adiabatic ionic motion. The Hamiltonian governing the dynamics of the nuclei in a

lattice with s atoms per unit cell can be expressed as follows:

$$\hat{H} = \sum_{ls} \frac{\boldsymbol{P}_{\alpha}(ls)^2}{2m_s} + U, \tag{2.8}$$

with

$$\boldsymbol{P}_{\alpha}(ls) = \frac{m_s \partial \boldsymbol{u}_{\alpha}(ls)}{\partial t}.$$
 (2.9)

where  $p_{ls}$  is the momentum of an atom of mass  $m_s$ , U is the potential energy, and  $u_{\alpha}(ls)$  denotes the  $\alpha$ -Cartesian component of the displacement of the s-th atom in the l-th unit cell from its equilibrium position [47, 79]. Each atom in the unit cell l of a crystal vibrates about its equilibrium position with the displacement of  $u_{\alpha}(ls)$ . Hence, the instantaneous position in terms of the equilibrium position of an atom s can be written as:

$$\mathbf{r}(ls) = \mathbf{R}(l) + \boldsymbol{\tau}(s) + \boldsymbol{u}(ls). \tag{2.10}$$

where,  $\mathbf{R}(l)$  is the unit cell translational vector and  $\boldsymbol{\tau}(s)$  is the basis vector of atom s [80]. If atomic displacements are small compared to the lattice parameter, the potential energy of the system can be harmonically approximated by expanding it in a Taylor series around the equilibrium position [81]. Hence, the potential energy of a given crystal can be expressed as

$$U = U_0 + \frac{1}{2} \sum_{ll'} \sum_{ss'} \sum_{\alpha\beta} \mathbf{\Phi}_{\alpha\beta} \{ls; l's'\} \boldsymbol{u}_{\alpha}(ls) \boldsymbol{u}_{\beta}(l's'), \tag{2.11}$$

with

$$\Phi_{\alpha\beta}(ls;l's') = \frac{\partial^2 U}{\partial \boldsymbol{u}_{\alpha}(ls)\boldsymbol{u}_{\beta}(l's')}\bigg|_{\boldsymbol{u}_{\alpha}(ls)\boldsymbol{u}_{\beta}(l's')=0}.$$
(2.12)

Where  $U_0$  represents the potential energy of the static crystal.  $\mathbf{u}_{\beta}(l's')$  denotes the  $\beta$ -Cartesian component of the displacement of the s'-th atom in the l'-th unit cell from its equilibrium position. The  $\Phi_{\alpha\beta}\{ls;l's'\}$  are the atomic force constants of the crystal due to the interaction between the atoms denoted by (ls) and (l's'). Within the harmonic approximation, the Hamiltonian can be expressed as [82]:

$$\hat{H} = U_0 + \sum_{ls} \frac{\boldsymbol{P}_{\alpha}(ls)^2}{2m_s} + \frac{1}{2} \sum_{ll'} \sum_{\alpha s'} \sum_{\alpha \beta} \boldsymbol{\Phi}_{\alpha\beta} \{ls; l's'\} \boldsymbol{u}_{\alpha}(ls) \boldsymbol{u}_{\beta}(l's'). \tag{2.13}$$

The equation of motion for the s-th atom can be expressed using Newton's second law by taking the derivative of the Hamiltonian with respect to atomic displacements and momenta in a Cartesian basis  $\alpha$  [79]. The equation of motion for the s-th atom in the l-th unit cell is expressed as:

$$m_s \ddot{\boldsymbol{u}}_{\alpha}(ls) = -\sum_{l's'\beta} \boldsymbol{\Phi}_{\alpha\beta} \{ls; l's'\} \boldsymbol{u}_{\beta}(l's'). \tag{2.14}$$

The displacement  $u_{\alpha}(ls)$  can be expressed as a plane wave of the following form with wavevector  $\mathbf{k}$  [83]:

$$\mathbf{u}_{\alpha}(ls) = \frac{1}{\sqrt{m_s}} a_{\mathbf{k}} \, \epsilon_{\mathbf{k},s} \exp[i\mathbf{k} \cdot (\mathbf{R}(l)) - i\omega_{\mathbf{k}} t], \qquad (2.15)$$

where  $\omega_{\mathbf{k}}$  is the frequency,  $a_{\mathbf{k}}$  is the vibrational amplitude, and  $\epsilon_{\mathbf{k},s}$  is the polarisation vector that signifies the direction in which the atoms oscillate. By taking the second derivative of the above displacement expression and substituting into Equation (2.14), we obtain:

$$\omega_{\mathbf{k},i}^2 \epsilon_{\mathbf{k},j} = \mathbf{D}_{\mathbf{k}} \cdot \epsilon_{\mathbf{k},j}. \tag{2.16}$$

where j labels different phonon branches sharing the same wave vector  $\mathbf{k}$ , and  $\mathbf{D}_{\mathbf{k}}$  is the dynamical matrix with elements defined by [84]:

$$\mathbf{D_k} = -\sum_{l'} \frac{\Phi_{\alpha\beta}\{ls; l's'\}}{\sqrt{m_s m_{s'}}} \exp\{i\mathbf{k} \cdot [\mathbf{R}(l') - \mathbf{R}(l)]\}. \tag{2.17}$$

If there are N number of atoms per primitive unit cell, the dynamical matrix will have  $3N \times 3N$  elements. The solutions to the Equation (2.16) gives 3N vibrational modes for each values of  $\mathbf{k}$ : 3 acoustical branches and 3N-3 optical branches [46, 85]. Since the vibrational modes exhibit the same periodicity as the reciprocal lattice, it is practical to limit the solution to all wave vectors  $\mathbf{k}$  within the first Brillouin zone [79]. For each polarisation mode in a specified propagation direction, the dispersion relation  $\omega(\mathbf{k})$  forms two distinct branches: the acoustical branch and the optical branch.

The acoustical branch typically corresponds to lower-frequency modes, which include

longitudinal (LA) and transverse (TA) acoustic modes. Conversely, the optical branch is characterised by higher-frequency modes, comprising longitudinal optical (LO) and transverse optical (TO) modes [47]. When the polarisation vector  $\boldsymbol{\epsilon}$  is parallel to the the wave vector  $\mathbf{k}$ , the wave is termed longitudinal, with particle displacements occurring parallel to the direction of wave propagation. If the polarisation vector  $\boldsymbol{\epsilon}$  is perpendicular to  $\mathbf{k}$ , the wave is termed as transverse, with particle displacements occurring perpendicular to the direction of propagation [86].

## 2.4 Defects due to doping

Intrinsic semiconductors have limited practical applications due to being neither effective conductors nor insulators, and their electrical conduction is heavily influenced by temperature. However, the conductivity of these semiconductors can be modified significantly by introducing impurities or dopants into the crystal lattice. This doping process creates defects in the otherwise perfect crystal structure, subsequently altering the material's properties. A semiconductor crystal with added dopants is referred to as an extrinsic semiconductor or a doped material. A semiconductor that is doped with a donor impurity, e.g. for silicon this is a dopant with five electrons in its outer shell, is called an n-type semiconductor (Figure 2.7a) and has electrons as majority carriers. Semiconductor that is doped with an acceptor impurity, e.g. for silicon this is a dopant with three electrons in its outer shell, is called a p-type semiconductor (Figure 2.7b) and has holes as majority carriers [11, 87, 88].

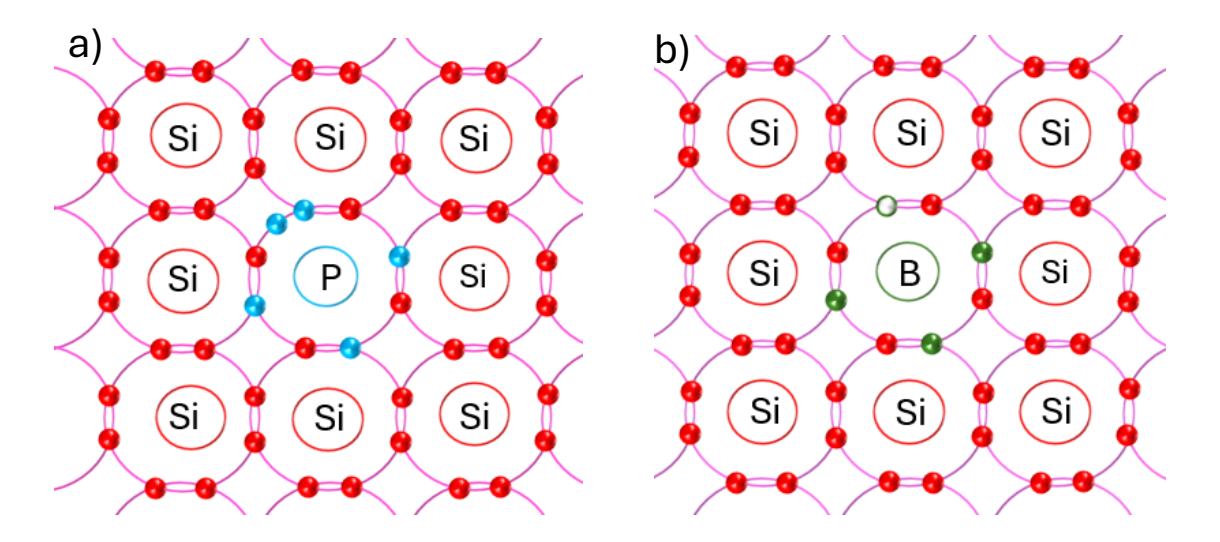


Figure 2.7: Schematic silicon crystal lattice with (a) pentavalent impurity atom (*n*-type), (b) trivalent impurity atom (*p*-type) [88].

At absolute zero, the Fermi level  $(E_f)$  of an intrinsic semiconductor is positioned in the middle of the energy gap, separating occupied electron energy levels (valance band) from empty energy electron levels (conduction band). Due to doping, in n-type semiconductors,  $E_f$  resides between the conduction band and the donor impurity energy levels  $(E_D)$ , as in Figure 2.8a. In p-type semiconductors,  $E_f$  lies between the valence band and the acceptor impurity energy levels  $(E_A)$ , as in Figure 2.8b [89].

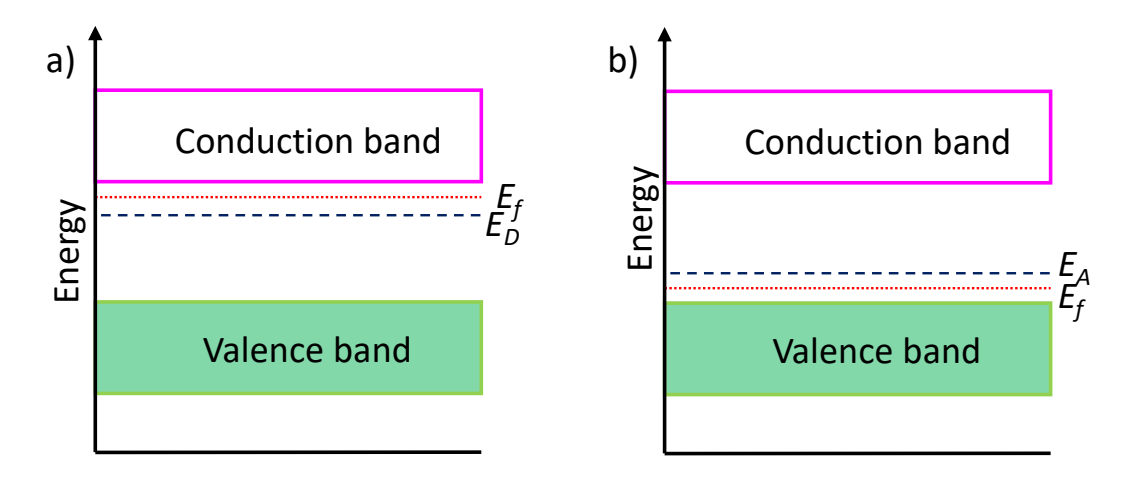


Figure 2.8: Schematic representation of the Fermi energy  $E_f$  of (a) an n-type and, (b) a p-type semiconductor at 0 K. In (a),  $E_D$  denotes the donor energy levels, and in (b),  $E_A$  represents the acceptor energy levels [89].

For shallow (energy levels with very low binding energies, on the order of  $10^{-2}$  eV) [90] donors, the energy level of donor electrons is positioned just below the bottom of the conduction band (Figure 2.8a). Therefore, donor electrons can easily move into the conduction band, becoming free conduction electrons and leaving behind positively charged ionised donors. Similarly, for the shallow acceptors, the acceptor atom accepts an additional electron from the valence band to form covalent bonds with all its nearest neighbours when it replaces a host atom. This creates a positively charged hole in the valence band and leaves the acceptor atom negatively ionised. The acceptor energy level is just above the top of the valence band (Figure 2.8b) [91, 92].

At low doping concentration, typically in the range of  $10^{15}$  to  $10^{18}$  atoms/cm<sup>3</sup>, semiconductor materials exhibit non-degenerate behaviour, where impurity atoms are sparsely distributed, creating discrete energy levels within the energy bandgap. In contrast, at high doping concentration, typically in the range of  $10^{19}$  to  $10^{20}$  atoms/cm<sup>3</sup>, the density of impurity atoms increases to the point where the wavefunctions associated with individual donor or acceptor atoms overlap significantly. This leads to a degenerate state where impurity states broaden out and merge with the conduction or valence bands, forming continuous energy bands. For instance, in degenerate n-type semiconductors, the Fermi level shifts into the conduction band, causing electronic states between the conduction band edge and the Fermi level to be predominantly occupied by electrons. Conversely, in degenerate p-type semiconductors, the Fermi level shifts into the valence band, filling most states between the valence band edge and the Fermi level with holes [60, 93, 94].

#### 2.4.1 Point defects

Doping processes induce zero-dimensional (extrinsic) defects in materials by introducing impurities to the host semiconductor crystal and produce a local distortion in the otherwise perfect lattice [95]. This leads to the modification in their physical properties, e.g. the electronic conduction [96]. Impurity atoms can occupy two different

types of lattice sites: (a) interstitial, where the impurity atom occupies an interstice between perfect lattice sites, and (b) substitutional, where an atom in the host lattice at a lattice site is replaced by the impurity atom [15].

In the context of DFT the energy required for a point defect of charge q to be formed is defined as:

$$E^{f}[X^{q}] = E_{tot}[X^{q}] - E_{tot}[bulk] - \sum_{i} n_{i}\mu_{i} + qE_{F} + E_{corr}.$$
 (2.18)

where  $E_{tot}[X^q]$  is the total energy of the supercell containing the defect  $X^q$  and  $E_{tot}[bulk]$  is the total energy of the perfect (defect-free) crystal lattice.  $n_i$  is an integer which denotes the number of atoms of species i that has been added  $(n_i > 0)$  to or removed  $(n_i < 0)$  from the host crystal lattice to create the defect,  $\mu_i$  is the chemical potential of species i.  $E_F$  is the Fermi energy level.  $E_{corr}$  represents a correction factor that adjusts for finite  $\mathbf{k}$ -point sampling in cases involving shallow impurities or for elastic electrostatic interactions. q = 0 for a neutral defect; if one electron is removed, q = 1; if one electron is added, q = -1 [97]. Point defects can occasionally jump from one lattice site or interstice to another, as atoms vibrate randomly due to thermal fluctuations, e.g. boron interstitials in silicon are mobile even at room temperature. These random jumps produce no effect for large numbers of atoms under equilibrium conditions, as there are as many jumps in one direction as in any other [98].

#### 2.4.2 Lattice distortion

Impurity atoms, which are comparable in size to the atoms of the host lattice, occupy substitutional sites and cause distortions that are spherically symmetric in crystal lattices that are close to being isotropic. On the other hand, smaller impurity atoms can occupy both interstitial sites and substitutional sites. When smaller impurity atoms reside in interstitial sites, the distortions produced vary according to the symmetry of these sites. The interstice sites, generally have volumes smaller than that of a single host atom. Hence, interstitial atoms tend to create substantial distortions among neighbouring atoms. This leads to the relatively large values of the defect formation energy

and can result in crystal volume expansions as significant as several atomic volumes per interstitial atom [15, 99].

The distortion and the additional energy in the lattice due to the defects depends on the amount of "space" between the atoms in the lattice and the "size" of the atoms introduced. In symmetric interstitial sites, such as octahedral or tetrahedral sites found in closely-packed lattices, interstitial defects induce spherically symmetric distortions. In contrast, distortions resulting from non-symmetric interstitial sites are themselves non-symmetric. The nature of these distortions influences the interactions between point defects and other imperfections within the crystal structure [15, 99].

Essentially, the presence of a point defect in a perfect crystal lattice causes the surrounding host atoms to be displaced from their original lattice positions, as in Figure 2.9, leading to a distortion of the local potential energy of the host crystal lattice.

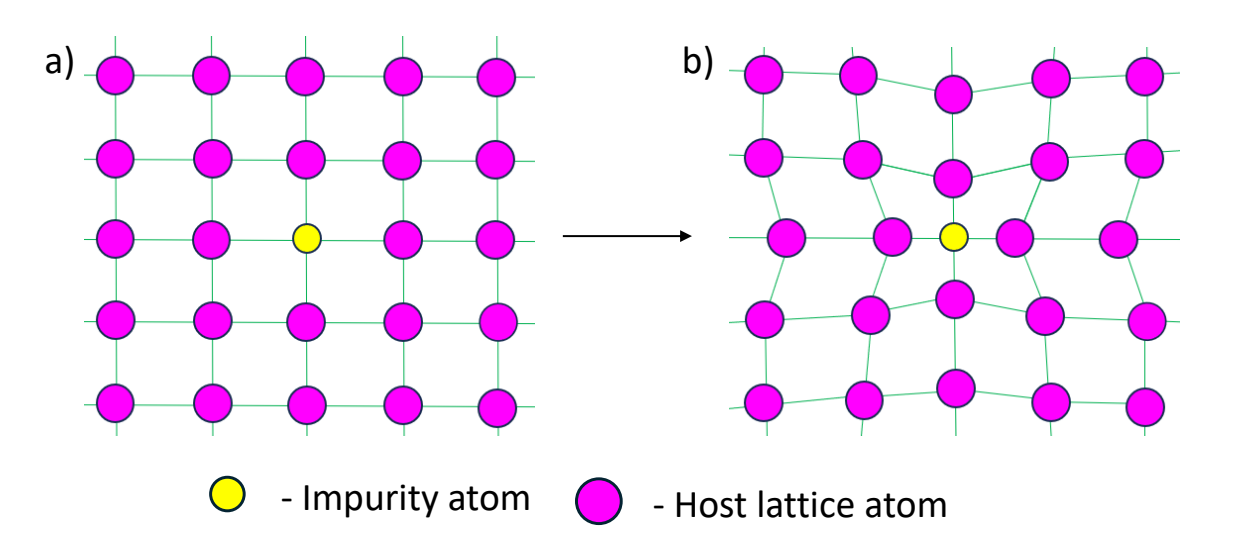


Figure 2.9: Schematic diagram of the lattice distortion due to single point defect in the host crystal lattice. (a) crystal lattice before the lattice relaxation, (b) distorted crystal lattice after the lattice relaxation [100].

This distortion due to a point defect can be viewed as the result of applying a distribution of external forces to each position in a perfect lattice, known as Kanzaki forces [100]. The Kanzaki force  $F_{\alpha}^{K}(ls)$  of a defect refers to the hypothetical set of forces that would

need to be applied to a perfect, defect-free lattice in order to produce the same elastic field as observed in a lattice containing a defect. This force can be obtained by expanding the potential energy of the crystal containing a defect up to quadratic terms in the displacements of the atoms from their positions in the undistorted lattice. The equilibrium equations are then constructed and solved by expanding the displacements in terms of normal coordinates. This approach leads to a set of 3s equations in the 3s unknown normal coordinates for each value of a wave vector  $\mathbf{k}$  [101, 102].

The forces  $F_{\alpha}(ls)$  induced by a point defect on neighboring atoms causes displacements  $\mathbf{u}_{\beta}(l's')$ , where  $F_{\alpha}(ls) = \sum_{l's'\beta} \mathbf{\Phi}_{\alpha\beta}\{ls;l's'\}\mathbf{u}_{\beta}(l's')$  and  $\mathbf{\Phi}$  is the the force constant matrix of the defect system. The equilibrium atomic positions around a defect can be obtained by introducing Kanzaki force  $F_{\alpha}^{K}(ls)$  in to the crystal lattice. The Kanzaki force is expressed as:

$$F_{\alpha}^{K}(ls) = \sum_{l's'\beta} \mathbf{\Phi}_{\alpha\beta}^{0}\{ls; l's'\} \boldsymbol{u}_{\beta}(l's'),$$

$$= F_{\alpha}(ls) - \sum_{l's'\beta} \boldsymbol{\Delta} \boldsymbol{\Phi}_{\alpha\beta}\{ls; l's'\} \boldsymbol{u}_{\beta}(l's').$$
(2.19)

where  $\Delta \Phi = \Phi - \Phi^0$ , and  $\Phi^0$  being the force constant matrix of the host crystal lattice. The Kanzaki force is designed to produce the same local distortion  $\boldsymbol{u}_{\beta}(l's')$  in the host crystal as the "direct" force  $F_{\alpha}(ls)$  causes in the defect system [100, 103].

#### 2.4.3 Local vibrational modes

The vibrational modes of a defect crystal can be obtained by the Kanzaki force. Since the defect system is relaxed, the displacement  $u_{\beta}(l's')$  can be expressed as:

$$\boldsymbol{u}_{\beta}(l's') = \sum_{\mathbf{k}j} \frac{1}{\sqrt{m_{s'}}} a_{\mathbf{k},j} \, \boldsymbol{\epsilon}_{\mathbf{k},j} \, \exp[i\mathbf{k} \cdot \mathbf{R}(l')]. \tag{2.20}$$

Given that the Kanzaki force is equivalent in magnitude to the forces producing the displacement field in the defect-free system, the equation of motion for the defect crystal in terms of the Kanzaki forces becomes [100, 101]:

$$F_{\alpha}^{K}(ls) = \sum_{l's'\beta} \mathbf{\Phi}_{\alpha\beta}\{ls; l's'\} \mathbf{u}_{\beta}(l's'). \tag{2.21}$$

To determine the eigen equation for the defect crystal, we follow a similar approach as that used for the defect-free crystal in section 2.3.1. By taking the second derivative of the displacement  $u_{\alpha}(ls)$  and substituting it into the equation of motion, we obtain:

$$\omega_{\mathbf{k},j}^{2} \boldsymbol{\epsilon}_{\mathbf{k},j} = \sum_{l's'\beta} \frac{\boldsymbol{\Phi}_{\alpha\beta} \{ls; l's'\}}{\sqrt{m_{s}m_{s'}}} \exp[i\mathbf{k} \cdot (\mathbf{R}(l') - \mathbf{R}(l))] \boldsymbol{\epsilon}_{\mathbf{k},j}. \tag{2.22}$$

The above expression can be written as:

$$\sqrt{m_s}\omega_{\mathbf{k},j}^2 \exp[i\mathbf{k} \cdot \mathbf{R}(l)] \boldsymbol{\epsilon}_{\mathbf{k},j} = \sum_{l's'\beta} \frac{\boldsymbol{\Phi}_{\alpha\beta}\{ls;l's'\}}{\sqrt{m_{s'}}} \exp[i\mathbf{k} \cdot \mathbf{R}(l')] \boldsymbol{\epsilon}_{\mathbf{k},j}. \tag{2.23}$$

Substituting the expression of  $\mathbf{u}_{\beta}(l's')$  from equation (2.20) in equation of motion (2.21), we get:

$$F_{\alpha}^{K}(ls) = \sum_{l's'\beta} \frac{\Phi_{\alpha\beta}\{ls; l's'\}}{\sqrt{m_{s'}}} a_{\mathbf{k},j} \, \boldsymbol{\epsilon}_{\mathbf{k},j} \, \exp[i\mathbf{k} \cdot \mathbf{R}(l')]. \tag{2.24}$$

By substituting equation (2.23) into the above equation we obtain:

$$F_{\alpha}^{K}(ls) = \sum_{\mathbf{k}j} \sqrt{m_s} \omega_{\mathbf{k},j}^{2} \exp[i\mathbf{k} \cdot \mathbf{R}(l)] \boldsymbol{\epsilon}_{\mathbf{k},j} a_{\mathbf{k},j}.$$
(2.25)

Since the eigenvectors  $\boldsymbol{\epsilon}_{\mathbf{k},j}$  satisfy the orthonormality condition, the above equation can be written using  $\boldsymbol{\epsilon}_{\mathbf{k},j} \cdot \boldsymbol{\epsilon}_{\mathbf{k}',j'}^* = \delta_{\mathbf{k},\mathbf{k}'} \ \delta_{j,j'}$  as [101]:

$$\omega_{\mathbf{k},j}^2 = \sum_{\mathbf{k}j} \frac{F_{\alpha}^K(ls)}{a_{\mathbf{k},j}\sqrt{m_s}} \exp[-i\mathbf{k}\cdot(\mathbf{R}(l) + \boldsymbol{\tau}(s'))]\boldsymbol{\epsilon}_{\mathbf{k},j}^*. \tag{2.26}$$

The above equation gives the vibrational modes of a crystal with defects. When light dopant atoms, such as boron in silicon, are introduced into the lattice, they generally lead to an increase in phonon frequencies, resulting in vibrational modes that lie above the optical branch. Although the force constants between the impurity atoms and the host lattice are typically reduced compared to those in the pure crystal, the lower atomic

mass of the impurity atom compensates for this reduction, leading to higher vibrational modes that fall above the optical branch [104].

Conversely, when heavier dopant atoms, such as phosphorus in silicon, are introduced into the lattice, they generally result in lower phonon frequencies, shifting vibrational modes into the acoustic region. The force constants between the impurity atoms and the host are further reduced compared to those in the pure crystal. This reduction in force constants, combined with the increased atomic mass of the heavier dopant, leads to lower vibrational frequencies, causing the phonon modes to fall within the acoustic band [104, 105]. In addition to a change in vibrational frequency, defect phonon modes are also found to be spatially localised around the defect. This compares to phonon modes in a perfect crystal, which extend over the entire specimen.

## 2.5 Point defects due to boron doping in silicon

Boron is the most commonly used impurity for creating p-type silicon. When boron atoms are introduced into silicon, they create point defects by occupying either substitutional or interstitial sites within the crystal lattice. Substitutional boron replaces a silicon atom, contributing to the intended p-type conductivity. However, boron atoms can also occupy interstitial positions, leading to the formation of boron interstitial clusters (BICs). At high doping concentrations, boron atoms can cluster together, sometimes in combination with native defects, to form electrically inactive complexes [106].

One of the primary effects of boron doping on silicon is the increase in carrier concentration. As the doping concentration increases, the number of holes increases, which leads to a reduction in the resistivity of the silicon. This is because resistivity is inversely proportional to the carrier concentration; as more carriers are available to conduct electric current, the material's ability to conduct electricity improves [107]. This is illustrated in Figure 2.10.

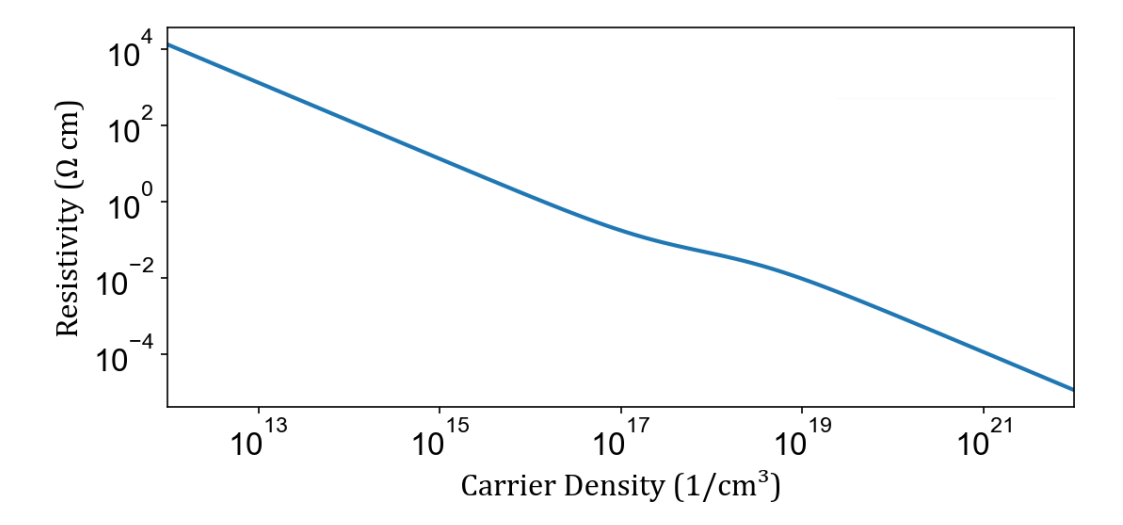


Figure 2.10: The dependency of the electrical resistivity of silicon at 300 K temperature on the p type (boron) doping concentration [107].

The increase in carrier concentration due to boron doping also has complex implications for carrier mobility. While the addition of boron increases the number of holes, it also introduces scattering centres in the form of ionised impurities and potential clusters. These scattering centres can impede the movement of carriers, thereby reducing their mobility (see Figure 2.11). The overall mobility of carriers in heavily boron doped silicon is determined by a balance between the increased number of carriers and the increased scattering events. At very high doping levels, the high concentration of dopants compensates for the reduction in mobility caused by the dominance of lattice scattering effects, resulting in enhanced conductivity [108–110].

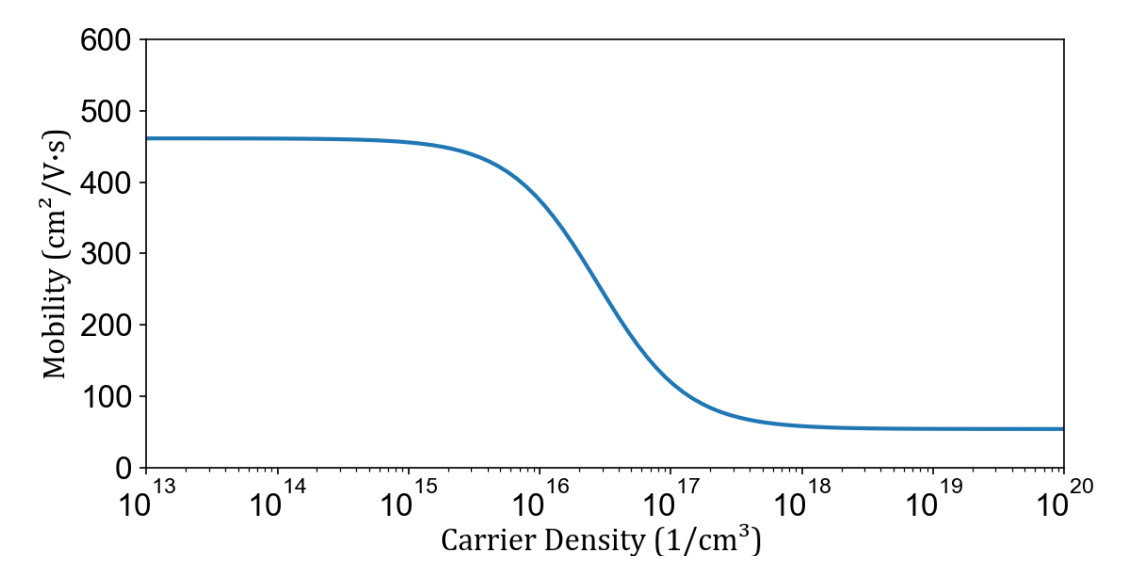


Figure 2.11: Electron mobility of silicon as a function of boron acceptor doping concentrations at 300 K temperature [108].

## 2.6 Summary

This chapter has provided a foundational overview of the structural and electronic properties of semiconductors, with a focus on silicon and its response to boron doping. Beginning with an outline of crystal lattices and reciprocal space, the discussion extended into the formation of electronic and phonon band structures, illustrating the quantum mechanical framework underlying semiconductor behaviour. The role of doping was explored in detail, highlighting how the introduction of boron atoms generates point defects, lattice distortions, and localised vibrational modes, all of which influence the electrical and vibrational characteristics of the material. Having examined how doping alters material properties at the atomic scale, the next chapter introduces scattering theory, a critical tool for probing these changes experimentally.

# **Scattering Theory**

Scattering theory is a fundamental concept in the study of materials, particularly in understanding how waves or particles interact with matter. In the context of electron diffraction, scattering theory provides the framework for interpreting how electrons are diffracted by the atomic structures of a material, revealing crucial details about its crystallographic properties. This chapter delves into the principles of scattering theory, starting with ideal single crystals and key concepts like Bragg diffraction, atomic scattering and structure factors, and thermal diffuse scattering due to phonons. It then covers diffuse scattering from point defects, so-called Huang diffuse scattering. This exploration provides the essential background to interpret the experimental results in this thesis.

## 3.1 Scattering from ideal single crystals

Electron scattering from ideal single crystals is a fundamental concept in solid-state physics and materials science, particularly in techniques like electron diffraction and electron microscopy. In an ideal single crystal, atoms are arranged in a perfectly periodic lattice, enabling coherent electron scattering. This coherence leads to distinct diffraction patterns, which are crucial for determining the crystal structure [111].

When an electron beam interacts with a crystal, the electrons are scattered by the peri-

odic potential created by the atoms in the crystal lattice. This interaction is governed by the wave nature of electrons, as proposed by de Broglie [112]. The mathematical description of electron scattering from a crystal involves solving the Schrödinger equation for an electron in the periodic potential of the crystal lattice. This potential can be expressed as a sum of plane waves using a Fourier series expansion:

$$V(\mathbf{r}) = \sum_{\mathbf{G}} V(\mathbf{G}) e^{i\mathbf{G} \cdot \mathbf{r}}, \tag{3.1}$$

where,  $\mathbf{G}$  are the reciprocal lattice vectors, and  $V(\mathbf{G})$  are the Fourier coefficients of the potential [113]. The periodic nature of the potential in an ideal crystal causes the scattered electron waves to interfere constructively or destructively depending on the geometry of the lattice and the wavelength of the incident electrons [114].

The geometry of scattered waves is described by the scattering vector  $\mathbf{Q}$ , which is defined as the difference between the incident wave vector  $\mathbf{k}_{in}$  and the scattered wave vector  $\mathbf{k}_{out}$ . As an electron beam passes through a crystal, it can be represented by a wave with a specific wave vector  $\mathbf{k}_{in}$ . Upon interacting with the atoms in the crystal, this wave scatters in various directions, resulting in each scattered wave having its own wave vector  $\mathbf{k}_{out}$ . The scattering vector  $\mathbf{Q}$  thus represents the change in the wave vector resulting from this scattering process [115, 116],

$$\mathbf{Q} = \mathbf{k}_{\text{in}} - \mathbf{k}_{\text{out}}.\tag{3.2}$$

The magnitude of  $\mathbf{Q}$  is related to the semi-angle of scattering  $\theta$  and the wavelength  $\lambda$  of the electrons by the equation[117],

$$|\mathbf{Q}| = \frac{2\sin\theta}{\lambda}.\tag{3.3}$$

This relationship forms the foundation for analysing the diffraction patterns that result

from electron scattering in crystals, as it helps determine how the scattered waves interfere with one another to create the observed patterns.

#### 3.1.1 Bragg diffraction

Bragg diffraction is based on the principle that when an incident wave, such as an electron wave, interacts with a periodic crystal lattice, diffraction occurs if the wave satisfies the Bragg condition which leads to the formation of strong, sharp Bragg diffraction spots. Bragg's law is expressed as [118]:

$$n\lambda = 2d_{hkl}\sin\theta_B,\tag{3.4}$$

where n is an integer,  $\lambda$  is the wavelength of the incident electrons,  $d_{hkl}$  is the interplanar spacing of the crystal planes, and  $\theta_B$  is the angle of incidence [119].

Equation (3.4) arises from the constructive interference of scattered waves (Figure 3.1a). For constructive interference to occur, the path difference between waves scattered from adjacent crystal planes must be an integer multiple of the wavelength. When this condition is met, the scattered waves reinforce each other, resulting in a strong diffraction peak. The spacing between lattice planes determines the angles at which these peaks are observed, while the wavelength of the incident wave influences the overall diffraction pattern [120].

At Bragg angle  $\theta_B$ , the magnitude of scattering vector  $\mathbf{Q}$  has a special value, denoted by  $\mathbf{Q}_B$ , which is equal to  $\mathbf{G}$ , where  $\mathbf{G}$  is a reciprocal lattice vector corresponding to the set of lattice planes responsible for the diffraction peak [121]. This can be expressed as:

$$\mathbf{Q}_B = \frac{1}{d_{hkl}} = \mathbf{G}.\tag{3.5}$$

This geometric interpretation of Bragg's law shows that the lattice planes act like

mirrors for the incident electron beam (Figure 3.1a). The diffraction spots observed in electron diffraction patterns are effectively the result of these planes reflecting the incident waves with the same phase [122].

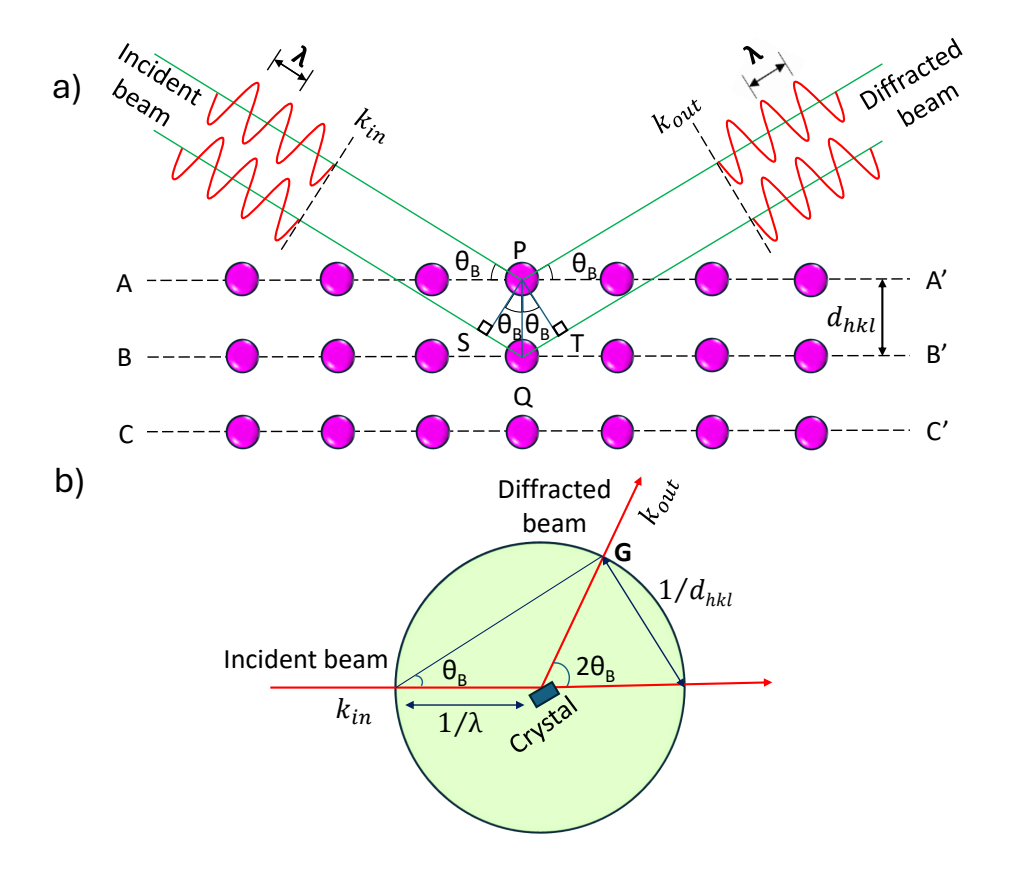


Figure 3.1: Illustration of Bragg's diffraction (a) and the Ewald sphere construction (b). In (a), the incident and diffracted beams are shown, with wave vectors  $\mathbf{k}_{\text{in}}$  and  $\mathbf{k}_{\text{out}}$  at the Bragg angle  $\theta_B$ , while the interplanar spacing is denoted by  $d_{hkl}$ . In (b), the Ewald sphere construction illustrates the relationship between the incident wave vector  $\mathbf{k}_{\text{in}}$ , diffracted wave vector  $\mathbf{k}_{\text{out}}$ , and the reciprocal lattice point  $\mathbf{G}$ , with the sphere radius equal to  $\frac{1}{\lambda}$ , showing the geometric condition for diffraction [120].

Bragg diffraction can also be visualised through the concept of the Ewald sphere (Figure 3.1b). The Ewald sphere is constructed by drawing a sphere centred on the incident wave vector  $\mathbf{k}_{in}$  with a radius equal to the magnitude of  $\mathbf{k}_{in}$ , which is  $\frac{1}{\lambda}$ , in reciprocal space. When an incident wave interacts with the crystal, it scatters to a new wave vector  $\mathbf{k}_{out}$  on the Ewald sphere. The Bragg condition is satisfied when the surface of the Ewald sphere intersects a reciprocal lattice point  $\mathbf{G}$ . This intersection signifies

that the scattering vector corresponds to a reciprocal lattice vector, thereby fulfilling Bragg's Law [123, 124].

Since a crystal is made up of repeating identical unit cells, analysing the diffraction from a single unit cell is enough to comprehend the diffraction behaviour of the entire crystal. Each atom within the unit cell scatters the electron beam, with the scattering intensity influenced by the atomic scattering factor  $f(\mathbf{Q})$  and the phase determined by the atom's specific position within the unit cell [62, 125].

#### 3.1.2 Atomic scattering factor

The atomic scattering factor, also known as the atomic form factor, describes how the amplitude of the wave scattered by an isolated atom varies as a function of the scattering angle [126]. Using the First Born Approximation (which assumes that the scattered intensity is weak), the atomic scattering factor is given by the Fourier transform of the electrostatic Coulomb potential  $V(\mathbf{r})$  of the atom as:

$$f(\mathbf{Q}) = C \int_{a}^{b} V(\mathbf{r}) e^{(i\mathbf{Q} \cdot \mathbf{r})} d\mathbf{r},$$
 (3.6)

where,  $C = \frac{2\pi me}{h^2}$ , m and e are the mass and charge of the electron, and h is the Planck constant. If an atom is isotropic, both the electrostatic potential and the scattering factor are spherically symmetric [127].

The Coulomb atomic potential is connected to the charge density through Poisson's equation, which includes contributions from both the atomic nucleus and the electrons surrounding the atom [128],

$$\nabla^2 V(\mathbf{r}) = \left[ \frac{-4\pi e(\rho_n(\mathbf{r}) - \rho_e(\mathbf{r}))}{\epsilon_0} \right], \tag{3.7}$$

where  $\rho_e(\mathbf{r})$  is the number density of the atomic electrons and  $\rho_n(\mathbf{r})$  is that of the atomic

nucleus. For a static atom, the nucleus can be approximated as a point charge of atomic number Z, simplifying the equation to:

$$\nabla^2 V(\mathbf{r}) = \left[ \frac{-4\pi e(Z\delta(\mathbf{r}) - \rho_e(\mathbf{r}))}{\epsilon_0} \right]. \tag{3.8}$$

By combining equation 3.6 with equation 3.8, the relationship between the scattering factor for electrons and the atomic form factor used in X-ray diffraction can be shown as [128]:

$$f(\mathbf{Q}) = \frac{2me^2}{\hbar^2 Q^2 \epsilon_0} [Z - f^*(\mathbf{Q})], \tag{3.9}$$

with,

$$f^*(\mathbf{Q}) = \int_a^b \rho_e(\mathbf{r}) e^{(i\mathbf{Q} \cdot \mathbf{r})} \, d\mathbf{r}. \tag{3.10}$$

The first term inside the brackets in equation 3.9 represents scattering due to the nucleus, while the second term accounts for scattering by the atomic electrons. The atomic scattering factor for electrons includes contributions from both the nuclear charge and the electron charge density of the atom [129].

The scattering amplitude  $f(\mathbf{Q})$  for electrons in the first Born approximation can also be parameterised as a sum of Lorentzian and exponential terms. This empirical expression is useful for practical calculations and fits experimental data effectively [130].

$$f(\mathbf{Q}) = \sum_{i=1}^{n} \left[ \frac{a_i}{\mathbf{Q}^2 + b_i} + c_i \exp(-d_i \mathbf{Q}^2) \right]$$
(3.11)

where,  $a_i, b_i, c_i$ , and  $d_i$  are fitting parameters. To demonstrate this, the atomic scattering factor has been plotted using this empirical expression for four different elements - silicon, carbon, germanium, and gold, as shown in Figure 3.2.

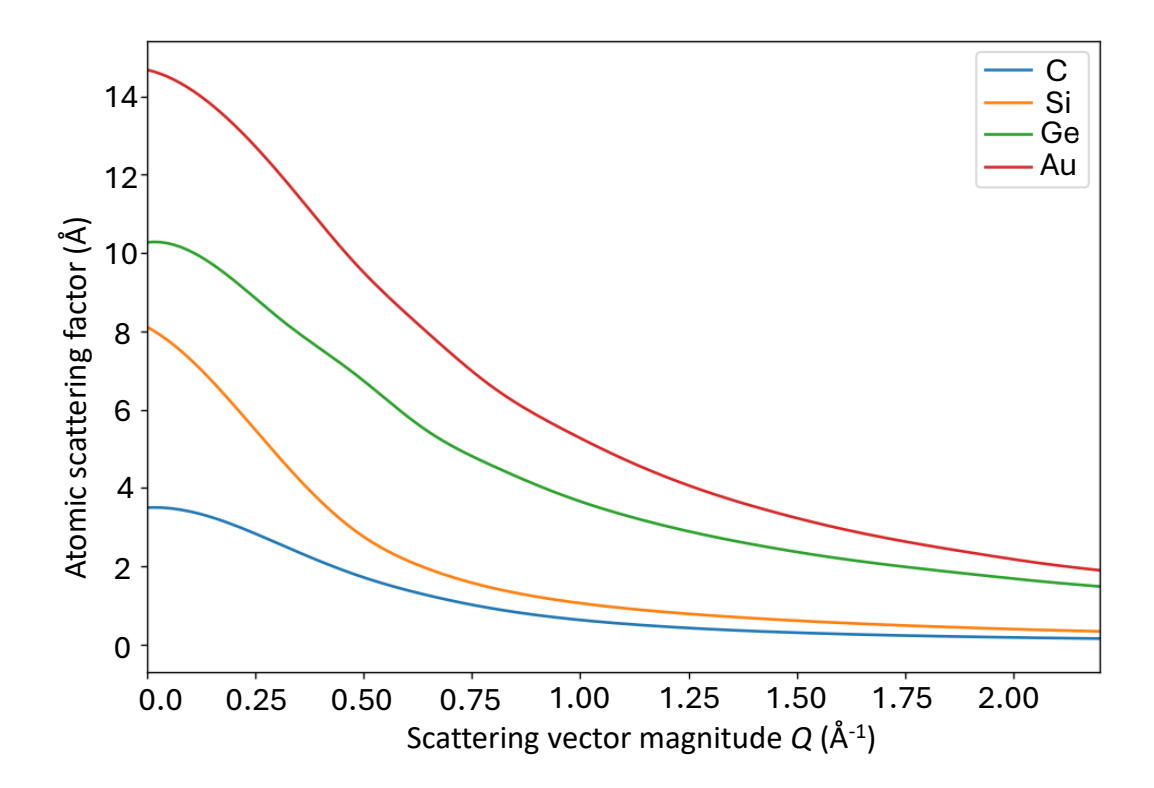


Figure 3.2: Graph of the atomic scattering factor  $f(\mathbf{Q})$  for carbon (C), silicon (Si), germanium (Ge), and gold (Au), computed using the empirical expression n Equation 3.11. The graph displays the atomic scattering factor as a function of scattering vector magnitude Q for each element, showcasing the variations in scattering properties among the different materials [130].

### 3.1.3 Structure factor and Bragg intensities

The structure factor describes how an incident electron wave is scattered by a crystal's periodic arrangement of atoms, incorporating contributions from all atoms within the unit cell. In electron diffraction, the structure factor is expressed as the sum of the atomic scattering factors of individual atoms, weighted by phase shifts due to their positions within the unit cell. For a crystal with s atoms, the structure factor  $F_{hkl}(\mathbf{Q})$  for a particular set of lattice planes can be written as [131]:

$$F_{hkl}(\mathbf{Q}) = \sum_{l,s} f_s(\mathbf{Q}) e^{i\mathbf{Q} \cdot \mathbf{R}(ls)}.$$
 (3.12)

where  $f_s(\mathbf{Q})$  is the atomic scattering factor and  $\mathbf{R}(ls)$  is the position vector of the  $s^{\text{th}}$  atom in the l unit cell. The structure factor determines which reflections will be observed in a diffraction pattern and follows selection rules specific to the crystal structure [132].

In some crystal structures, certain reflections do not appear in the diffraction pattern due to the specific atomic arrangement and symmetry of the lattice. These forbidden reflections occur when the structure factor for certain Miller indices hkl is zero. Forbidden reflections result from destructive interference of scattered waves due to symmetry constraints within the crystal lattice. When the structure factor equals zero, the scattered waves from the atomic planes corresponding to those indices cancel each other out. As a result, those specific reflections are absent from the diffraction pattern, provided the specimen is thin enough to ensure weak (i.e. kinematic) scattering. Forbidden reflections are useful for understanding the symmetry and atomic arrangement within the crystal [133].

Since the structure factor encapsulates both the amplitude and phase of the scattered waves by summing the contributions of all atoms in the unit cell, the Bragg intensity  $I_{\text{Bragg}}(\mathbf{Q})$  of the diffracted beam can be expressed in terms of the structure factor.  $I_{\text{Bragg}}(\mathbf{Q})$  is proportional to the square of the modulus of the structure factor [134]:

$$I_{\text{Bragg}}(\mathbf{Q}) \propto \left| \sum_{l,s} f_s(\mathbf{Q}) e^{i\mathbf{Q} \cdot \mathbf{R}(ls)} \right|^2.$$
 (3.13)

For elastic scattering, the magnitude of incoming wave vectors and the scattered wave vectors are equal, i.e,  $|\mathbf{k}_{in}| = |\mathbf{k}_{out}| = \frac{2\pi}{\lambda}$ . Whenever the scattering vector( $\mathbf{Q}$ ) is equal to a reciprocal lattice vector( $\mathbf{G}$ ), Bragg scattering from all atoms in the crystal can take place, provided the structure factor is non-zero. Equation 3.13 is valid for thin specimens (kinematic scattering). For thicker specimens, multiple scattering can occur, which means the Bragg beam intensity is no longer determined by the structure factor.

Therefore, reflections with zero structure factor can have some intensity provided the specimen is thick enough. Chapter 5 describes the multislice procedure for calculating Bragg beam intensities under multiple scattering conditions.

#### 3.1.4 Thermal diffuse scattering

Compared to an ideal crystal, the Bragg intensities are altered due to the displacement of lattice atoms from their equilibrium positions caused by thermal vibrations. These atomic displacements result in a modification of the scattered intensities. When thermal vibrations are introduced, the intensity of the scattered electron wave by the crystal is expressed as the time-averaged intensity, since the atomic displacements u(ls) are functions of time. The kinematic intensity of the scattered wave, incorporating displacements due to thermal vibrations, is given by [135]:

$$I(\mathbf{Q}) \propto \left\langle \left| \sum_{l,s} f_s(\mathbf{Q}) e^{i\mathbf{Q} \cdot [\mathbf{R}(ls) + u(ls)]} \right|^2 \right\rangle,$$
 (3.14)

In the above expression,  $\mathbf{R}(ls)$  denotes the position of atom in the l-th unit cell, which is decomposed into:

$$\mathbf{R}(ls) = \mathbf{R}(l) + \boldsymbol{\tau}(s), \tag{3.15}$$

where,  $\mathbf{R}(l)$  is the lattice vector and  $\boldsymbol{\tau}(s)$  is the atomic basis vector within a unit cell. By substituting  $\mathbf{R}(ls) = \mathbf{R}(l) + \boldsymbol{\tau}(s)$  and expanding the squared magnitude of the sum of the exponential terms, the equation 3.14 is expressed as:

$$I(\mathbf{Q}) \propto \sum_{l,l',s,s'} f_s(\mathbf{Q}) f_{s'}(\mathbf{Q}) e^{-i\mathbf{Q} \cdot [\mathbf{R}(l') - \mathbf{R}(l) + \boldsymbol{\tau}(s') - \boldsymbol{\tau}(s)]} \times \left\langle e^{i\mathbf{Q} \cdot [\boldsymbol{u}_{\alpha}(ls) - \boldsymbol{u}_{\beta}(l's')]} \right\rangle.$$
(3.16)

Under the Gaussian approximation, the average of the exponential term can be rewritten as:

$$\left\langle e^{i\mathbf{Q}\cdot[\boldsymbol{u}(ls)-\boldsymbol{u}(l's')]}\right\rangle = e^{-\frac{1}{2}\left\langle[\mathbf{Q}\cdot(\boldsymbol{u}(ls)-\boldsymbol{u}(l's'))]^2\right\rangle},$$
 (3.17)

$$= e^{-\frac{1}{2}\langle (\mathbf{Q} \cdot \boldsymbol{u}(ls))^2 \rangle} e^{-\frac{1}{2}\langle (\mathbf{Q} \cdot \boldsymbol{u}(l's'))^2 \rangle} e^{\langle (\mathbf{Q} \cdot \boldsymbol{u}(ls))(\mathbf{Q} \cdot \boldsymbol{u}(l's')) \rangle}. \tag{3.18}$$

Given the translational symmetry of the crystal lattice, the mean squared displacement for a particular atom and site is the same across all equivalent sites in the lattice. This implies that  $\langle (\mathbf{Q} \cdot \boldsymbol{u}(l's'))^2 \rangle = \langle (\mathbf{Q} \cdot \boldsymbol{u}(ls))^2 \rangle$ . The mean squared displacement expression (3.18) can be simplified by using the atomic displacements due to all lattice vibration modes [136]. The atomic displacement can be expressed as a sum of plane waves each with wavevector  $\mathbf{k}$  in the following form [83]:

$$\boldsymbol{u}(ls) = \mathbf{Re} \frac{1}{\sqrt{m_s}} \sum_{\mathbf{k},j} a_{\mathbf{k},j} \, \boldsymbol{\epsilon}_{\mathbf{k},j,s} \, e^{[i\mathbf{k}\cdot\mathbf{R}(l)-i\omega_{\mathbf{k},j}t]}. \tag{3.19}$$

Here,  $\sqrt{m_s}$  is the atomic mass,  $\omega_{\mathbf{k},j}$  is the frequency,  $a_{\mathbf{k},j}$  is the vibrational amplitude, and  $\epsilon_{\mathbf{k},j,s}$  is the polarisation vector. By using equation 3.19, the mean squared displacement can be rewritten as:

$$\frac{1}{2}\langle |\mathbf{Q} \cdot (\boldsymbol{u}(ls) - \boldsymbol{u}(l's'))|^2 \rangle = M_s + M_{s'} - \sum_{\mathbf{k},j} \frac{|a_{\mathbf{k},j}|^2}{2\sqrt{m_s m_{s'}}} \times (\mathbf{Q} \cdot \boldsymbol{\epsilon}_{\mathbf{k},j,s})^* (\mathbf{Q} \cdot \boldsymbol{\epsilon}_{\mathbf{k},j,s'}) \times e^{i\mathbf{k} \cdot [\mathbf{R}(l') - \mathbf{R}(l)]}, \tag{3.20}$$

where,  $M_s$  and  $M'_s$  are the Debye-Waller factors, which accounts for how atomic vibrations can reduce the intensity of scattering. For an atom labeled s (or s' for a different atom), the Debye-Waller factor  $M_s$  can be expressed as [137]:

$$M_s = \frac{1}{4m_s} \sum_{\mathbf{k},j} |a_{\mathbf{k},j}|^2 |\mathbf{Q} \cdot \boldsymbol{\epsilon}_{\mathbf{k},j,s}|^2.$$
 (3.21)

For cubic systems, this reduces to:

$$M_s = \frac{\mathbf{Q}^2}{12m_s} \sum_{\mathbf{k},i} |a_{\mathbf{k},j}|^2 |\boldsymbol{\epsilon}_{\mathbf{k},j,s}|^2.$$
 (3.22)

The square amplitudes of the vibrational modes  $|a_{\mathbf{k},j}|^2$  can be determined from the mean kinetic energy and total energy of the crystalline solid, which is modelled as a

collection of harmonic oscillators, leading to the expression [138]:

$$|a_{\mathbf{k},j}|^2 = \sum_{\mathbf{k},j} \frac{\hbar}{N\omega_{\mathbf{k},j}} \coth\left(\frac{\hbar\omega_{\mathbf{k},j}}{k_{\rm B}T}\right),$$
 (3.23)

where, N is the total number of unit cells in the crystalline solid, T is the temperature, and  $k_{\rm B}$  is the Boltzmann constant.

Incorporating the mean squared displacements and Debye-Waller factors into the intensity expression 3.14 yields,

$$I(\mathbf{Q}) \propto N \sum_{l=1}^{N} \sum_{s,s'=1}^{n} f_s(\mathbf{Q}) f_{s'}(\mathbf{Q}) e^{(-M_s - M_{s'})} e^{-i\mathbf{Q} \cdot [\mathbf{R}(l) + \boldsymbol{\tau}(s') - \boldsymbol{\tau}(s)]} e^{[\mathbf{G}_{l,s,s'}(\mathbf{Q})]}, \qquad (3.24)$$

with,

$$\mathbf{G}_{l,s,s'}(\mathbf{Q}) = \frac{\hbar}{2N\sqrt{m_s m_{s'}}} \sum_{\mathbf{k},j} \left\{ \frac{1}{\omega_{\mathbf{k},j}} (\mathbf{Q} \cdot \boldsymbol{\epsilon}_{\mathbf{k},j,s})^* (\mathbf{Q} \cdot \boldsymbol{\epsilon}_{\mathbf{k},j,s'}) \right.$$

$$\times \coth\left(\frac{\hbar\omega_{\mathbf{k},j}}{k_{\mathrm{B}}T}\right) e^{i\mathbf{k}\cdot[\mathbf{R}(l)]} \right\}.$$
(3.25)

This intensity formula for electron thermal diffuse scattering from a single crystal provides a comprehensive picture of how atomic vibrations contribute to the scattering process.

To make the thermal diffuse scattering (TDS) intensity more practical for numerical computation, the expression 3.24 can be simplified by expanding the exponential term involving  $\mathbf{G}_{l,s,s'}(\mathbf{Q})$  using a Taylor series expansion. The term  $\mathbf{G}_{l,s,s'}(\mathbf{Q})$ , which accounts for the atomic displacements due to thermal vibrations (phonons), is assumed to be small for practical purposes. This assumption is reasonable because the displacements of atoms in a crystal due to phonon vibrations are typically small at room temperature compared to the interatomic distances [45].

By expanding  $\exp[\mathbf{G}_{l,s,s'}(\mathbf{Q})]$ , the total intensity (Equation 3.24) can be expressed as a series of terms:

$$I(\mathbf{Q}) = I_0(\mathbf{Q}) + I_1(\mathbf{Q}) + I_2(\mathbf{Q}) + \dots,$$
 (3.26)

where,  $I_0(\mathbf{Q})$  is the zeroth-order term, corresponding to Bragg diffraction, the first-order term,  $I_1(\mathbf{Q})$  corresponding to first-order TDS,  $I_2(\mathbf{Q})$  is the second-order term, corresponding to the second-order TDS, and so on.

The first-order term,  $I_1(\mathbf{Q})$ , often dominates the thermal diffuse scattering (TDS), and is given by [139, 140]:

$$I_1(\mathbf{Q}) \propto \frac{N\hbar}{2} \sum_{\mathbf{Q},j} \frac{1}{\omega_{\mathbf{Q},j}} \coth\left(\frac{\hbar\omega_{\mathbf{Q},j}}{k_{\mathrm{B}}T}\right) |\mathbf{F}_j(\mathbf{Q})|^2,$$
 (3.27)

with,

$$\mathbf{F}_{j}(\mathbf{Q}) = \sum_{s} \frac{f_{s}(\mathbf{Q})}{\sqrt{m_{s}}} \exp(-M_{s})(\mathbf{Q} \cdot \boldsymbol{\epsilon}_{\mathbf{Q},j,s}) \exp(-i\mathbf{K}_{\mathbf{Q}} \cdot \boldsymbol{\tau}(s)).$$
(3.28)

Equation 3.27 is a simplified version of 3.24. It describes the scattering intensity resulting from interactions with phonons of wavevector  $\mathbf{Q}$ , and is primarily used to study lattice dynamics through TDS measurements in section 8.

## 3.2 Diffuse scattering from point defects

While TDS arises from the thermal vibrations of atoms (phonons) within the crystal, leading to temperature-dependent diffuse scattering intensity around Bragg peaks, diffuse scattering from point defects originates from static lattice distortions caused by structural imperfections such as vacancies, substitutional atoms, or interstitials.

Unlike TDS, where atomic vibrations are dynamic and vary with temperature, the displacements caused by defects are 'largely' static and independent of temperature. The resulting diffuse scattering pattern is therefore determined by the type and concentration of defects, as well as the displacement fields they induce.

Compared with the ideal crystal, the Bragg intensities are modified due to the shift

of the atoms from their ideal lattice sites to new sites, caused by introduction of defects such as vacancies, interstitials, or substitutional atoms. The position of atoms s includes the term u(lst) which represents the displacement vector associated with the  $l^{th}$  unit cell, caused by the introduction of a defect at position t. The total static displacement  $u^d(ls)$ , caused by all defects in the crystal, can be expressed as the superposition of displacements produced by each individual defect. Thus, it can be written as the sum of displacements due to each defect [141]:

$$\boldsymbol{u}^{d}(ls) = \sum_{t} C_{t} \ \boldsymbol{u}(lst), \tag{3.29}$$

where,  $C_t$  is the defect concentration at position t. In addition to the modification in atomic positions of the host crystal, introduction of point defects into the crystal lattice also alters the atomic scattering factor in regions where defects are present. This is caused by a change in the local composition (e.g. vacancy or substitutional defect) [142].

In the kinematic approximation, the scattering intensity  $I(\mathbf{Q})$  of the defect system is given by [143]:

$$I(\mathbf{Q}) \propto \left\langle \left| \sum_{ls} f(\mathbf{Q}) e^{i\mathbf{Q} \cdot (\mathbf{R}(ls) + u^d(ls))} + f^D(\mathbf{Q}) \right|^2 \right\rangle,$$
 (3.30)

where  $\langle \cdots \rangle$  represents the average over all defect configurations, and  $f^D(\mathbf{Q})$  is the scattering amplitude of all defects. The diffuse scattering intensity  $I_{\text{Diff}}(\mathbf{Q})$  due to defects can be obtained by subtracting above equation 3.30 from Bragg scattering intensity 3.13 [144].

$$I_{\text{Diff}}(\mathbf{Q}) \propto \left\langle \left| \sum_{ls} f(\mathbf{Q}) e^{i\mathbf{Q} \cdot (\mathbf{R}(ls) + u^d(ls))} + f^D(\mathbf{Q}) - \sum_{ls} f(\mathbf{Q}) e^{i\mathbf{Q} \cdot \mathbf{R}(ls)} \right|^2 \right\rangle.$$
 (3.31)

Using equation 3.29 for total static displacement, the above equation can be rewritten as:

$$I_{\text{Diff}}(\mathbf{Q}) \propto \sum_{ls} \left\langle \left| (f(\mathbf{Q})e^{i\mathbf{Q}\cdot\mathbf{R}(ls)} \prod_{t} e^{i\mathbf{Q}\cdot\mathbf{u}(lst)C_{t}} + f^{D}(\mathbf{Q}) - \sum_{ls} f(\mathbf{Q})e^{i\mathbf{Q}\cdot\mathbf{R}(ls)} \right|^{2} \right\rangle.$$
(3.32)

The term  $i\mathbf{Q} \cdot \mathbf{u}(lst)C_t$  in  $e^{i\mathbf{Q} \cdot \mathbf{u}(lst)C_t}$  is the static Debye-Waller factor which represents the contribution of static displacements to the scattering intensity. The product of the exponential term of the static Debye-Waller factor can be simplified, assuming the static atomic displacements caused by defects are small compared to the interatomic distances, as [141, 142, 145]:

$$\prod_{t} e^{i\mathbf{Q}\cdot\mathbf{u}(lst)C_{t}} = 1 + i\sum_{t} C_{t}\mathbf{Q}\cdot\mathbf{u}(lst).$$
(3.33)

By substituting the above equation, The diffuse scattering intensity due to defects (Equation 3.32) can be simplified as:

$$I_{\text{Diff}}(\mathbf{Q}) \propto \sum_{ls} \left\langle \left| if(\mathbf{Q}) \sum_{t} C_{t} \mathbf{Q} \cdot \boldsymbol{u}(lst) e^{i\mathbf{Q} \cdot \mathbf{R}(ls)} + f^{D}(\mathbf{Q}) \right|^{2} \right\rangle.$$
 (3.34)

For the static displacement u(lst), the diffuse scattering intensity gives the Fourier transform:

$$\tilde{\boldsymbol{u}}(\mathbf{Q}) = \sum_{t} C_{t} \boldsymbol{u}(lst) e^{i\mathbf{Q} \cdot \mathbf{R}(ls)}.$$
(3.35)

By using the above equation, equation 3.34 can be written as:

$$I_{\text{Diff}}(\mathbf{Q}) \propto \left\langle \left| if(\mathbf{Q})\mathbf{Q} \cdot \tilde{\boldsymbol{u}}(\mathbf{Q}) + f^{D}(\mathbf{Q}) \right|^{2} \right\rangle.$$
 (3.36)

The second term in the above equation 3.36 is the Laue scattering from the defect itself [134]. The atomic scattering factor  $f^D(\mathbf{Q})$  of the defect atoms takes on different forms depending on the nature of the defect. For interstitial impurities,  $f^D(\mathbf{Q})$  is given by  $f^D(\mathbf{I})e^{(i\mathbf{Q}\cdot\mathbf{R}(\mathbf{I}))}$ , where  $f^D(\mathbf{I})$  is the scattering factor of the interstitial impurity

and  $\mathbf{R}(\mathbf{I})$  is the interstitial position. For substitutional impurities, it is the difference between the scattering factor of the interstitial impurity and that of the normal atoms, i.e.,  $f^D(\mathbf{Q}) = f^D(\mathbf{I}) - f(\mathbf{Q})$ . In the case of vacancies, the structure factor is  $f^D(\mathbf{Q}) = -f(\mathbf{Q})$  [146, 147].

### 3.2.1 Huang diffuse scattering

The first term in equation 3.36 is the Huang diffuse scattering due to lattice distortion. The scattering intensity is given by the Fourier transform of the distortion field when the scattering vector  $\mathbf{Q}$  is approximately equal to the reciprocal lattice vector  $\mathbf{G}$  ( $\mathbf{Q} \approx \mathbf{G}$ ), i.e  $\mathbf{Q} = \mathbf{G} + \mathbf{g}$ , where  $\mathbf{g}$  is the deviation from the Bragg reflection and is small compared to  $\mathbf{G}$  [148]. The diffuse scattering observed near the Bragg reflections, where the intensity is particularly strong, is known as Huang diffuse scattering  $I_{\text{HDS}}$  [149, 150].

$$I_{\text{HDS}}(\mathbf{Q}) \propto f^2(\mathbf{Q}) \left| \mathbf{Q} \cdot \tilde{\boldsymbol{u}}(\mathbf{Q}) \right|^2,$$
 (3.37)

where,  $\tilde{\boldsymbol{u}}(\mathbf{Q})$  is the Fourier transform of the elastic displacement field.

For an isotropic defect in an isotropic medium the displacement field, and its Fourier transform, are both isotropic. Since the scattered intensity (Equation 3.37) depends on  $\mathbf{Q}.\tilde{\boldsymbol{u}}(\mathbf{Q})$ , we can expect zero intensity whenever  $\mathbf{Q}$  perpendicular to  $\tilde{\boldsymbol{u}}(\mathbf{Q})$ . For an isotropic defect this happens on a plane perpendicular to  $\mathbf{G}$  through the reciprocal lattice point. When  $\mathbf{g} \to 0$  we can expect maximum scattering intensity in the direction of  $\mathbf{G}$  ( $\mathbf{Q}//\tilde{\boldsymbol{u}}$ ) and has the approximate functional form [134, 151, 152]:

$$I_{\text{HDS}}(\mathbf{Q}) \sim \frac{\mathbf{Q}^2}{\mathbf{g}^2}.$$
 (3.38)

For isotropic defects, the diffraction contrast from spherically symmetrical coherency strains resulting from spherical domains should lead to a butterfly-like pattern (Figure 3.3). For anisotropic defects, the diffuse scattering intensity is averaged due to the random distribution of the defects orientations. Each defect orientation yields a different zero intensity plane and the zero intensity plane is no longer perpendicular to **G**.

Zero intensity planes of different defect orientation may however coincide for symmetry reasons [134, 148]. Low-symmetry defects lead to scattering in all directions without distinct zero-intensity planes or lines.

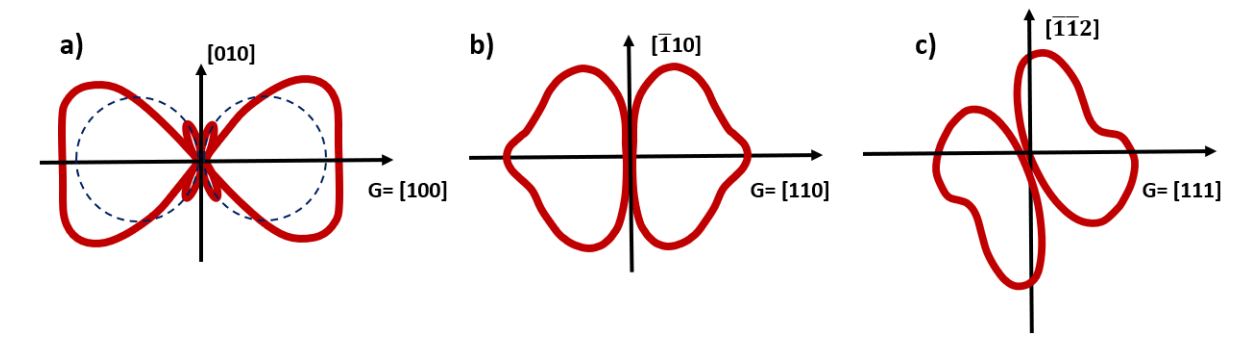


Figure 3.3: Isointensity curves for an isotropic point defect in Cu for different reflections. a) [100] reflection (dotted curve, isotropic approximation); (b) curve in (001) plane for a [110] reflection; (c) curve in  $(1\overline{1}0)$  plane for a [111] reflection [148].

## 3.3 Summary

This chapter has outlined the theoretical framework underpinning electron scattering phenomena in crystalline materials. Starting with scattering from ideal single crystals, the principles of Bragg diffraction, atomic and structure factors, and thermal diffuse scattering were described to clarify how periodic atomic arrangements and lattice vibrations influence diffraction patterns. The discussion then turned to diffuse scattering from point defects, highlighting how imperfections within the lattice can subtly alter scattering signatures. The following chapter will introduce the experimental techniques used to probe these scattering phenomena through electron microscopy and spectroscopic methods.

# **Experimental Techniques**

This chapter provides a overview of the experimental techniques employed in this thesis to investigate the effects of degenerate boron doping in silicon. It begins by outlining the instrumentation and working principles of transmission electron microscopy (TEM), detailing its structural components, the interaction of the electron beam with matter, and modes of operation. It also discusses limitations such as spherical and chromatic aberrations of the lenses. Next, the chapter delves into scanning transmission electron microscopy (STEM), which combines the advantages of both TEM and scanning electron microscopy, allowing for high-resolution imaging and the analysis of vibrational properties through monochromated electron energy loss spectroscopy (EELS). In addition to these primary techniques, the chapter covers secondary experimental methods that contribute to the overall material characterisation, including Raman Spectroscopy, Hall Effect measurements, and Secondary Ion Mass Spectrometry (SIMS), which provide complementary information on the structural, electronic, and compositional properties of the boron doped silicon.

# 4.1 Transmission electron microscopy

Transmission electron microscopy (TEM) is a pivotal technique in the field of materials science and biology that allows researchers to observe the fine structure of materials at the atomic level. The foundations of TEM can be traced back to the early 20th century,

when scientists began to explore the dual wave-particle nature of electrons, a concept proposed by de Broglie in 1924 [153]. This breakthrough led to the realisation that electrons, due to their significantly smaller wavelength compared to visible light, could be utilised to surpass the resolution limitations imposed by optical microscopes [154]. As a result, TEM became an essential tool for examining material properties at the nanoscale, providing critical insights into the nature of crystal defects and the microstructural characteristics of various crystalline materials [155].

The first transmission electron microscope was constructed by Max Knoll and Ernst Ruska in 1931, marking a transformative moment in microscopy history. Their pioneering work enabled the use of high-energy electron beams to achieve high resolution, paving the way for TEM as an essential tool for examining material properties at the nanoscale [156]. By transmitting a high-energy electron beam, typically around 200 keV, through a thin specimen ( $\sim$  100-150 nm thick), TEM allows for the investigation of the internal structure of materials with exceptional detail [157].

The transmitted electrons can be either elastically or inelastically scattered. Elastically scattered electrons provide crucial information about the crystalline structure via diffraction patterns and contribute to high-contrast images, while inelastically scattered electrons reveal insights into the material's electronic and vibrational properties via techniques like electron energy loss spectroscopy (EELS) [158, 159]. The resolving power of TEM can reach down to 0.1 nm, which is significantly better than that of conventional optical microscopes [160]. Such exceptional resolution has led to investigations of materials at the atomic level, especially investigations on nanoscale features like point defects [161], grain boundaries [162], and dislocations [163], which are critical to understanding the mechanical, vibrational and electronic properties of crystalline materials. For example, TEM has been instrumental in analysing semiconductor materials used in microelectronics, where atomic-level insights can significantly influence device performance [164].

Despite its strengths, TEM has inherent limitations. One significant challenge is the requirement for samples to be extremely thin (generally about 100 nm) to allow for sufficient electron transmission [157]. This necessitates sample preparation techniques such as ion milling or focused ion beam (FIB) milling, which can unintentionally introduce structural and chemical changes, leading to potential artefacts in the obtained data [165]. Additionally, the interaction of the electron beam with sensitive materials can cause radiation damage, limiting the usability of TEM for certain types of specimens [166].

#### 4.1.1 TEM instrumentation

The main components of a TEM include: the electron gun (source of electrons); gun alignment controls; condenser lenses (magnetic lenses for beam collimation); objective lens (for image focusing and initial magnification); apertures (to restrict the electron beam diameter); intermediate lens; projector lens; sample holder; viewing screen; and detectors.

Two kinds of electron sources have been used in TEMs: thermionic source and field emission source. Thermionic guns (Figure 4.1a) operate by heating materials like lanthanum hexaboride (LaB<sub>6</sub>) or tungsten to high temperatures. This heating provides electrons in these materials with enough energy to overcome the work function barrier ( $E_w$ ), the energy threshold that keeps electrons bound to the solid, allowing them to escape and form a continuous electron beam (Figure 4.1b). Materials like LaB<sub>6</sub> and tungsten are well-suited for thermionic guns due to their high melting points, which enable them to withstand the intense heat required for electron emission. LaB<sub>6</sub> cathodes produce brighter and more coherent beams due to their smaller tip radius and lower work function. Tungsten filaments, although less efficient, offer a cost-effective and simpler alternative [167, 168]. Field Emission Guns (FEGs)(Figure 4.1c), on the other hand, emit electrons through a process driven by a strong electric field at a very sharp single crystal tungsten tip. This electric field facilitates the field emission process, allowing

electrons to tunnel through the potential barrier and escape into the vacuum (Figure 4.1d). FEGs produce a highly focused electron beam with a small energy spread and high brightness, making them ideal for high-resolution imaging. However, FEGs are more expensive to operate and require ultra-high vacuum conditions to prevent contamination of the tip, which is essential for maintaining stable performance [168–170].

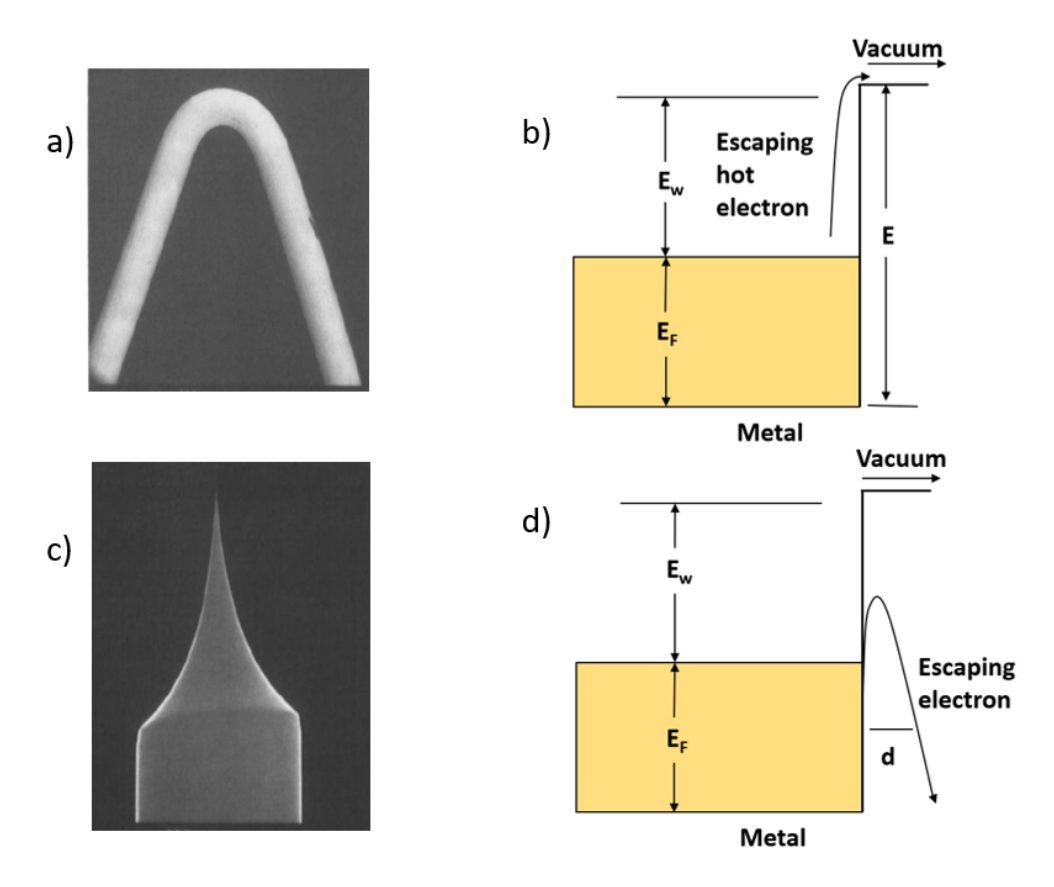


Figure 4.1: (a) Tungsten hairpin filament of a thermionic emitter, (b) The energy-level diagram of thermionic emission, the symbol E denotes the energy required to transfer an electron from the lowest energy state within the metal to the vacuum, (c) Tungsten field emission gun, (d) Energy-level diagram of field emission, d denotes the potential barrier width [171].

After electrons are emitted from either the thermionic or field emission source, they are accelerated by a high voltage, forming an electron beam. This beam is then aligned and focused onto the sample using the TEM's magnetic lenses. In TEM, following the electron source there are two condenser lenses (C1 and C2), as in Figure 4.2. The

C1 lens is responsible for controlling the spot size of the beam by creating a crossover point for the electrons emitted from the gun gun. C1 effectively demagnifies the electron beam. The C2 lens, on the other hand, regulates the convergence angle of the beam, enabling the generation of either a parallel or a convergent beam depending on the operational mode selected [168].

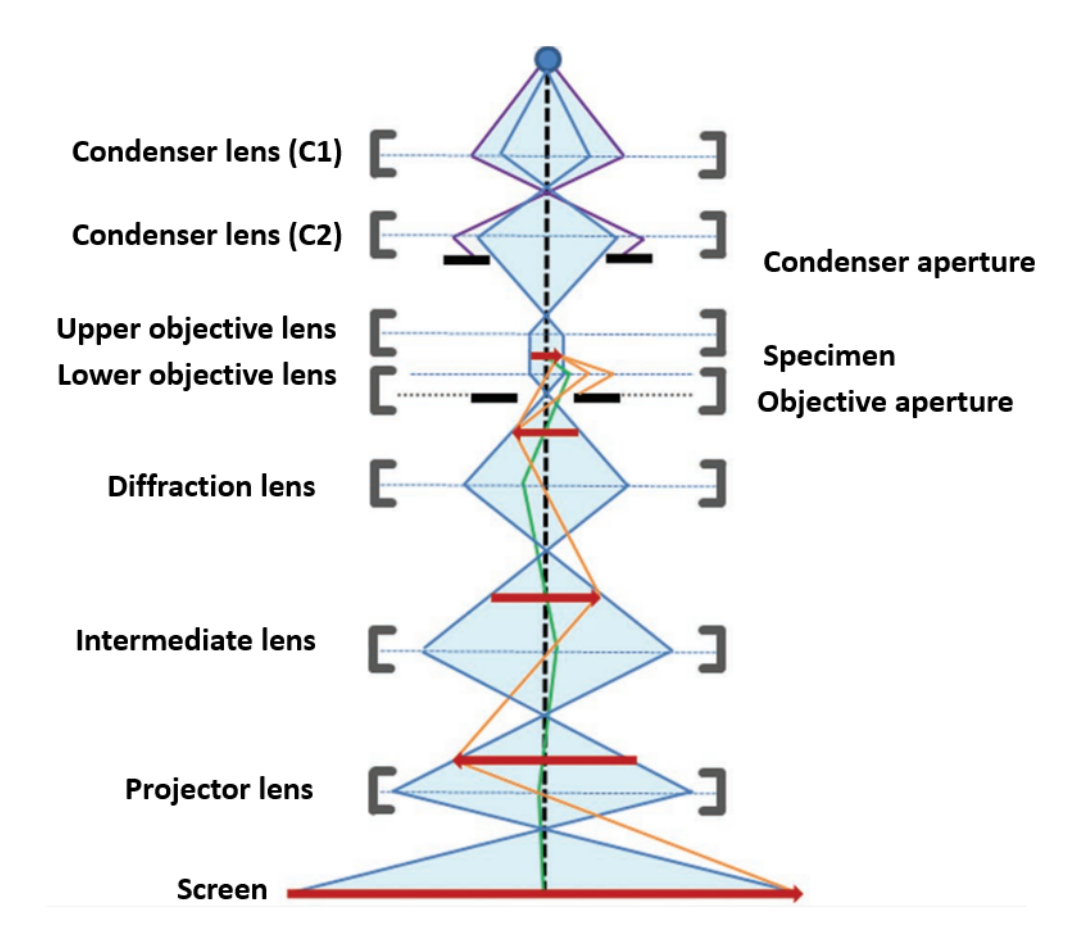


Figure 4.2: A schematic diagram of an electron microscope. The electron beam is illustrated in blue, while gray brackets indicate the lenses. Black bars represent the apertures, and a red arrow signifies the specimen and its (intermediate) images. The trajectories of scattered electrons are shown in orange and green [172].

Following the condenser lenses, the objective lenses serve as a critical component of the TEM. Most TEMs feature an objective twin-lens system (Figure 4.2) that consists of two electromagnetic lenses: one positioned above the sample to provide additional control over the beam and another below the sample that magnifies the image by approximately 50 times [172]. The intermediate lens, located further down the TEM column (Figure 4.2), is responsible for magnifying the initial image generated by the objective lens and projecting it onto the viewing screen in imaging mode. By adjusting the excitation of the intermediate lens, it can also project the diffraction pattern, which is focused on the back focal plane (BFP) of the objective lens, onto the viewing screen in diffraction mode.

#### 4.1.2 Aberrations

In TEM, various lens aberrations such as spherical  $(C_s)$  aberration, chromatic  $(C_c)$  aberration and astigmatism significantly impact image quality and resolution. Spherical aberration, as in Figure 4.3a, arises because electrons that are farther from the optical axis are bent more strongly by the magnetic lens than those near the optical axis, leading to the formation of a disk instead of a perfect point focus. As a consequence, instead of converging to a single point, these electrons form a disk-like pattern. Chromatic aberration (Figure 4.3b), on the other hand, occurs due to differences in electron speeds as they travel through the lens; slower electrons are focused more effectively than faster ones, resulting in multiple focal points instead of a single one. Spherical aberration can be corrected by using multipole correctors, such as hexapole or quadrupole/octupole elements, which create additional magnetic or electrostatic fields to counteract the aberration. Chromatic aberration can be minimised by using energy filters or monochromators to select electrons of a narrow energy range, thus reducing the spread caused by energy differences. Astigmatism arises when magnetic lenses, which are ideally assumed to possess perfect rotational symmetry, exhibit imperfections due to factors such as machining errors, variations in the lens material, asymmetry in windings, and contamination on apertures. These imperfections can lead to elliptical rather than circular symmetry in the lens. This issue is commonly resolved using stigmators, small coils that create a compensating magnetic field to balance the inhomogeneities causing astigmatism [168, 171, 173].

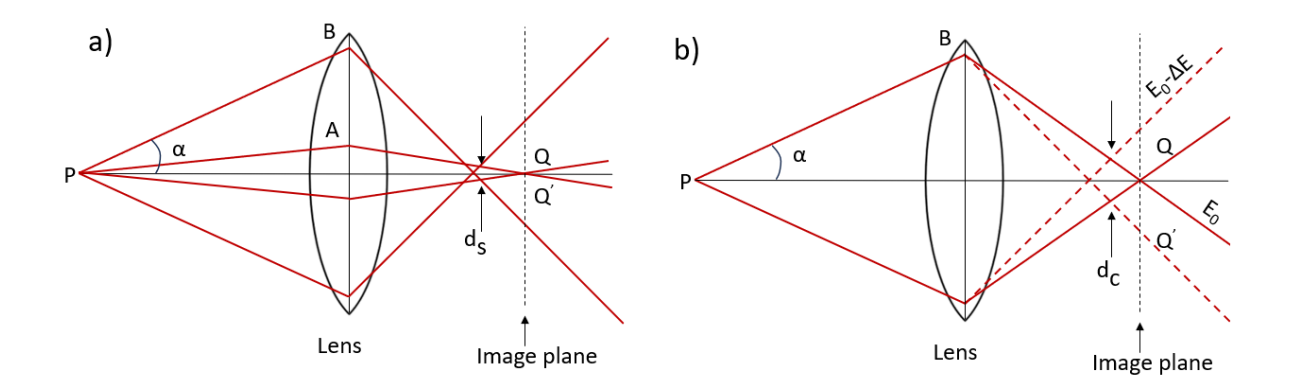


Figure 4.3: Schematic representation of (a) spherical aberration ( $C_s$ ) and (b) chromatic aberration ( $C_c$ ) in an electron lens.  $d_s$  and  $d_c$  are the minimum diameters for spherical and chromatic aberrated electron beams, respectively [171].

#### 4.1.3 The modes of operation

The operation of TEM is fundamentally organised around two primary modes: diffraction mode and imaging mode (Figure 4.4). In both modes, the objective lens plays a critical role in controlling how the resulting data is captured. In diffraction mode, the objective lens collects electrons that have passed through unscattered or scattered by the specimen at different angles to create a diffraction pattern (DP) in the backfocal plane (BFP). This diffraction pattern contains essential information about the specimen's crystal structure and periodicity. Subsequently, these scattered electrons are recombined by the lens system to form an image in the image plane, which allows for detailed structural analysis of the specimen. The ability to switch between these modes allows for the examination of either diffraction data or imaging features at various resolutions [168, 174].

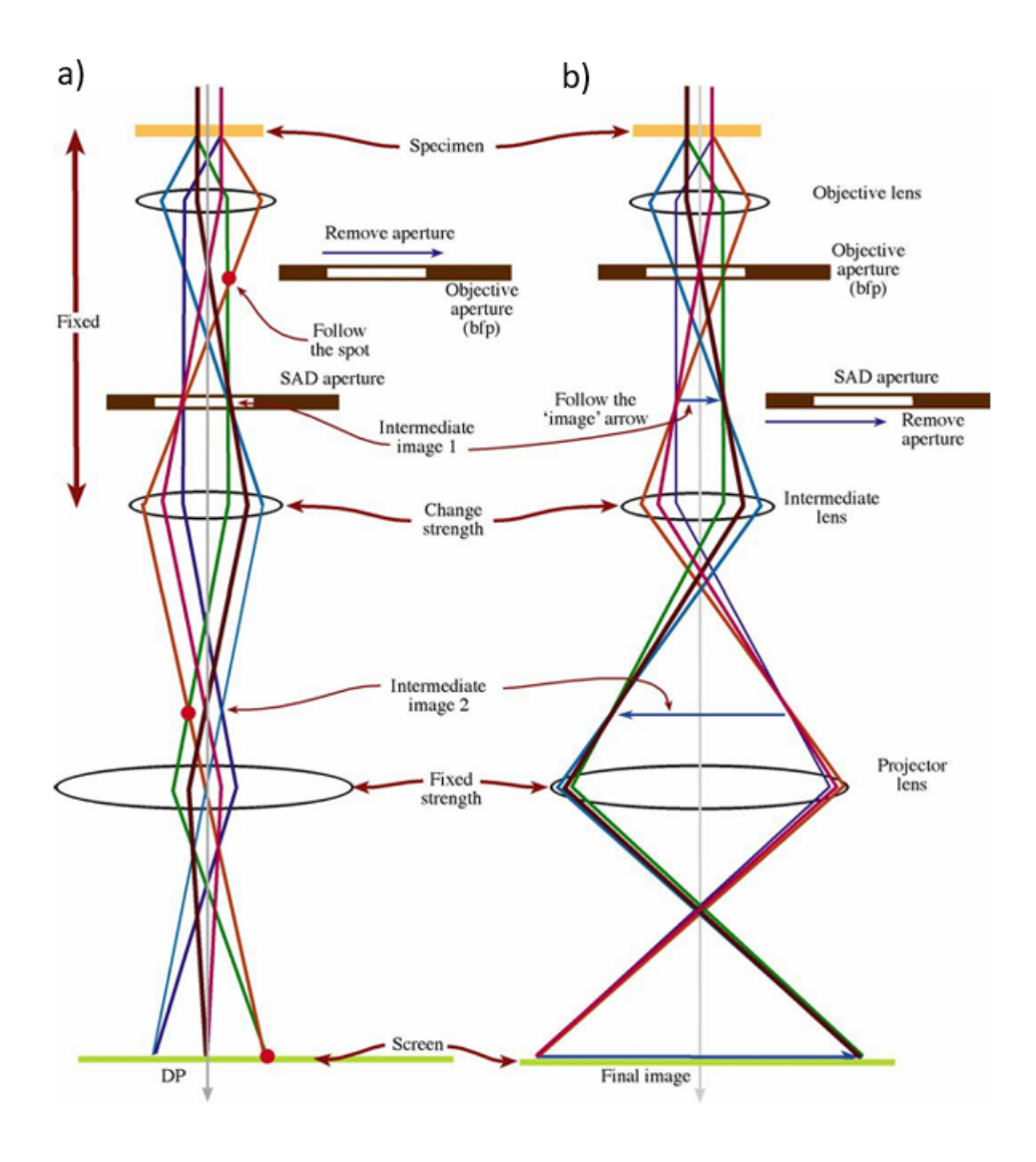


Figure 4.4: This diagram represents the optical paths and operational modes in a transmission electron microscope (TEM). (a) diffraction mode, and (b) imaging mode [168].

One of the key operations within diffraction mode is micro/nano-diffraction (Figure 4.4). In this mode, the goal is to isolate diffraction data from a specific area of the specimen, reducing the information from unrelated regions. A typical DP may contain electrons scattered from the entire illuminated area of the specimen, which can pose significant challenges. For instance, specimen irregularities such as uneven thickness and deformation can cause diffraction patterns to become diffuse, and intense direct beam illumination can saturate the diffraction pattern, making the analysis difficult. To mitigate these issues, micro/nano-diffraction is employed to refine the diffraction

pattern by limiting the illuminated region of the specimen. By doing so, a specific area of interest within the sample can be selected, enhancing the clarity of the diffraction data [168, 175].

There are two primary strategies to perform micro/nano-diffraction by limiting the illuminated area of the specimen: reducing the size of the electron beam or inserting an aperture that selectively allows only a portion of the electrons to pass through and form a diffraction pattern. The first method, which involves manipulating the condenser lenses to converge the electron beam at the specimen, is used for creating convergent beam electron diffraction (CBED) patterns [168]. The second and more common method involves using a selected-area aperture. This aperture is inserted into one of the image planes of the imaging lens, which is conjugate with the specimen plane. This configuration creates a virtual aperture at the specimen's location, enabling the selection of a specific region to contribute to the diffraction pattern. By choosing the correct area through the aperture, a more precise diffraction pattern can be obtained [174].

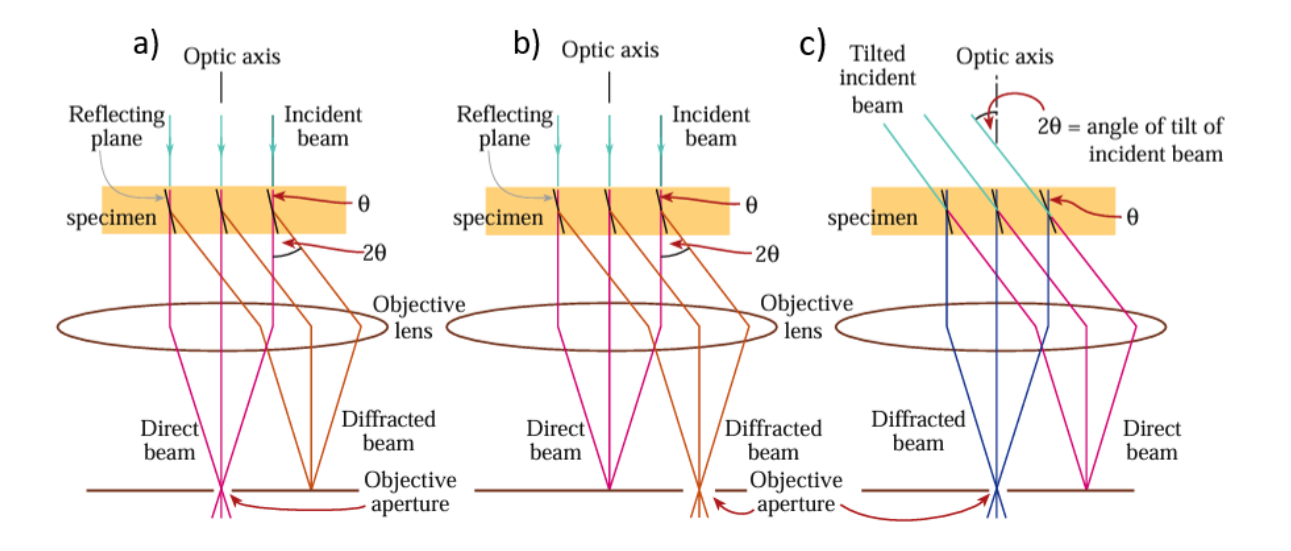


Figure 4.5: Ray diagrams of imaging modes in a transmission electron microscope (TEM). (a) Bright-field (BF) mode, where the objective aperture selects the unscattered (direct) beam. (b) Dark-field (DF) mode, with the objective aperture selecting a diffracted beam. (c) Centred DF imaging with a tilted incident beam [168].

Image mode can be divided into two primary types: bright-field (BF) and dark-field (DF) imaging. These modes differ in how the transmitted electrons are detected to form an image. In bright-field imaging, the objective aperture is placed in such a way that it allows only the unscattered (electrons that suffered no angular deviation) electrons to pass through to the detector, as in Figure 4.5a. This results in an image where the sample appears dark compared to the surrounding vacuum. On the other hand, dark-field imaging selected the diffracted electrons rather than the transmitted ones. DF imaging highlights areas of the samples that scatter the electron beam in a particular direction. The sample appears bright in these regions, contrasting with the surrounding dark vacuum [155, 176]. Because the scattered electron beam is travelling at an angle to the optic axis (Figure 5b) a standard DF image is blurred by the spherical aberration in the objective lens. To overcome this the incident electron beam can be tilted using specialised coils located above the specimen, such that the desired scattered beam now passes along the optic axis (Figure 5c). This mode of operation is called 'centred' DF imaging.

## 4.1.4 Scanning transmission electron microscopy

Scanning transmission electron microscopy (STEM) is a technique that utilises a converged electron beam for imaging and analysis. In contrast to TEM, which employs a nearly parallel electron beam with a small convergence angle, STEM focuses the beam into a finely converged probe with a relatively large convergence angle (as shown in Figure 4.6). The probe scans across the sample in a raster pattern, constructing an image pixel by pixel, with the signal recorded based on the probe's position. This serial data acquisition method results in slower imaging compared to TEM. The resolution depends on the probe size, which is influenced by parameters such as, beam current, and aberrations in the objective lens. The condenser and objective lenses project the electron source onto the sample to form the probe, which is demagnified to limit its contribution to the final spot size [168, 177, 178].

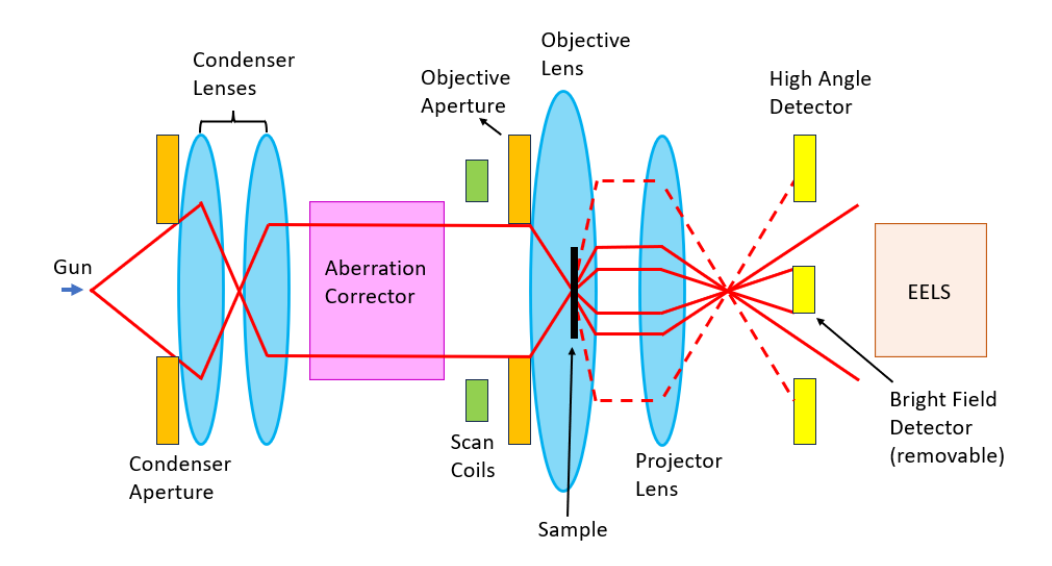


Figure 4.6: Electron optics in a scanning transmission electron microscope (STEM), showing the trajectory of electron beams as they pass through optical components such as condenser, objective, projector lenses and apertures. The diagram also shows the array of detectors used to capture transmitted electron signals [179].

STEM employs a variety of detectors to capture different types of electron scattering, enabling multiple imaging modes (as shown in Figure 4.7). Bright-field (BF) imaging is achieved by using a BF detector that collects electrons scattered within a probe semi-convergence angle from the optical axis. Dark-field (DF) imaging is performed using an annular detector, which collects electrons scattered outside the BF disc. This setup forms an image known as the annular dark-field (ADF) image. For higher-angle scattering, a high-angle annular dark-field (HAADF) detector is used, collecting electrons scattered at angles typically greater than five times the probe semi-convergence angle, which is particularly useful for imaging heavier elements due to Rutherford scattering. In Rutherford scattering, electrons are deflected at larger angles by nuclei, causing the heavier atoms to appear brighter in the resulting image. This effect is utilised in HAADF imaging, which is often referred to as 'Z-contrast' imaging due to the distinct contrast between elements with different atomic numbers (Z). Heavier atoms scatter electrons more strongly, generating a greater signal and appearing brighter in the image compared to lighter atoms [168, 178].

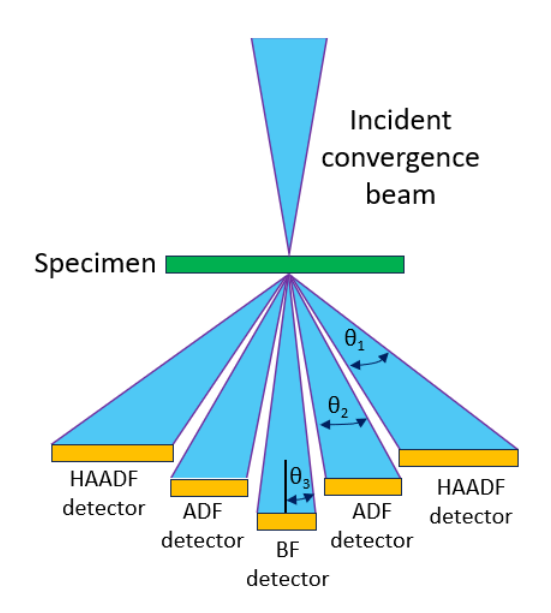


Figure 4.7: Schematic of STEM detection geometry showing different detectors used for various angular ranges of scattered electrons[168].

The resolution of STEM images is primarily limited by spherical aberration due to the rotational symmetry of the probe-forming electromagnetic lenses. This limitation has driven significant efforts to improve resolution by correcting these aberrations. In 1947, Scherzer proposed that breaking the rotational symmetry of the optical system could overcome these inherent aberrations and enhance resolution. This idea paved the way for the development of aberration correctors, which rely on non-round elements known as multipoles (Figure 4.8) to correct spherical aberration. Multipoles, named after their rotational symmetry (e.g., quadrupoles, hexapoles, and octupoles), allow for the correction of aberrations that would otherwise be impossible with traditional round lenses. There are two primary types of aberration correctors: quadrupole-octupole (QO) correctors and hexapole correctors [179].

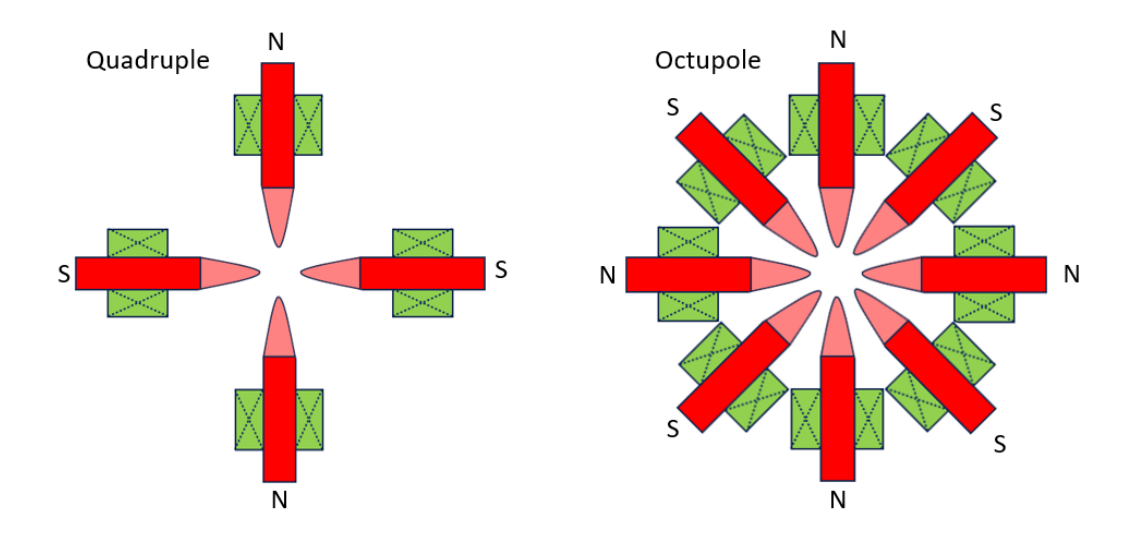


Figure 4.8: Diagram of magnetic multipoles used for spherical aberration correction shows the top view of poles with alternating polarities [179].

In a quadrupole-octupole (QO) corrector (Figure 4.9), the alternating combination of multipoles is used to correct spherical aberration. The first quadrupole creates a line focus along the negative spherical aberration axis of the first octupole. The octupole introduces negative spherical aberration along a pair of axes perpendicular to the beam propagation direction (e.g., the x and y axes), while simultaneously creating positive spherical aberration along axes oriented at 45° to these directions. To continue the correction process, two additional quadrupoles are employed. The second and third quadrupoles produce a line focus along the perpendicular direction for the second octupole, while the final quadrupole is used to reform the beam into a round shape. The two octupoles impart negative spherical aberration in the x and y axes, but also cause some four-fold distortion of the beam. A third octupole, acting on the round beam, is required to correct this distortion and eliminate the aberration [180]. The quadrupoles act as focusing and defocusing lenses: along the x axis, the quadrupole compresses the beam, while along the perpendicular y axis, it spreads the beam out. This arrangement ensures that the beam undergoes the necessary transformations to achieve the desired spherical aberration correction, resulting in a properly focused and round beam [179–181].

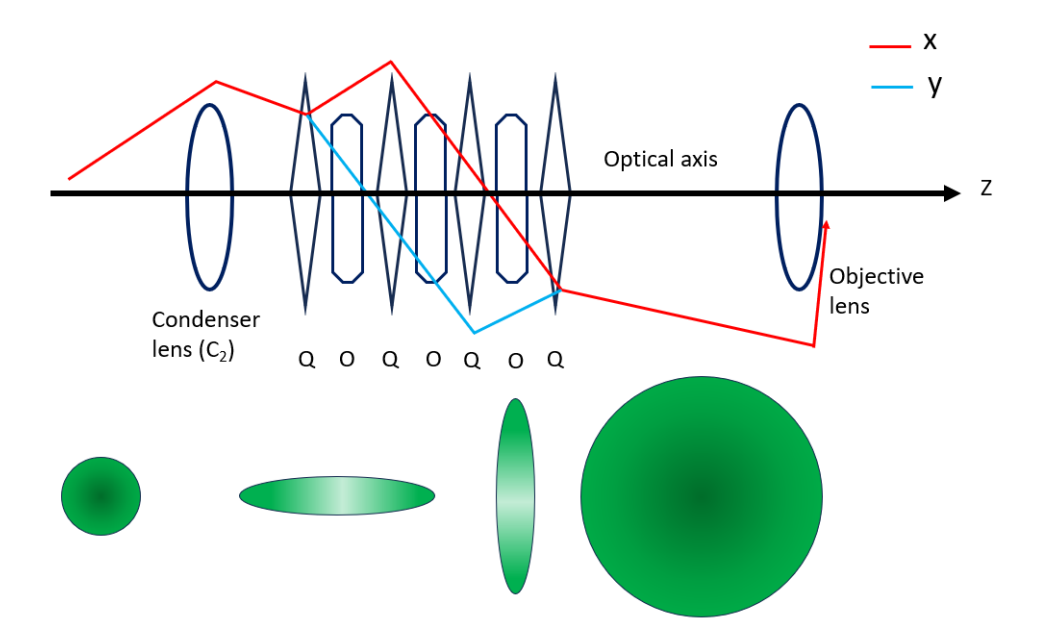


Figure 4.9: A diagram of the trajectories of axial rays in the x and y directions through the QO aberration corrector (with z along the optic axis) [180].

With the integration of multipole aberration correctors, STEM imaging has achieved remarkable improvements in spatial resolution. In addition to the abberation correctors, the introduction of monochromators (MC) into STEM instrumentation has led to enhanced spatial resolution in STEM imaging and a significant improvement in the energy resolution achievable for electron energy loss spectroscopy (EELS). Several monochromator designs have been developed for STEM, incorporated into existing microscope columns. The design we focus on here is the alpha-type magnetic monochromator, which was used in conjunction with the aberration correctors in the SuperSTEM facility employed in this work. An alpha-type monochromator works by using two parallel energy filters (magnetic prisms) and an energy selection slit placed between them (Figure 4.10).

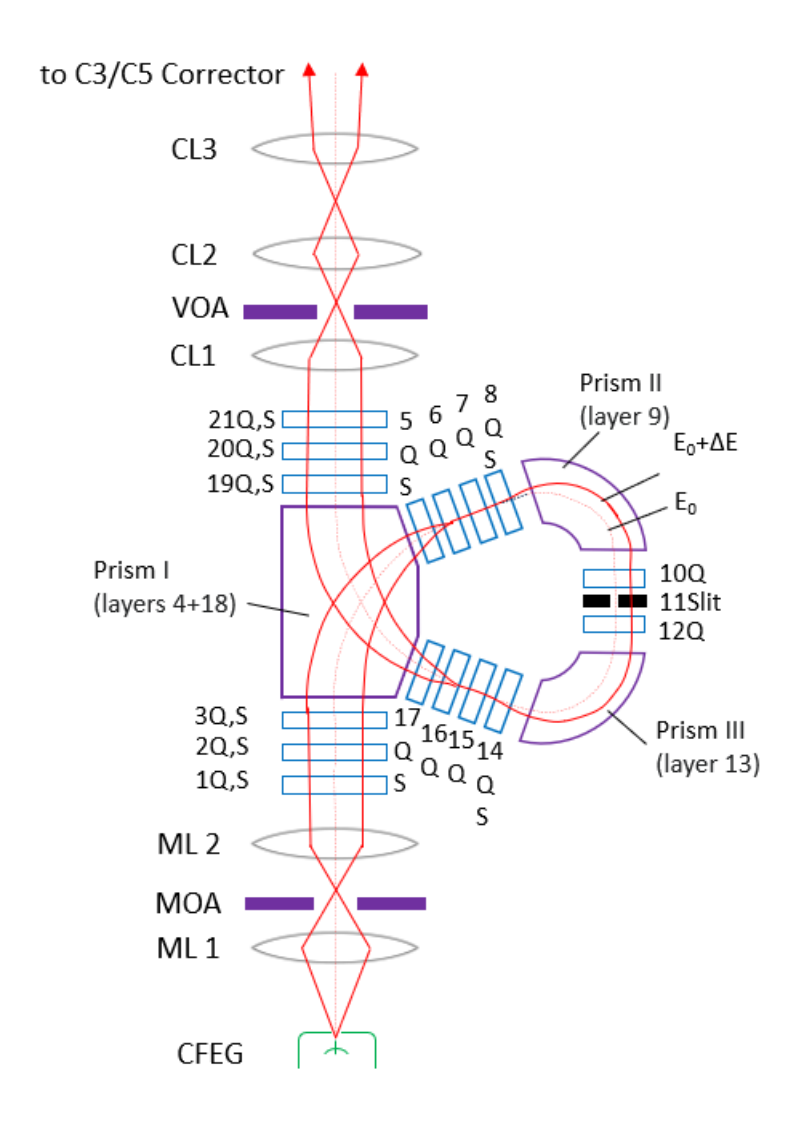


Figure 4.10: Schematic cross section of alpha shaped monochromator of STEM column [182].

The incident electron beam first passes through the first magnetic energy filter, which disperses the electron beam. The dispersed beam then enters the energy selection slit which allows only electrons of a narrow energy range to pass through. The energy resolution after monochromation by the slit improves as the width of the energy selection slit narrows. However, as the energy resolution increases, the number of monochromated electrons decreases due to the selective energy filtering by the slit. After the electron beam is dispersed by the first and second magnetic energy filters, it enters the third filter, where the electrons are effectively directed in the opposite manner. At this

stage, the third energy filter undisperses the beam, counteracting the dispersion introduced by the first two filters. Once the dispersion is corrected, the beam is re-directed along the electron optic axis, where it is then focused onto the specimen for imaging or spectroscopy. The quadrupoles, positioned between the first and second prisms (Figure 4.10), control the energy dispersion and adjust the spectrum's magnification. The quadrupole after the second prism fine-tunes first-order abberations to cancel energy dispersion at the exit crossover, ensuring proper beam alignment. Sextupoles, located in both halves of the monochromator, correct second-order aberrations, maintaining the beam's accuracy and preventing distortions. Together, quadrupoles and sextupoles optimise the monochromator's performance, ensuring a precise, energy-selective beam output [182, 183].

## 4.1.5 Electron energy loss spectroscopy

Electron energy loss spectroscopy (EELS) is a powerful analytical method in TEM and STEM that measures the energy distribution of electrons that have interacted with a specimen and lost energy through inelastic scattering. These energy losses result from various electron-specimen interactions, and their analysis provides information about the material's physical and chemical properties. The energy loss of primary electrons typically ranges from 0 eV to several keV. Generally, energy losses up to 50 eV correspond to interactions with valence electrons, including plasmon scattering and phonon excitations. Losses beyond 50 eV are associated with core electron excitations, revealing element-specific ionisation edges that provide insights into atomic composition and bonding environments [168, 184]. By exposing the specimen to a beam of electrons with a known, narrow range of kinetic energies, EELS detects energy losses due to inner-shell ionisations and other scattering processes, allowing for the identification of elemental components. This capability extends to determining atomic composition, chemical bonding, valence and conduction band properties, and surface-specific phenomena. It can also provide element-specific pair distance distribution functions, offering a detailed picture of the material at the atomic level [185, 186]. With electron beam monochromation, EELS is capable of achieving energy resolutions down to a few millielectron volts (meV), which enables it to resolve both vibrational and electronic modes of energy losses.

The energy loss is measured using the dispersive properties of a homogeneous magnetic field in an EEL spectrometer. EELS instrumentation relies on a magnetic prism (Figure 4.11), in which a uniform magnetic field **B** is produced by an electromagnet equipped with precisely shaped pole pieces. When high-energy electrons pass through a magnetic field **B**, oriented perpendicular to their momentum  $m_e \nu$ , they are deflected along a circular trajectory due to the Lorentz force. The radius r of this trajectory is given by the equation [159, 187]:

$$r = \frac{\gamma m_e \nu}{eB} \tag{4.1}$$

Here, e represents the electron charge,  $m_e$  is the electron mass,  $\nu$  is the electron speed, and  $\gamma$  is the relativistic correction factor. The radius of the circular path varies with the energy of the electrons, allowing the spectrometer to separate them based on their energy losses. An EEL spectrum is obtained by collecting electrons sorted by their energy, offering a detailed distribution of energy losses for analysis [187].

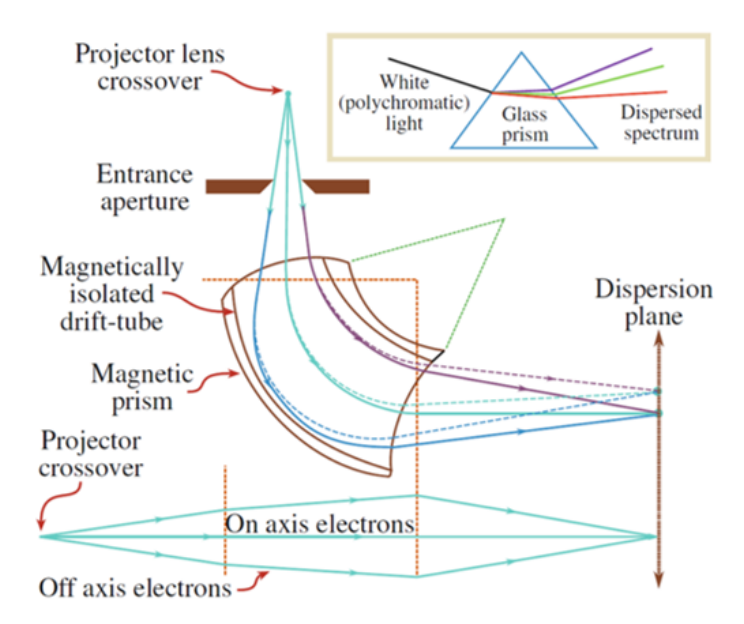


Figure 4.11: Schematic of an electron energy loss spectroscopy (EELS) system illustrating the dispersion of electrons through a magnetic prism, analogous to the dispersion of white light through a glass prism, with the formation of a spectrum in the dispersion plane [168].

An energy-loss spectrum typically consists of three main regions: the zero-loss peak, the low energy-loss peaks (primarily from plasmon excitations), and the high energy-loss peaks (associated with ionisation losses). An example EELS spectrum is shown in Figure 4.12, highlighting these regions. The zero-loss peak mainly comprises electrons that have experienced minimal energy loss. While it is called the "zero-loss" peak, it also contains electrons that have undergone slight energy losses, which are below the resolution of the EEL spectrometer, such as those due to phonon excitations. The full width at half maximum (FWHM) of the zero-loss peak is commonly used to define the resolution of the EELS system. This width results from both the intrinsic resolution of the spectrometer and the energy spread of the electron beam [188]. The low-loss region refers to the energy range up to approximately 50 eV, where electrons experience energy loss due to phenomena such as plasmon oscillations or inter-band transitions. Plasmons can be thought of as the quantised version of free electrons oscillations in the material. The oscillations occur due to weak interactions between electrons and are non-localised.

The energy lost by the electron due to generating a plasmon of frequency  $\omega_p$  is given by the equation [159, 188]:

$$E_p = \frac{h}{2\pi}\omega_p = \frac{h}{2\pi}\sqrt{\frac{ne^2}{\epsilon_0 m}} \tag{4.2}$$

where, h represents Planck's constant, e and m denote the charge and mass of an electron, respectively,  $\epsilon_0$  is the permittivity of free space, and n signifies the density of free electrons. In the energy-loss spectrum, the plasmon peak is a prominent feature. It is typically the second-most significant peak after the zero-loss peak and can be used to estimate the specimen thickness (t). The specimen thickness relies on the relationship between the intensity of the total energy loss spectrum peak  $(I_t)$  and the zero-loss peak  $(I_0)$ , as well as the total energy loss mean free path  $(\lambda_t)$ , which is material-specific. This relationship can be expressed as follows [168, 189]:

$$t = \lambda_t \frac{I_t}{I_0}. (4.3)$$

The thickness measurement using EELS has distinct advantages over other thickness measurement techniques, as it can be applied to any specimen, whether amorphous or crystalline, across a wide range of thicknesses [168].

Apart from collective plasmon excitations, other excitations, such as valence state excitations and low-lying core state excitations, are also present in the low-loss region. The energy associated with plasmon excitations is typically in the range of 5–25 eV. The position and width of these plasmon peaks are related to the electronic structure of the material and can be utilised to distinguish between different materials [187]. Finally, in a core-loss process, an inner-shell electron in the sample is excited from an occupied state to an unoccupied state above the Fermi level. The initial state is a bound core state, while the final state depends on the band structure of the solid. The position of the energy loss edges in the core-loss region (greater than 50 eV to a few keV) provides valuable information about the chemical composition of the sample and its local elec-

tronic structure, as these transitions are specific to the element and the shell involved (e.g., K, L, or M shells) [179].

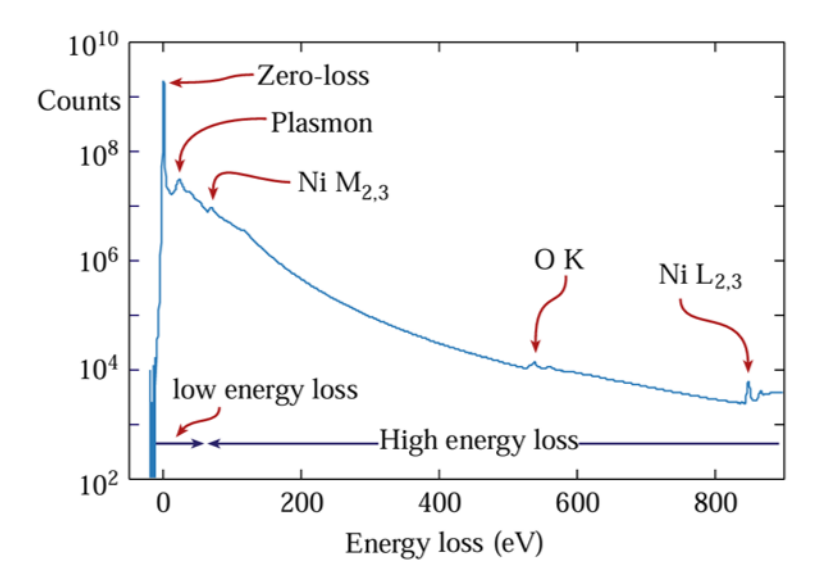


Figure 4.12: Example of an EELS spectrum highlighting key features, including the zero-loss peak, plasmon peak, and energy loss edges associated with specific elements [168].

# 4.2 Raman spectroscopy

Raman spectroscopy is a powerful vibrational spectroscopic technique used to study the vibrational, rotational, and other low-frequency modes of molecules. It is named after the Indian physicist C. V. Raman, who first discovered the effect in 1928 [190]. Raman spectroscopy is based on the interaction between light and matter. When monochromatic light, typically from a laser, strikes a molecule of a material, the energy of the photons can be transferred to or from the molecule, resulting in an inelastic scattering process. This scattering can cause a shift in the energy of the scattered photons compared to the incident photons. The amount of energy shifted corresponds to the vibrational energy levels of the molecule, enabling Raman spectroscopy to probe the vibrational modes of the material.

## 4.2.1 Theory

When electromagnetic waves interacts with molecules, an electric dipole within the molecule is induced, as the atoms in the molecule become polarised. Polarisation occurs when the centre of negative charge (i.e. the electrons) is displaced from the atomic nuclei upon the interaction with an external electromagnetic field. This results in an induced electric dipole moment. The extent to which this dipole moment is induced depends on how easily the molecule's electron cloud can be distorted, which is characterised by the molecule's polarisability  $(\alpha)$  in response to the external electric field  $(\mathbf{E})$ . The induced dipole oscillates at the frequency of the external electromagnetic field, and this oscillation generates an electromagnetic wave, which is scattered in all directions [191, 192]. In the case of elastic scattering, or Rayleigh scattering, the polarisability is considered static, i.e. it does not change over time, leading to no frequency shift in the scattered electromagnetic wave. The frequency of the scattered wave remains the same as that of the incident light. However, Raman noticed that when a molecule is vibrating, the polarisability of the molecule changes with time. The vibrational motion (phonons) causes fluctuations in the electron cloud, leading to variations in the dipole moment as the molecule vibrates. This results in inelastic scattering, where the frequency of the scattered light differs from that of the incident light. The energy difference between the incident and scattered photons corresponds to the energy of the molecular vibrations [191, 192].

There are two main types of Raman scattering (as shown in Figure 4.13): Stokes and anti-Stokes scattering. In Stokes scattering, the scattered photon has less energy  $h(\nu_0 - \nu_1)$  than the incident photon, and the energy difference is transferred to the molecule, exciting it to a higher vibrational state. Conversely, in anti-Stokes scattering, the scattered photon has more energy  $h(\nu_0 + \nu_1)$  than the incident photon, and the energy is transferred from the molecule to the scattered photon, causing the molecule to relax to a lower vibrational state. Stokes scattering typically results in stronger signals than anti-Stokes scattering due to the higher population of molecules in the lower

energy states at room temperature [193, 194].

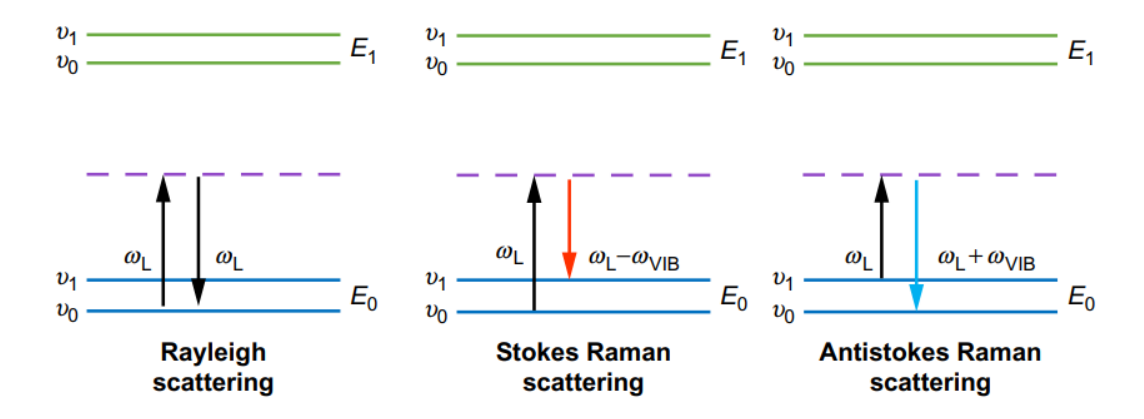


Figure 4.13: Energy level diagrams illustrating Rayleigh, Stokes, and Anti-Stokes Raman scattering [193].

#### 4.2.2 Instrumentation

Raman spectroscopy relies on highly monochromatic light, typically provided by continuous wave laser sources. Among these, helium-neon (He-Ne) lasers are a common choice, emitting a single wavelength at 632.8 nm. The wavelength of monochromatic light used in Raman spectroscopy varies, with the most common sources emitting in the range of 532 to 785 nm. The optical setup, as illustrated in Figure 4.14, uses a microscope system to illuminate and collect light from a microscopic area of the sample. The microscope has a high numerical aperture (NA) to effectively collect the Raman-scattered light over a wide solid angle [195].

Next, a pinhole spatial filter eliminates diffraction rings and high frequency noise surrounding the focused spot, ensuring a clean, focused laser beam to illuminate the sample. Then the monochromated beam is reflected by a beam splitter and passes through an objective lens to illuminate the sample. The Raman-scattered light from the sample is collected by a wide-aperture objective lens and focused onto an adjustable pinhole spatial filter located in the microscope's image plane. This pinhole spatial filter ensures that only light from the focused area of the sample reaches the spectral analyser

and detector. By adjusting it, the spatial resolution can be improved to 1  $\mu$ m with a  $100\times$  objective lens [120, 196].

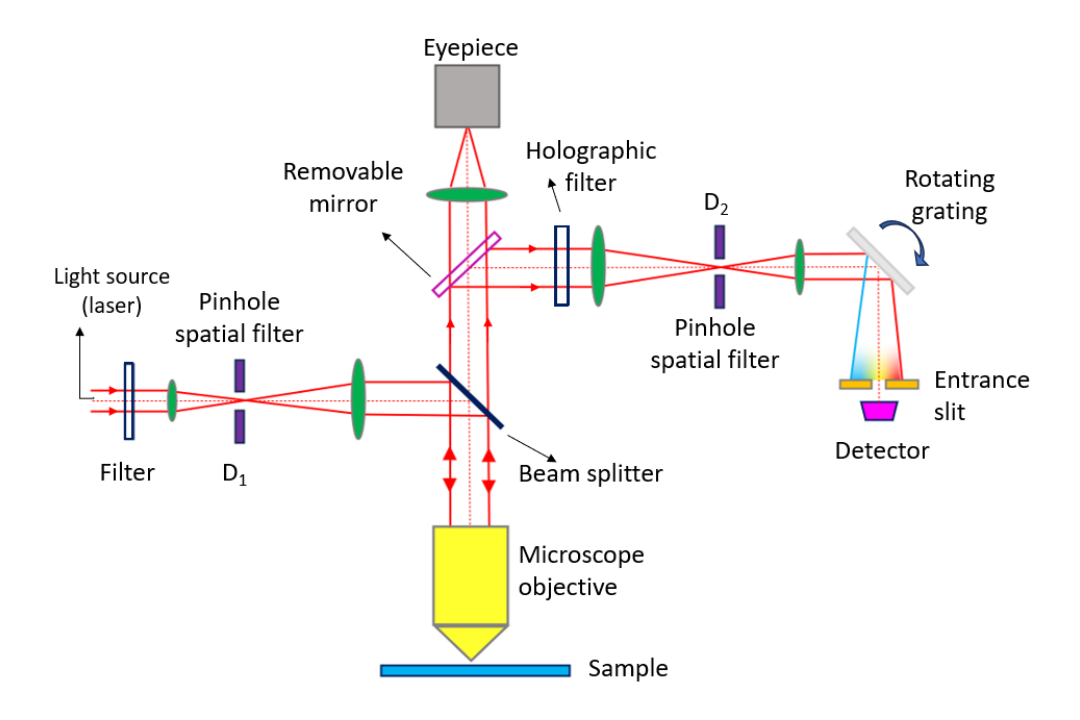


Figure 4.14: Optical diagram of a Raman spectroscopy system. The setup includes a laser source, spatial filters ( $D_1$  and  $D_1$ ), beam splitter, microscope objective for focusing the beam on the sample, holographic filter, and a rotating grating spectrometer for spectral analysis. The removable mirror allows the beam to be directed to the eyepiece for visualisation or to the detector for Raman signal acquisition[120].

Since the Raman scattering is intrinsically weak, it is important to suppress the signal from Rayleigh scattering. Holographic filters are commonly employed in Raman instruments nowadays to filter the Rayleigh signal out. The Raman-scattered light is then dispersed by a diffraction grating, which is the core component of the spectral analyser. The diffraction grating disperses the light according to its wave number, based on principles similar to Bragg's Law, where different wavelengths are diffracted at discrete angles. This allows the system to resolve Raman shifts with a spectral resolution of 1 cm<sup>-1</sup>. Modern Raman systems use a rotating diffraction grating to cover a wide spectral range, typically from 400 to 4000 cm<sup>-1</sup> [120, 195].

The dispersed light is detected by either single-channel or multi-channel detectors. Single-channel detectors, such as photomultiplier tubes (PMTs), were used in the spectrometer for this work and are commonly employed in Raman studies. PMTs are known for their high sensitivity, low background noise, wide wavelength range, reliability, and relatively low cost. However, their main disadvantage is their low throughput, as they can only read one wavelength at a time. This limitation results in longer acquisition times to record a full spectrum. Despite this, their characteristics make them a popular choice for many Raman applications. The resulting data is then processed and plotted as a Raman spectrum, providing valuable insights into the sample's vibrational properties [197].

## 4.3 Focused ion beam

The focused ion beam (FIB) system is a versatile tool with a wide array of applications across scientific research and industrial sectors. The working principle of FIB involves focusing a beam of charged ions, typically gallium, onto the surface of a sample. These ions are accelerated to high energies (usually between 2 kV and 30 kV) and interact with the material, causing both physical sputtering (ejection of atoms from the sample surface) and electronic excitations. The sputtering process allows for the controlled milling or etching of a surface with high precision, while the electronic interactions generate secondary electron emissions, which are detected to provide high-resolution images of the sample surface. FIB systems are often integrated with scanning electron microscopes (SEM), offering simultaneous imaging and milling capabilities. While its primary use is precision milling, it is also essential for several specialised tasks. One of its most notable applications is the preparation of samples for TEM, where it enables the creation of thin lamellae with nanometer precision [198].

#### 4.3.1 Instrumentation

A typical FIB system includes a sample chamber maintained under high vacuum, an ion column with an ion source, accelerating, focusing, and scanning optics, and a series of detectors for secondary electron and ion detection. Many FIB systems also incorporate an electron column, called dual-beam FIB (Figure 4.15), typically mounted vertically above the stage, which focuses on the same point onto the sample as the ion column. This setup enables simultaneous use of both the ion and electron beams in a system known as a dual-beam FIB [199].

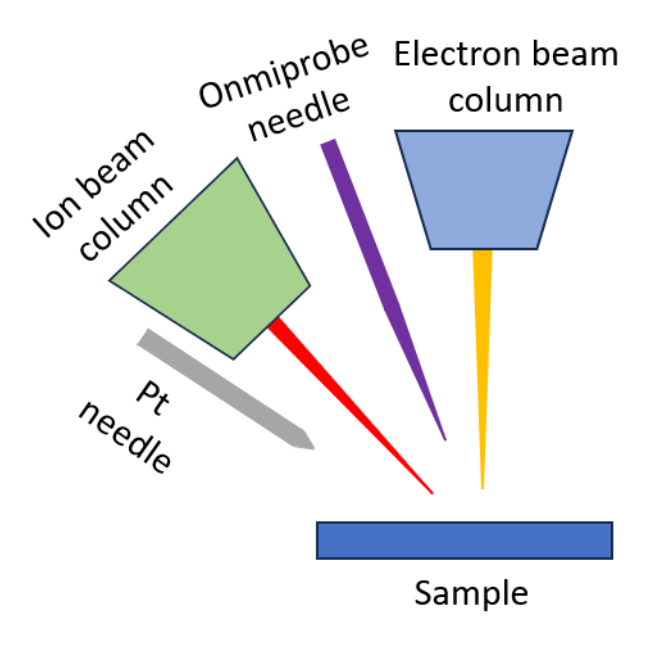


Figure 4.15: A schematic of the arrangement of an ion beam column, electron beam column, Omniprobe needle, and Pt needle with respect to the sample in a dual-beam system [200].

The focused ion beam (FIB) system uses a liquid metal ion source (LMIS), typically gallium (Ga), which is heated to near evaporation and then flows to coat a sharp, heat-resistant tungsten needle. The Ga flows to the needle tip, forming a Taylor cone under the influence of an electric field. This field causes field evaporation, emitting Ga ions, which are then accelerated down the ion column. The LMIS operates at low emission currents (1–3  $\mu$ A) to maintain a stable beam, as higher currents can lead to droplets and

instability. The ion current is controlled by the extractor and a suppressor (4.16). The suppressor adjusts the extraction current by applying an electric field of upto +2kV, ensuring a constant beam current without disturbing the needle tip. This is crucial for stable operation, as changes in the extractor voltage can cause beam drift. The suppressor also helps maintain consistent ion emission by counteracting contamination effects [201].

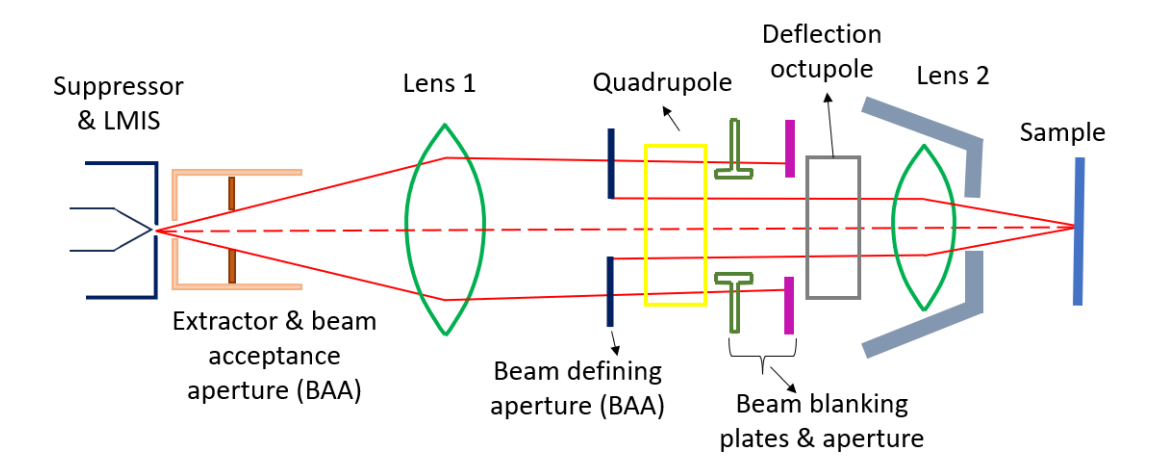


Figure 4.16: A ray diagram detailing the key components of a FIB system, including the suppressor, extractor, beam defining aperture, lenses, quadrupole, and the sample [200].

In ion beam columns, the ion beam is shaped by a series of lenses and passes through an interchangeable aperture with varying hole sizes, which control the beam diameter and determine the final beam current. Additional components include deflection plates to raster the beam across the sample surface, stigmation poles to maintain a spherical beam profile, and a high-speed beam blanker to redirect the beam onto a stop, such as a Faraday cup. Ions require electrostatic components for focusing and steering, as their charge-to-mass ratio makes electromagnetic lenses impractically heavy, unlike those used for electrons [199, 202].

For the ion beam to interact with the sample precisely, the sample is mounted on a grounded stage with three-axis translation, rotation, and tilt capabilities. The stage is designed with eucentric point, ensuring the field of view remains centred when the specimen is tilted. This point, where the two beams cross (in dual-beam FIB), allows for accurate alignment. The region of interest is moved to this eucentric point using translation and rotation, and then tilted for the desired angle of beam incidence. The instrumentation also includes a gas injection system (GIS), which is essential for site-specific deposition or etching. Common deposition materials are tungsten and platinum. During TEM sample preparation, a protective layer of platinum or tungsten is deposited to protect the region of interest from ion beam damage during milling. Depending on the application, the emitted signal after ion beam interaction with the sample can be detected using appropriate detectors within the sample chamber. Traditional detectors, such as those found in SEM, can be used to detect the electrons or X-rays produced by the interaction of the ion beam with the sample. The ions sputtered from the sample can also be detected using a range of detectors, including charge electron multipliers [199, 200, 202].

Preparation of TEM specimens involves the following steps: (a) identification of the region of interest, (b)bringing the specimen to eucentric height, (c) platinum deposition using GIS, initially by the electron beam for materials which are too sensitive to ion beam and then ion beam, (d) ion milling (with Ga ions at 30 kV and 2.7 nA) to make a lamella by forming trenches adjacent to the platinum coated region using cleaning cross-section mode (Figure 4.17a) and then under cut the sample(Figure 4.17b), e) lift the lamella out using an Omniprobe (Figure 14.17c), (f) transferring the lamella onto a TEM grid, and welding with platinum (Figure 4.17d), (g) cleaning the specimen's surface with a low energy gallium beam (at 5 kV or lower) by tilting the milled surface of the specimen at 54° with respect to the beam (Figure 4.17e) so that the final thickness of the lamella is less than 100 nm (Figures 4.17f).

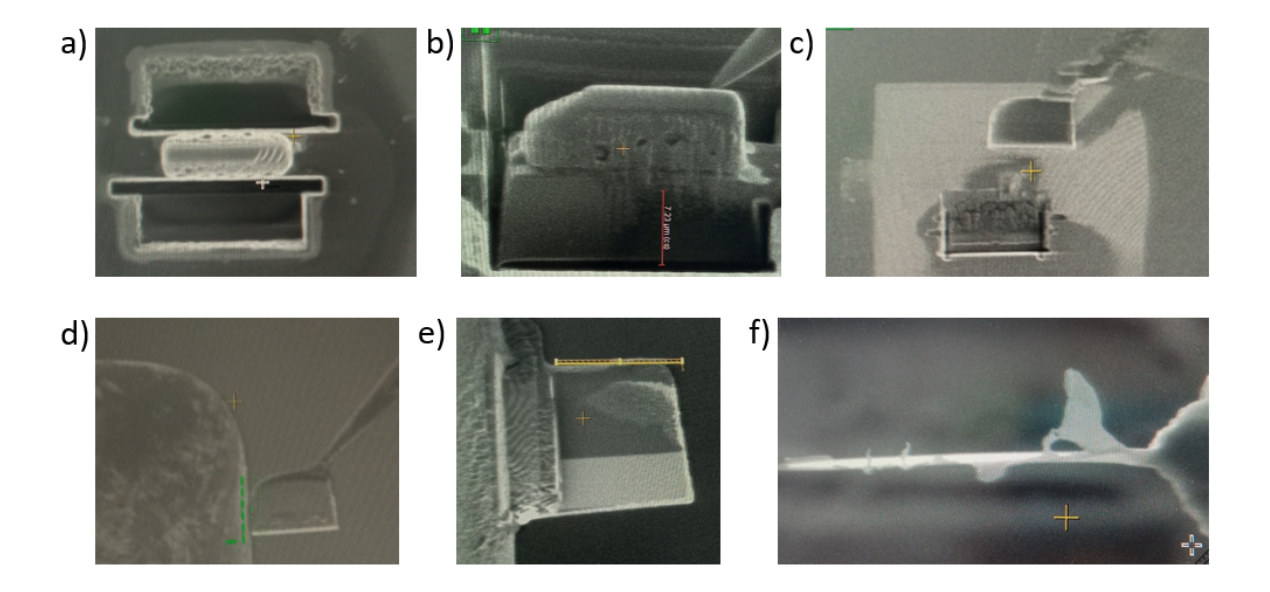


Figure 4.17: (a) Ion milled trenches adjacent to the platinum coated region, (b) attached omniprobe with the platinum deposition, (c) lifting the sample out using omniprobe, (d) the lamella near a TEM grid before attaching. (e) the lemalla before coarse thinning, and (f) the final polished lemalla.

## 4.3.2 Modes of operation

When ions collide with the sample, they transfer energy to the atoms in the material through inelastic collisions. Example include displacement of surface atoms, often causing the ejection of atoms or clusters, a process known as sputtering. This phenomenon is central to material removal, enabling precise milling and patterning. There can be excitation of the sample's surface atoms or electrons, leading to the emission of secondary electrons [203].

FIB systems primarily operate in three main modes (Figure 4.18): imaging, milling, and deposition. In imaging mode, the ion beam scans across the surface of the sample, and detectors capture secondary electrons emitted as a result of ion-sample interactions. This mode provides high spatial resolution but may result in sample damage due to the high-energy ions. The resolution is generally lower than that of an SEM owing to the greater mass of ions compared to electrons. In milling mode, controlled sputter-

ing of the material by the ion beam is used to create nano and micro-scale structures, cross sections for analysis, or precisely defined trenches. Finally, in deposition mode, a platinum needle is positioned near the sample, and the focused ion beam is directed at the specimen region of interest. Secondary electrons from the ion beam-specimen interactions causes platinum from the needle to be deposited onto the sample surface in precise locations. This mode is particularly useful for tasks such as applying protective layers, repairing devices, or creating functional features, with platinum often used for its excellent conductivity and protective properties [201].

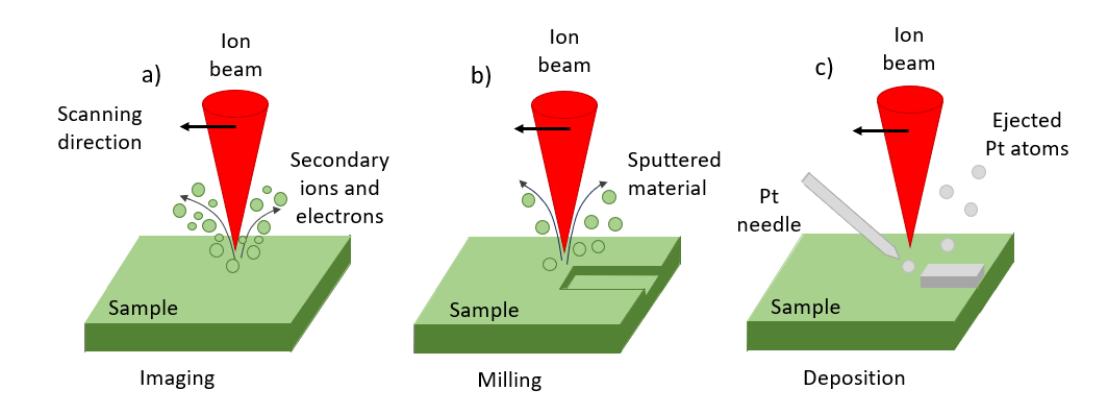


Figure 4.18: Illustration of three modes of FIB: (a) imaging via secondary ions and electrons, (b) milling by sputtering material, and (c) deposition using a Pt needle.

# 4.4 Secondary ion mass spectroscopy

Secondary ion mass Spectroscopy (SIMS) is a powerful analytical technique primarily used for the detailed characterisation of the surface composition and layer structure of solid materials. It operates by bombarding a material with primary ions (typically in the keV range), which penetrate the solid to a certain depth, depositing energy along their track (Figure 4.19). At energies ranging from a few keV to tens of keV, energy deposition primarily occurs through nuclear collisions, known as nuclear stopping power, as opposed to electronic stopping power that dominates at much higher energies (MeV range). This energy induces the emission of secondary particles, including positive or negative ions, electrons, and neutrals. The process involves collision

cascades, which cause intense fragmentation and bond breaking near the ion track, producing mainly atomic particles. Moving outward from the ion track, where energy deposition decreases, intact molecules may be emitted if they gain enough energy to overcome surface binding forces. The secondary ions, which can be atomic or molecular, provide significant information about both the surface and deeper regions of the sample, depending on the mechanisms involved in secondary ion formation [204, 205].

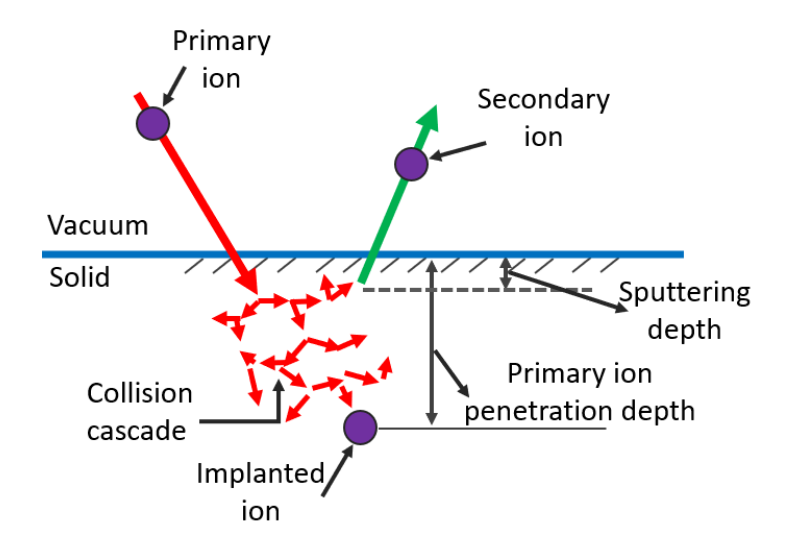


Figure 4.19: Schematic of ion-solid interactions in SIMS [205].

#### 4.4.1 Instrumentation

A secondary ion mass spectrometer (SIMS) consists of five key components: a primary ion gun that generates the primary ion beam; a primary ion column for accelerating and focusing the beam onto the sample; a high-vacuum sample chamber; a mass analyser that separates ions according to their mass-to-charge ratio; and a detector for measuring the ion intensity [206]. SIMS requires a high vacuum (below  $10^{-10}$  mbar) to prevent secondary ions from colliding with background gases and to minimise surface contamination [207]. Three types of ion guns are commonly used: electron ionisation sources for generating gaseous ions (e.g.,  $Ar^+$ ,  $O_2^+$ ,  $SF_5^+$ ), surface ionisation sources for producing Cs<sup>+</sup> ions, and liquid metal ion guns (LMIG) such as Ga [206]. The choice of ion source depends on the required current, beam dimensions, and the sample being analysed. For

instance, an oxygen primary beam  $(O_2^+)$  is used to generate positive secondary ions, while a caesium primary beam  $(Cs^+)$  is used to generate negative secondary ions [208]. The mass analyser can be a sector field, quadrupole, or time-of-flight (ToF) type, with ToF being the most common in static SIMS due to its ability to detect all secondary ions simultaneously. In a ToF analyser, ions are accelerated to a constant kinetic energy from an acceleration potential (V) of 3–8 kV, and their flight time (t) through a tube of distance (L) to the detector is measured. The flight time is calculated using the formula [120]:

$$t = L(2V)^{-\frac{1}{2}} \left(\frac{m}{z}\right)^{\frac{1}{2}} \tag{4.4}$$

This allows the mass to charge ratio  $(\frac{m}{z})$  of the ions to be determined, with heavier ions having longer flight times compared to lighter ones. Detectors include Faraday cups for high current signals, electron multipliers for single ion detection, and microchannel plates for lateral resolution combined with fluorescence detection. Detection limits range from  $10^{12}$  to  $10^{16}$  atoms per cubic centimetre, depending on the instrument and conditions.

# 4.4.2 Modes of operation

In static SIMS mode, the intensity and size of the primary ion beam are controlled so that the disturbed volume does not overlap with adjacent areas affected by previous ion impacts. This mode allows for the collection of data on an essentially unaltered sample surface, where the effects of ion implantation are minimised. Studies show that SIMS spectra remain consistent when ion fluence is below  $10^{-13}$  ions per cm<sup>2</sup>, which suggests that the sample surface is not significantly modified under such conditions [3]. Static SIMS is commonly used to analyse surface compositions with minimal depth alteration [120].

Conversely, dynamic SIMS involves higher primary ion fluences, which progressively erode the sample surface. This process enables the acquisition of depth profiles, with secondary ion intensities recorded as a function of the increasing ion fluence. By calibrating ion fluence with depth, a high-resolution depth profile can be achieved, making

dynamic SIMS particularly useful for thin films, layered materials, and for tracking elemental or molecular changes from the surface to the bulk [209].

## 4.5 Hall measurements

Temperature-resolved Hall measurement is an important technique for Understanding how charge carriers behave in semiconductors across different temperatures is fundamental to characterising their electrical properties. One of the most widely used techniques for this purpose is the temperature-resolved Hall measurement, which allows for the determination of charge carrier concentration, mobility, and resistivity as a function of temperature. This method provides crucial insights into how doping affects carrier dynamics.

#### 4.5.1 Principle

The Hall effect, first discovered by Edwin Hall in 1879, is a phenomenon that occurs when a current-carrying material is placed in a perpendicular magnetic field. The Hall effect results in the deflection of charge carriers in the material, which leads to the formation of a transverse voltage — known as the Hall voltage. This voltage arises due to the Lorentz force acting on the charge carriers in the material, causing them to accumulate on one side of the conductor. By carefully measuring this voltage, we can deduce important information about the charge carriers, including their concentration and type (whether they are positive or negative), which are crucial for understanding the material's electrical properties [210].

# 4.5.2 Hall measurement setup

In a typical Hall measurement setup (Figure 4.20), a current ( $\mathbf{I}_x$ ) is driven through a thin conducting material with a magnetic field ( $\mathbf{B}_z$ ) applied perpendicular to the plane of the slab. As the current flows through the material, the charge carriers (electrons

or holes) move along the length of the conductor in response to the applied electric field ( $\mathbf{E}_{x}$ ). For materials with electrons as the charge carriers, these carriers flow in the direction opposite to the current, while in materials with holes, the charge carriers move in the same direction as the current. The magnetic field applied perpendicular to the plane of the conductor exerts a Lorentz force on the charge carriers, causing them to accumulate on one side of the conductor. This accumulation results in the creation of a transverse electric field ( $\mathbf{E}_{y}$ ), known as the Hall electric field, which counteracts the magnetic force. Once equilibrium is reached, the transverse electric field balances the magnetic force, leading to no net movement of charge carriers in the y-direction [85]. The Hall voltage ( $V_H$ ) generated due to this accumulation of charge is related to the Hall electric field ( $\mathbf{E}_{y}$ ) by:

$$V_H = E_y w, (4.5)$$

where, w is the width of the material. The carrier concentration n can then be determined from the measured Hall voltage using the following equation:

$$n = \frac{I_x B_z}{V_H qt} \tag{4.6}$$

where  $I_x$  is the current, q is the charge of the carriers, t is the thickness of the slab, and  $V_H$  is the measured Hall voltage. For materials with holes as the charge carriers, the Hall voltage will have an opposite polarity compared to those with electrons. The sign of the Hall voltage thus reveals the type of charge carriers in the material, with a positive Hall voltage indicating holes and a negative Hall voltage indicating electrons. This distinction allows Hall measurements to determine not only carrier concentration but also the type of conductivity in a semiconductor [46].

Temperature plays a critical role in determining both the Hall voltage and the carrier concentration in semiconductors. At low temperatures, carrier freeze-out occurs as thermal energy is insufficient to ionise the dopant atoms, leading to a significant decrease in free charge carriers (n) and an increase in  $V_H$ . In this freeze-out regime, most of the dopants remain in their neutral state, and conduction is dominated by any

free charge carriers from shallow impurities. As temperature increases, more dopant atoms ionise, increasing the carrier concentration and reducing  $V_H$ . This follows the Arrhenius-type relation [58]:

$$n \propto exp\left(\frac{-E_a}{k_b T}\right) \tag{4.7}$$

where  $k_b$  is the Boltzmann constant, T is the temperature, and  $E_a$  is the dopant activation energy, which represents the energy required to ionise a dopant atom. In non-degenerate semiconductors, this relationship dominates the temperature dependence of the carrier concentration. However, in heavily doped semiconductors, the situation is different. Due to the high doping concentration, the Fermi level moves deeper into the valence band, and leads to ionisation even at low temperatures. As a result, n becomes less temperature-dependent, and the variation in  $V_H$  is primarily influenced by changes in carrier mobility rather than carrier concentration [211].

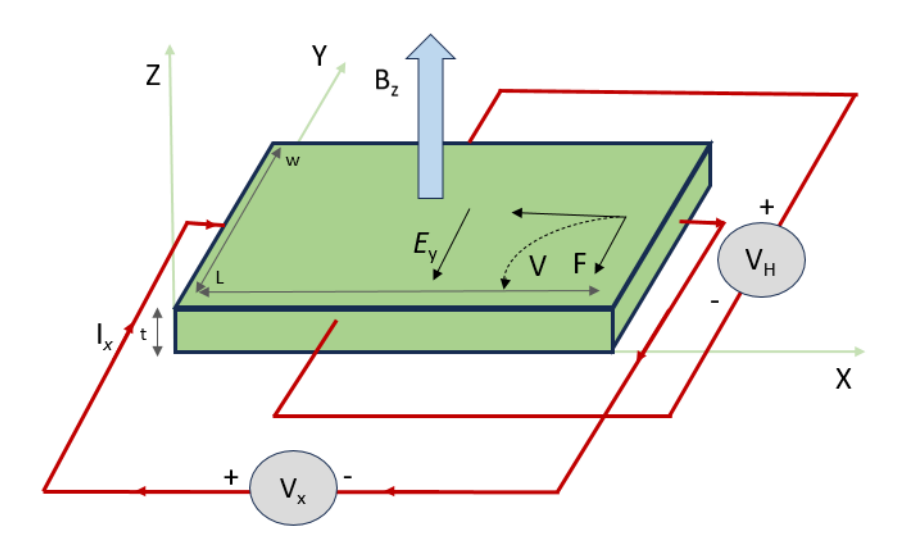


Figure 4.20: Schematic diagram of the Hall effect measurement setup. A rectangular silicon sample (dimensions:  $L \times W \times t$ ) is placed in a perpendicular magnetic field ( $\mathbf{B}_z$ ), with a constant current ( $\mathbf{I}_x$ ) applied along its length. Due to the Lorentz force, charge carriers are deflected, creating a transverse Hall voltage ( $V_H$ ) across the width of the sample [210, 212].

# 4.6 Summary

This chapter has provided a comprehensive overview of the experimental techniques employed to investigate the structural, electronic, and vibrational characteristics of degenerate boron-doped silicon. It began with a detailed explanation of TEM, including its fundamental principles, instrumentation, and operational modes, highlighting its ability to probe atomic-scale features. The chapter then introduced scanning STEM and EELS, both of which enable nanoscale imaging and phonon analysis. Supplementary techniques such as Raman spectroscopy were presented to complement EELS findings, offering an optical means of identifying vibrational modes. FIB methods were outlined as essential for site-specific sample preparation, particularly in generating thin lamellae for TEM analysis. The chapter also detailed the use of SIMS for high-sensitivity elemental profiling, and concluded with an in-depth discussion of Hall measurements, including temperature-dependent setups to assess carrier type, mobility, and concentration. Collectively, these methods form a robust experimental foundation for the subsequent investigation of boron-induced effects in silicon, enabling the investigations of structural, electronic, scattering and vibrational properties.

# **Simulation Techniques**

# 5.1 Density functional theory

Quantum mechanical simulations of material properties generally involves solving the many-body Schrödinger equation, which describes the interactions between all particles (electrons and nuclei) in a system. This equation, in its complete form, is incredibly complex, especially for materials with a large number of particles. The direct solution of the Schrödinger equation for such systems is computationally not possible due to the vast number of degrees of freedom involved. A significant simplification is made through the Born-Oppenheimer approximation, which assumes that the nuclei of a system, being much heavier than the electrons, move much slower. Consequently, the nuclei are treated as static in comparison to the rapidly moving electrons. By applying the Born-Oppenheimer approximation, the total wavefunction of the system can be separated into nuclear and electronic components. This allows for the simplification of the problem by focusing on the electronic degrees of freedom while assuming that the nuclei are fixed in place [213].

The electronic Hamiltonian  $(\hat{H})$ , describing the total energy of the system's electrons, within the Born-Oppenheimer approximation is given by [34]:

$$\hat{H} = \hat{T} + \hat{V}_{ext} + \hat{V}_{ee}. \tag{5.1}$$

Where,  $\hat{T}$  represents the kinetic energy of the electrons,  $\hat{V}_{ext}$  represents the external potential due to the interaction of the electrons with the fixed nuclei, and  $\hat{V}_{ee}$  accounts for the electron-electron Coulomb interaction. Solving the electronic part of the above Schrödinger equation directly still remains computationally demanding. To overcome the difficulties associated with directly solving the many-body Schrödinger equation, density functional theory (DFT) simplifies the problem by using the electron density as the primary variable to describe the system's properties [34].

The foundational work of DFT is built on the two Hohenberg-Kohn theorems, which form the theoretical basis for DFT by demonstrating that the ground-state properties of a system can be determined from the electron density  $n(\mathbf{r})$  alone. This is a significant simplification because, instead of working with a wavefunction that depends on the positions of all the electrons in the system, we can instead focus on the much simpler electron density, which depends only on three spatial coordinates.

The first Hohenberg-Kohn theorem states that the external potential  $V(\mathbf{r})$ , governing the interaction between the electrons and the external environment (static nuclei), is uniquely determined by the ground-state electron density  $n_0(r)$ . In other words, each ground-state wavefunction corresponds to a unique potential, and each ground-state electron density corresponds to a unique ground-state wavefunction. If two different external potentials,  $V_A(\mathbf{r})$  and  $V_B(\mathbf{r})$ , produce the same ground-state wavefunction  $\phi_0(\mathbf{r})$ , then these potentials must be identical except for an additive constant. This implies that the ground-state wavefunction uniquely defines the external potential, and consequently, the potential  $V(\mathbf{r})$  can be determined from the wavefunction alone. The second Hohenberg-Kohn theorem complements this by introducing the energy functional E[n], which expresses the total energy of the system as a functional of the electron density. It can be written in general form as [214]

$$E[n] = F_{KH}[n] + \int n(\mathbf{r}) V(\mathbf{r}) d^3 \mathbf{r}, \qquad (5.2)$$

where,  $F_{KH}[n]$  is known as the universal Hohenberg-Kohn functional, defined as

$$F_{KH}[n] = T[n] + U[n], \qquad (5.3)$$

with T[n] representing the exact kinetic energy of the interacting electrons and U[n] the electron-electron interaction energy. The energy functional E[n] encompasses all terms that are independent of the external potential and therefore applies universally to many-electron system. The theorem states that the value of this energy functional is minimised when the electron density corresponds to the true ground-state density  $n_0(\mathbf{r})$ . If there were any other electron density  $n(\mathbf{r})$  that produced a lower energy than  $n_0(\mathbf{r})$ , it would violate the variational principle, which is not physically possible. Therefore, the electron density that minimises the energy functional must correspond to the ground state. Together, these theorems simplify the complex many-body problem by reducing it to a functional of the electron density, which depends only on three spatial coordinates, rather than the wavefunction that depends on the positions of all electrons in the system [215, 216].

## 5.1.1 Kohn-Sham equations

While the Hohenberg-Kohn theorems provide a solid theoretical foundation, they do not directly provide a practical method for calculating material properties due to the interacting nature of electrons. The Kohn-Sham approach, introduced by Kohn and Sham in 1965 [217], simplifies the problem by treating the interacting many-body electron system as a fictitious system of non-interacting electrons that generate the same ground state electron density as the interacting system. This is achieved by replacing the many body wavefunction  $|\phi\rangle$  by a set of single-particle wavefunctions  $\psi_i(\mathbf{r})$ , each governed by a single-particle Hamiltonian. The interacting system is thus described by a system of non-interacting particles moving in a Kohn-Sham potential  $V_{\rm KS}$ , which includes the external potential, the Hartree potential, and the exchange-correlation potential, yet yield the same ground-state electron density of the real interacting system.

The Kohn-Sham equation is written as [65]

$$\left[ -\frac{\hbar^2}{2m} \nabla^2 + V_{KS}(\mathbf{r}) \right] \psi_i(\mathbf{r}) = \epsilon_i \psi_i(\mathbf{r}), \tag{5.4}$$

with

$$V_{KS}(\mathbf{r}) = V_{\text{ext}}(\mathbf{r}) + V_{H}(\mathbf{r}) + V_{XC}(\mathbf{r}), \tag{5.5}$$

where,  $\psi_i(\mathbf{r})$  are the Kohn–Sham orbitals,  $\epsilon_i$  are the corresponding eigenvalues, and  $V_{\text{XC}}(\mathbf{r})$  is the exchange-correlation potential. The external potential  $V_{\text{ext}}(\mathbf{r})$  defines the interaction between electron and atomic nuclei. The Hartree potential  $V_{\text{H}}(\mathbf{r})$  describes the classical Coulomb repulsion between an electron and the total electron density and is given by:

$$V_{\rm H}(\mathbf{r}) = \int \frac{n(\mathbf{r}')}{|\mathbf{r} - \mathbf{r}'|} d\mathbf{r}'. \tag{5.6}$$

However, the Hartree potential includes a self-interaction term, as the electron being considered contributes to the total density. Since this self-interaction is unphysical, it must be corrected, along with other missing quantum effects, by the exchange-correlation potential  $V_{\rm XC}(\mathbf{r})$ , which is defined as the functional derivative of the exchange-correlation energy  $E_{\rm XC}[n]$ . This term accounts for both exchange effects, which arise due to the antisymmetry of the wavefunction, and correlation effects [65, 218, 219].

Solving the Kohn-Sham equations requires an iterative approach due to the circular nature of this method, as illustrated in Figure 5.1.

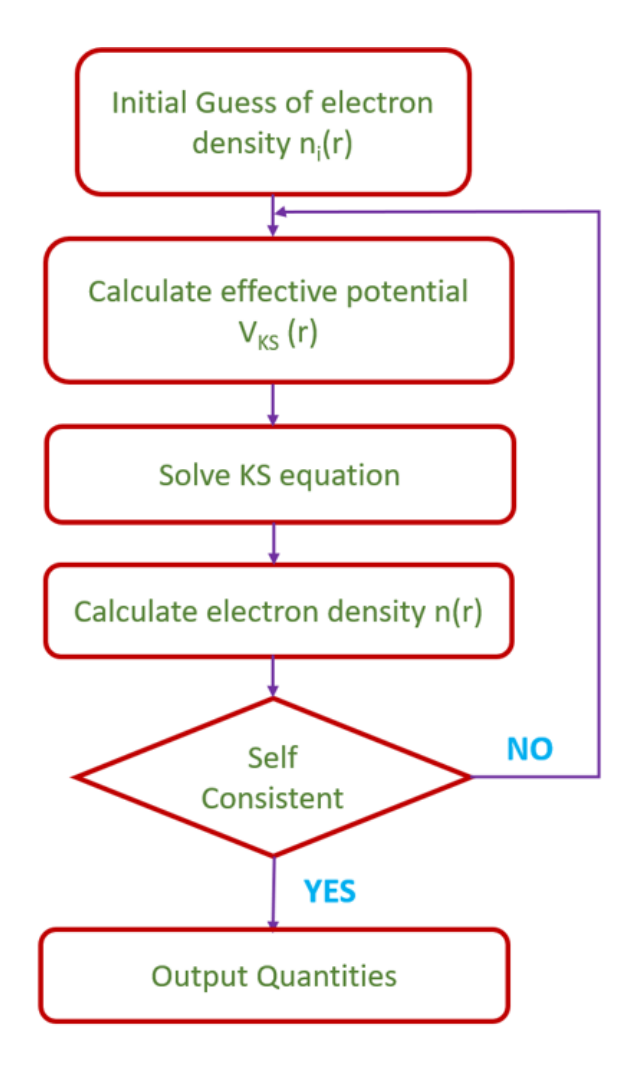


Figure 5.1: Schematic illustration of the self-consistent cycle for solving the Kohn–Sham equations [219].

The Hartree potential depends on the electron density, but determining the density requires solving the Kohn-Sham wavefunctions, which in turn requires solving the Kohn-Sham equations. This creates a circular dependency, which is resolved iteratively. First, an initial trial electron density is assumed. The equations are then solved to obtain single-electron wavefunctions, from which a new electron density is computed. This process repeats until self-consistency is reached, ensuring that the final electron density accurately represents the system's ground state [217, 219].

#### 5.1.2 The exchange-correlation functional

Unlike the external and Hartree potentials, the exact form of the exchange-correlation energy is unknown. As a result, approximations are required to make DFT calculations practical while maintaining a reasonable level of accuracy. The exchange-correlation functional is expressed as a functional of the electron density  $n(\mathbf{r})$ , which means that  $E_{\text{XC}}[n]$  depends on the distribution of electrons in space. The exact functional is defined as:

$$E_{\rm XC}[n] = \int \epsilon_{\rm XC}(\mathbf{r}) \ n(\mathbf{r}) \ d\mathbf{r}$$
 (5.7)

where  $\epsilon_{\text{XC}}(\mathbf{r})$  represents the exchange-correlation energy density. Physically, the exchange-correlation energy may be interpreted as the Coulomb interaction between the electronic density and the associated exchange-correlation hole. This 'hole' arises due to the reduction in the probability of finding two electrons close together, a consequence of the Pauli exclusion principle and the Coulomb repulsion. In essence, the exchange-correlation energy captures the subtleties of electron–electron interactions that go beyond a simple mean-field treatment [220].

One of the simplest and most extensively employed approximations is the Local-Density Approximation (LDA). In this thesis, LDA has been used due to its computational simplicity. In the LDA, the exchange-correlation energy at any point in space is assumed to be the same as that of a uniform electron gas having the same local electron density. Because the electron density is assumed to be uniform at each point  $\mathbf{r}$ , this local treatment ensures that the exchange-correlation hole satisfies important physical constraints such as the charge-conservation sum rule and the requirement that the probability of finding another electron at the same position is correctly reduced. Although the LDA has been remarkably successful for many systems, particularly those where the electron density varies slowly, it has limitations in systems with rapid density variations or strong electron correlation effects. Nevertheless, the LDA remains a cornerstone of DFT due to its simplicity and the physical insight it provides into the exchange and correlation phenomena in many-electron systems [220, 221].

### 5.1.3 Pseudopotentials

In DFT calculations, the Kohn–Sham equations are solved by expanding the single-electron wavefunctions in a chosen basis set and diagonalising the resulting Hamiltonian matrix. For periodic systems, the plane-wave basis set is the preferred choice due to its inherent compatibility with periodic boundary conditions and its systematic convergence, which is controlled by adjusting the kinetic energy cut-off [213]. Although Bloch's theorem indicates that electronic wavefunctions can be expanded in a discrete set of plane waves, using a plane-wave basis to describe all electrons is impractical. Tightly bound core electrons and the rapidly oscillating valence electron wavefunctions within the core region would require an excessively large number of plane waves, leading to a computationally demanding all electron calculation.

Since the physical properties of solids are predominantly determined by the valence electrons, the pseudopotential approximation is employed to simplify the problem. This approximation replaces the strong Coulomb potential from the nucleus and core electrons with a weaker, effective pseudopotential acting on pseudo-wavefunctions, as given in Figure 5.2.

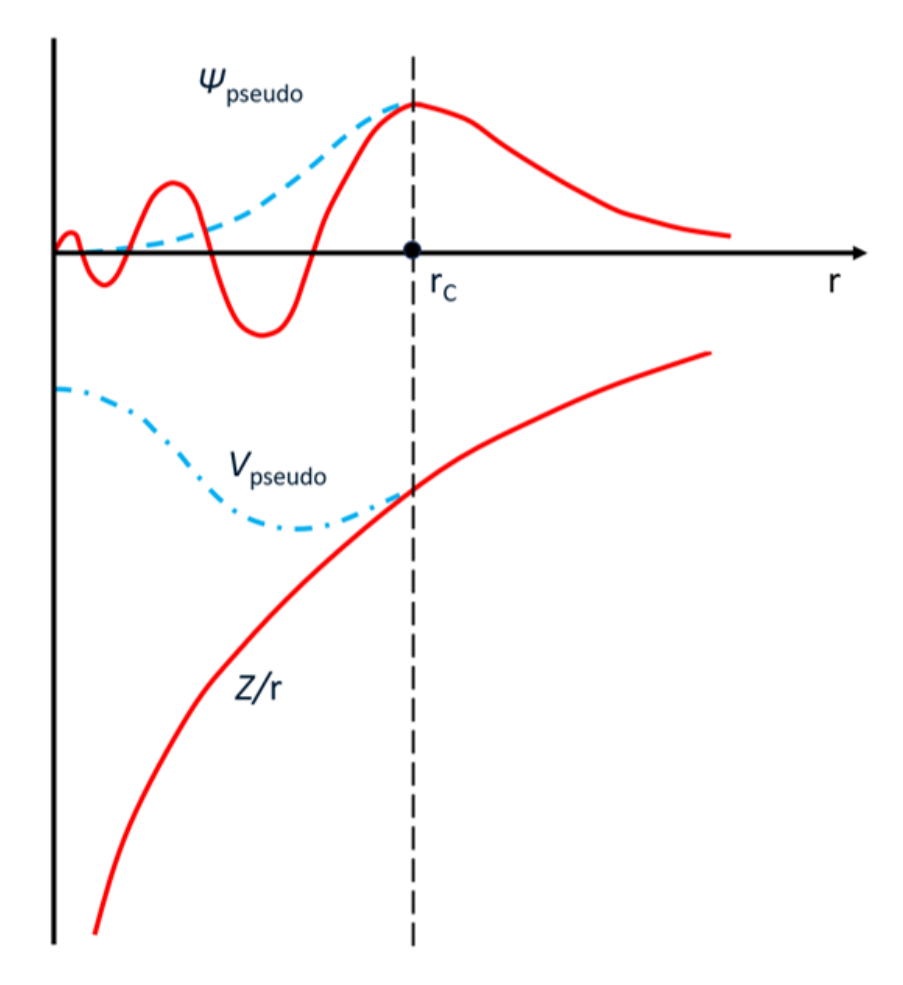


Figure 5.2: Schematic illustration of the 'screened nuclear' potential (solid lines) and pseudopotential (dashed lines), along with their corresponding wavefunctions [222].

The pseudopotential is designed such that its scattering properties (or phase shifts) for the pseudo-wavefunctions are identical to those produced by the core electrons and ions when interacting with valence electrons, but in such a manner that the pseudo-wavefunctions exhibit no radial nodes within the core region. Outside the core region, defined by the cut-off radius  $r_C$ , the pseudopotential is constructed to be identical to the all-electron potential, thereby ensuring that the scattering properties of the pseudo-wavefunctions match those of the true all-electron wavefunctions. This careful construction ensures that, although the detailed behaviour of the core electrons is not explicitly treated, their overall effect on the valence electrons is accurately reproduced. As a result, the number of plane waves required for convergence is drastically reduced, making the computation far more efficient [222].

Two main types of pseudopotentials are commonly used in DFT calculations: norm-conserving and ultrasoft pseudopotentials. Norm-conserving pseudopotentials are constructed so that the pseudo-wavefunctions coincide with the true all-electron wavefunctions outside a defined core radius and conserve the integrated charge density within this core region [223]. Ultrasoft pseudopotentials relax the norm-conservation constraint imposed by norm-conserving pseudopotentials, thereby enabling a smoother effective potential. This adjustment reduces the number of plane waves needed to describe the system, resulting in a more computationally efficient representation. This is particularly useful when modelling large-scale, heavy or complex periodic systems, as the reduced plane-wave count significantly lowers computational cost without sacrificing accuracy [224]. In this thesis, norm-conserving pseudopotentials (NCP) are used, as silicon is the material under consideration, and this approach is well-suited for accurately modelling its phonon dispersion.

#### 5.1.4 Phonon calculations - Finite displacement method

For this thesis, the finite displacement method is utilised to compute the phonon dispersion of boron-doped silicon systems, enabling a detailed analysis of the vibrational behaviour introduced by defect configurations. It builds upon the discussion on phonon band structure already presented in the previous chapter, where the fundamental equations governing phonon behaviour were detailed. The core principle of the finite displacement method involves displacing atoms within a supercell, evaluating the forces acting on other atoms, and extracting the interatomic force constants (IFCs) based on the resulting forces. These force constants are then used to compute the phonon dispersion relations.

Phonons are formulated within the harmonic approximation, in which the total energy of a system is expanded as a Taylor series in terms of atomic displacements. The

force  $F_{\alpha}$  on atom s due to a displacement  $\boldsymbol{u}_{\beta}(l's')$  of atom s' is given by [225, 226]:

$$F_{\alpha} = -\sum_{l's'\beta} \mathbf{\Phi}_{\alpha\beta} \{ ls; l's' \} \mathbf{u}_{\beta}(l's'), \tag{5.8}$$

where,  $\Phi_{\alpha\beta}\{ls;l's'\}$  is the interatomic force constant matrix. The force constants are obtained by computing the forces on all atoms following a small, finite displacement of a single atom. The method relies on the Hellmann-Feynman theorem [227], which allows forces to be determined directly from the self-consistent DFT potential. The calculation begins with the construction of a supercell, which must be large enough to capture the interactions between displaced atoms and their neighbours while minimising artefacts from periodic boundary conditions. The choice of supercell size is critical, as it affects the convergence of the force constants and the accuracy of phonon dispersion relations. Each atom in the supercell is displaced individually along Cartesian directions by a small but finite amount. For each displacement, the forces acting on all atoms in the supercell are calculated. These forces are differentiated to obtain the IFCs [226]:

$$\mathbf{\Phi}_{\alpha\beta}\{ls;l's'\} = -\frac{\partial F_{\alpha}}{\partial \boldsymbol{u}_{\beta}(l's')},\tag{5.9}$$

The IFCs are then transformed into reciprocal space to construct the dynamical matrix:

$$\mathbf{D_{k}} = -\sum_{l'} \frac{\Phi_{\alpha\beta}\{ls; l's'\}}{\sqrt{m_s m_{s'}}} \exp\{i\mathbf{k} \cdot [\mathbf{R}(l') - \mathbf{R}(l)]\}. \tag{5.10}$$

Diagonalising the above dynamical matrix at each phonon wave vector  $\mathbf{k}$  yields the phonon frequencies and vibrational eigenmodes.

To ensure accuracy, convergence tests must be conducted for supercell size, **k** vector sampling, and self-consistent field (SCF) convergence thresholds. Using crystal symmetries can significantly reduce computational expense by decreasing the number of required displacements. To further optimise efficiency, a short-range approximation is often employed, assuming that force constants beyond a certain interaction range are negligible. In DFT, this approach allows for the accurate determination of phonon dispersion relations using a relatively small supercell [228].

# 5.2 Multislice

The multislice method is a widely used technique for simulating electron diffraction and high-resolution images in transmission electron microscopy (TEM), especially when dealing with complex materials, including defective structures. The method plays a crucial role in the calculation of the transmitted electron wavefunction as it propagates through the specimen under specific illumination conditions, taking into account the quantum mechanical interactions between the electrons and the material. Various methods have been developed for this purpose, with the Bloch-wave (BW) method [229] and the multislice method [230] being the most prominent. The multislice method is preferred over others for modelling both perfect and defective crystal structures, as it provides an efficient means of handling the complex diffraction and scattering processes that occur within the sample. Unlike the BW method, which is more suited for perfect crystals, the multislice approach is capable of modelling materials with defects, such as vacancies, interstitials, which makes it especially useful for studies of doped semiconductors like boron-doped silicon. This method is based on solving the Schrödinger equation for each thin slice of the specimen, with the electron wavefunction updated iteratively as it propagates through each slice. This process effectively simulates how electrons interact with the atomic potentials in the sample, allowing for the prediction of diffraction patterns and high-resolution images [231].

#### 5.2.1 Multislice simulation- Static atoms

The multislice method is based on a few key principles of wave propagation and scattering. In particular, it relies on Huygens' principle to describe the electron beam propagation through free space [232]. In multislice simulation, as shown in Figure 5.3, the specimen is divided into thin slices along the electron beam direction (the z-axis), with each slice having a thickness equal to the periodic planar spacing along the z-axis. The potential within each slice is treated as a 2D projection of the 3D electrostatic potential. The electrostatic potential  $V(\mathbf{r})$  is determined by the Coulomb fields of the

individual atoms, and it is assumed that this potential can be approximated as a superposition of the potentials from each atom in the specimen [233]. Mathematically, the potential at a point  $\mathbf{r}$  within the material is given by:

$$V(\mathbf{r}) = \sum_{i} V_i(\mathbf{r} - \mathbf{r}_i), \tag{5.11}$$

where,  $V_i$  is the atomic potential of  $i^{\text{th}}$  atom, which has position vector  $\mathbf{r}_i$ . This potential is typically calculated assuming a spherical Coulomb potential for each atom in free space (i.e. with no bonding), but more complex potentials can be used depending on the material and the level of accuracy required [234]. Next, this three-dimensional electrostatic potential is projected along the z-axis (the direction of electron beam propagation) to obtain a two-dimensional projected potential for each slice of the specimen. This projection is based on the assumption that the slice is sufficiently thin, such that the incident electron wave passes through it with minimal deflection. The projected potential  $V_n(\mathbf{R})$  for the  $n^{th}$  slice is given by:

$$V_n(\mathbf{R}) = \int_{n\Delta z}^{(n+1)\Delta z} V(\mathbf{R} - \mathbf{R}_i, z) dz,$$
 (5.12)

where,  $\Delta z$  is the thickness of each slice. This projection simplifies the problem, as it reduces the three-dimensional electrostatic potential to a two-dimensional function that varies only with the in-plane coordinates x and y. Here the position vector  $\mathbf{r}$  is decomposed into its in-plane coordinates  $\mathbf{R} = (x, y)$  and the slice-normal coordinate z, such that  $\mathbf{r} = (\mathbf{R}, z)$  [234, 235].

The next step in the simulation is the calculation of the phase grating, which describes how the incident electron wave is modulated by the potential of the slice. This modulation results in a phase shift that depends on the local electrostatic potential  $V_n(\mathbf{R})$ . The phase grating is expressed as [236]:

$$t_n(\mathbf{R}) = \exp(i\sigma V(\mathbf{R})), \tag{5.13}$$

where,  $t_n(\mathbf{R})$  is the transmission function for the  $n^{\text{th}}$  slice, and  $\sigma = 2\pi e \lambda m_e/h^2$  is the interaction constant, with  $m_e$  being the electron mass,  $\lambda$  the wavelength of the elec-

trons, and h Planck's constant. The transmission function describes how the electron wave is phase-shifted as it passes through the potential of the slice [236, 237].

After the transmission function has been applied to the incident electron wave for a given slice, the wave function is propagated to the next slice using the Fresnel propagator  $p(\mathbf{R}, \Delta z)$ . This propagator describes the diffraction of the electron wave in free space between the slices, and it is given by [238]:

$$p(\mathbf{R}, \Delta z) = \frac{1}{i\lambda\Delta z} \exp\left[\frac{i\pi}{\lambda\Delta z}(x^2 + y^2)\right]. \tag{5.14}$$

The Fresnel propagator represents the phase shift due to diffraction over a distance  $\Delta z$ . To compute the wavefunction at the next slice, the wavefunction for the slice of interest is convolved with the Fresnel Propagator. This process repeats till the wavefunction passes through all slices. The exit wavefunction after propagation is given by [239]:

$$\psi_{(n+1)}(\mathbf{R}) = p(\mathbf{R}, \Delta z) \otimes t_n(\mathbf{R})\psi_n(\mathbf{R}). \tag{5.15}$$

Convolution in real space is computationally expensive, especially for large grids. Therefore, it is more efficient to perform this step in reciprocal (Fourier) space. The Fourier space approach allows the problem to be solved efficiently using fast Fourier transforms (FFTs) [235]. The propagation is then computed by multiplying the transmission-modified wave function by the propagator in Fourier space and the exit wave function  $\psi_{(n+1)}(\mathbf{R})$  is given as

$$\psi_{(n+1)}(\mathbf{R}) = \mathcal{F}^{-1}[\widetilde{p}(\mathbf{k}, \Delta z)\mathcal{F}[t_n(\mathbf{R})\psi_n(\mathbf{R})]], \tag{5.16}$$

where,  $\mathbf{k}$  is the 2D vector in the Fourier space and  $\tilde{p}(\mathbf{k}, \Delta z)$  is the Fourier transform of the propagator [130]. Once the exit wave function has been obtained through the multislice propagation through all slices in the sample, the next step is to calculate the diffraction pattern that corresponds to the electron scattering in reciprocal space. This is done by Fourier transforming the exit wave function and then taking the square modulus to obtain the diffraction intensity [238].

$$I(\mathbf{k}) = |\mathcal{F}[\psi_{\text{exit}}(\mathbf{R})]|^2. \tag{5.17}$$

Up to this point, the theory has been based on the assumption of static atoms, where the atoms in each slice are in fixed positions.

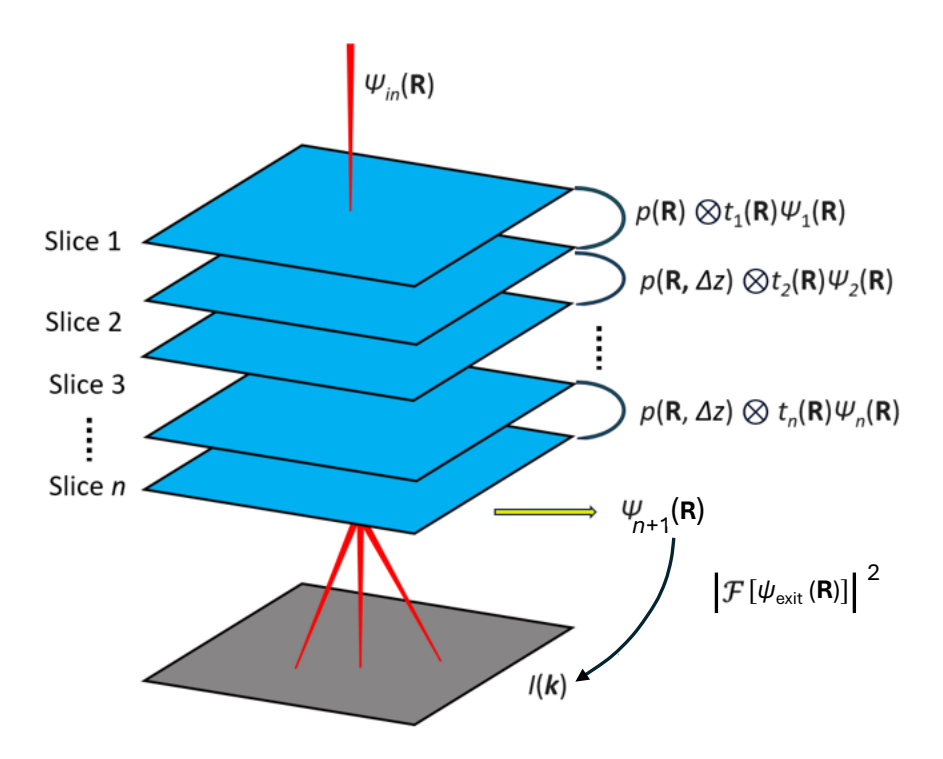


Figure 5.3: Schematic of the multislice method, where the incident electron wavefunction is sequentially propagated through multiple slices of the projected crystal potential. The diffraction intensity distribution is obtained by taking the squared modulus of the Fourier-transformed exit wavefunction.

# 5.2.2 Multislice simulation - Frozen phonon

The above idealised scenario does not account for the vibrational motion of atoms due to thermal effects. However, in reality, atoms in a crystalline material are in constant thermal motion, even at low temperatures. To simulate this effect, the frozen phonon (FP) model was introduced, which incorporates the atomic displacements due to thermal vibrations. These displacements are represented by a random distribution of atomic positions around their equilibrium positions and are introduced into the multislice method by modifying the potential. The projected potential  $V_n^{\rm FP}(\mathbf{R})$  for

slice n in the presence of atomic displacements is given by [240]:

$$V_n^{\text{FP}}(\mathbf{R}) = \int_n^{n+\Delta z} V_i(\mathbf{R} - \mathbf{R}_i - \sqrt{\langle u_i^2 \rangle} \cdot \mathbf{g}_{i,\tau}, z) dz, \qquad (5.18)$$

where,  $\sqrt{\langle u_i^2 \rangle}$  represents the temperature-dependent mean square displacements (MSD) of atom i, and  $\mathbf{g}_{i,\tau}$  are two-dimensional Gaussian normal variables that describes the random displacement of atom in the direction of the slice at a particular frozen phonon configuration  $\tau$ . The displacements are treated as random variables that follow a Gaussian distribution, with the temperature-dependent MSD given by the Einstein model [240].

Once the atomic displacements are introduced into the projected potential, the multislice operation is performed using the same framework as in the static case to obtain the diffraction patterns. Since the atomic displacements are random, a single FP configuration  $\tau$  will only provide a snapshot of the material's behavior at one instant in time. To obtain a realistic diffraction pattern that accounts for the statistical nature of thermal vibrations, diffraction patterns over multiple FP configurations ( $\tau = 1, 2, ..., N$ ) are averaged. Hence, the frozen phonon model allows for the simulation of the diffraction patterns arising from thermal vibrations, by displacing atoms from their equilibrium positions and averaging the resulting diffraction patterns over multiple configurations of atomic displacements using the below equation [240, 241].

$$I^{\text{FP}}(\mathbf{k}) = \frac{1}{N} \sum_{\tau}^{N} I_{\tau}^{\text{FP}}(\mathbf{k})$$
 (5.19)

Despite incorporating thermal diffuse scattering, the FP model remains elastic. This is because the model assumes the electron interacts with frozen atomic displacements, which do not involve real-time phonon creation or significant inelastic scattering. The electron passage time is much shorter than atomic vibrations, making the scattering process effectively elastic, with the averaging over static configurations simulating phonon effects without actual phonon creation. However, by averaging over many frozen phonon configurations, the FP model statistically reproduces the effects of phonon scattering [242].

# 5.3 Summary

This chapter outlined the theoretical and computational frameworks employed throughout this thesis to investigate boron-doped silicon. It began with an overview of density functional theory (DFT), focusing on the Kohn-Sham approach, exchange-correlation functionals, and the use of norm-conserving pseudopotentials to simplify the treatment of core electrons. The finite displacement method was introduced as the primary tool for calculating phonon dispersion, relying on interatomic force constants derived from DFT-based force calculations within supercells. Attention was then turned to multislice simulations, with detailed discussion of the static and frozen phonon (FP) models used to replicateselected area electron diffraction patterns. The FP model, in particular, allowed thermal vibrations to be statistically accounted for via configurational averaging, bridging the gap between elastic simulations and thermally-induced diffuse scattering. Together, these techniques provide a robust and comprehensive toolkit for probing both the vibrational and electron scattering behaviours of defected crystalline systems.

# Influence of Boron Defects on the Vibrational Properties of Silicon

# 6.1 Preliminary characterisation of boron doped Si sample

Degenerate boron doped silicon wafers were purchased from a commercial source (University Wafer). The primary aim of the preliminary characterisation was to confirm the degenerate doping and verify the presence of boron as the dopant in the silicon sample. To achieve this, Hall measurements were employed to confirm the degenerate doping level, while SIMS provided confirmation of the presence of boron in the sample. Hall measurements were performed by Dr Laurie Phillips (University of Liverpool), while SIMS was carried out by Prof Guillaume Zoppi (Northumbria University). Additionally, Raman spectroscopy was performed to gain insight into the vibrational properties of the sample and further support the confirmation of degeneracy. These results were crucial for establishing the basic properties of the sample before proceeding with further investigations.

#### 6.1.1 Hall Measurements

To ensure the boron-doped silicon sample exhibits degenerate doping behaviour, preliminary Hall measurements were carried out across a temperature range of 10 K to 320 K. The hole concentration in the boron-doped silicon remains effectively constant across the temperature range. This is expected, given that the dopant concentration is extremely high (around  $10^{20}$  atoms/cm<sup>3</sup>), and the boron ions are ionised even at 0K. Thus, there is little to no fluctuation in the hole concentration across the temperature range. The carrier concentration is maintained near its maximum, corresponding to the dopant concentration, with no significant changes occurring over the investigated temperature range. This is illustrated in Figure 6.1, where the hole concentration is shown to be fluctuating around  $10^{20}$  atoms/cm<sup>3</sup> across the temperature range, confirming the ionisation of boron even at low temperature.

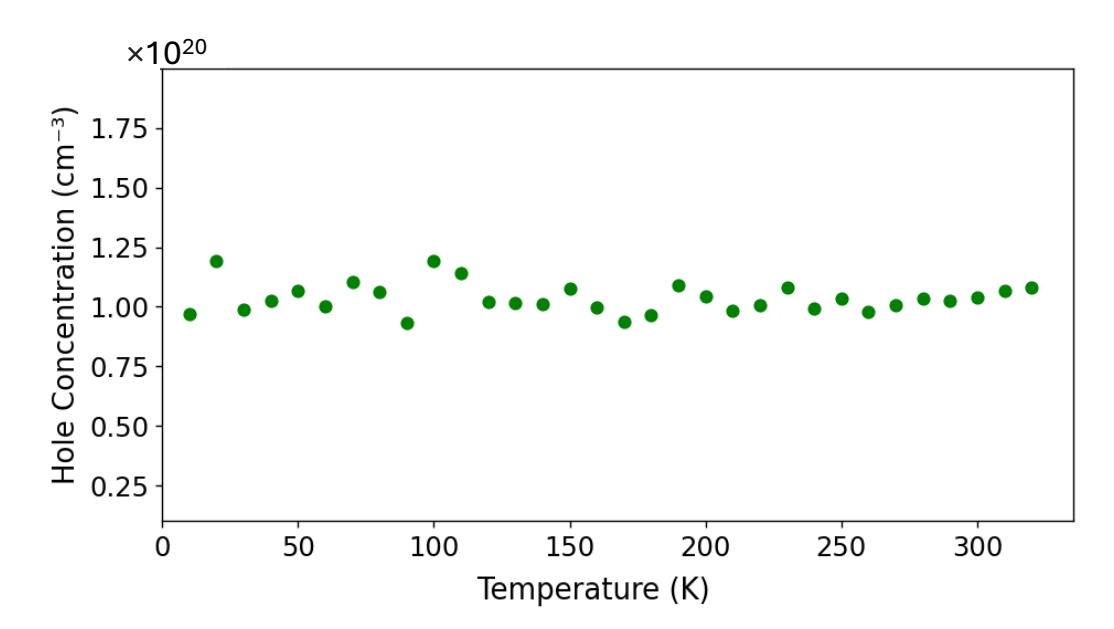


Figure 6.1: Hall measurements of boron-doped silicon conducted across a temperature range of 10 K to 320 K to determine the hole concentration.

#### 6.1.2 SIMS

The Hall measurements conducted on the boron-doped silicon sample confirmed the degenerate doping concentration of  $10^{20}$  atoms/cm<sup>3</sup> and identified the type of defect

defect (i.e. donors or acceptors) present. However, the technique could not specify the precise defect species responsible. To address this limitation, secondary ion mass spectroscopy (SIMS) analysis was performed to confirm the presence of boron as the primary defect in the silicon sample (Figure 6.2). The experiment utilised an oxygen ion beam with a beam energy of 5 keV, a current of 800 nA, and a diameter of 200  $\mu$ m in a dynamic scanning mode. The analysis employed multiple ion detection (MID) mode to monitor isotopes of silicon ( $^{28}$ Si,  $^{29}$ Si,  $^{30}$ Si) and boron ( $^{10}$ B,  $^{11}$ B), with the instrument output displaying counts per second (cps) on a logarithmic scale over time.

In the SIMS analysis, <sup>29</sup>Si was chosen instead of the more abundant <sup>28</sup>Si. By selecting <sup>29</sup>Si, which is less abundant (around 4.7%) [243], the SIMS instrument was able to distinguish signals for both boron and silicon simultaneously. This allowed for more precise analysis of the boron content, without interference from the dominant <sup>28</sup>Si isotope. However, this choice led to an underrepresentation of the actual silicon content, as the silicon signal was solely from <sup>29</sup>Si. The relative intensities of isotopes, such as <sup>28</sup>Si and <sup>29</sup>Si, typically reflect their relative abundances accurately in SIMS. However, subtle mass fractionation effects can still occur. When comparing isotopes of different elements like silicon and boron, the signal intensities do not necessarily directly correspond to their actual concentrations due to differences in ionisation efficiency and sputtering yields between the elements [205].

As shown in Figure 6.2, the underrepresentation of silicon in the SIMS data resulted in an apparent boron-to-silicon ratio of one boron atom per 65 silicon atoms. In contrast, the Hall measurement revealed a ratio of one boron atom per 500 silicon atoms. While the SIMS data likely overestimated the boron concentration, it still confirms the presence of boron in the silicon matrix, verifying boron as the primary defect species in the sample.

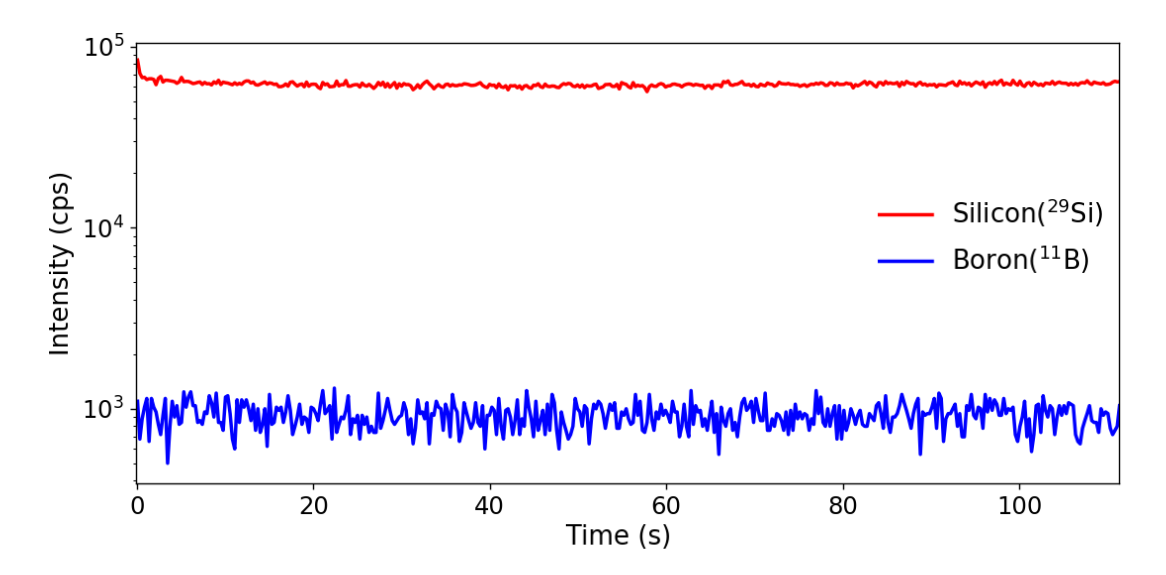


Figure 6.2: Secondary Ion Mass Spectrometry (SIMS) profiling of boron-doped silicon showing the signal from boron (<sup>11</sup>B) and silicon (<sup>29</sup>Si) isotopes.

#### 6.1.3 Raman spectroscopy

Raman spectroscopy was employed to characterise elemental silicon (Si), low borondoped silicon (Low-B-Si), and heavily (degenerate) boron-doped silicon (High-B-Si). The measurements were carried out using a laser beam with a wavelength of 633 nm and a power of 5 mW, a grating of 1800 gr/mm, and a microscope objective with  $50 \times$  magnification. The spot size was  $500~\mu\text{m}$ , with an acquisition time of 10--15 seconds and an accumulation number of 5. The acquisition was performed in single mode at room temperature. The Raman spectra, presented in Figure 6.3, reveal the characteristic phonon peak of elemental silicon at approximately  $515~\text{cm}^{-1}$ , attributed to the longitudinal optical (LO) and transverse optical (TO) phonon modes arising from Si-Si bonding. For low boron-doped silicon, this peak remains sharp and unshifted compared to elemental silicon, indicating the negligible impact of low boron concentrations on the crystal lattice vibrational dynamics.

In heavily boron-doped silicon, however, several distinct features emerge. The Raman peak centred around 515 cm<sup>-1</sup> becomes asymmetric, slightly shifted towards the lower

frequency, exhibit a distinct minimum around 492 cm<sup>-1</sup> alongside the central peak, and significantly broadened. These changes in the line shape indicate Fano resonance which is caused by the interaction between discrete optical phonon modes and the continuum of free-carrier transitions within the valence band [244] introduced by high boron doping. Additionally, increased electron-phonon coupling and localised strain effects contribute to the broadening and deviation from the ideal Lorentzian line shape. A new Raman feature is observed around 615 cm<sup>-1</sup>, likely to arise from vibrations due to Si-B bonding. This peak highlights the vibrational changes in the silicon lattice due to the incorporation of boron atoms. The high-B-Si spectrum also exhibits a higher background intensity, particularly at lower wavenumbers. This behaviour results from enhanced free carrier absorption and scattering effects, which are more pronounced in heavily doped semiconductors [245]. Finally, the wavelength cutoff near 650 cm<sup>-1</sup> limits any optical modes or vibrational features beyond this cutoff. Consequently, while the analysis captures phonon modes within the accessible spectral range, any shorter wavelength optical modes that might provide further insight into the vibrational or electronic properties of High-B-Si remain undetectable.

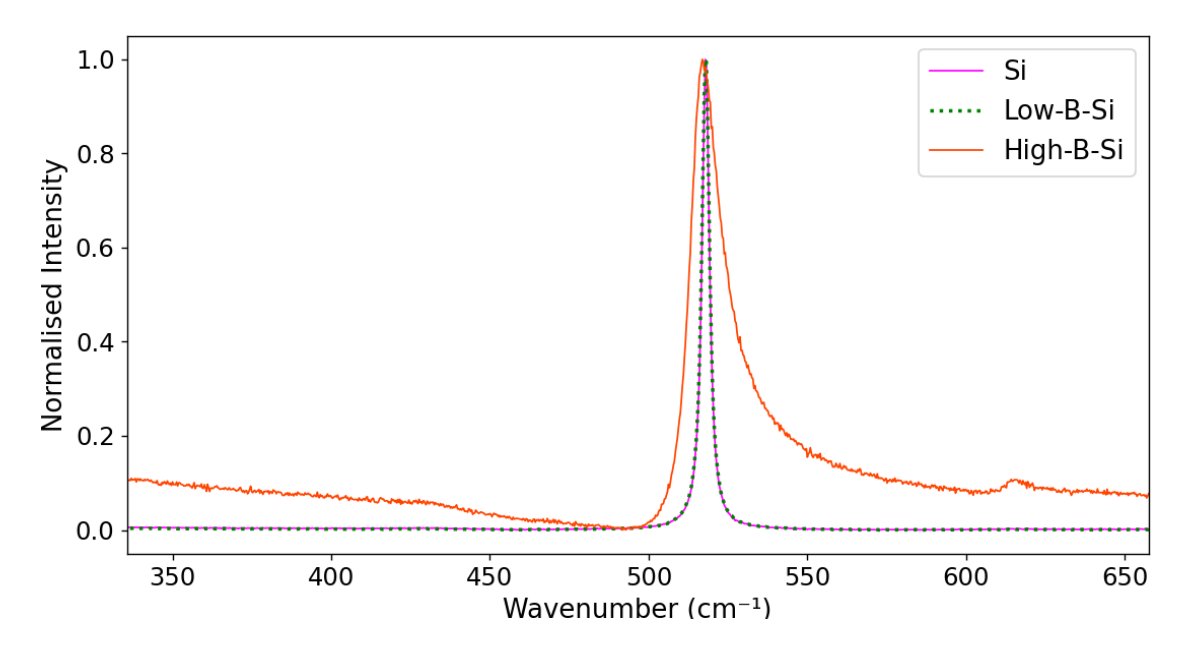


Figure 6.3: Raman spectrum of elemental silicon (Si), low boron-doped silicon (Low-B-Si), and heavily (degenerate) boron-doped silicon (High-B-Si).

# 6.2 Experimental EELS measurements of phonon modes in boron doped silicon

Pure silicon (Si) and degenerately boron doped silicon (High-B-Si) samples were investigated using momentum-resolved electron energy loss spectroscopy (EELS) in scanning transmission electron microscopy (STEM) mode. The primary objective of these measurements was to identify possible localised vibrational modes associated with boron incorporation. All EELS data were acquired by Dr Shihao Wang and Professor Quentin Ramasse at the SuperSTEM Laboratory, Daresbury, UK. STEM-EELS data were collected at an accelerating voltage of 60 kV using the Nion UltraSTEM 100 MC microscope, equipped with a Nion Iris EELS spectrometer and a Dectris ELA hybrid-pixel direct electron detector. This advanced setup, incorporating an ultra-high energy resolution electron beam monochromator [246], is particularly well-suited for vibrational EELS measurements, enabling the detection of subtle phonon features associated with dopants. Both full  $\omega$ -q phonon dispersion map and single-spectrum acquisitions at selected momentum transfers were collected. The motivation for employing both acquisition modes is discussed in the following sections.

### 6.2.1 Momentum-resolved EELS spectra

Momentum-resolved EELS was performed in diffraction mode to measure how electron energy loss due to inelastic scattering varies with momentum transfer. The technique works by projecting inelastically scattered electrons into the EELS spectrometer so that both energy and momentum information are captured at once. A rectangular slot was inserted at the spectrometer entrance in place of the usual circular aperture. This slot acts as a narrow "window" through the diffraction pattern, selecting electrons scattered along a specific direction in reciprocal space. By aligning the slot along the 400 systematic row of the [001] zone-axis diffraction pattern, electrons scattered along the  $\Gamma$ -X- $\Gamma$  direction of the Brillouin zone were allowed to enter the spectrometer (Figure

6.4a). The spectrometer disperses the electrons with respect to their energy losses, typically bending them through 90 degrees, so that one axis on the detector represents energy loss ( $\omega$ ) and the other represents momentum transfer (q). The result is a two-dimensional  $\omega$ -q map, showing how energy loss change with scattering vector. For the EELS spectra acquisition, a 50 milli-second acquisition time per frame was employed to balance energy resolution and signal-to-noise ratio. A total of 15,000 frames are aligned to correct for any misalignments in the zero loss peak and then summed to produce a cleaner spectrum. The effective energy resolution, i.e. full-width-at-half-maximum (FWHM) for the zero loss peak in vacuum, is 7 meV. The dispersion is 3 meV/channel. The STEM probe semi-convergence angle is 2 mrad, which gives a diffraction limited probe diameter of  $\sim$ 30 Å and a momentum resolution of 0.04 Å<sup>-1</sup>.

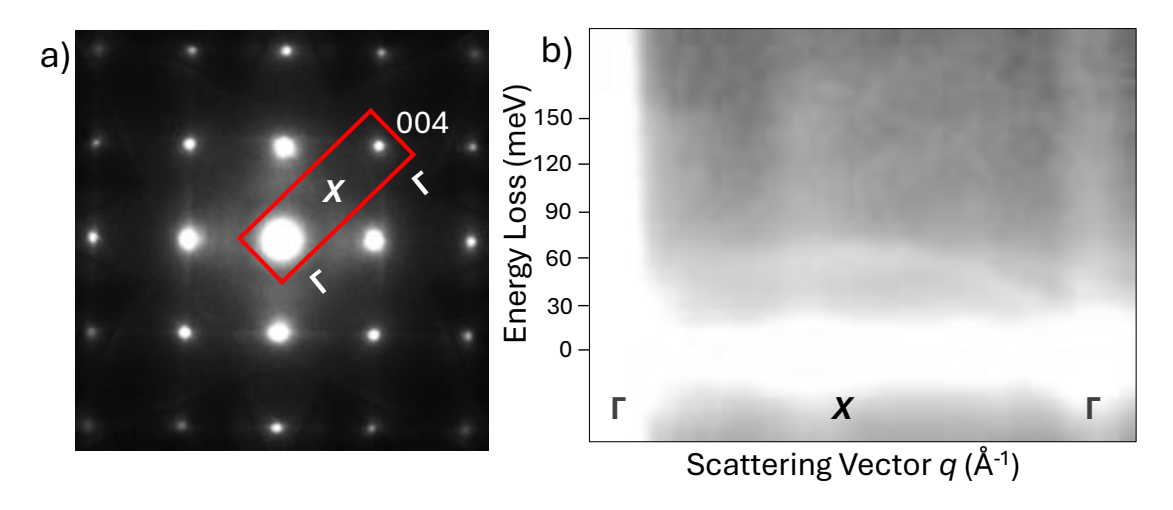


Figure 6.4: (a) Diffraction pattern of degenerately boron-doped silicon oriented along the [100] zone axis, with the selected  $\Gamma$ -X- $\Gamma$  path defined by the slot aperture (red rectangle) connecting the 000 and 004 reflections. (b) Momentum-resolved EELS of degenerately boron-doped silicon showing the energy–momentum ( $\omega$ -q) dispersion along the  $\Gamma$ -X- $\Gamma$  direction.

The STEM-EELS  $\omega-q$  map for High-B-Si measured along the  $\Gamma$ -X- $\Gamma$  direction is shown in Figure 6.5a. The dominant features are the longitudinal acoustic (LA) and optical phonon branches from the silicon matrix. For reference, the DFT simulated phonon dispersion curves for silicon along the  $\Gamma$ -X- $\Gamma$  direction are shown in Figure 6.5b. Since boron is lighter than silicon, it only contributes to optical modes rather than acoustic

ones. The complex background from both the EELS zero loss peak and LA phonon makes it difficult to identify defect modes due to boron. Furthermore, other artefacts are also present, such as the spurious intensity (circled feature in Figure 6.5a), which is thought to be due to stray scattering from the EELS slot aperture edges.

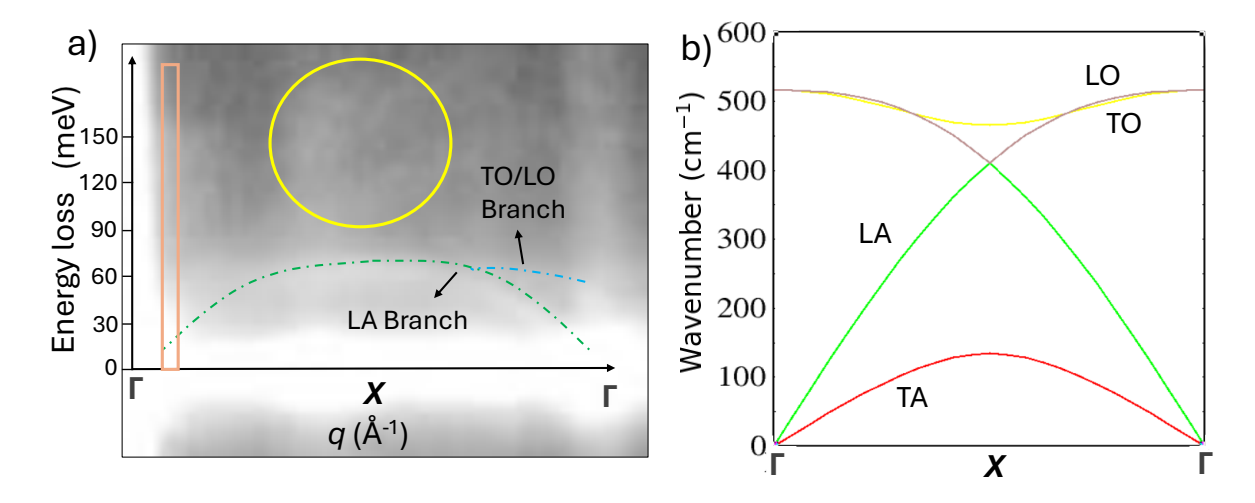


Figure 6.5: (a) Momentum-resolved EELS dispersion measurements of phonons in degenerate boron doped silicon. (b) Phonon dispersion curves of Si along  $\Gamma$ -X- $\Gamma$ , showing the transverse acoustic (TA), longitudinal acoustic (LA), transverse optical (TO), and longitudinal optical (LO) phonon branches.

To enhance detection of any weak defect modes, EELS spectra over a narrower q-range close to the direct beam were extracted (orange rectangle in Figure 6.5a). This was motivated by the following considerations: (i) the dominant LA phonon branch energy is suppressed near zero q, simplifying the background, (ii) the intensity of the direct beam is higher, offering an improved signal-to-noise ratio, and (iii) scattering from the edges of the slot aperture is minimised due to proximity to the direct beam, thereby reducing unwanted artefacts. The selected q-range is annotated in Figure 6.5a.

The extracted EELS spectrum (Figure 6.6) reveals additional intensity above background in the  $\sim$ 100-150 meV energy range, considerably higher than the optical phonon mode (64 meV) for elemental silicon. This extra intensity is likely due to boron-induced phonon defect modes. To isolate this contribution, a background fitting procedure was

applied. A power law function was used to model the underlying background signal (inset in Figure 6.6), enabling accurate subtraction and revealing the defect-related contribution, as illustrated in Figure 6.7).

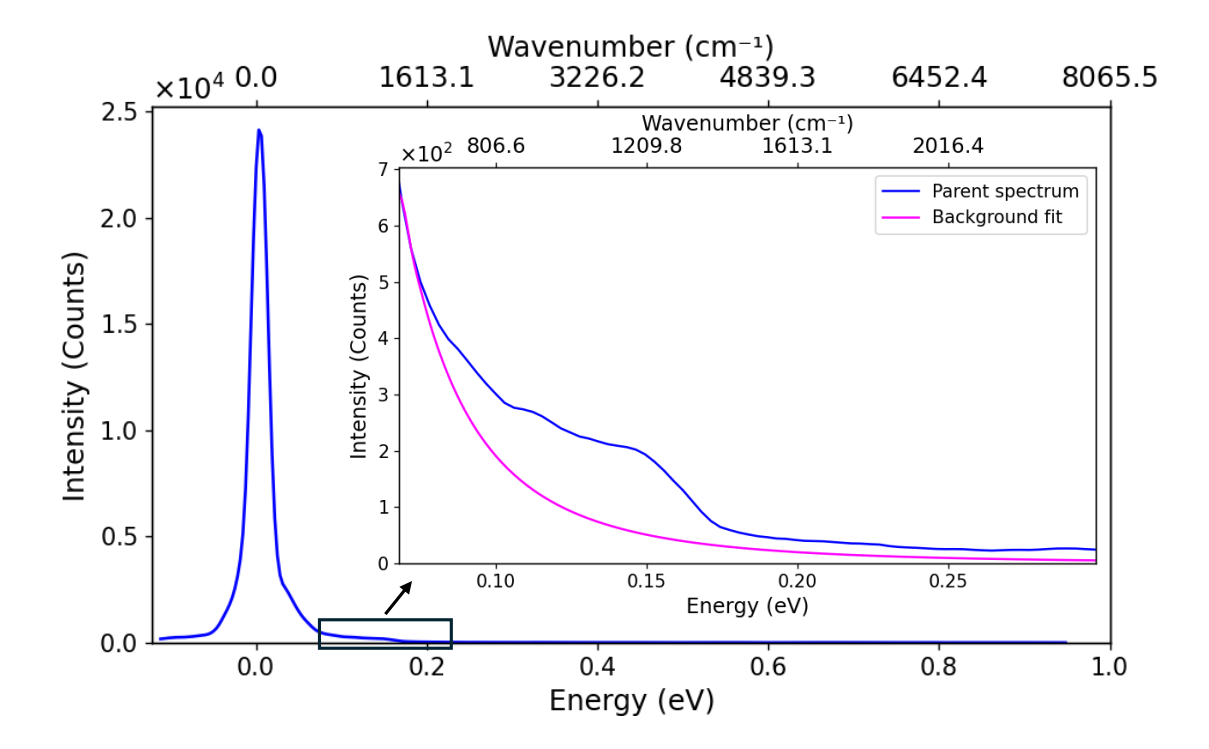


Figure 6.6: Parent spectrum, extracted from a narrow q-range close to the direct beam (box region in Figure 6.5(a)), with background fit (inset) using power law to isolate the phonon signal.

The extracted signal, shown in Figure 6.7, displayed a broad peak. Due to the 7 meV EELS energy resolution, resolving any closely spaced phonon modes is not feasible, as they would appear as a single broadened feature in the spectrum. Consequently, a single Gaussian function was fitted to represent the entire defect signal, providing an effective characterisation of defect modes within the limitations of the instrument. From Gaussian fitting, the peak maximum was determined to be 131 meV or 1060 cm<sup>-1</sup>. The FWHM of the Gaussian fit was 60 meV or 484 cm<sup>-1</sup>.

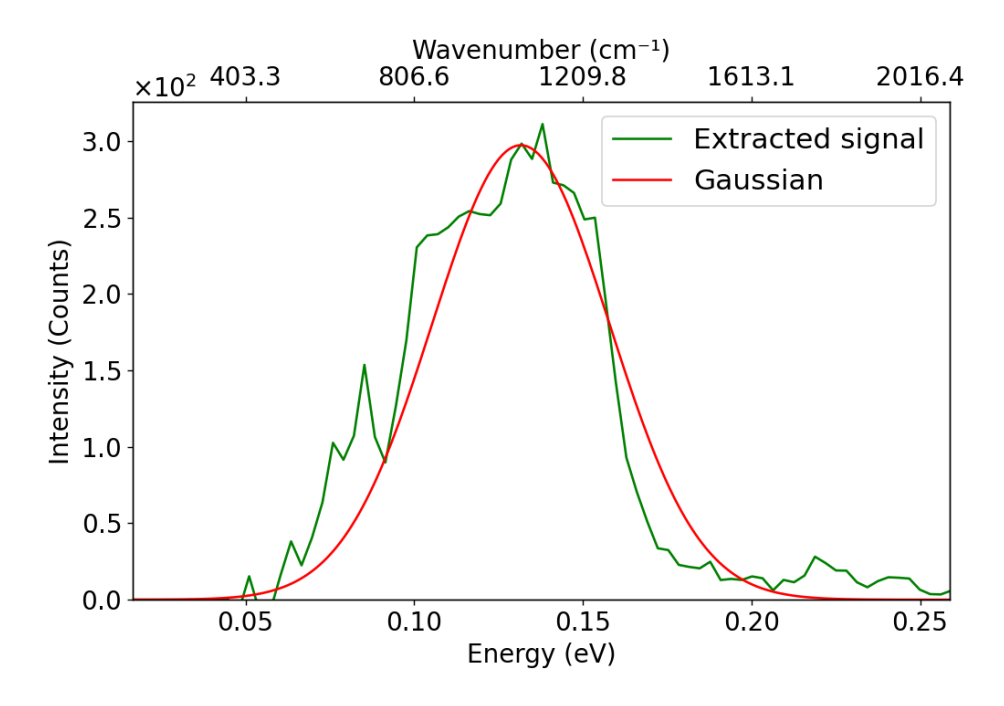


Figure 6.7: Gaussian fit of the high-energy optical modes associated with boron.

### 6.2.2 Momentum integrated EELS spectra

Momentum-integrated STEM-EELS was employed to further validate the presence of boron-induced defect modes and to address limitations introduced by slot aperture artefacts, such as the spurious background intensity observed in the  $\omega$ -q map. This decision was based on the observation that the boron-induced defect signal consistently appeared at an energy of approximately 131 meV across  $\Gamma \to X$ , indicating no significant q-dependence. Momentum integrated STEM-EELS provided an advantage over momentum-resolved STEM-EELS by eliminating diffraction effects associated with the rectangular slot used, thereby reducing background artefacts and enhancing spectral clarity. Momentum-integrated EELS spectra have better signal-to-noise ratio than momentum-resolved EELS spectra, which can make it easier to detect weak, non-dispersive phonon modes, such as commonly observed with defects. The idea behind momentum-integrated EELS is to study the energy loss due to phonons by averaging the EELS spectra over a selected range of scattering vectors, achieved by controlling where the spectrometer collects scattered electrons in the diffraction plane. In this ap-

proach, on-axis measurements are performed by centring the spectrometer aperture on the transmitted beam, thereby collecting electrons scattered through very small angles. For off-axis measurements, the electron beam is tilted so that the bright-field disk is displaced in the diffraction plane. As a result, the spectrometer, which remains fixed in position, now collects electrons scattered outside the central transmitted beam.

The on-axis and off-axis momentum integrated EELS spectra for both Si and High-B-Si were acquired at an accelerating voltage of 60 kV. A STEM probe semi-convergence angle of 30.5 mrad was maintained throughout all measurements. The probe angle is sufficiently large to detect all phonon modes within the first Brillouin zone, so that the resulting EELS spectra are momentum integrated (rather than momentum resolved). The collection semi-angle varied depending on the geometry: a 2 mm circular aperture was used for on-axis acquisition, corresponding to a collection angle of 44 mrad, while a 1 mm aperture was employed in the off-axis configuration, yielding a smaller collection angle of 22 mrad. For off-axis collection the centre of the STEM bright-field disc was deflected by 55 mrad away from the centre of the EELS entrance aperture. Off-axis EELS spectra have the advantage that the zero loss peak is suppressed, making background subtraction easier, although there is also less signal intensity. The on-axis spectra were acquired with a dwell time of 10 milliseconds per pixel. For each on-axis dataset, 30,000 frames were collected, and a total of over 210,000 frames (30,000  $\times$  7 datasets) were summed to enhance the signal-to-noise ratio (SNR). In contrast, off-axis spectra, which are inherently noisier due to their reduced signal intensity and angular displacement from the direct beam, were acquired with a longer dwell time of 30 ms. Each off-axis dataset consisted of 15,000 frames, and four such datasets (totalling 60,000 frames) were combined to improve SNR. The effective energy resolution, as estimated by the ZLP full-width-at-half-maximum (FWHM) for the STEM probe incident on the specimen, was 12 meV and 14 meV for the on-axis and off-axis spectra, respectively. The dispersion was 1.2 meV/channel.

The collected spectra showed a noticeable increase in noise beyond 0.08 eV, especially

in the higher-energy part of the data. Since this part of the spectrum is where boron-induced defect modes appear, these signals can be easily hidden or misinterpreted due to the high noise level, making it difficult to draw reliable conclusions. To improve the quality of the data and make sure that important features were not lost in the noise, we first applied a Savitzky–Golay (S-G) filter, as shown in Figure 6.8 . This is a common method used to smooth out fluctuations in the data while still keeping the main shapes and peaks in the spectrum intact. It works by fitting a small set of points in the spectrum with a low-degree polynomial and moving this fit across the entire dataset without heavily distorting the real features of the spectrum.

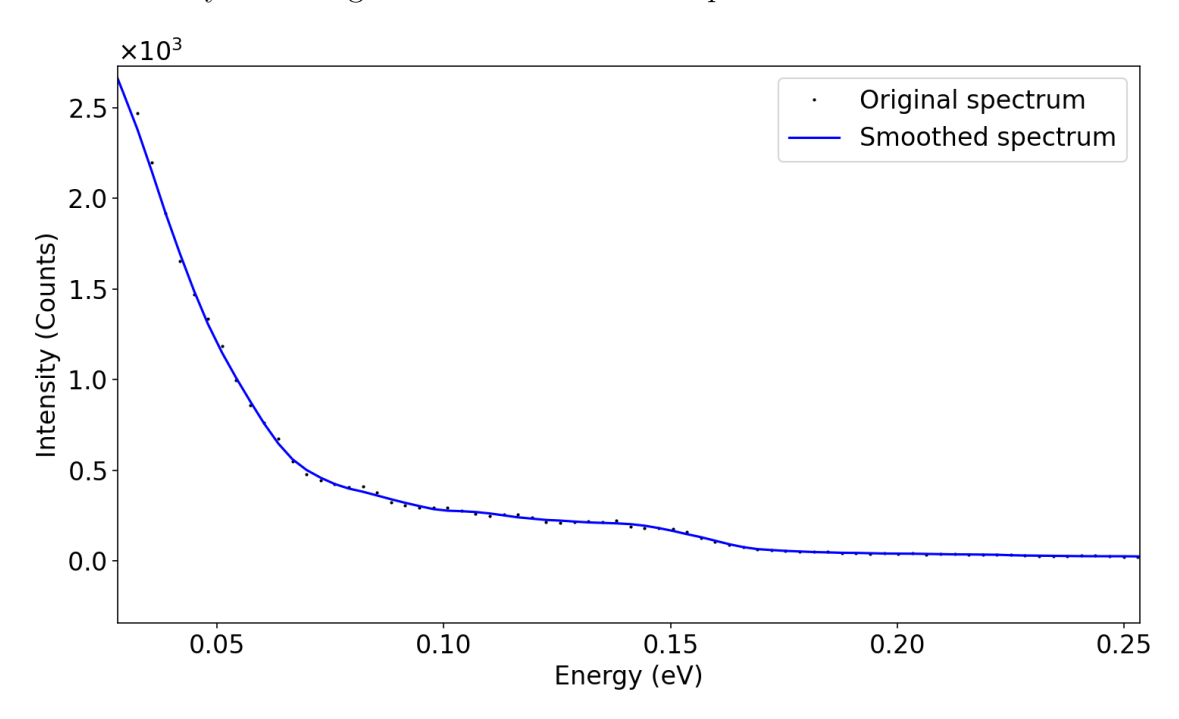


Figure 6.8: Savitzky-Golay (S-G) filtered off-axis EELS spectrum for High-B-Si.

After the smoothing step, the next stage involved isolating the inelastic component of the spectra by removing the contribution from the zero-loss peak (ZLP). Despite high energy resolution, the tail of the ZLP can extend into the low-energy loss region, over-lapping with subtle phonon features and potentially masking weak defect signals. To address this, a reflected tail method was used. This method assumes that the shape of the ZLP is approximately symmetric around its maximum, which can be experimentally achieved in a monochromated electron microscope. By taking the left-hand side of the ZLP, i.e. the portion of the spectrum at negative energy losses and mirroring it onto the

right-hand side, an estimated profile of the elastic background was constructed. This reflected tail was then subtracted from the smoothed spectrum, effectively removing the influence of the elastic scattering and revealing only the inelastic signal. The smoothed spectrum and the extracted inelastic signal are shown in Figures 6.9 and 6.10. Figures 6.9a and 6.9b shows the off-axis EELS spectra for Si and High-B-Si, respectively. In both cases, the smoothed spectra are shown alongside the extracted inelastic components following reflected tail subtraction. Similarly, Figures 6.10a and 6.10b present the on-axis EELS spectra for Si and High-B-Si.

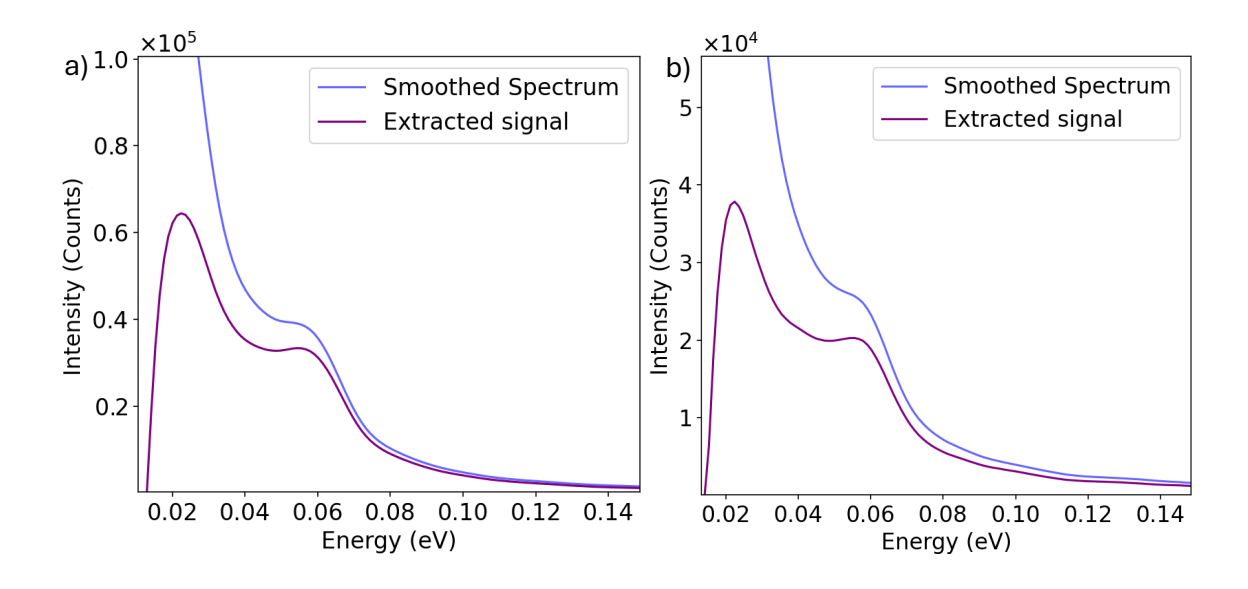


Figure 6.9: Off-axis smoothed spectrum and the extracted inelastic signal plotted together for (a) Si, and (b) High-B-Si.

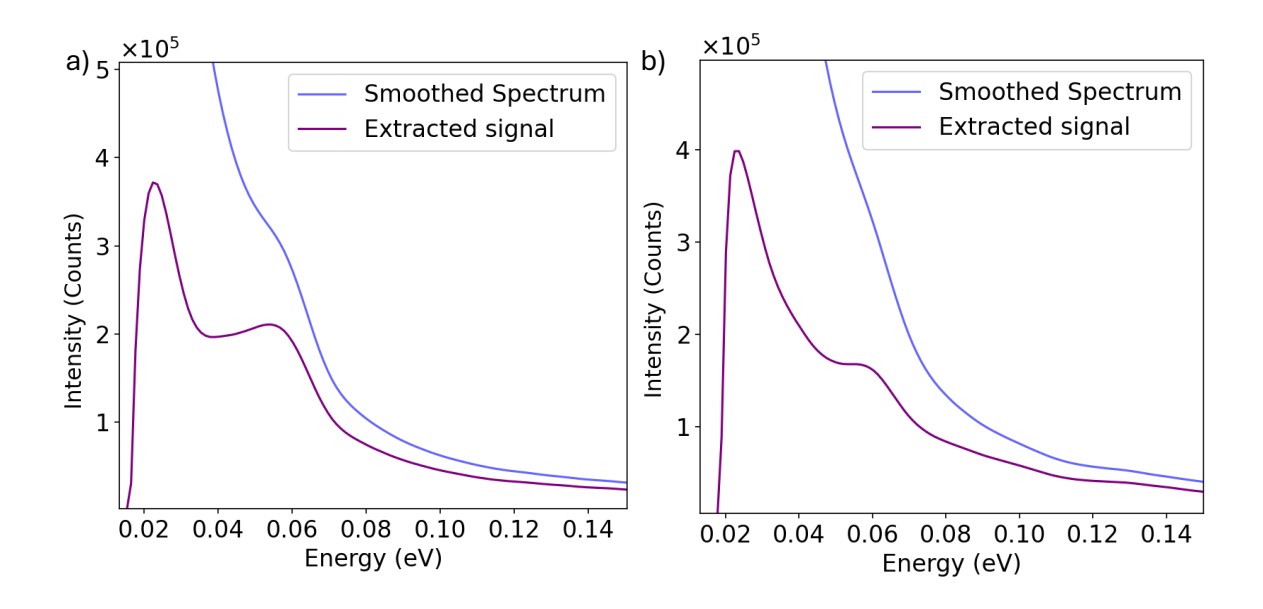


Figure 6.10: On-axis smoothed spectrum and the extracted inelastic signal plotted together for (a) Si, and (b) High-B-Si.

Following this, each extracted inelastic spectrum was normalised to the LO/TO phonon peak intensity of silicon at 64 meV. This step was necessary to ensure fair comparison between Si and High-B-Si, as it accounts for variations in signal intensity caused by differences in sample thickness and incident electron dose. A power law background was then fitted and subtracted from each spectrum to remove residual broad signal contributions unrelated to defect vibrational features. The normalised and background-subtracted spectra for both off-axis and on-axis configurations are presented in Figures 6.11 and 6.12, respectively.

Figure 6.11a shows the off-axis result for Si, while Figure 6.11b presents the corresponding data for High-B-Si. Similarly, Figure 6.12a displays the on-axis spectrum for Si, and Figure 6.12b shows the High-B-Si data. Each plot includes the normalised signal.

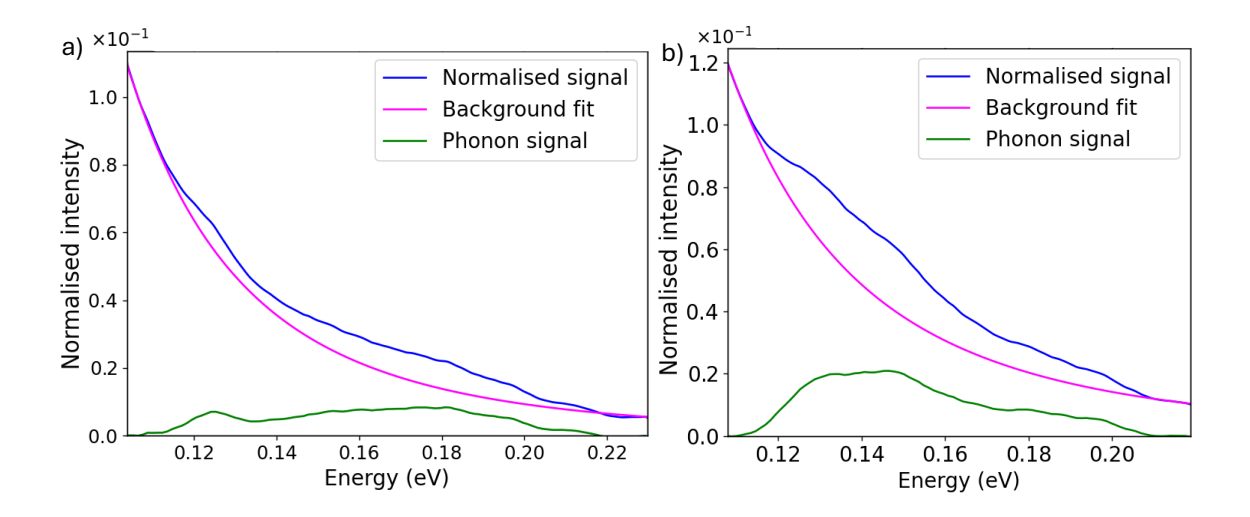


Figure 6.11: Background subtracted off-axis EELS intensity for (a) Si, and (b) High-B-Si plotted alongside the background fit and the normalised smoothed spectrum.

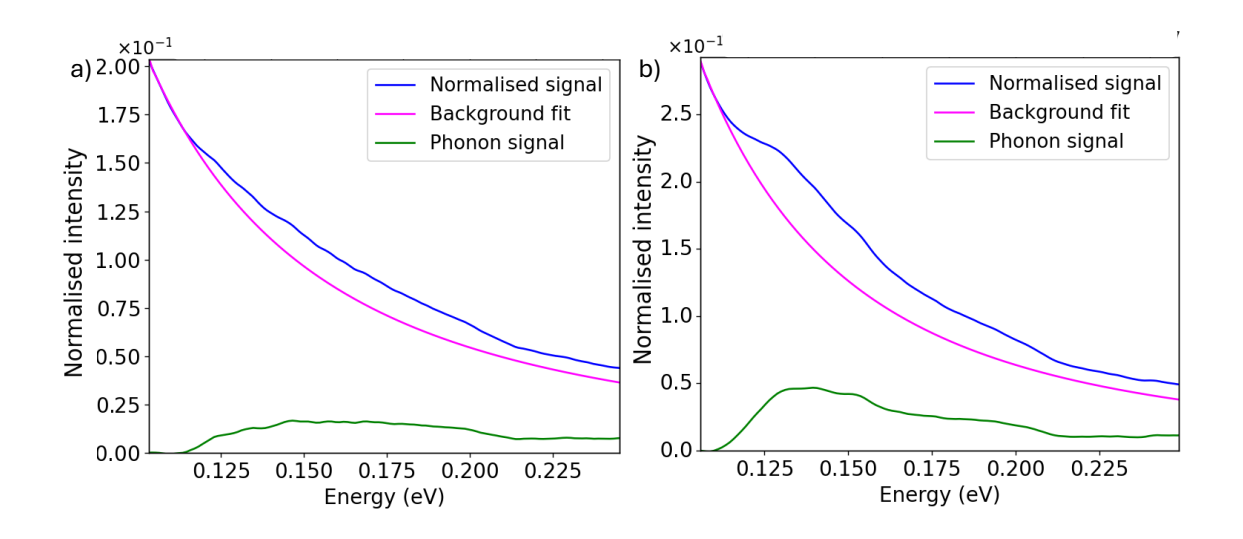


Figure 6.12: Background subtracted on-axis EELS intensity for (a) Si, and (b) High-B-Si plotted alongside the background fit and the normalised smoothed spectrum.

To further investigate the phonon modes and isolate the impact of degenerate boron doping, the background subtracted signals were compared between Si and High-B-Si in both on-axis and off-axis configurations. The results of these comparisons are presented in Figures 6.13a and 6.13b, respectively.

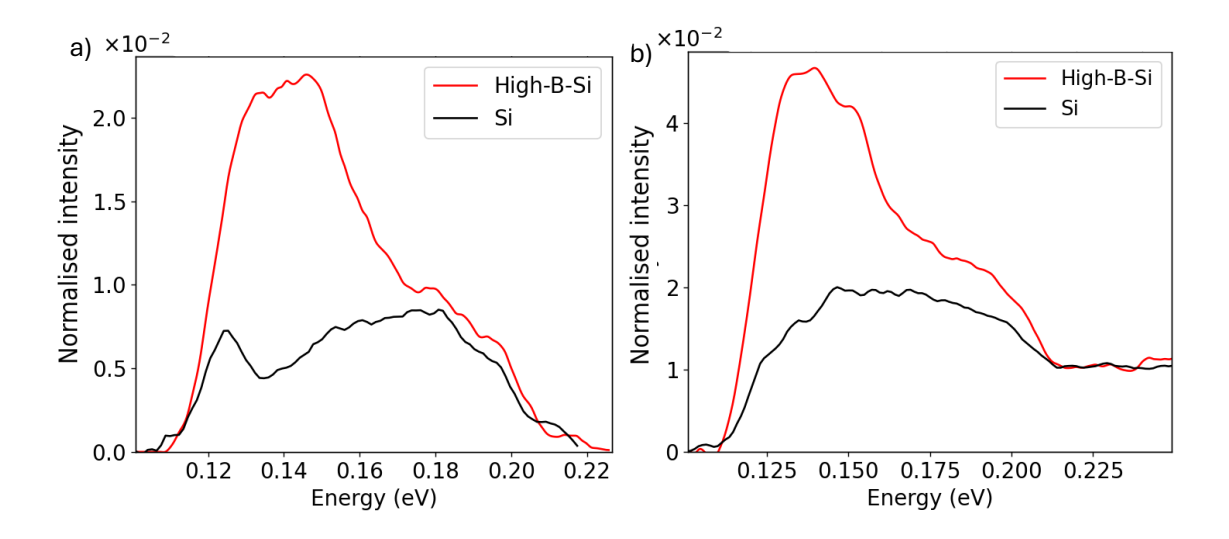


Figure 6.13: Comparison of background subtracted signal of Si and High-B-Si for (a) off-axis, and (b) on-axis EELS collection geometries.

In both Figures 6.13a and 6.13b, there is a noticeable weak signal in the 100–250 meV range in Si. This intensity, while unexpected for intrinsic silicon, is likely attributable to unintentional light-element impurities such as oxygen or carbon, which may have been incorporated during the crystal growth process [247]. These impurities can introduce local vibrational modes, giving rise to the observed weak background in this energy range.

In contrast, the High-B-Si spectra in both Figures 6.13a and 6.13b show a stronger signal in the 110–150 meV range, clearly exceeding that of the impurity signal observed in Si. This enhancement is consistent with the introduction of boron defect-induced phonon modes, which introduce additional optical phonon modes due to boron-boron and boron-silicon interactions. The distinction between the two spectra, especially the amplified signal in the High-B-Si case, supports the interpretation that these high-intensity features are indeed related to boron incorporation, beyond any background introduced by residual impurities.

To isolate the vibrational contribution specifically due to boron incorporation, the residual impurities induced signal of Si was subtracted from that of High-B-Si, for both

off-axis and on-axis configurations. The resulting difference spectra are shown in Figure 6.14. In both cases, the subtraction reveals a broad residual feature in the 110–150 meV energy range, which was previously obscured by underlying background. This residual signal highlights the optical vibrational modes introduced by boron doping. The broadness of the feature across both configurations suggests that the boron-induced phonon modes are not sharply defined but rather spread across a range of energies, likely due to the distribution of boron atoms within the silicon matrix.

To characterise the structure of this residual signal, each spectrum was least squares fitted using two Gaussian functions. This choice was motivated by the presence of a broader phonon signal due to multiple local vibrational modes, rather than a single sharply defined phonon peak. In both configurations, the first Gaussian peak (blue shaded region) is located between 120–135 meV, while the second Gaussian peak (orange shaded region) is located between 140–150 meV. The first Gaussian provides the most accurate representation of the primary boron-induced phonon mode, given its close alignment with the observed spectral peak. Therefore, the phonon energy associated with the first Gaussian peak is taken to represent the characteristic contribution of degenerate boron doping to the vibrational spectrum. The second Gaussian is tentatively assigned to differences in non-boron impurity levels in the Si and High-B-Si samples. The peak maximum of the first Gaussian was determined to be 132.4 meV for the off-axis configuration and 131.7 meV for the on-axis configuration, indicating good consistency between the two independent measurements.

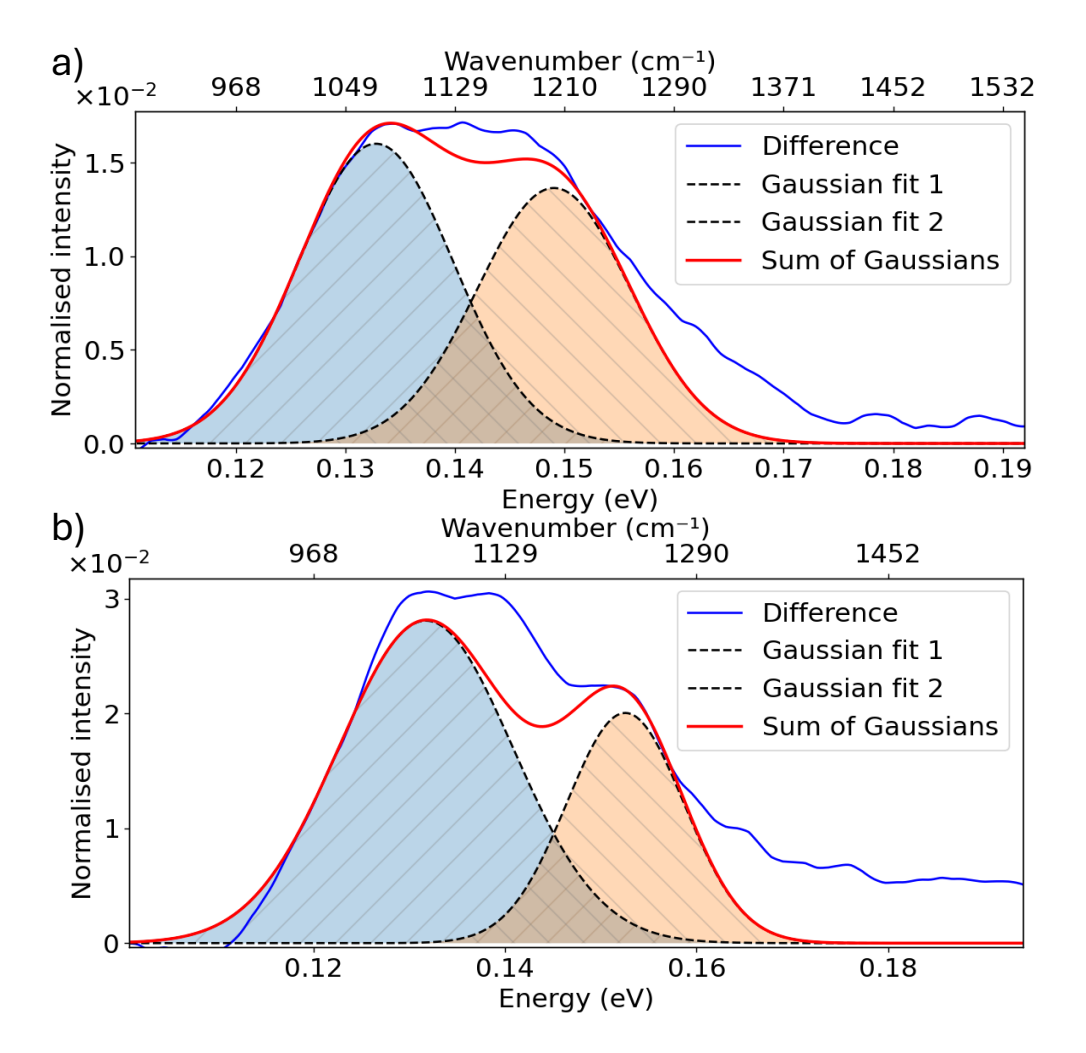


Figure 6.14: Difference spectrum obtained by subtracting the signal of Si from that of High-B-Si for both (a) off-axis, and (b) on-axis EELS spectra. The difference spectrum is modelled by least squares fitting two Gaussian functions. The sum of the Gaussians is overlaid to evaluate the goodness of fit and the extent to which the Gaussian model captures the spectral features.

It should be noted, however, that it was challenging to precisely pinpoint the exact phonon energy of the boron-induced mode due to limitations in detector energy resolution (approximately 7 meV), which may cause overlapping or merging of closely spaced modes, potentially masking finer structure in the defect signal. Nevertheless, the Gaussian fitting approach enables a reasonable approximation of the defect phonon characteristics and supports the conclusion that boron introduces distinct, localised optical vibrational modes around 132 meV or 1065 cm<sup>-1</sup>.

# 6.3 Simulation of phonon modes for boron defects in silicon

This section presents the simulation results of phonon modes for various boron defect configurations in silicon. The purpose of these simulations was to reproduce and understand the experimentally measured phonon wavenumber of High-B-Si obtained via monochromated-EELS. By employing DFT through the CASTEP code, we investigated how different defect types, ranging from isolated substitutional and interstitial boron atoms to clusters of boron interstitials, influence the vibrational properties of the host silicon lattice.

#### 6.3.1 Convergence tests

To ensure both the accuracy and computational efficiency of the phonon dispersion calculations, a series of convergence tests were performed prior to conducting the full simulations of boron defect systems in silicon. These included convergence with respect to the supercell size, the plane-wave cutoff energy, and the Monkhorst-Pack (MP) **k**-point mesh. All convergence tests were carried out by employing norm-conserving pseudopotentials and the local density approximation (LDA) for the exchange-correlation functional.

Since phonon calculations are based on periodic boundary conditions, any defect introduced into the system is replicated in all directions. A supercell that is too small can result in unphysical defect-defect interactions between the defect and its periodic images in adjacent cells, leading to unphysical phonon mode generation. To mitigate such interactions while maintaining computational feasibility, we also conducted a convergence test on the supercell size for both substitutional boron acceptors and interstitial boron defects by calculating the phonon dispersion curves along the  $\Gamma$  to X direction of the Brillouin zone for supercells containing 64, 216, and 512 silicon atoms.

For the single boron interstitial system, the highest optical phonon wavenumber along the  $\Gamma$  to X direction differed by approximately 20 cm<sup>-1</sup> between the 64-atom and 216atom supercells. For the boron acceptor defect, the difference in the highest optical phonon wavenumber was around 10 cm<sup>-1</sup>. Increasing the supercell size to 512 atoms caused no significant change in the phonon wavenumber. All phonon calculations were performed using a plane-wave cutoff energy of 700 eV and a  $2\times2\times2$  MP k-point mesh, which were kept consistent across all supercells to ensure comparability. Based on these results, we concluded that the 64-atom supercell is sufficiently large for phonon dispersion calculations for both defect types. However, it should be noted that the acceptor defect system, when modelled using the 64 atom supercell, does not accurately reproduce the hole concentration observed in experimental Hall measurements. The 64 atom supercell corresponds to a boron concentration of approximately  $8 \times 10^{20} \text{cm}^{-3}$ , which significantly exceeds the typical experimental doping levels of  $10^{20} \text{cm}^{-3}$  observed in Hall measurements. This leads to a higher concentration of boron than is experimentally observed, which can be considered a limitation of using this supercell for the acceptor system. Despite this, due to the minimal difference in the phonon wavenumber between the 64 atom and 216 atom supercells, and the substantial reduction in computational cost, the 64 atom supercell was selected.

Following the selection of the 64-atom supercell, the convergence of the total ground-state energy with respect to the plane-wave cutoff energy was evaluated for a single boron acceptor within a 64-atom silicon supercell. The plane-wave cutoff energy determines the maximum kinetic energy of the basis set used to represent the electronic wavefunctions. An insufficient cutoff can lead to incomplete convergence and inaccurate forces and energies. For the convergence test, the cutoff energy was varied from 100 eV to 600 eV, while the MP  $\bf k$ -point grid was fixed at  $2\times2\times2$ . The total ground-state energy of the system was monitored as a function of the cutoff energy, as in Figure 6.15.

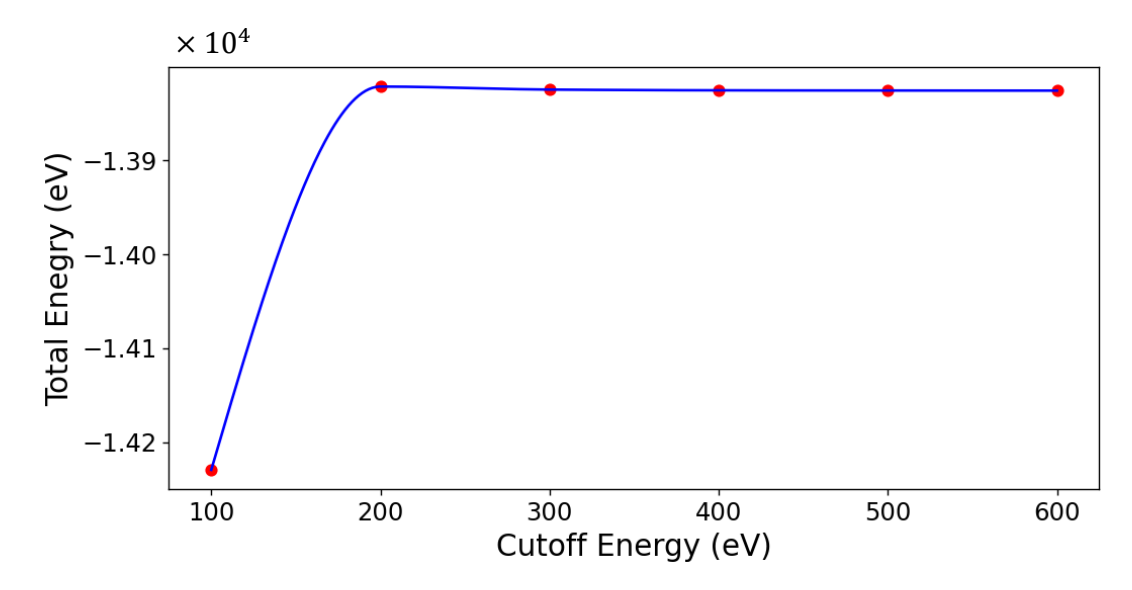


Figure 6.15: Variation of the total energy of a 64-atom silicon supercell containing a single boron acceptor as a function of the plane-wave cutoff energy.

As the cutoff energy increased, the total energy initially rose significantly between 100 eV and 200 eV, correcting the artificial overbinding observed at low cutoff energies. Beyond 300 eV, the total energy changes became progressively smaller, indicating convergence. At 500 eV, the total energy reached -13825.49 eV, with a further increase to 600 eV resulting in only a marginal change of less than 0.1%. Based on these results, a cutoff energy of 500 eV was selected for all subsequent simulations, providing an appropriate balance between accuracy and computational cost.

A similar convergence test was conducted for the MP  $\mathbf{k}$ -point sampling. In this case, the plane-wave cutoff energy was held fixed at 500 eV, and the number of  $\mathbf{k}$ -points along each reciprocal lattice vector direction was incrementally increased from 1 to 4. The energy variation exhibited a rapid convergence with respect to the  $\mathbf{k}$ -point mesh, as in Figure 6.16. A single  $\mathbf{k}$ -point  $(1\times1\times1)$  produced a noticeably higher total energy of -13818.35 eV, indicating poor sampling of the Brillouin zone. A denser  $2\times2\times2$  grid resulted in a significantly lower energy of -13825.49 eV, close to the fully converged value. Further increasing the grid density to  $3\times3\times3$  and  $4\times4\times4$  led to marginal energy reductions, reaching -13825.58 eV and -13825.59 eV, respectively. Given the minimal gain in accuracy beyond the  $2\times2\times2$  mesh and the increased computational cost asso-

ciated with denser grids, the  $2\times2\times2$  **k**-point grid was deemed sufficient for all defect systems under investigation.

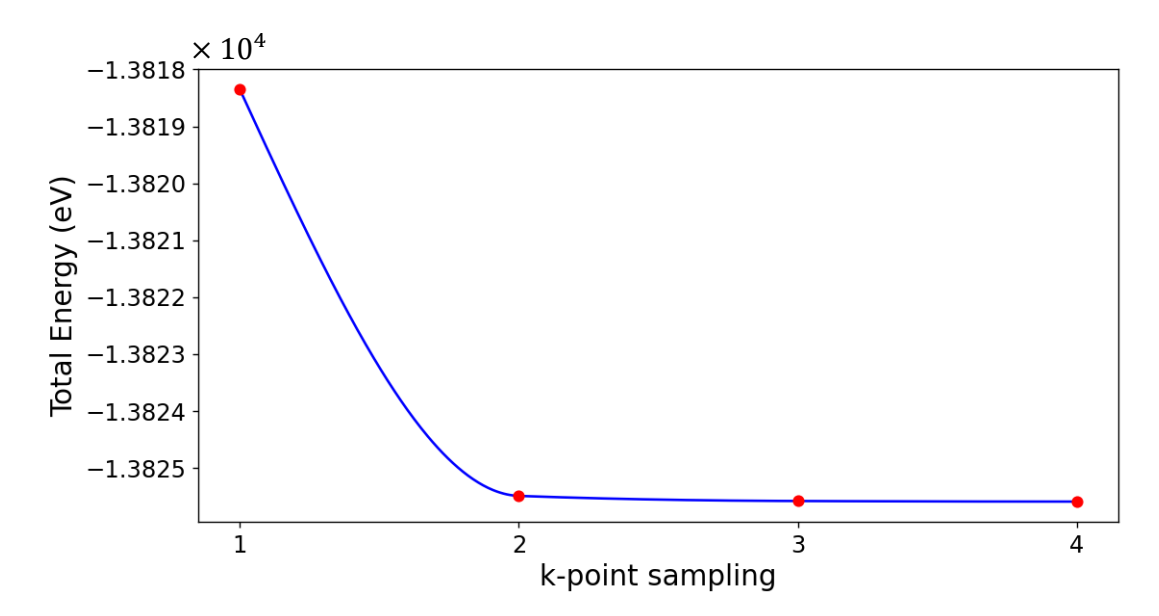


Figure 6.16: Variation of the total energy of a 64-atom silicon supercell containing a single boron acceptor as a function of the **k**-point grid density.

# 6.3.2 Structural configurations of boron defects in silicon

Various boron defect configurations using DFT were simulated to understand the influence of degenerate boron doping on the vibrational properties of silicon. Vibrational modes are highly sensitive to the local atomic environment, bonding distortions, and defect-induced strain fields, meaning that the structure and arrangement of boron atoms within the silicon lattice play a critical role in shaping the observed phonon behaviour. Therefore, careful modelling of individual boron defects and clusters was necessary to link specific structural features to experimentally measured phonon modes. It is assumed that boron dopants are the primary contributors to the experimentally observed defect peak, and that any interactions between boron and unintentional other light impurities can be largely neglected. This assumption is supported by Hall measurements indicating degenerate p-type extrinsic behaviour, confirming that the boron concentration is significantly higher than the impurities. The defect systems studied in this work include isolated substitutional boron acceptors, boron interstitials, and boron

interstitial clusters. Each defect type was constructed to reflect physically plausible configurations that could arise during high-concentration doping conditions.

The single substitutional boron acceptor defect ( $\mathrm{B}^-$ ) was modelled by replacing a silicon atom with a boron atom at a lattice site (Figure 6.17a), thus mimicking the conventional p-type dopant configuration in silicon. For the single boron interstitial defect ( $\mathrm{B}^0_i$ ), the neutral boron atom was placed at the midpoint of a silicon nearest-neighbour tetrahedron edge (Figure 6.17c), corresponding to an energetically favourable interstitial position based on previous theoretical studies [248]. In addition to modelling the neutral boron interstitial, a single negatively charged boron interstitial ( $\mathrm{B}^-_i$ ) was also constructed in order to investigate whether the formation of such an ionised interstitial is energetically favourable under degenerate doping conditions. Furthermore, a system containing two nearest-neighbour ionised boron acceptors (2B<sup>-</sup>) (Figure 6.17b) was also modelled to explore the interactions between substitutional boron atoms at high doping concentrations.

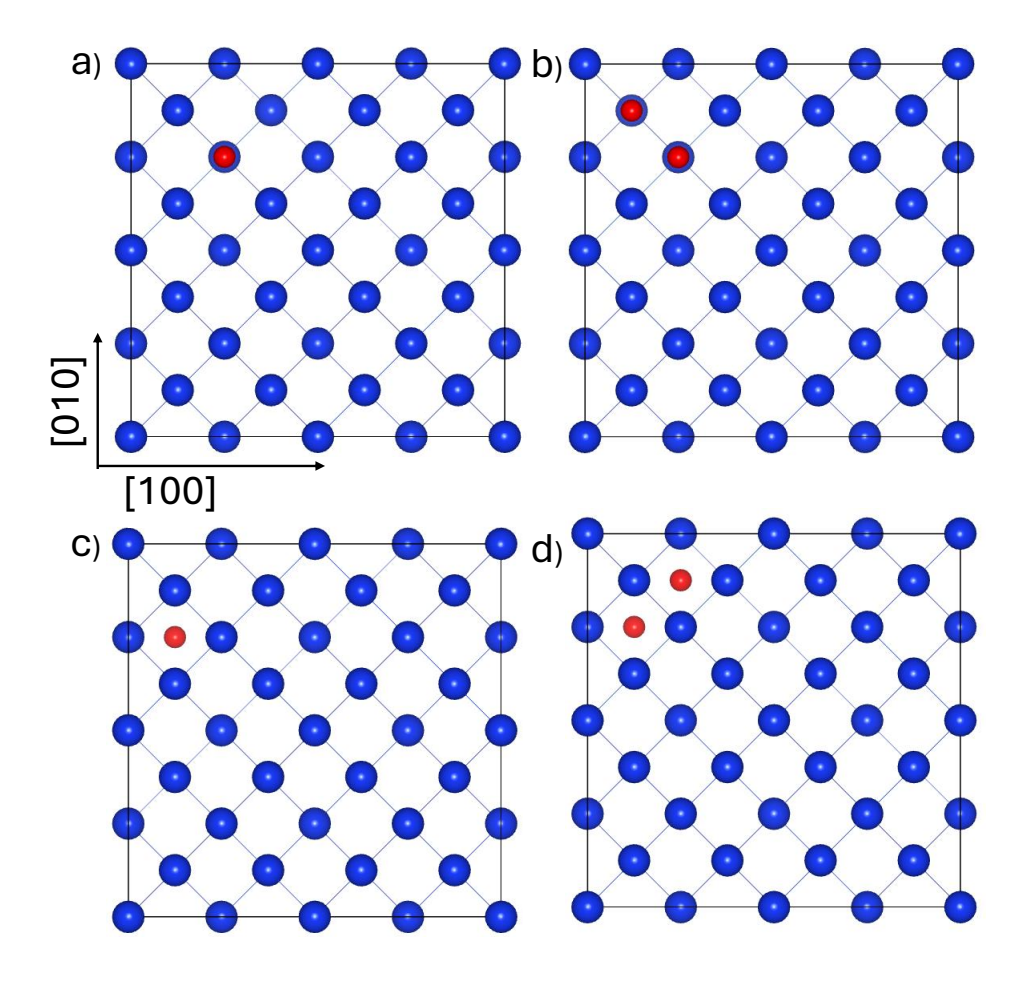


Figure 6.17: Structural configurations of, (a) a single boron acceptor (B<sup>-</sup>), (b) two nearest-neighbour ionised boron acceptors (2B<sup>-</sup>), (c) a neutral boron interstitial (B<sub>i</sub><sup>0</sup>), and (d) two boron interstitials cluster (2B<sub>i</sub><sup>0</sup>), boron defects in silicon as viewed along [001]. Red and blue atoms represent boron and silicon atoms, respectively.

To simulate boron interstitial clustering, systems containing multiple neutral boron interstitials ( $XB_i^0$ , where X=2 or 3) were constructed. In the two boron interstitial cluster system ( $2B_i^0$ ), the two neutral boron atoms were arranged to maintain nearest-neighbour positioning, simulating a tightly bound defect pair (Figure 6.18a).

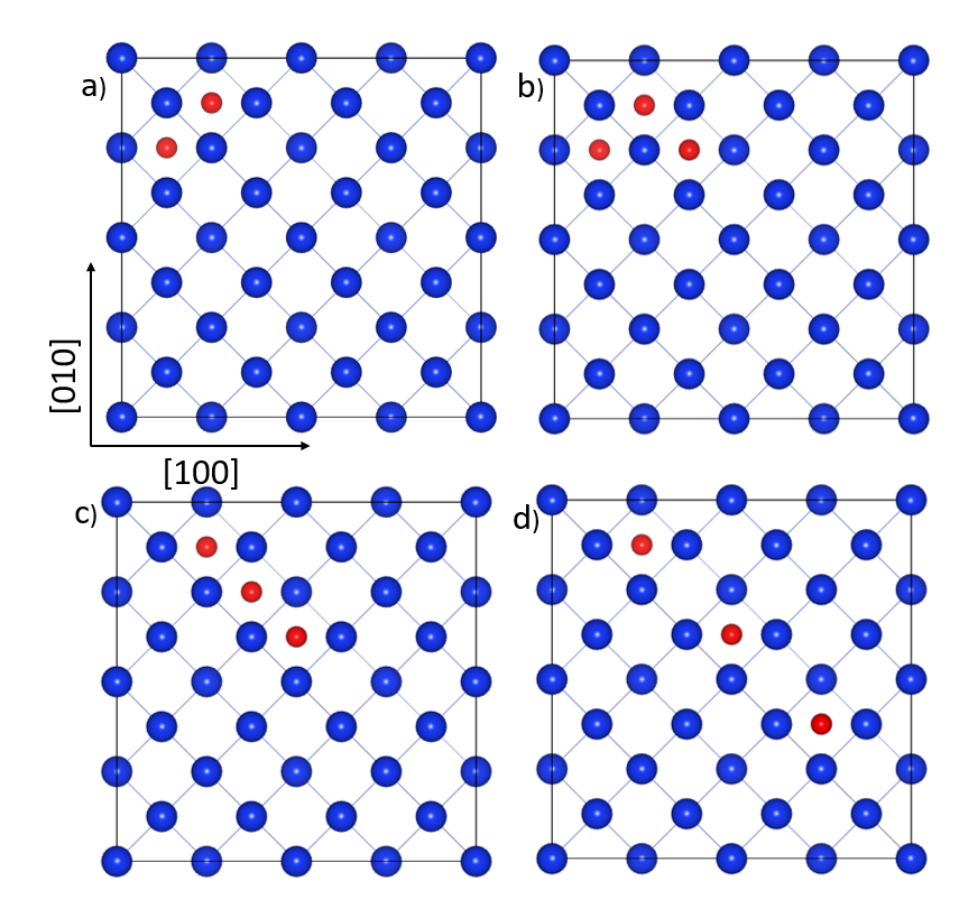


Figure 6.18: Structural configurations of boron defects in silicon as viewed along [001]. (a) The boron interstitial cluster  $(2B_i^0)$  with two neutral boron atoms in interstitial sites.(b) Boron interstitial cluster  $(3B_i^0$  - confi 1) with three neutral boron atoms illustrates a tightly bound trio of interstitials. (c) Boron interstitial cluster  $(3B_i^0$  - confi 2) shows three neutral boron atoms arranged in a linear fashion, forming a less compact structure. (d) Boron interstitial cluster  $(3B_i^0$  - confi 3) shows a linear arrangement with alternating boron interstitial atoms and empty interstitial spaces.

Three-boron interstitial clusters  $(3B_i^0)$  were investigated in three distinct configurations to capture a range of physical arrangements, each with differing packing densities. It is important to note that an exhaustive search of all possible cluster configurations has not been performed in this study. The primary goal was to identify the physical nature of the point defects that contribute to the phonon wavenumbers observed experimentally. In configuration 1  $(3B_i^0$  - confi 1), all three interstitial boron atoms were confined within a single silicon unit cell, representing the most compact and strongly interacting cluster (Figure 6.18b). Configuration 2  $(3B_i^0$  - confi 2) depicted a linear arrangement of the

boron atoms aligned along the  $[\overline{1}1\overline{1}]$  direction, with moderate spacing between the atoms, thereby spanning multiple unit cells (Figure 6.18c). Configuration 3 ( $3B_i^0$  - confi 3) presented a further delocalised configuration in which the interstitial boron atoms were again aligned along the  $[\overline{1}1\overline{1}]$  direction but with alternating boron interstitial atoms and empty interstitial spaces (Figure 6.18d). In all interstitial cluster configurations, the interstitial boron atoms were clustered on the same ( $10\overline{1}$ ) crystallographic plane.

### 6.3.3 Defect formation energies

The calculation of defect formation energies provides critical insight into the stability of various boron-related defects within silicon. Understanding these energies is essential to determine which configurations are energetically favourable and thus most likely to occur under realistic doping conditions. All defect structures were simulated within a 64-atom silicon supercell. The supercells were geometry optimised prior to the defect formation energy calculations. The geometry optimisation employed Norm-conserving pseudopotentials (NCP) with the Local Density Approximation (LDA) exchange-correlation functional, a plane-wave basis cutoff energy of 500 eV, and a Monkhorst-Pack **k**-point grid of  $2 \times 2 \times 2$  to sample the Brillouin zone. The structural relaxation process for all systems continued until the residual force on each atom was less than  $0.05 \text{ eV}\text{Å}^{-1}$ , the energy difference between consecutive ionic relaxation steps per ion was below  $5 \times 10^{-5} \text{ eV}$ , and the maximum displacement was  $<1 \times 10^{-3} \text{ Å}$ . After structural relaxation, total energy calculations were performed for both defected and perfect silicon cells, and the defect formation energies were obtained following the formalism outlined below [249]:

$$E_f = E_{\text{defect}}^T - E_{\text{perfect}}^T - \sum_i n_i \mu_i + q E_F, \tag{6.1}$$

where  $E_{\text{defect}}^T$  and  $E_{\text{perfect}}^T$  represent the total energies of the supercell with and without the defect, respectively. The term  $n_i$  is the number of atoms of species i added or removed, while  $\mu_i$  denotes the chemical potential of species i. Here, q is the charge state of the defect and  $E_F$  the Fermi energy level. The chemical potentials used were defined as  $\mu_{\rm Si} = E_{\rm Si}^T/N_{\rm Si}$  for silicon, where  $E_{\rm Si}^T$  is the total energy of a silicon supercell with no defects and  $N_{\rm Si}$  is the number of silicon atoms, calculated from a defect-free silicon supercell energy, and  $\mu_{\rm B} = E_{\rm B}^T/N_{\rm B}$  for boron, where  $E_{\rm B}^T$  is the total energy of the rhombohedral boron primitive cell and  $N_{\rm B}$  is the number of boron atoms.

The calculated formation energies are presented in Table 6.1. The single boron acceptor (B<sup>-</sup>) configuration exhibits the lowest formation energy of 2.17 eV for isolated defects. This result strongly suggests that at low doping concentrations, boron atoms preferentially occupy substitutional lattice sites, thus acting as effective dopants and providing holes to the silicon lattice when ionised. The substitutional boron impose relatively little uniform strain on the silicon lattice because the boron atom fits well within the tetrahedral framework, resulting in a low defect formation energy. A single neutral boron interstitial  $(\mathbf{B}_i^0)$  exhibits a considerably higher formation energy of 3.73 eV, indicating that isolated interstitials are less favourable compared to substitutional boron under these conditions as it forces the surrounding silicon atoms out of their equilibrium positions, causing significant lattice distortion compared to single boron acceptor. Furthermore, the formation energy of an ionised boron interstitial  $(B_i^-)$  is even higher at 5.77 eV, indicating that isolated charged interstitials are unlikely to form since the added charge increases local electrostatic repulsion. As a result, for all subsequent calculations involving boron interstitials and clusters, only the neutral charge state  $(B_i^0)$  was considered.

As the boron concentration increases, the spatial separation between boron atoms reduces to the point where interactions between them become significant. Table 6.1 reveals that the formation of interstitial clusters becomes energetically favourable compared to acceptor clusters. Specifically, the formation energy of a neutral two-boron interstitial cluster  $(2B_i^0)$  is 5.10 eV, corresponding to 2.55 eV per boron atom, which is lower than the formation energy per atom for two neighbouring acceptors  $(2B^-)$  at 2.60 eV. The preference for interstitial clustering over substitutional defect clustering

at high concentrations arises because substitutional boron atoms, carrying a negative charge, experience mutual repulsion, making close proximity less favourable. In contrast, neutral interstitial clusters avoid such repulsive interactions, allowing a denser and more stable arrangement.

When the number of boron atoms in a cluster increases further, the total lattice distortion grows, which raises the total defect formation energy, but the per-atom energy can decrease if there is bonding between neighbouring atoms. For instance, the most compact cluster configuration ( $3B_i^0$ - confi 1) yields an average formation energy per atom of 1.90 eV, significantly lower than that of a single boron acceptor. Less densely packed configurations, however, such as  $3B_i^0$ - confi 2 and  $3B_i^0$ - confi 3, exhibit higher formation energies per atom (2.38 eV and 3.41 eV respectively), demonstrating the critical role of packing density in stabilising boron clusters. These results suggests that at high boron concentrations, boron clustering in the form of interstitial aggregates is favoured in addition to the acceptor formation.

Table 6.1: Formation energies of boron point defect configurations in silicon. Numbers within brackets denote the formation energy per atom.

| Defect type          | Defect formation energies(eV) |
|----------------------|-------------------------------|
| B <sup>-</sup>       | 2.17                          |
| $\mathbf{B}_{i}^{0}$ | 3.73                          |
| $\mathrm{B}_{i}^{-}$ | 5.77                          |
| $2B^{-}$             | 5.19(2.60)                    |
| $2\mathrm{B}_i^0$    | 5.10(2.55)                    |
| $3B_i^0$ - confi 1   | 5.71 (1.90)                   |
| $3B_i^0$ - confi 2   | 7.13 (2.38)                   |
| $3B_i^0$ - confi 3   | 10.22 (3.41)                  |

The simulation of an octahedrally shaped 6-neutral interstitial boron cluster  $6B_i^0$  configuration showed further reduction in the formation energy per atom (1.75 eV). However, the geometry optimisation process revealed significant local strain around the cluster as shown in Figure 6.19b, suggesting that although such clusters are energetically favourable, they impose considerable distortions on the silicon lattice. The build-up of strain may ultimately limit the size and packing density of boron interstitial clusters that

can be accommodated within the crystal without leading to the formation of extended defects or the breakdown of the lattice structure.

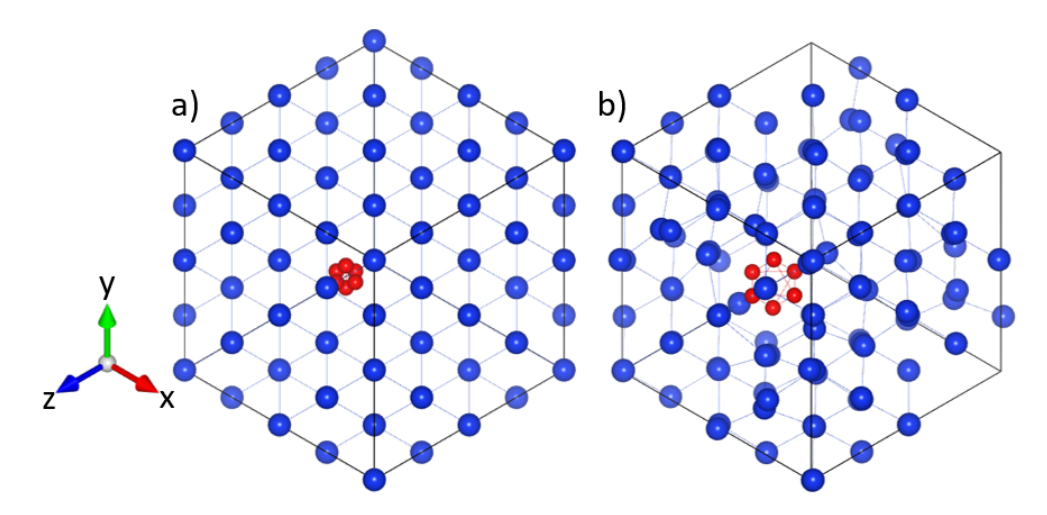


Figure 6.19: Silicon supercell containing an octahedrally shaped  $6B_i^0$  interstitial cluster, viewed along the [111] crystallographic direction. (a) Initial configuration of the cluster before geometry optimisation. (b) Relaxed configuration after geometry optimisation, showing the local distortion and strain induced in the surrounding silicon lattice.

#### 6.3.4 Phonon modes

Following the calculation of formation energies, phonon dispersion simulations were performed for each boron defect configuration to gain insight into their influence on silicon's vibrational properties. The phonon modes associated with these defect configurations were found to be non-dispersive along  $\Gamma$  to X. This invariance of vibrational wavenumber across momentum space indicates that the defect-induced modes are highly localised. This is demonstrated in Figure 6.20, which shows the phonon dispersion of a boron acceptor defect in an 8-atom supercell, calculated using a  $5 \times 5 \times 5$  k-point grid and a plane-wave cutoff energy of 500 eV.

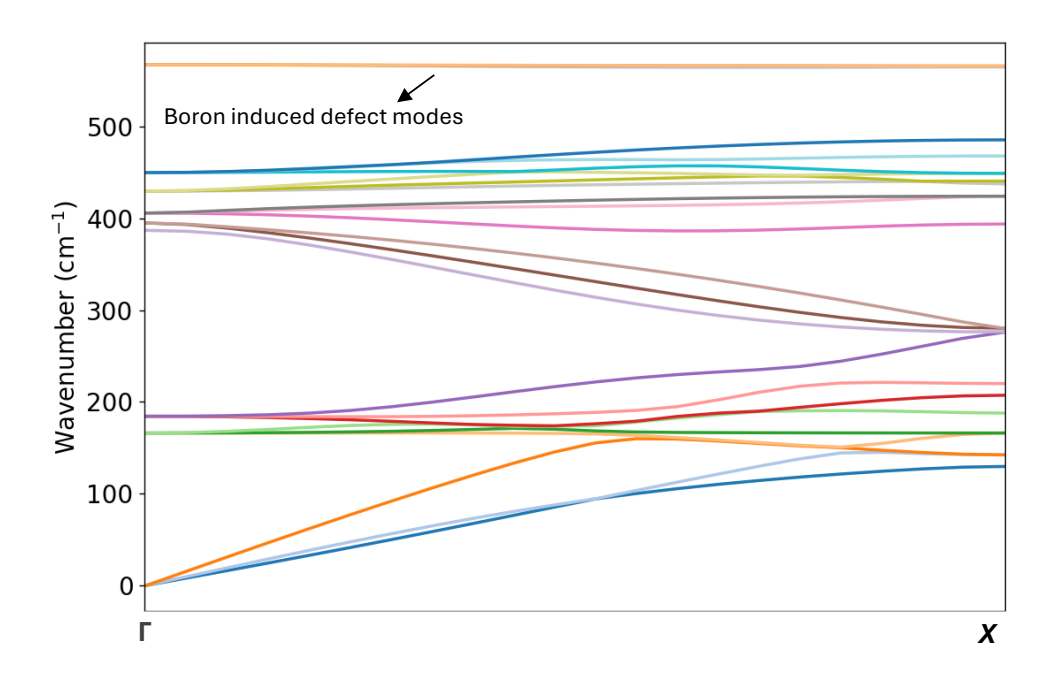


Figure 6.20: Phonon dispersion curves of a single boron acceptor defect in an 8-atom silicon cell along the  $\Gamma \to X$  direction. The phonon branches are folded due to the larger cell size.

The DFT simulated, vibrational wavenumbers for the different point defect configurations are summarised in Table 6.2. For a system with N atoms, there are a total of 3N vibrational modes, consisting of three acoustic and 3(N-1) optical modes. Since boron is lighter than silicon, it only contributes to optical modes rather than acoustic ones. Table 6.2 therefore lists wavenumbers for the  $3N_{\rm B}$  number of highest energy modes for each defect configuration, where  $N_{\rm B}$  is the number of boron atoms in the defect. Note that all three defect-related vibrational modes for the  ${\rm B}^-$  acceptor are degenerate, meaning they occur at the same energy, so only one wavenumber needs to be listed. The mode for  ${\rm B}^-$  is located at 632 cm, which is only slightly higher in energy than the 516  ${\rm B}^-$  optical phonon mode of pure silicon. Because these two modes are so close in energy, the  ${\rm B}^-$  mode cannot explain the much higher energy defect modes, such as the one observed at 1065 cm<sup>-1</sup> in the STEM-EELS measurements. The wavenumber difference between the  ${\rm B}^-$  and silicon optical modes is approximately 116 cm<sup>-1</sup>, which is comparable to the effective energy resolution of the measurements, 12 meV (97 cm<sup>-1</sup>) for on-axis and 14 meV (113 cm<sup>-1</sup>) for off-axis spectra. This limited resolution likely

explains why the  $B^-$  modes were not observed experimentally, despite a measured hole concentration of  $10^{20}$  cm<sup>-3</sup> using the Hall technique. For interstitial boron atoms, a broader and higher range of vibrational wavenumbers are observed, due to replacing the relatively stiff Si-B bonds with lighter mass boron atoms that are only weakly bonded. The maximum wavenumber generally increases with cluster size, provided the packing density is sufficiently high; for example, 840, 937 and 1015 cm<sup>-1</sup> for  $B_i^0$ ,  $2B_i^0$  and  $3B_i^0$  (configuration 1), respectively. The maximum wavenumber (825 cm<sup>-1</sup>) for the  $3B_i^0$  configuration 3 is lower than the other two  $3B_i^0$  configurations and also has a negative frequency. This is attributed to the reduced packing density of the boron interstitials, which effectively decouples the boron atoms from one another and led to an unstable geometry.

The maximum wavenumbers for  $3B_i^0$  configurations 1 and 2 are similar to the 1065 cm<sup>-1</sup> peak wavenumber extracted from STEM-EELS. This suggests that in addition to dopant acceptor ions the specimen also contains interstitial clusters. The broad Gaussian fit 1 in Figure 6.14a and 6.14b, with full-width-at-half-maximum (FWHM) values of 0.017 eV (137 cm<sup>-1</sup>) for the on-axis spectrum and 0.021 eV (169 cm<sup>-1</sup>) for the off-axis spectrum, are consistent with the wide range of defect phonon wavenumbers expected for interstitial boron clusters, although it is likely that there are also multiple cluster sizes and configurations in our sample, which will also contribute to the broadening. A further complication is that not all defect modes will contribute equally to the EELS phonon spectrum. In fact, the oscillator strength depends on  $\mathbf{q} \cdot \mathbf{e}$ , where  $\mathbf{q}$  and  $\mathbf{e}$  are the scattering and phonon polarisation vectors, respectively [250]. Phonon modes with polarisation vector perpendicular to the sample plane cannot therefore be excited by the focussed STEM probe.

Table 6.2: Vibrational wavenumbers of boron point defect configurations in silicon. The defect phonon modes for a B<sup>-</sup> acceptor are triply degenerate.

| Defect type        | Wavenumber $(cm^{-1})$                       |
|--------------------|--|
| B-                 | 632  |
| $B_i^0$            | 532, 770, 840                                |
| $2B_i^0$           | 528, 548, 697,700, 733, 937                  |
| 2B <sup>-</sup>    | 494, 525, 525, 586, 586, 619                 |
| $3B_i^0$ - confi 1 | 511, 515, 529, 563, 612, 708, 720, 949, 1015 |
| $3B_i^0$ - confi 2 | 502, 507, 521, 538, 638, 709, 731, 895, 1212 |
| $3B_i^0$ - confi 3 | 504, 507, 511, 524, 587, 652, 772, 793, 825  |

### 6.4 Conclusion

The combined use of monochromated STEM-EELS and DFT has provided a detailed understanding of how boron incorporation influences the vibrational properties of silicon. Experimentally, momentum-resolved and momentum-integrated EELS spectra revealed the presence of high-energy optical phonon modes in degenerately boron doped silicon that are absent in intrinsic silicon. These boron-induced features were consistently observed around 132 meV in the momentum-resolved EELS spectrum as well as in both on-axis and off-axis geometries, with Gaussian fitting indicating broad phonon peaks characteristic of boron-induced vibrational modes arising from cluster configura-

tions. DFT simulations confirmed that substitutional boron (B<sup>-</sup>) modes lie too close to the intrinsic silicon optical phonon mode, and the interstitial boron atoms and clusters produced a broad range of defect phonon modes with  $3B_i^0$  - confi 1 and  $3B_i^0$  - confi 2 giving rise to the optical phonon modes that are close to the experimentally observed phonon wavenumber (1065 cm<sup>-1</sup>). The boron defect modes for all defect configurations were found to be non-dispersive in reciprocal space, confirming their localised nature. These results indicate that, in degenerately boron doped silicon, in addition to substitutional acceptor dopants, interstitial boron clusters are also present and contribute significantly to the vibrational spectrum, leading to the emergence of high-energy localised optical phonon modes.

# Diffuse scattering analysis: Elemental vs. Boron-Doped Silicon

This chapter presents a comparative analysis of undoped and heavily (degenerate) boron-doped silicon using selected area electron diffraction (SAED) to examine how boron-induced strain and phonon modes influence electron scattering. Diffraction patterns are acquired along [100] and [110] zone axes to reveal zone-specific scattering behaviour, and multislice simulations incorporating both substitutional and interstitial boron cluster configurations are used to interpret the observed changes in scattering intensity distribution. SAED patterns were acquired and simulated at cryogenic temperature to distinguish thermal diffuse scattering and static strain effects. By combining experimental and simulated approaches, the study builds a detailed picture of how boron incorporation perturbs the silicon lattice and modifies its scattering response.

### 7.1 SAED techniques and indexing DPs

Selected area electron diffraction (SAED) technique was employed to obtain the diffraction patterns (DPs) of both degenerate boron-doped silicon (High-B-Si) and elemental silicon (Si). The diffraction patterns of both High-B-Si and Si can be indexed in a manner that identifies high-symmetry zone axes [UVW], which are expected to give rise to

the highest Bragg intensities. To determine the zone axis, the vector cross product of two adjacent Bragg spots near the direct beam was taken, where each spot represents a specific set of crystallographic planes. The indices of the individual diffracted spots are obtained by measuring the distance from the unscattered beam to a diffraction spot and comparing it with the theoretically calculated interplanar spacing  $d_{hkl}$  of the planes of atoms. For instance, in Figure 7.1, which shows the electron diffraction pattern of boron-doped silicon, the interplanar spacing hkl is found by taking the reciprocal of the distance between spots A and C, which measures 2.09 Å. This is then compared to the calculated values for all interplanar spacings that result in non-zero structure factors. Spot A is indexed as the 220 reflection, while spot B is indexed as the  $02\bar{2}$  reflection. The indexing is constrained by the observed angle between these two reflections, which is  $60^{\circ}$  (as shown in Figure 7.1). The indices for the zone axis are then derived by taking the vector cross product of the 220 and  $02\bar{2}$  reflections, yielding the zone axis direction of  $[\bar{1}11]$ . A similar process is followed for the diffraction patterns shown in Figures 7.3 and 7.4, with all reflections indexed in the same manner.

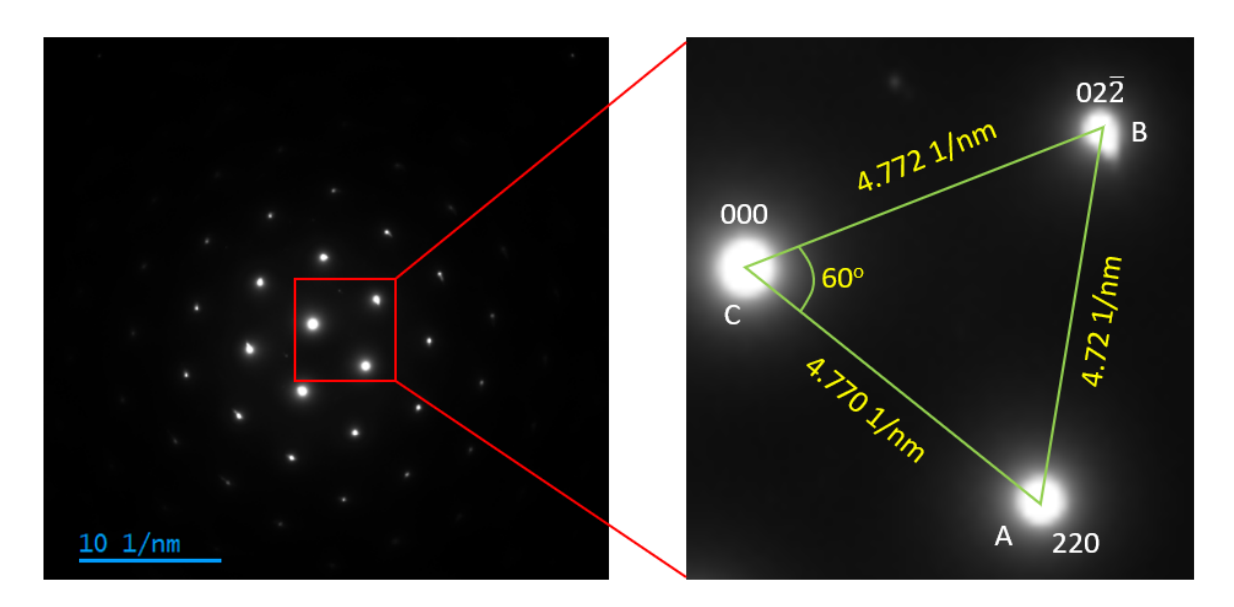


Figure 7.1: Indexing of the electron diffraction pattern from boron doped Si along  $[\bar{1}11]$ .

## 7.2 Effects of strain due to boron doping in silicon at room temperature

The effect of strain due to degenerate boron doping in silicon was analysed through transmission electron microscopy at room temperature. The goal was to better understand how boron doping modifies the structure and phonon scattering behaviour of silicon, particularly in degenerate doping conditions where the doping concentration is high. To do this, selected area diffraction patterns (SADPs) were acquired from both Si and High-B-Si in the [100] and [110] zone axes orientations at 200 kV.

In addition to the experimental measurements, the selected area electron diffraction patterns for both Si and High-B-Si in the [100] and [110] zone axes orientations were simulated using the multislice algorithm in AbTEM software. For the simulation of High-B-Si diffraction patterns, two types of supercells were used: one representing boron acceptor and the other based on the interstitial boron cluster configuration 1  $(3B_i^0$  - confi 1). The boron acceptor system was chosen based on Hall measurements, which confirmed the presence of degenerate doping of acceptor atoms. The inclusion of the  $3\mathrm{B}_{i}^{0}$  – confi 1 in the simulations was motivated by its close correspondence with the actual defect structure present in the sample, as demonstrated in Chapter 6, where this configuration was shown to closely match the localised high energy optical phonon modes observed experimentally in degenerately boron doped silicon. Furthermore, scanning transmission electron microscopy- high angle annular dark field (STEM-HAADF) images were acquired for both Si and High-B-Si samples to complement the diffraction analysis. The HAADF images were acquired at the SuperSTEM laboratory, by Prof Quentin Ramasse. These experimental and simulations observations form part of the results discussed below, specifically focusing on room temperature data.

### 7.2.1 The role of boron concentration in diffuse scattering at low scattering angles

Si and High-B-Si samples were prepared using Focused Ion Beam (FIB). STEM HAADF images were acquired for both Si (Figure 7.2a) and High-B-Si (Figure 7.2b) samples to confirm the absence of FIB artefacts in both samples and to ensure that any changes in diffuse scattering in High-B-Si arise solely due to the presence of boron.

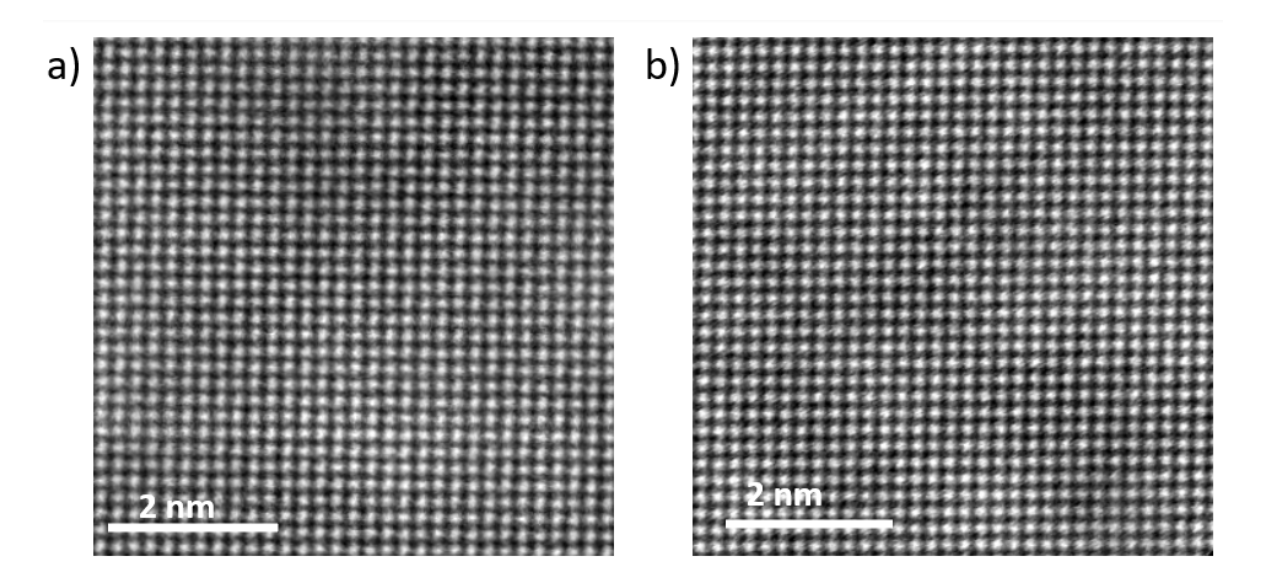


Figure 7.2: STEM HAADF images of (a) Si, and (b) High-B-Si.

Initial examination by STEM-HAADF revealed randomly distributed, bright atoms, which were presumed to be re-deposited Pt atoms from FIB-TEM specimen preparation. These surface atoms were removed using gentle ion-milling with a 500 V voltage for 10 minutes, followed by 300 V for 8 minutes, employing the Fischione nanomill at SuperSTEM. STEM HAADF images after the nanomill show no observable differences between the Si and High-B-Si. One potential reason for the lack of visible difference could be the slightly thicker nature of the High-B-Si sample  $(t/\lambda \sim 0.57$  at 60 kV). The atomic number contrast due to individual boron atoms embedded in a silicon host lattice is less visible for thicker specimens.

The  $t/\lambda$  (thickness-to-inelastic mean free path) ratio was measured using electron en-

ergy loss spectroscopy (EELS), and efforts were made to ensure that the thicknesses of the two samples were closely matched. For the [100] zone axis, the  $t/\lambda$  ratio was 0.59 for elemental silicon (Si) and 0.58 for High-B-Si at 200 kV. For the [110] zone axis, the  $t/\lambda$  ratio was 0.94 for Si and 0.94 for High-B-Si at 200 kV. The selected area diffraction patterns (SADPs) were acquired under identical diffraction conditions. As this is a comparative study, ensuring similar sample thicknesses and consistent experimental conditions was essential to isolate the effects of boron concentration on diffuse scattering. Figures 7.3 and 7.4 shows SADPs of Si and High-B-Si for the [100] and [110] zone axes.

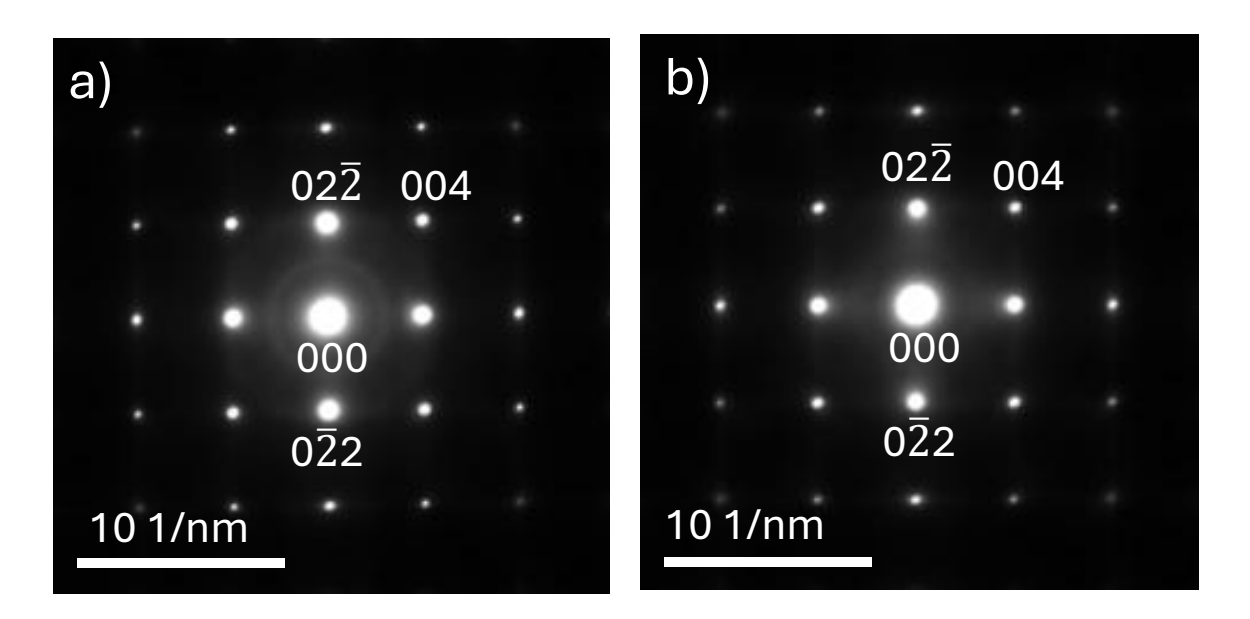


Figure 7.3: Selected Area Electron Diffraction Patterns (SADPs) of silicon (Si) and heavily boron-doped silicon (High-B-Si). (a) [100] zone axis SADP of Si, (b) [100] zone axis SADP of High-B-Si

136

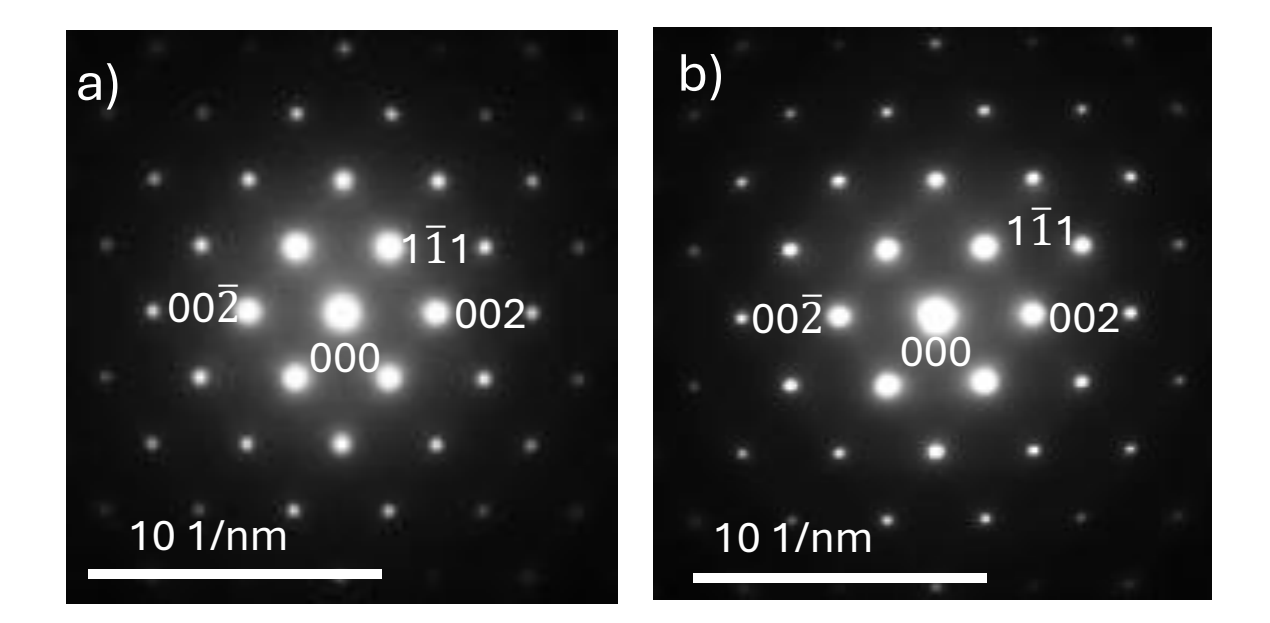


Figure 7.4: Selected Area Electron Diffraction Patterns (SADPs) of silicon (Si) and heavily boron-doped silicon (High-B-Si). (a) [110] zone axis SADP of Si, and (b) [110] zone axis SADP of High-B-Si.

To further analyse the effect of boron doping on low angle scattering, the diffraction patterns are also presented on a logarithmic intensity scale (Figure 7.5). In diffraction patterns, the Bragg reflections are often very intense, while the diffuse scattering and weaker diffraction features can be several orders of magnitude lower in intensity. If a linear intensity scale is used, the strong reflections may dominate, making the weaker features nearly invisible. A logarithmic scale helps to compress this intensity range, allowing both strong and weak features to be observed more clearly.

In the SADPs of Si and High-B-Si (Figure 7.5a and 7.5b), a ring feature is observed around the unscattered beam in the [100] zone axis, which can be attributed to amorphisation of the surface during FIB specimen preparation. This amorphisation is global, resulting in the formation of a ring at low scattering angles. The radius of the ring corresponds to the d-spacing of the [111] plane, approximately 0.308 nm, leading to the conclusion that it is due to amorphisation. The intensity of the ring is however much weaker than the Bragg reflections (see Figure 7.6a).

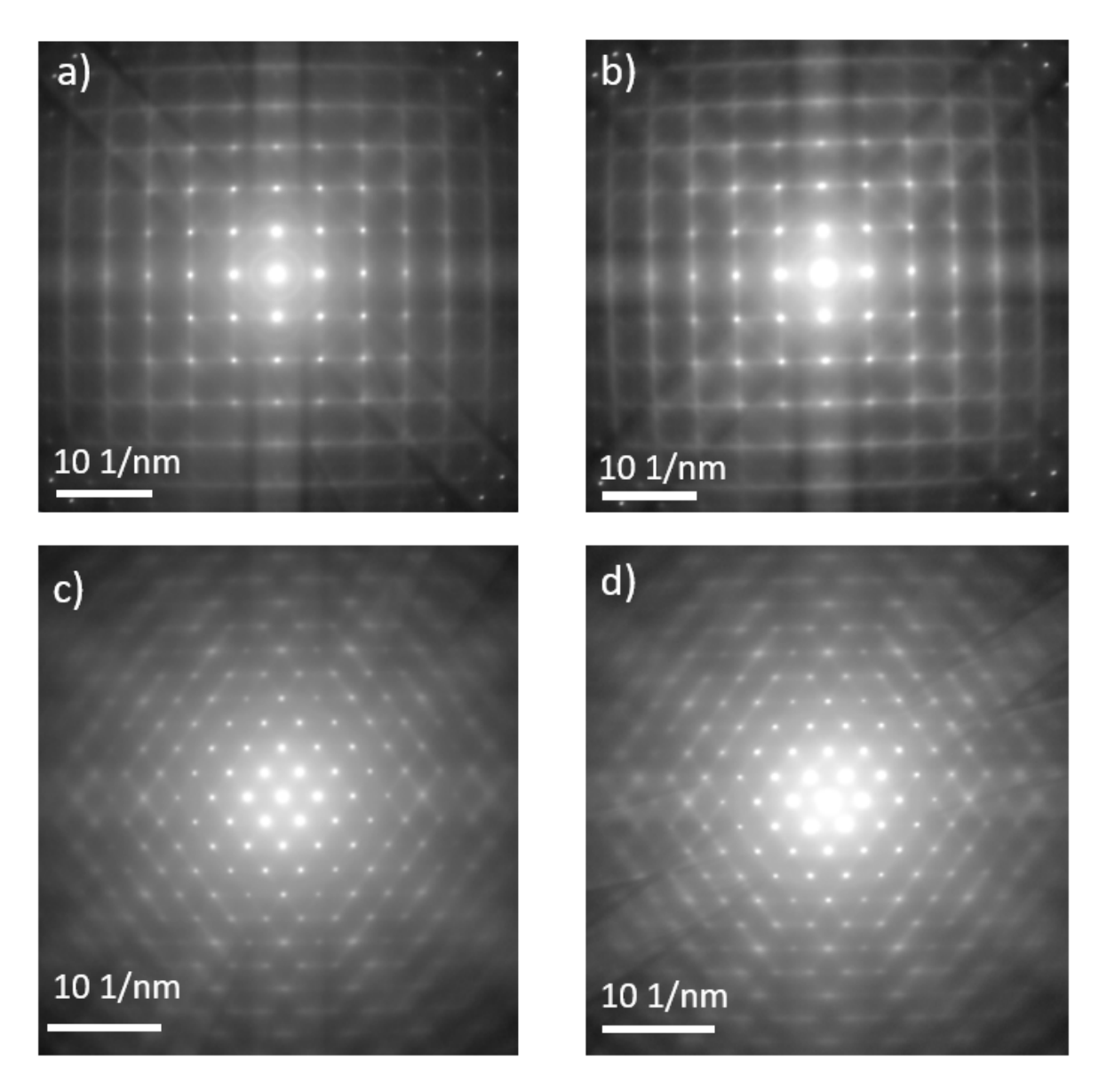


Figure 7.5: Selected Area Electron Diffraction Patterns (SADPs) of silicon (Si) and heavily boron-doped silicon (High-B-Si). (a) [100] zone axis SADP of Si, (b) [100] zone axis SADP of High-B-Si, (c) [110] zone axis SADP of Si, and (d) [110] zone axis SADP of High-B-Si. The SADPs are displayed in a logarithmic intensity scale.

For the [100] zone axis, the SADP of Si (Figure 7.5a) shows sharp Bragg reflections with streaking arising from (largely acoustic) phonon scattering along  $\langle 110 \rangle$  crystallographic directions around the Bragg reflections. For the High-B-Si, the SADP (Figure 7.5b) reveals that the Kikuchi lines are unexpectedly sharper compared to those in Si. Additionally, the streaking along the  $\langle 110 \rangle$  directions is more pronounced and narrower in High-B-Si. Similarly, for the [110] zone axis, the Kikuchi lines in Si (Figure 17.5c)

are well-defined, with sharp, high-contrast bands over a relatively weak diffuse background. In High-B-Si (Figure 7.5d), the Kikuchi lines again appear sharper due to strain-induced lattice distortions.

While boron doping creates strain fields around the dopant atoms, these strain fields are highly localised and inhomogeneous, meaning they do not uniformly distort the crystal lattice on a large scale. Rather than causing a general loss of crystallinity, the strain from boron atoms results in subtle, localised distortions that influence the electron-phonon interaction in a way that enhances the diffuse scattering process. The additional phonons introduced by boron doping, particularly those above silicon's optical mode frequency, and the inhomogeneous lattice strain lead to increased inelastic and incoherent scattering of electrons. These inelastically and incoherently scattered electrons may satisfy Bragg conditions, allowing them to undergo coherent scattering and form sharper Kikuchi lines. In other words, the inhomogeneous strain and the additional phonon modes likely redistributes scattering intensity, enhancing the contrast and sharpness of the Kikuchi lines.

To further investigate the impact of boron doping on the structural and scattering properties of silicon, a comparative analysis of the intensities from the diffraction spots from the [100] and [110] zone axes orientations of Si and H-B-Si was carried out at low scattering angles. For this purpose, 12 SADPs were collected from both Si and High-B-Si samples along the [100] and [110] zone axes at room temperature. As mentioned before, the  $t/\lambda$  ratio for these set of SADPs was similar to maintain consistency in the data analysis. These SADPs were then summed to enhance the scattering features. Intensity profiles were extracted along specific directions near selected diffraction spots in the integrated diffraction patterns. To ensure a direct and meaningful comparison between the SADPs of Si and High-B-Si, a normalisation procedure was applied to account for differences in total intensity. This was performed separately for integrated diffraction patterns acquired along the [100] and [110] zone axes. First, the sum of all pixel intensities was extracted for both Si and High-B-Si SADPs along each zone axis.

A scaling factor was then determined separately for each zone axis as the ratio of the total intensity of the Si SADP to that of the High-B-Si SADP. The total intensity of the High-B-Si SADP was then multiplied by this scaling factor so that the total intensity of High-B-Si matched that of Si for each zone axis independently. This normalisation provides a clearer, relative assessment of how the boron doping affects the scattering behaviour of the material, independent of extrinsic variables (e.g. fluctuations in electron beam current) that could influence the absolute intensity of the diffraction pattern. For the [100] zone axis, the  $0\bar{2}2$  and  $02\bar{2}$  spots were chosen (Figure 7.6a). For the [110] zone axis, the  $00\bar{2}$  and 002 spots were chosen, again with the unscattered beam between them (Figure 7.6b). Since the change in the lattice parameter for High-B-Si is very small, and the diffraction patterns were acquired on two separate days, the diffraction patterns of High-B-Si were calibrated with respect to Si d-spacing between spots to ensure accurate comparisons.

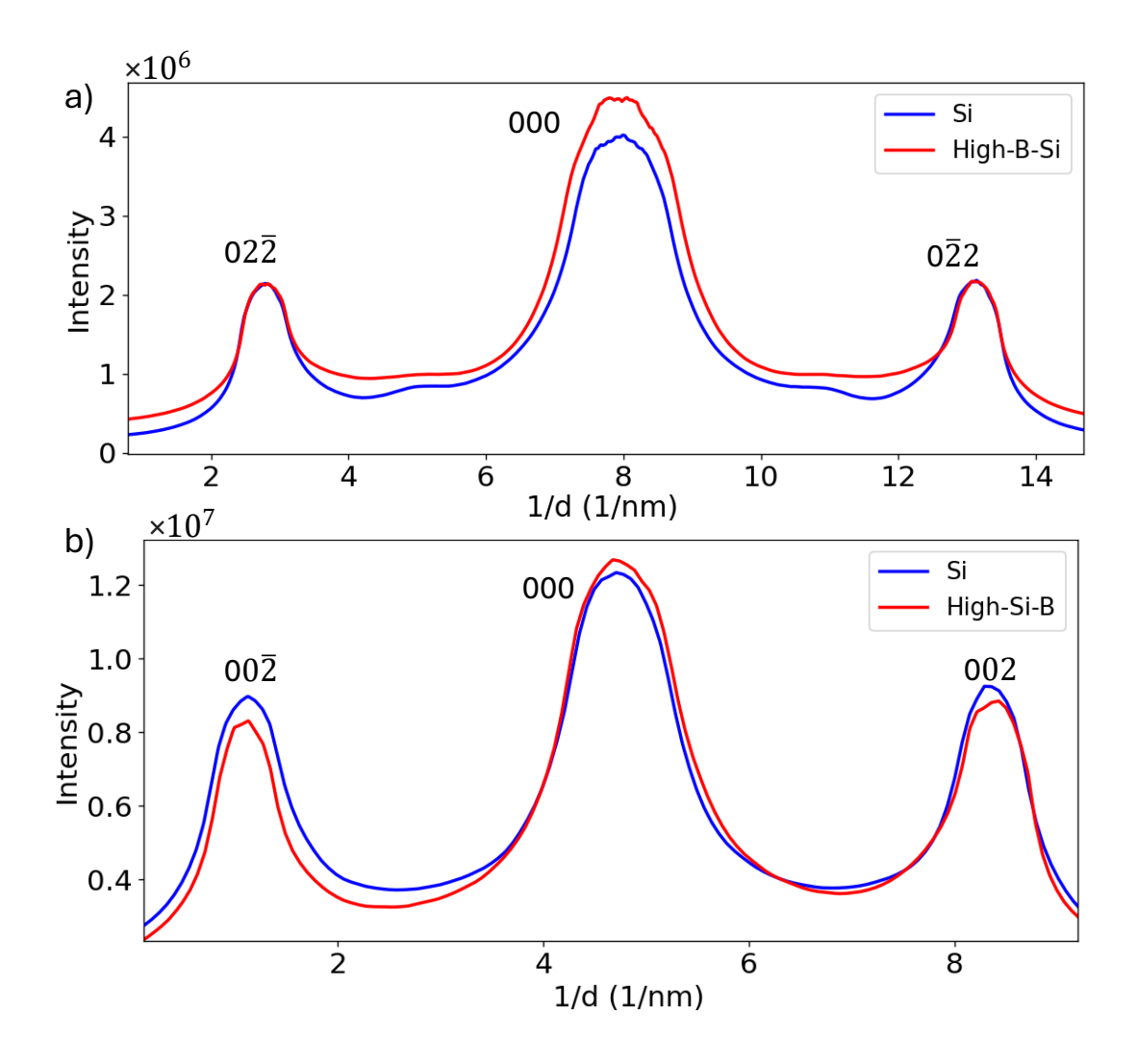


Figure 7.6: Intensity profiles comparison of symmetrical diffraction spots for elemental silicon (Si) and heavily boron-doped silicon (High-B-Si) along the (a) [100] and (b) [110] zone axes.

Since the  $02\overline{2}$  and  $0\overline{2}2$  spots for the [100] zone axis and the  $00\overline{2}$  and 002 spots for the [110] zone axis are symmetric, the analysis focused on one spot from each pair:  $02\overline{2}$  for the [100] zone axis and 002 for the [110] zone axis. These were fitted with a Gaussian function, and the subsequent analysis was based on these fitted parameters. Here, we are essentially examining  $\mathbf{g}$  values close to the Bragg reflections.

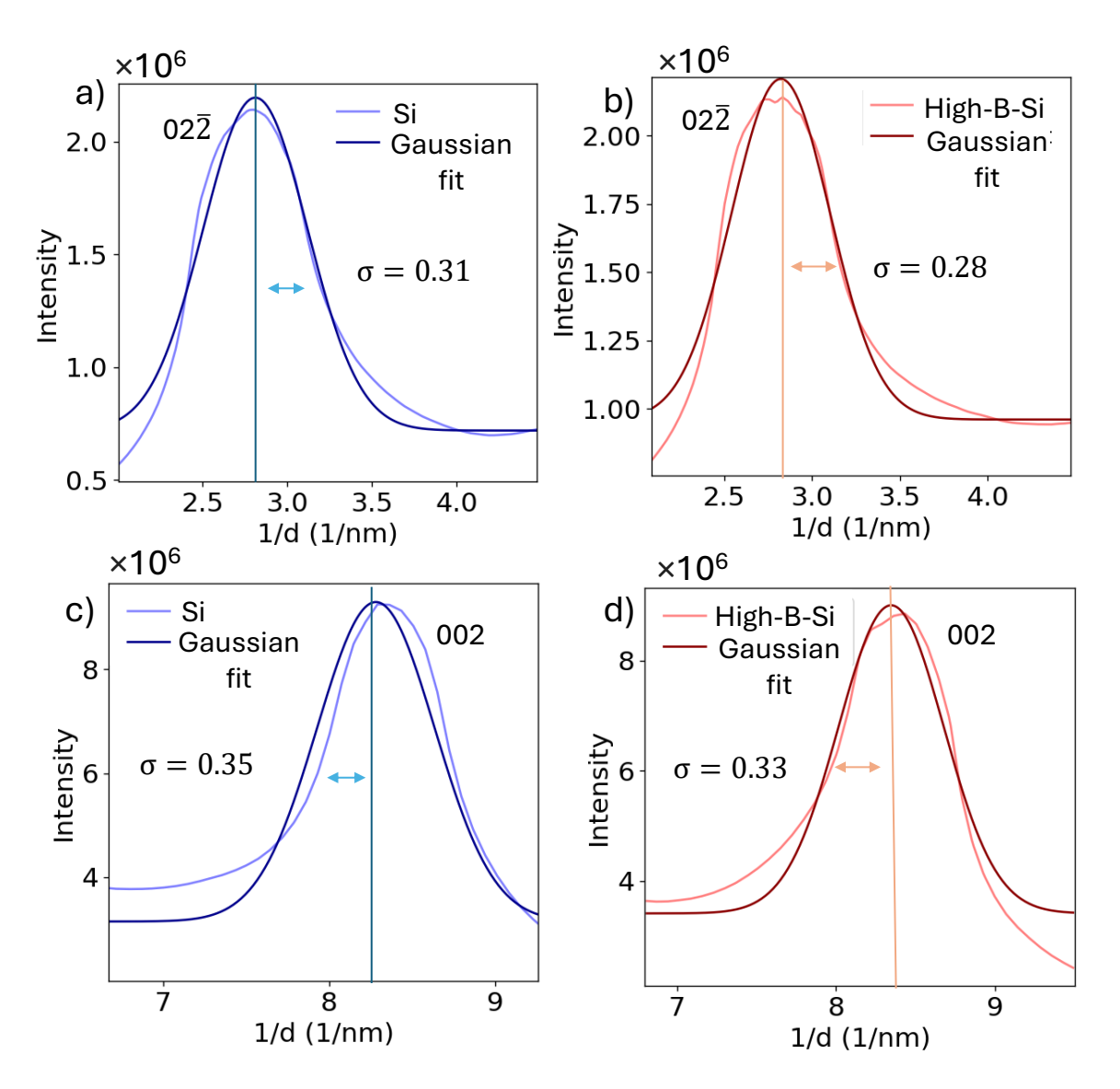


Figure 7.7: Gaussian fit of the diffraction peaks for silicon (Si) and boron-doped silicon (H-B-Si) from the  $02\bar{2}$  diffraction spot for a) the [100] zone axis of silicon and b) the [100] zone axis of boron-doped silicon, and from the 002 diffraction spot for c) the [110] zone axis of silicon and d) the [110] zone axis of boron-doped silicon.

For the  $02\overline{2}$  diffraction spots in the [100] zone axis, Gaussian fitting demonstrates a slight difference in the standard deviation (sigma) values. The Si data exhibits a sigma of 0.31 nm<sup>-1</sup>(Figure 7.7a), while for High-B-Si, the sigma decreases to 0.28 nm<sup>-1</sup>(Figure 7.7b). Similarly, for the 002 diffraction spots in the [110] zone axis, Si shows a sigma of 0.35 nm<sup>-1</sup>(Figure 7.7c), while for High-B-Si, sigma decreases to 0.33 nm<sup>-1</sup>(Figure 7.7d).

These results suggest that, contrary to expectations, the diffraction spots for High-B-Si are not significantly broader than those for Si, indicating that strong diffuse scattering from strain is not a dominant factor. Normally, one would expect a peak broadening with  $1/g^2$  dependency from the long-range displacement field of point defects [148], where  $\mathbf{g}$  represents the deviation from the Bragg condition. This dependency arises because long-range displacement fields from the defect contribute more significantly at lower scattering angles (small  $\mathbf{g}$ ). However, in this case, the observed diffraction broadening does not follow the expected trend, suggesting that the displacement field associated with boron is more localised rather than extended over long ranges. This could explain why the expected strain-induced broadening is not as prominent in the low- $\mathbf{g}$  region, and why the overall diffuse scattering from strain appears to be less significant than anticipated. Additionally, factors such as amorphisation of silicon and the detector point spread function could further obscure the expected scattering trends, particularly at lower scattering angles.

To further assess the influence of degenerate boron doping on low angle scattering, multislice simulations were performed using the AbTEM software. The simulations aimed to replicate the SADPs observed experimentally and to provide insight into how boron incorporation affects electron scattering behaviour. A pristine silicon supercell (Si) containing 512 atoms was used to model the undoped system. For High-B-Si, two supercells were constructed: one with a single boron acceptor (High-B-Si-acc), comprising a total of 512 atoms, and another with an interstitial boron cluster (3B $_i^0$  - confi 1), consisting of 515 atoms. The total cell volume after geometric relaxation for the Si and interstitial boron cluster (High-B-Si-int) systems was 10252 Å $_i^3$ , while the volume for the High-B-Si-acc system was 10055 Å $_i^3$ . For the [100] zone axis, the unit cell length along the beam direction was 21.72 Å for both the Si and High-B-Si-int systems, and 21.58 Å for the High-B-Si-acc system. This was divided by 16 to obtain slice thicknesses of 1.36 Å and 1.35 Å, respectively. Each of these systems was then repeated 20 times along the z-axis, resulting in a total thickness of 43.4 nm for the Si and High-B-Si-int systems, and 43.2 nm for the High-B-Si-acc system. These thicknesses were chosen based on the

 $t/\lambda$  measurements for experimental [100] diffraction patterns (Section 7.2.1). Prior to stacking along the beam direction, the defect-containing supercells (both High-B-Si-int and High-B-Si-acc) were shifted in the x and y directions to produce a more randomised spatial distribution of boron atoms, thereby better representing the disordered nature of real doped systems. This shifting was performed while carefully preserving the tetrahedral bonding geometry of the surrounding silicon lattice, ensuring no unrealistic bond distortions were introduced.

For the [110] zone axis, the slicing must account for the fact that the atomic layers are arranged along the face diagonal direction of the cubic unit cell. The effective length of the supercell along [110] is given by  $\sqrt{2}a$ , where 'a' is the supercell dimension, leading to a diagonal length of 30.72 Å for the Si and High-B-Si-int systems and 30.52 Å for the acceptor system. To ensure that each slice contains exactly one atomic layer, this length is divided by 16, resulting in a slice thickness of 1.92 Å and 1.91 Å, respectively. Each of these systems was then repeated 14 times along the z-axis, resulting in a total thickness of 43 nm for the Si and High-B-Si-int systems, and 42.7 nm for the High-B-Si-acc system. Since the beam direction of [110] zone axis is along the cube face diagonal, re-orienting the supercell would naturally create gaps between adjacent slices. To address this, the multislice simulation duplicates the supercell in regions where gaps appear and then crops it to obtain a cubic supercell with a length of 30.72 Å for for the Si and High-B-Si-int systems and 30.52 Å for the acceptor system. This allows the simulation to reconstruct the potential seamlessly, avoiding artefacts that might arise from physical gaps in the repeated structure. A beam view of  $3B_i^0$ confi 1 (High-B-Si-int) along the [100] and [110] zone axes is shown in Figure 7.8 to illustrate how the AbTEM multislice simulation views the supercell for these specific orientations.

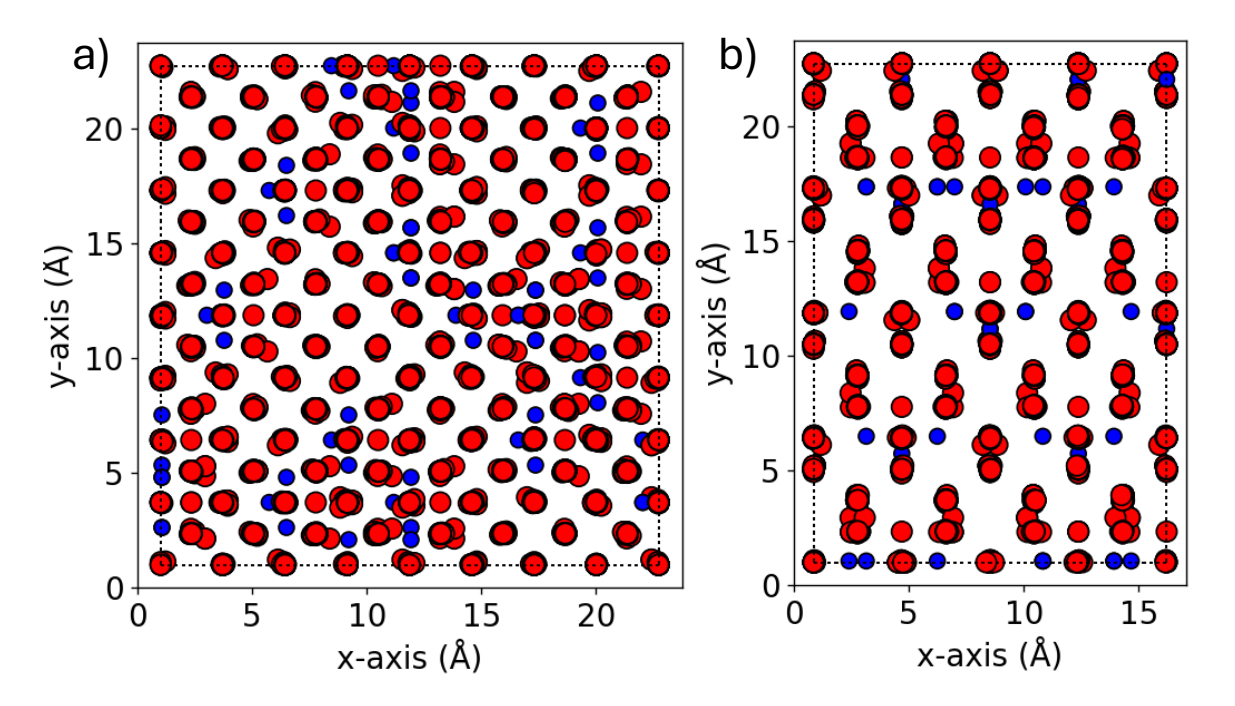


Figure 7.8: Projection view of the interstitial boron cluster system (High-B-Si-int) along the (a) [100], and (b) [110] zone axes. The red atoms represent silicon, and the blue atoms represent boron.

The simulations used an electron beam energy of 200 keV. Atomic thermal vibrations were modelled using the frozen phonon approach, which follows the Einstein model, treating each atom as vibrating independently in a harmonic potential. The standard deviation ( $\sigma$ ) of atomic displacements, representing the root-mean-square displacement (RMSD), was estimated for boron using the formulation described by Soma and Matsuo [251]. For silicon, the RMSD was taken directly from values reported by Muller et al. [252]. Debye temperature for boron was taken from experimental data reported by Slack et al. [253]. All RMSD values were calculated for a temperature of 297 K, yielding 0.076 Å for silicon and 0.0816 Å for boron. The infinite projection method was used to assign the entire potential of each atom to a single slice. Simulations utilised 100 frozen phonon configurations (as determined by the seed value of 1) and employed the Kirkland parametrisation of the atomic scattering factors. The grid points were set to 512. The SADPs for Si and High-B-Si, including both the acceptor and interstitial systems for High-B-Si, were simulated for the [100] and [110] zone axes. Figures 7.9a–c and 7.10a–c display the simulated SADPs for Si, High-B-Si-int, and High-B-Si-acc,

while Figures 7.9d and 7.10d present corresponding the comparative intensity profiles at low scattering angles. These simulations allow a direct comparison of the scattering behaviour between the systems.

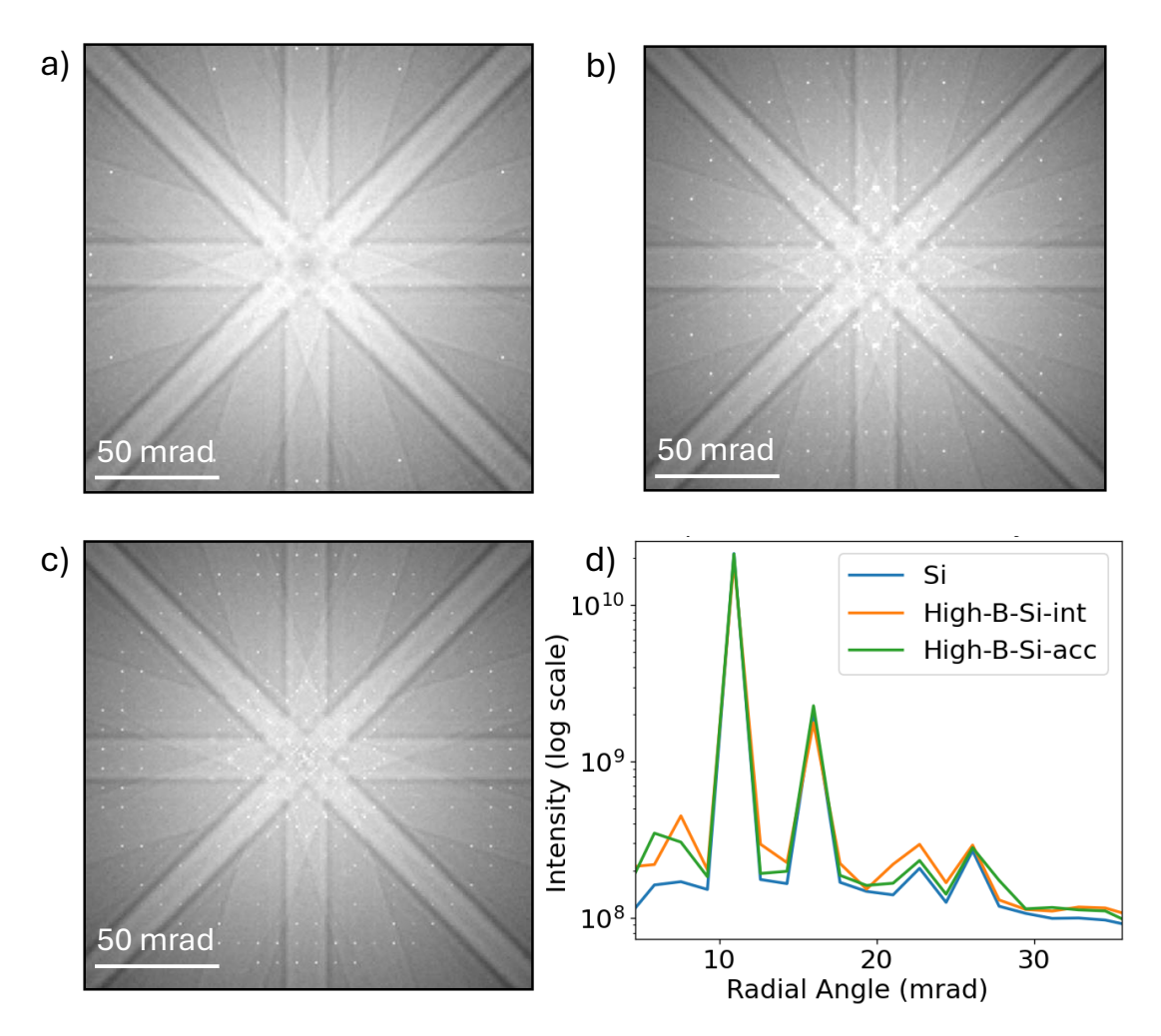


Figure 7.9: Simulated SADPs for (a) Si, (b) High-B-Si-int, and (c) High-B-Si-acc along the [100] zone axis, all displayed on a logarithmic intensity scale. Panel (d) shows the corresponding radial intensity profiles extracted from each pattern, plotted on a logarithmic scale.

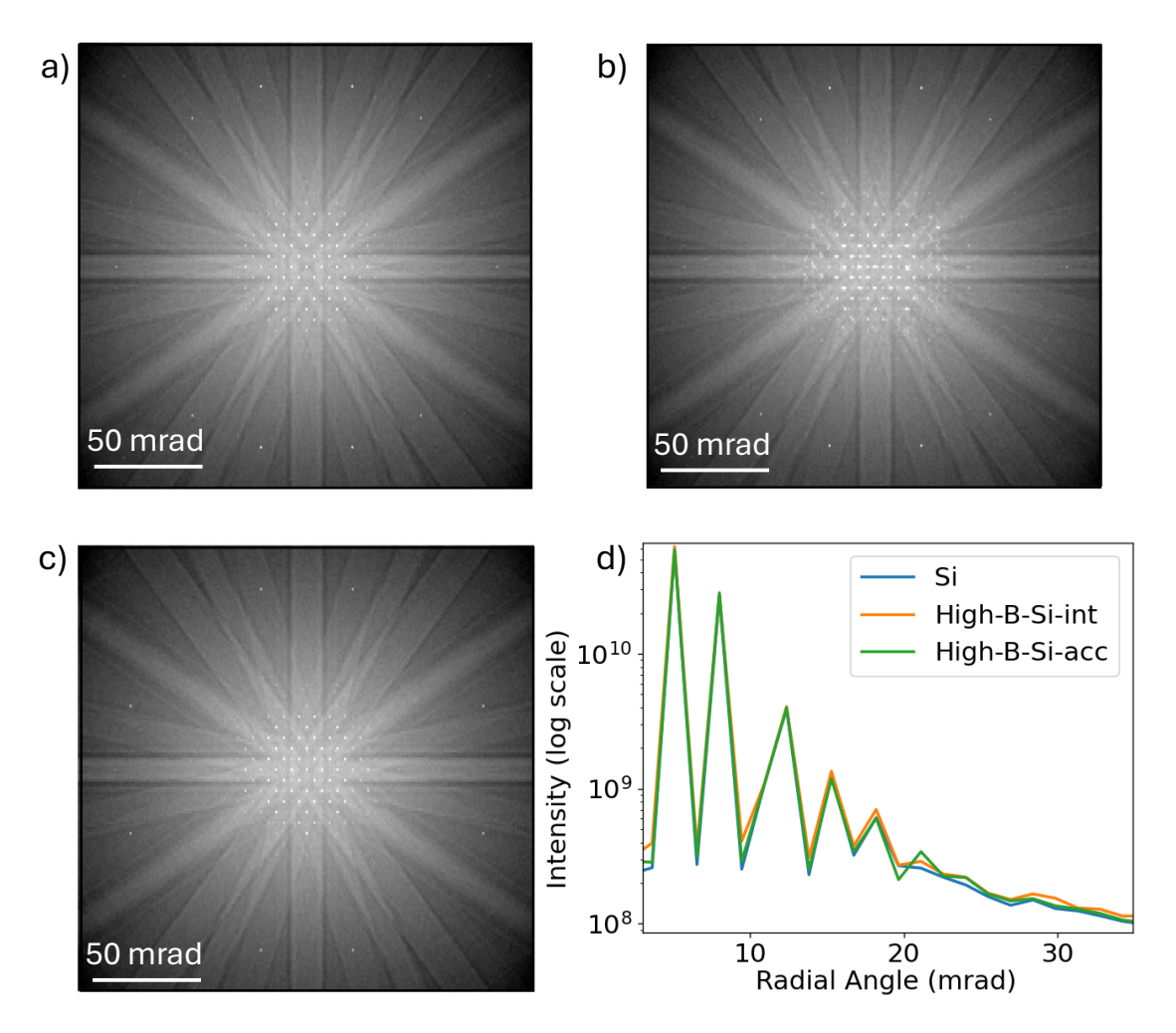


Figure 7.10: Simulated SADPs for (a) Si, (b) High-B-Si-int, and (c) High-B-Si-acc along the [110] zone axis, all displayed on a logarithmic intensity scale. Panel (d) shows the corresponding radial intensity profiles extracted from each pattern, plotted on a logarithmic scale.

The comparison intensity profiles from Figures 7.9d and 7.10d for the [100] and [110] zone axes provide a clearer assessment of how boron doping alters the scattering behaviour of the crystal. Notably, the defect-containing systems exhibit a slightly higher diffuse background intensity at low scattering angles compared to Si. This trend is consistent across both zone axes and supports the experimental SADPs (Figures 7.5b and 7.5d), where High-B-Si demonstrated enhanced low-angle scattering despite the absence of significant peak broadening. The enhancement observed in the simulated patterns may arise from the localised strain fields introduced by the boron defects, which perturb the surrounding lattice and lead to an increase in phonon-mediated

inelastic scattering. These localised distortions redistribute electron scattering intensity without compromising the overall crystallinity, as evidenced by the persistence and sharpness of Kikuchi lines in both experimental and simulated datasets. The agreement between simulation and experiment reinforces the interpretation that inhomogeneous, short-range strain introduced by degenerate doping is responsible for the subtle but measurable increase in diffuse intensity observed at room temperature.

To further support this, individual silicon's atomic displacements for the supercells of High-B-Si-acc and single interstitial (High-B-Si-single-acc) were calculated. Although the three boron interstitial cluster system ( $3B_i^0$ - confi 1) would more accurately capture the strain information, the presence of multiple boron atoms made displacement analysis more complex and less interpretable. Instead, the single interstitial system was used to demonstrate that interstitial boron defects produce more spatially complex strain than acceptor boron. The graph below shows the magnitude of silicon atom displacements as a function of distance from the boron site. Figure 7.11a presents the data for the acceptor boron system, while Figure 7.11b illustrates the data for the interstitial boron system. Each dot on the plot corresponds to a specific magnitude of displacement at a given radial distance, and multiple atoms can share the same magnitude if they experience uniform displacement at a specific radial distance, leading to overlap of some data points in the plot. In the High-B-Si-acc system, the displacement of silicon atoms is more uniform, as indicated by fewer points on the plot, suggesting that many atoms have similar magnitudes of displacement. This implies that the strain field created by the acceptor boron is local and relatively homogeneous. In contrast, the High-B-Si-single- int system exhibits a greater number of points, reflecting more non-uniform displacement of silicon atoms. This indicates that the strain field from interstitial boron is more complex and spatially varied, with silicon atoms experiencing a wider range of magnitudes of displacement. The displacements of silicon atoms in close proximity to the boron interstitial atom are significantly higher compared to the boron acceptor. This increased displacement leads to more strain in the system, as the local distortion of the silicon lattice is more pronounced around the interstitial boron

atoms. This greater strain contributes to the enhanced low angle scattering observed in the simulation. While the displacement magnitudes in the High-B-Si-acc system are lower, they are not negligible. Even this moderate strain contributes to increased scattering at low angles, as observed in the simulated intensity enhancement for the acceptor system. This suggests that both types of defects, acceptors and interstitial clusters, induce measurable lattice strain that redistributes scattering intensity into the low angle region. Hence, the enhanced Kikuchi line intensity observed experimentally in High-B-Si is more likely to arise from the combined strain fields of both defect types as they both are present in the sample.

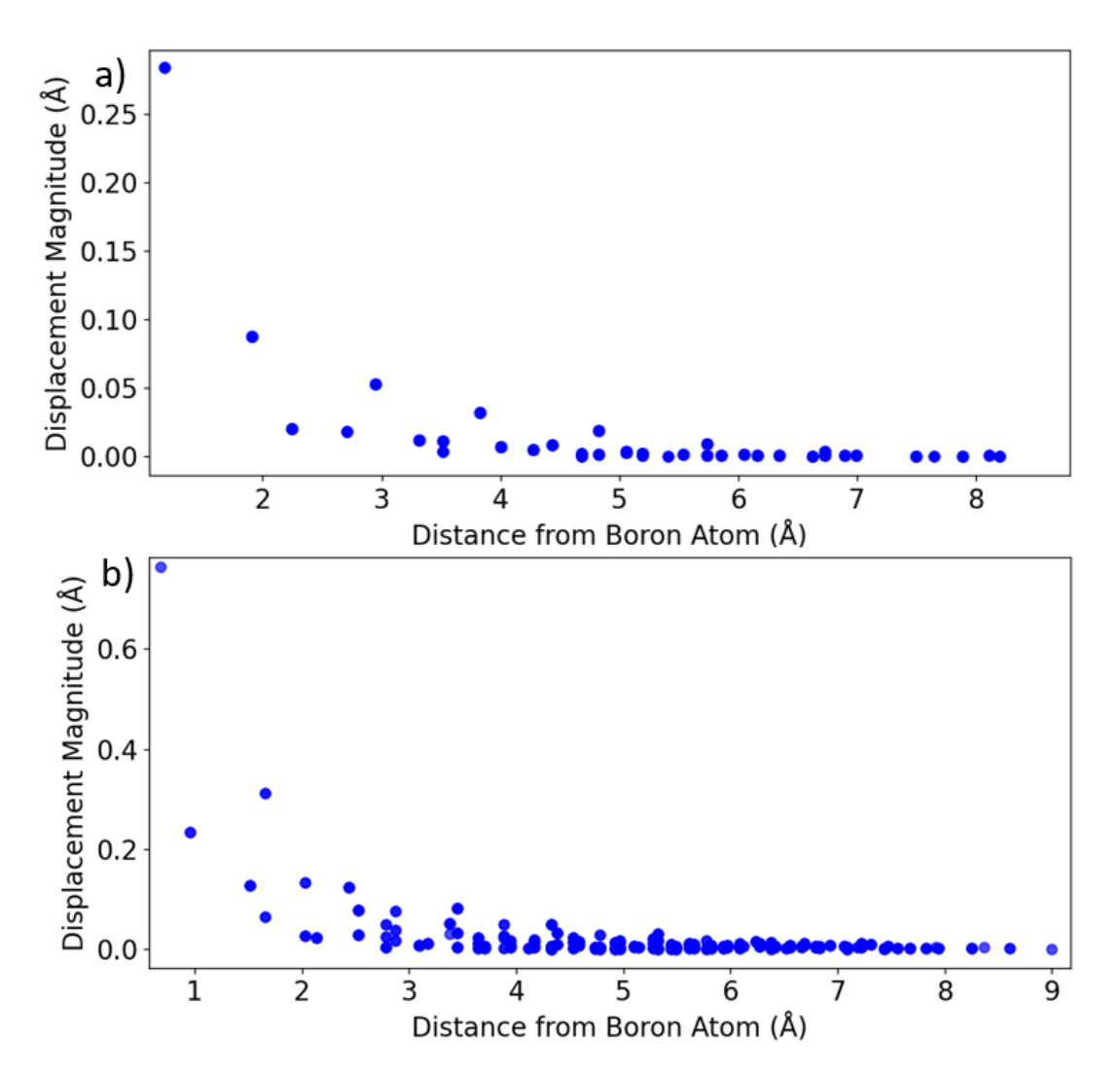


Figure 7.11: Magnitude of silicon atomic displacements as a function of distance from the boron site for a a) single acceptor boron configuration (High-B-Si-acc), and (b) single interstitial boron configuration (High-B-Si-single-int).

### 7.2.2 The role of boron concentration in diffuse scattering at high scattering angles

The scattering behaviour of Si and High-B-Si was further investigated at high scattering angles, extending the analysis from the previous section where low scattering angles were examined. Here, the focus is on understanding the effects of degenerate boron doping on the diffuse scattering at high scattering angles with a combination of experimental data and simulations. From the integrated experimental SADPs, radial intensity profiles were extracted by measuring the intensity from the centre of the SADP along the radial direction. The radial intensity profiles for both Si and High-B-Si were then compared along the [100](Figure 7.12) and [110] (Figure 7.13) zone axes at the high scattering angle region.

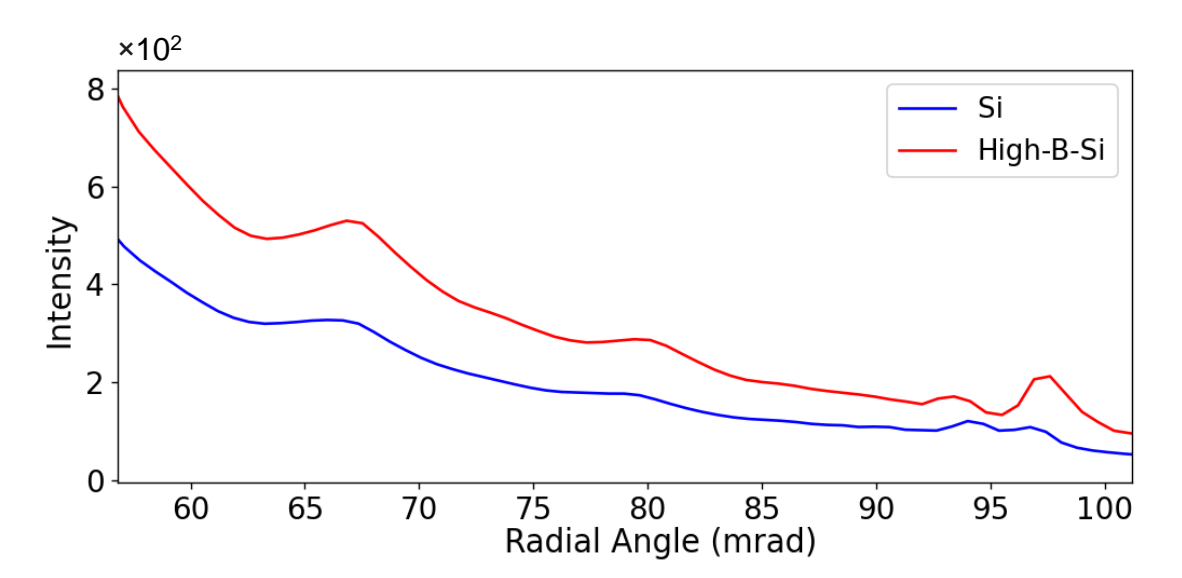


Figure 7.12: Comparison of radial intensity profiles for Si and High-B-Si along the [100] axis.

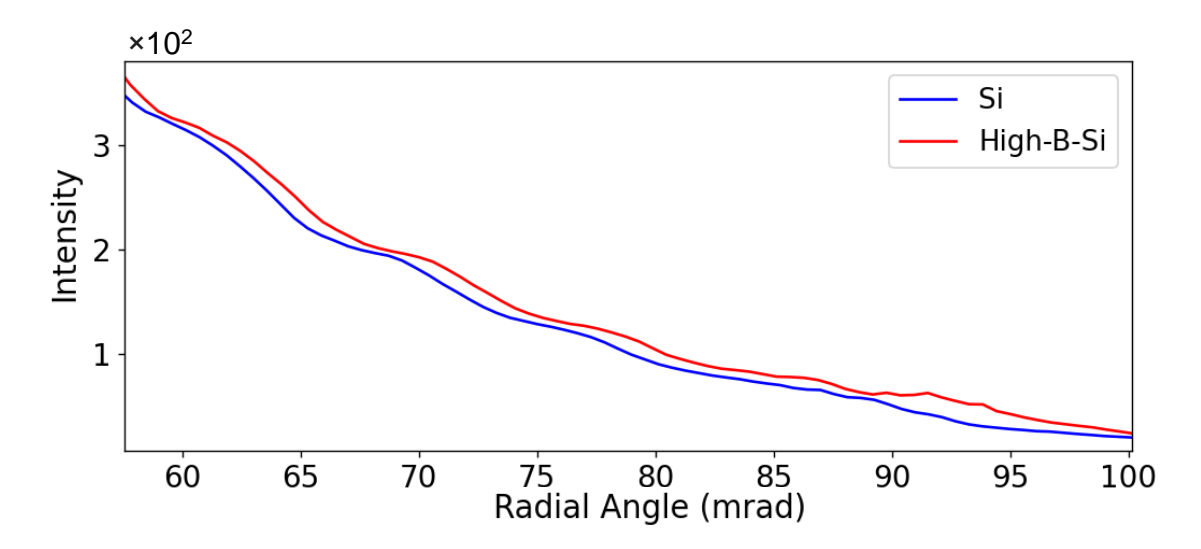


Figure 7.13: Comparison of radial intensity profiles for Si and High-B-Si along [110] zone axis.

The experimental results from Figure 7.12 and Figure 7.13 revealed an anomalous intensity trend for High-B-Si at high scattering angles. Typically, because High-B-Si has a lower atomic number (Z) compared to Si, it would be expected to show lower intensity at high scattering angles than Si due to unscreened Rutherford scattering which is directly proprtional to  $Z^2$ . However, experimental data demonstrated that High-B-Si exhibits enhanced intensity at high scattering angles compared to Si.

This behaviour is likely attributable to strain induced Huang scattering and thermal diffuse scattering (TDS). The presence of boron in the silicon lattice, particularly for a degenerate concentration, creates local strain fields, which scatter more electrons to higher angles. The strain induced scattering from boron atoms could possibly the reason for the enhanced intensity at high scattering angles, as observed experimentally. In addition, as established in the previous chapter, boron incorporation significantly modifies the phonon spectrum, introducing high energy localised optical phonon modes around 132 meV. These defect induced phonon modes provide additional inelastic scattering that redistribute electrons to larger scattering angles. Thus, the observed high angle intensity enhancement in the experimental data is best interpreted as the combined result of localised strain and phonon mediated inelastic scattering. The experimentally

observed anomalous high angle scattering behaviour is consistent with previous studies, such as that by Perovic  $et\ al.$ , which noted similar scattering anomalies in degenerately doped silicon [40].

To further interpret this behaviour, the extracted radial intensity profiles at high scattering angles from frozen phonon multislice simulated SADPs of the three systems, elemental silicon (Si), single boron acceptor (High-B-Si-acc), and three boron interstitial cluster (High-B-Si-int), were compared for the [100] and [110] zone axes, as shown in Figure 7.14.

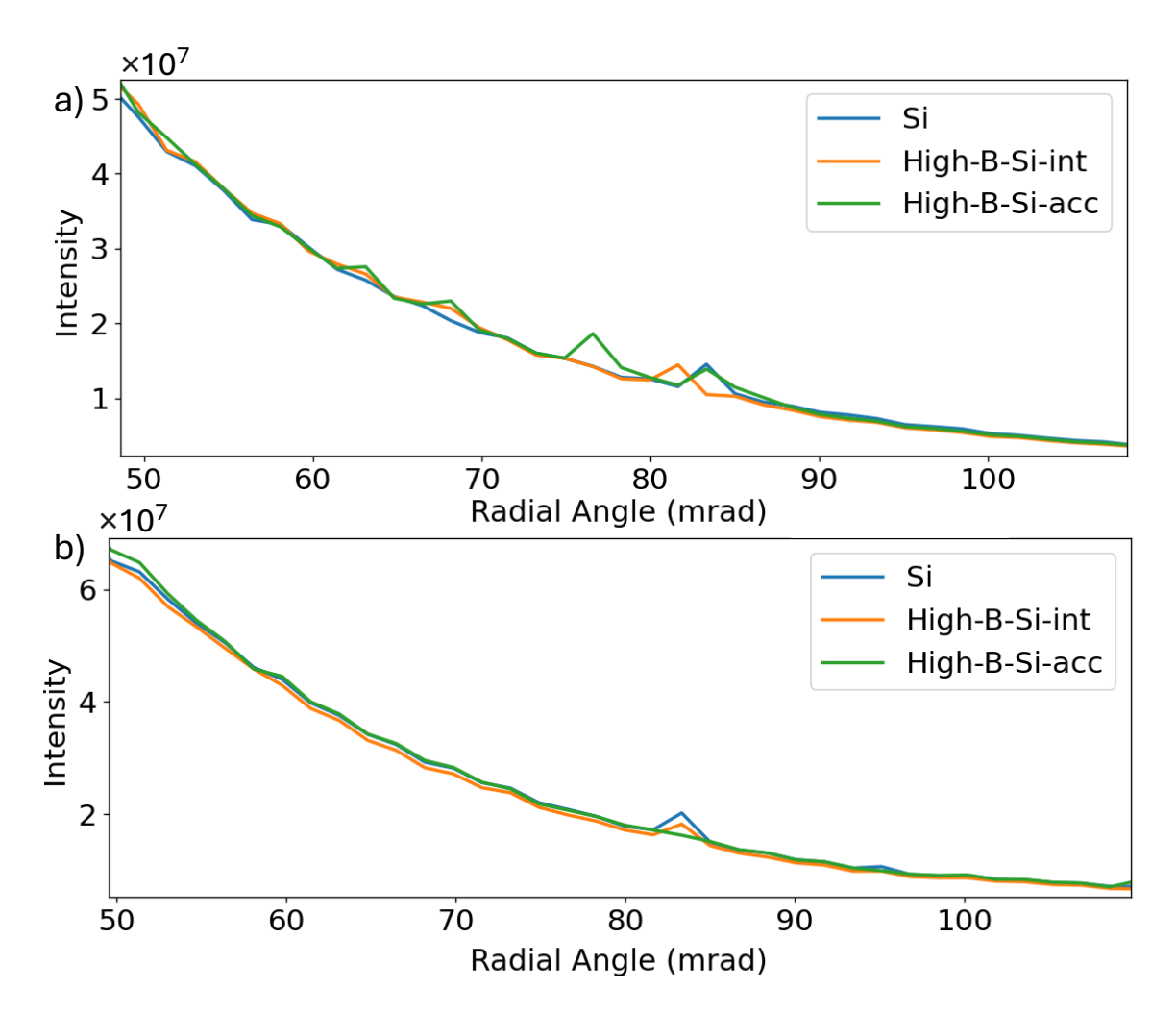


Figure 7.14: Comparison of radial intensity profiles for Si, High-B-Si-acc, and High-B-Si-int, calculated along (a) the [100] and (b) the [110] zone axes. The intensity profiles were extracted from frozen phonon multislice simulations.

The anomalous scattering observed experimentally is not reproduced in the corresponding multislice simulations, as shown in Figures 7.14a and 7.14b. In the simulated data, all systems, Si, High-B-Si-acc, and High-B-Si-int, exhibit nearly identical scattering intensities at high angles for both zone axes. This could be from a fundamental limitation of the frozen phonon multislice model employed in the simulations. The simulations were performed using the frozen phonon approximation based on the Einstein model, wherein atoms undergo independent, uncorrelated Gaussian-distributed displacements defined by their RMSD. While this approach successfully captures basic thermal diffuse scattering, it does not account for the boron induced localised high energy optical phonon modes ( $\sim 132 \text{ meV}$ ) shown in the previous chapter. Therefore, it is likely that the simulations underestimate the high-angle scattering intensity because they do not capture scattering from these localised high energy defect phonon modes. The Gaussian-displacement approach used in the frozen phonon approximation only reflects the mean thermal vibration amplitude and lacks the vibrational complexity of real materials containing defect induced phonon modes. The effect of Huang scattering due to static displacements should however be accounted for in the multislice simulations. Figure 14 nevertheless indicates that its effect is weak compared to thermal vibrations. This is discussed further in Section 1.3.2.

### 7.3 Effects of temperature on diffuse scattering

The anomalous high-angle scattering observed observed experimentally in High-B-Si at room temperature ould be due to a combination of strain due to point defects and phonon interactions. At room temperature, both Huang scattering, caused by local strain fields around defects, and TDS might contribute to the diffuse intensity. However, to determine the primary cause of the enhanced high angle scattering in High-B-Si, it is essential to separate these two effects.

To achieve this, SADPs of High-B-Si were obtained at room temperature and close to liquid nitrogen temperature (-178°C), where TDS is significantly suppressed, and

allowing for a clearer observation of the cause of the anomalous intensity. In parallel, SADPs were simulated using the multislice algorithm for Si, High-B-Si-acc and High-B-Si-int for the experimentally observed temperature, providing an idealised representation of electron scattering with almost no contibutions from thermal vibrations. By comparing the room temperature radial intensity profiles of Si and High-B-Si with the radial intensity of High-B-Si obtained at cryogenic conditions, it is possible to assess how boron induced strain fields influence high angle scattering.

### 7.3.1 Cryogenic temperature calibration using EELS

To ensure the accuracy of the cryogenic temperatures reached during the acquisition of SADPs from High-B-Si, a temperature calibration was performed using EELS measurements of aluminum (Al) based on the method described by Kumar et al. (2024). This approach is based on the principle that the bulk plasmon energy of a metal, particularly Al, exhibits a temperature-dependent shift due to changes in electron density arising from thermal expansion or contraction. As the temperature decreases, the aluminium lattice contracts, increasing electron density and thereby causing a measurable shift in the plasmon energy. This phenomenon allows the plasmon energy to be used as a nanothermometer. The plasmon energy  $E_p(T)$  at a given temperature is related to the reference plasmon energy  $E_p(T_0)$  (taken at  $T_0 = 300$ K) by the free-electron model as [254]:

$$E_p(T) = E_p(T_0) \left[ 1 - \frac{3}{2} f(T) \right],$$
 (7.1)

where f(T) represents the thermal expansion integral. The theoretical f(T) was calculated numerically using empirical expansion coefficients for Al at different temperatures and fitted using the polynomial expansion:

$$f(T) \approx \alpha_0 (T - T_0) + \frac{\alpha_1}{2} (T - T_0)^2 + \frac{\alpha_2}{3} (T - T_0)^3 + \frac{\alpha_3}{4} (T - T_0)^4 + \frac{\alpha_4}{5} (T - T_0)^5$$
(7.2)

where  $\alpha_0 = 2.318 \times 10^{-5} \text{ K}^{-1}$ ,  $\alpha_1 = 2.117 \times 10^{-8} \text{ K}^{-2}$ ,  $\alpha_2 = -1.708 \times 10^{-10} \text{ K}^{-3}$ ,

 $\alpha_3 = -1.247 \times 10^{-12} \text{ K}^{-4}, \ \alpha_4 = -6.187 \times 10^{-15} \text{ K}^{-5}$  are the fitting constants.

To assess the actual temperature of the sample during the cryo-TEM experiment, theoretical values of f(T) were first computed across the relevant cryogenic range using equation 7.2. The EEL spectra (0.1 eV/channel dispersion) of Al were acquired at room temperature and liquid nitrogen cryogenic temperature (-176 °C). In contrast to previous studies [254] that employed the first plasmon peak, the fifth plasmon peak was selected in this study. This is because the plasmon shift is below the energy resolution of our EELS spectrometer. The peak shift however increases linearly for higher order plasmon modes, making it easier to detect. Furthermore, the fifth plasmon peak, being located at a higher energy, is more isolated from ZLP tailing and background artefacts, thus enabling more reliable peak fitting. After performing background subtraction, the fifth plasmon peak was fitted using a Gaussian function to extract the peak maximum. The resulting background-subtracted fifth plasmon peaks at room temperature and cryogenic temperature are shown in Figure 7.15. At room temperature, the extracted energy was 76.4 eV, while at cryogenic temperature, it shifted to 76.9 eV, indicating a clear shift in plasmon energy as expected from lattice contraction of Al. These experimental plasmon energies were then used in the rearranged form of equation 7.1 to calculate empirical values of f(T). The resulting f(T) value at cryogenic temperature was subsequently matched to the theoretical f(T) value derived from equation 7.2, yielding a corresponding actual sample temperature of -152.15 °C. This result confirms a measurable offset between the sample holder temperature and the true sample temperature and validates that the sample reached a cryogenic temperature of -150 °C during diffraction data acquisition.

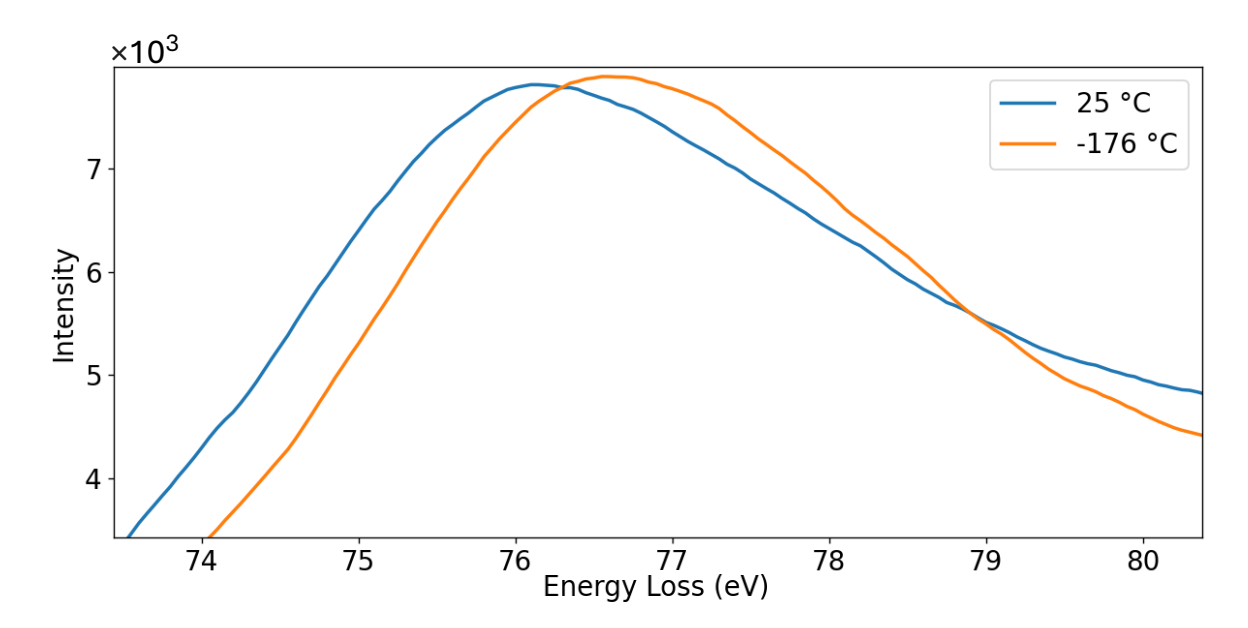


Figure 7.15: Comparison of background-subtracted EELS spectra of the fifth plasmon peak of Al at room temperature (25 °C) and cryogenic temperature (-176 °C)

### 7.3.2 Radial intensity analysis

Radial intensity profiles at high scattering angles were extracted from SADPs acquired along the [100] zone axis for both Si and High-B-Si at room temperature (22°C) and cryogenic temperatures (experimentally observed –178°C for High-B-Si and –179°C for Si; calibrated temperatures –152 °C and –153 °C respectively). The resulting raidal intensity profiles comparison is presented in Figure 7.16.

The High-B-Si sample at room temperature exhibits an enhanced high-angle scattering signal compared to Si (Figure 7.16), due to a combination of TDS and local strain induced Huang scattering. Upon cooling to cryogenic temperatures, the High-B-Si shows a noticeable reduction in intensity. This decrease is consistent with the expected suppression of TDS at low temperatures, as thermal vibrations diminish and phonon populations are significantly reduced. At -152 °C, the phonon energy available to the lattice is approximately 10.4 meV. As a result, phonon modes with energies above this energy are effectively eliminated due to the cooling. This includes the vast majority of optical phonon modes in silicon, as well as any high-energy localised boron induced

defect modes (~132 meV) previously identified in High-B-Si.

The cryogenic High-B-Si profile more closely resembles that of Si, indicating that the majority of the enhanced scattering at room temperature arises from thermally activated inelastic scattering processes rather than static strain alone. Importantly, the Si sample also shows a slight reduction in intensity at cryogenic temperatures, though the magnitude of change is less pronounced due to the absence of dopant related vibrational and strain effects. This observation suggests that the elevated scattering at room temperature is primarily driven by TDS, and that any static strain related scattering from boron defects is either minimal or not detectable.

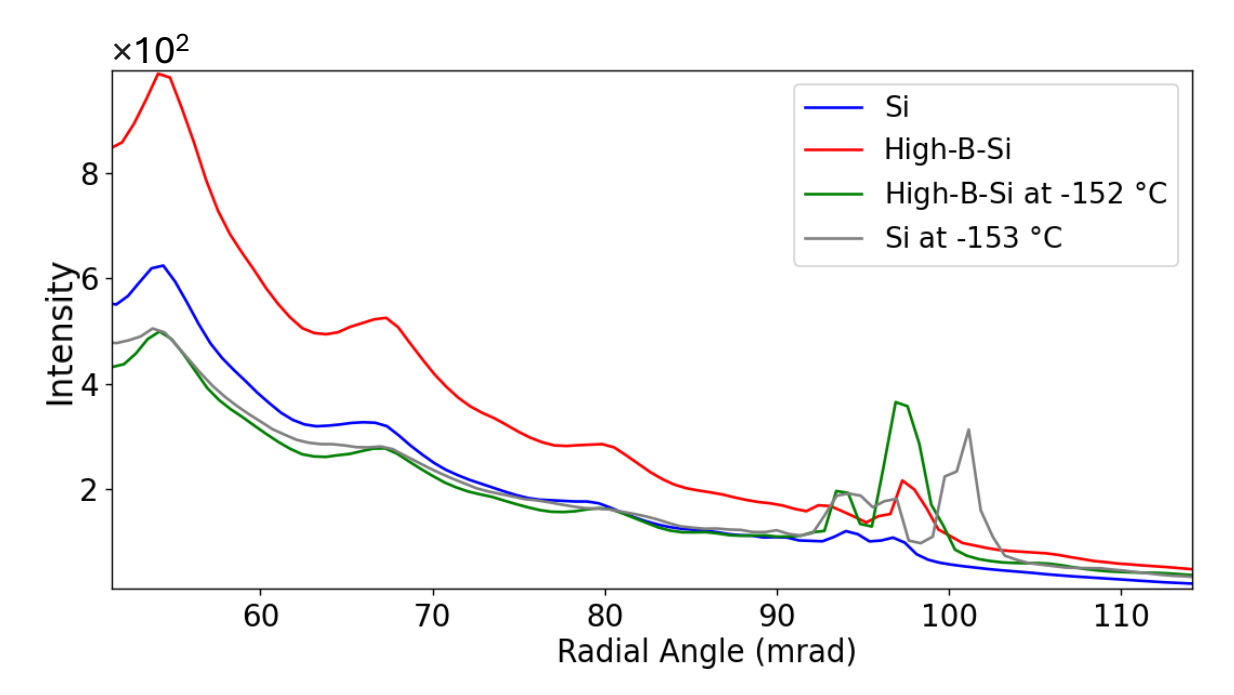


Figure 7.16: Radial intensity profiles extracted from SADPs acquired along the [100] zone axis for Si and High-B-Si at room temperature and cryogenic temperatures.

To further investigate the nature of the high angle scattering enhancement observed experimentally, multislice simulations were performed for Si, High-B-Si-acc, and High-B-Si-int at a cryogenic temperature of -152 °C. In the frozen phonon simulations, the RMSD were calculated to reflect the target temperature of -152 °C, with RMSD values of 0.042 Å for silicon and 0.045 Å for boron, derived using the temperature-scaling relation described by Kirkland [130]:

Wobble = Wobble<sub>0</sub> 
$$\sqrt{\frac{T}{300}}$$
 (7.3)

where Wobble is RMSD of an atom at temperature T, and Wobble<sub>0</sub> is the RMSD at the reference temperature of 300 K. The simulated diffraction patterns and their corresponding radial intensity profiles at -152 °C are presented in Figure 7.17, where Figure 7.17a-c shows the SADPs of Si, High-B-Si-acc, and the High-B-Si-int system. Figure 7.17d provides a direct comparison of the high angle intensity profiles for all of three systems.

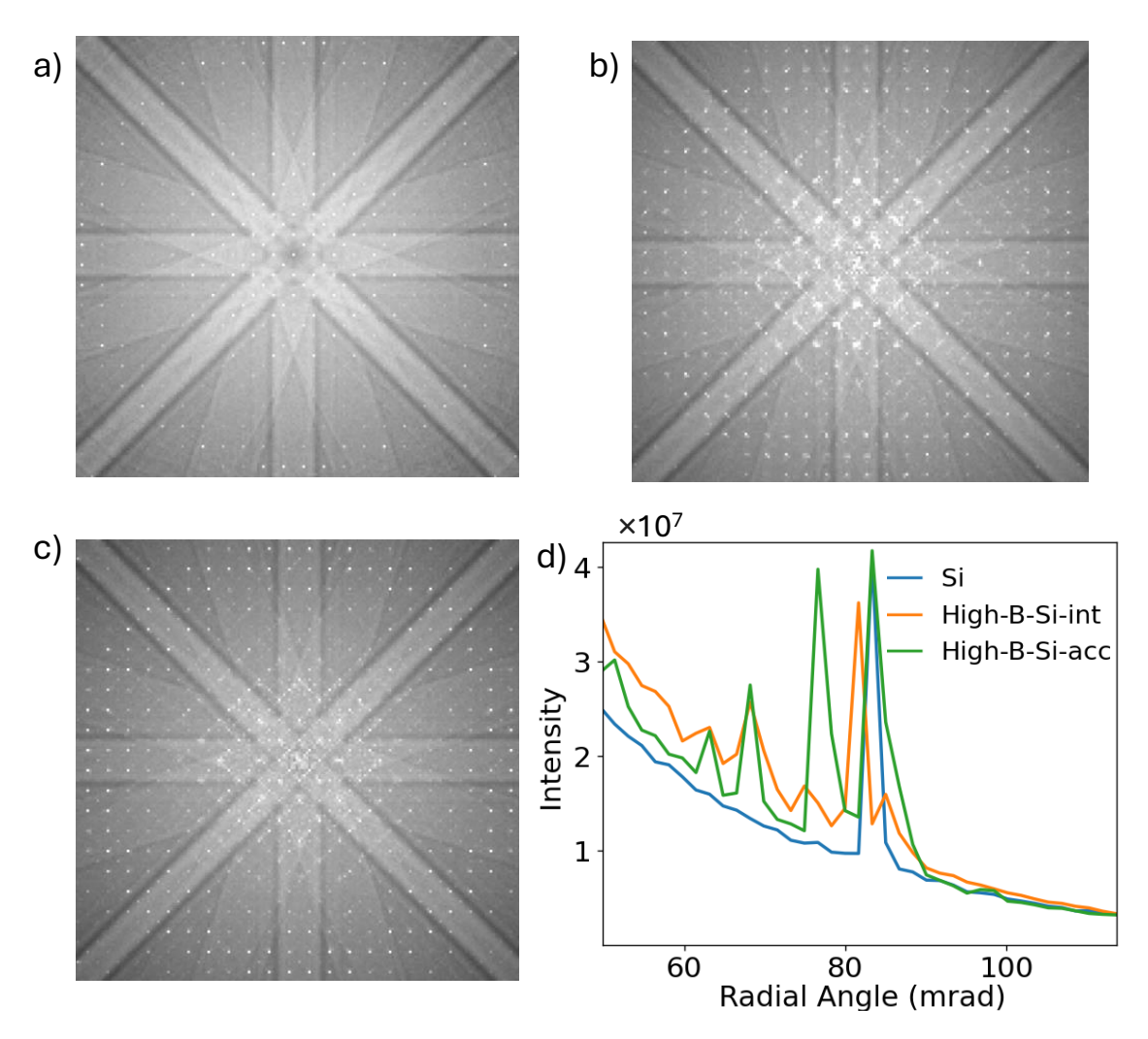


Figure 7.17: Simulated SADPs for (a) Si, (b) High-B-Si-acc, and (c) High-B-Si-int at -152 °C, displayed on a logarithmic intensity scale, with corresponding high-angle radial intensity profiles comparison shown in (d).

The simulation results show a distinct enhancement in high angle scattering for both boron-doped configurations when compared to pure Si (Figure 7.17), even at cryogenic temperatures where TDS is largely suppressed. Among the two boron defect systems, High-B-Si-int displays the highest intensity, followed by High-B-Si-acc, with Si exhibiting the lowest. These trends clearly suggest that static lattice strain due to the boron incorporation causes measurable high angle diffuse scattering, when TDS is significantly reduced. However, this simulation result stands in contrast to the experimental cryogenic data, where the high-angle intensity of High-B-Si closely resembles that of Si. The experimental outcome implies that once thermal vibrations are removed from the defect system, the dominant contribution to high angle scattering diminishes significantly, which means that the primary contributor to this anomaly is TDS.

This contradiction between simulation and experiment raises a key question: why does the experimental cryogenic data not capture this strain induced enhancement as clearly? One likely explanation lies in the spatial distribution of interstitial boron clusters within the actual sample. In the simulations, the cluster defect configuration is densely embedded when repeated along the beam direction. However, in the experimental sample, it is possible that the distribution of interstitial clusters is more sparse and inhomogeneous. As a result, the macroscopic contribution of static strain to diffuse scattering may be diluted, falling below the detection threshold once TDS is suppressed. While the interstitial boron cluster system used in the simulations ( $3B_i^0$ -confi 1) was shown in the previous chapter to closely match the boron induced high-energy phonon modes observed experimentally via EELS, we cannot assert with certainty what the concentration of interstitial clusters in the sample is. Although Hall measurements reported a  $10^{20}~{\rm cm^{-3}}$  hole concentration (Subsection 6.1.1), this corresponds to negatively charged boron acceptor ions, while the interstitial clusters are electrically neutral. It is therefore possible that the interstitial cluster concentration used in multislice simulations is larger than the true value.

To further validate the boron induced strain effects, additional multislice simulations

were performed in static mode for the doped systems, in which the atomic positions were fixed and the RMSD set to zero. In this configuration, atoms do not vibrate thermally, and any diffuse intensity therefore arises solely from static displacements of atoms from their ideal lattice positions around boron defects. Both the acceptor (Figure 7.18a) and interstitial defect (Figure 7.18b) systems show additional diffuse intensity relative to pristine Si under these static conditions. This intensity originates from diffuse scattering of electrons by atoms displaced from their ideal sites due to the local strain field introduced by boron incorporation. Those diffuse scattered electrons then satisfied Bragg conditions, giving rise to Kikuchi-like bands in the simulated diffraction patterns. These bands are a characteristic signature of strain-induced diffuse scattering, distinct from thermal diffuse scattering. In other words, even when atomic motion is completely frozen, the static strain field produced by boron defects redistributes electron intensity away to form kikuchi bands.

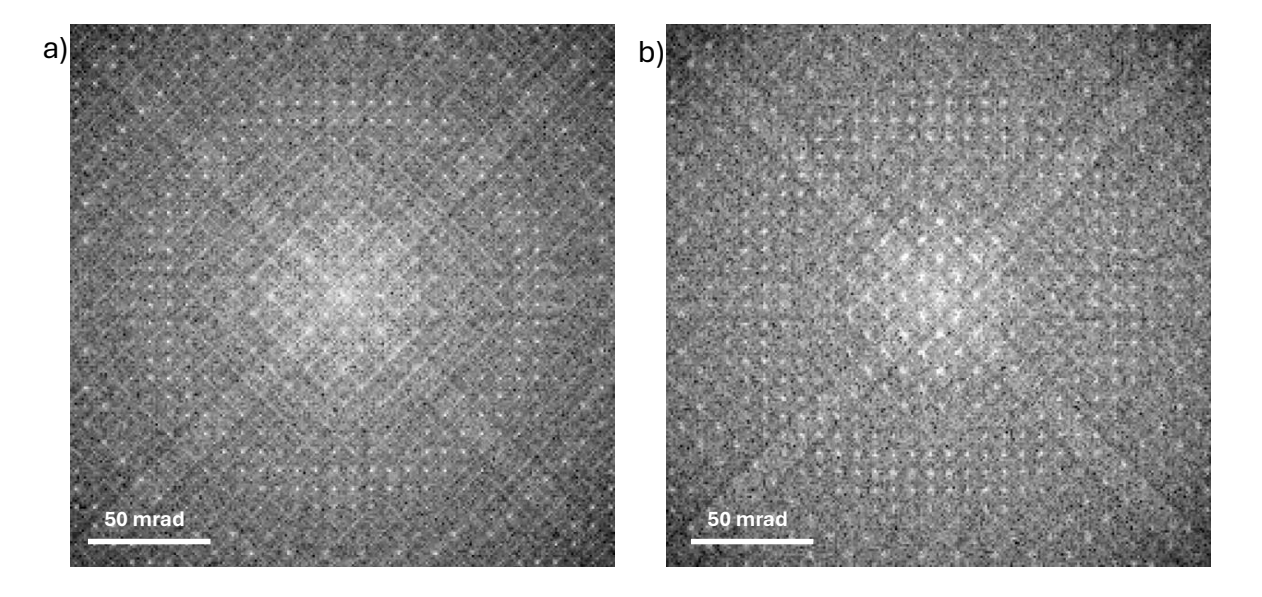


Figure 7.18: Simulated SADPs for (a) High-B-Si-acc, and (b) High-B-Si-int at 0K, displayed on a logarithmic intensity scale.

Thus, the anomalous high angle scattering observed at room temperature in High-B-Si is primarily driven by defect phonon mode TDS, but the underlying strain field, especially from interstitial boron clusters, is nonetheless capable of enhancing scattering if present in sufficient density. The simulations serve as a confirmation that strain effects

are indeed intrinsic to the defect structures, even if their manifestation in practice is modulated by sample-specific factors.

### 7.4 Conclusion

This chapter examined the impact of degenerate boron doping on the scattering behaviour of silicon, combining experimental SADPs and multislice simulations to analyse both low and high angle scattering responses. At low scattering angles, High-B-Si exhibited enhanced diffuse intensity without significant Bragg's peak broadening and sharper Kikuchi lines compared to Si. This was attributed to localised and inhomogeneous strain fields introduced by boron incorporation, which enhances the Kikuchi lines intensity without compromising crystallinity. Simulations supported this interpretation, showing increased low angle scattering for both acceptor and interstitial cluster configurations. At high scattering angles, experimental data at room temperature revealed an anomalous intensity increase in High-B-Si relative to Si. However, this enhancement was not reproduced in the simulations. The likely cause is the omission of boron induced high energy localised phonon modes ( $\sim$ 132 meV) from the frozen phonon model, which only accounts for thermal vibrations via uncorrelated Gaussian displacements. Cryogenic experiments confirmed that the high angle scattering enhancement is primarily due to defect phonon mode TDS as, upon cooling, the diffuse intensity in High-B-Si reduced significantly and closely matched that of Si. Simulations at – 152 °C, however, showed enhanced scattering due to static strain. This discrepancy is attributed to differences in interstitial boron defect density and distribution; simulations use dense defects when repeated along the electron beam direction, whereas the experimental sample may have sparse and spatially variable interstitial clusters. The anomalous diffuse scattering in High-B-Si thus arises from both static strain and boron induced localised high energy phonon modes. While strain plays a role, particularly at low angles and in simulations, its experimental impact is significantly modulated by defect distribution and boron induced vibrational modes.

# Comparative Analysis of Experimental and Theoretical Thermal Diffuse Scattering (TDS) in Silicon

In this chapter, the calculation of first-order thermal diffuse scattering (TDS) intensities for pristine silicon is presented, using phonon eigenvalues and eigenvectors obtained from ab initio density functional theory (DFT) calculations via CASTEP. The aim is to use this theoretical data to estimate TDS contributions along specific high symmetry paths in the first Brillouin zone, and to compare these with experimentally extracted TDS intensities along a particular reflection from selected area electron diffraction patterns (SADP). This forms a bridge between theoretical lattice dynamics and experimentally observed inelastic scattering in transmission electron microscopy (TEM). The broader goal is to establish a methodological basis for integrating phonon simulations with experimental TDS analysis.

### 8.1 Theoretical background

The formulation of first-order TDS used here is adapted from the analytical framework originally developed for X-ray diffraction by Xu and Chiang [84]. Although electron

diffraction involves stronger multiple scattering, and thus typically requires a dynamical theory, the first-order TDS expression remains a valuable approximation when seeking to understand phonon-mediated intensity variations along a specific direction in the reciprocal space.

The calculation of first-order TDS intensity  $I_1(\mathbf{Q})$  for silicon begins with phonon dispersion simulations performed on the two silicon atom primitive unit cell along high symmetry directions in the first Brillouin zone. DFT implemented within CASTEP was used to obtain phonon frequencies  $(\omega_{\mathbf{Q},j})$  and eigenvectors  $(\epsilon_{\mathbf{Q},j,s})$  along the  $\Gamma$ -K path. The resulting phonon dispersion curves are shown in Figures 8.1, illustrating the six phonon branches that arise from two silicon atoms.

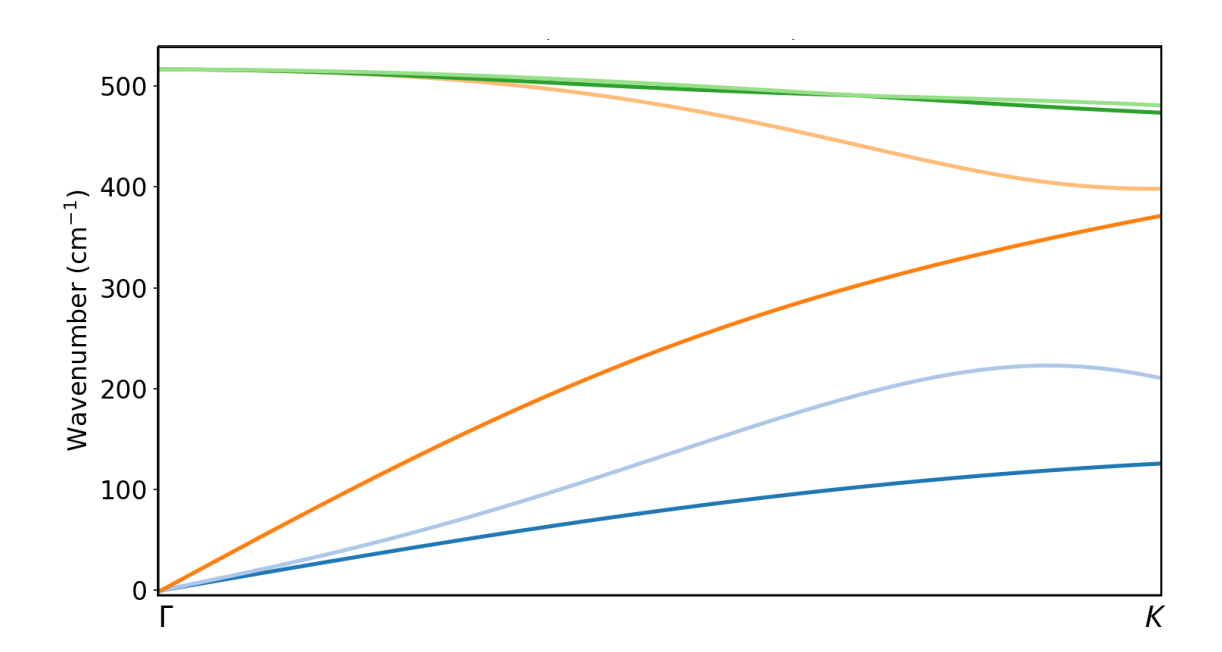


Figure 8.1: Phonon dispersion curves of silicon along  $\Gamma$ -K.

To determine the scattering vector  $\mathbf{Q}$  corresponding to these paths, the reciprocal lattice vectors  $\mathbf{G}_{hkl}$  were calculated using the expression:

$$\mathbf{G}_{hkl} = h\mathbf{a}_1^* + k\mathbf{a}_2^* + l\mathbf{a}_3^*, \tag{8.1}$$

where, h, k and l are the Miller indices of the reflection  $\mathbf{G}$ , and  $\mathbf{a}_1^*$ ,  $\mathbf{a}_2^*$  and  $\mathbf{a}_3^*$  are the reciprocal lattice basis vectors. This was applied to obtain the reciprocal lattice vec-

tors for the 022 reflection, corresponding to the Miller indices (0,2,2). This reflection was selected because it was observed in the experimental electron diffraction pattern of silicon, obtained along the [100] zone axis. Subsequently, the scattering vectors  $\mathbf{Q}$  were determined as vectors extending from the origin (000) in reciprocal space and tracing the direction  $000\rightarrow022$ . These scattering vectors lie along the  $\Gamma$ -K- $\Gamma$  path, consistent with the phonon dispersion calculations, and serve as the scattering vectors at which the first-order TDS intensity was evaluated.

The intensity of first-order TDS at these scattering vectors was then computed using the expression derived and discussed in detail in Chapter 2:

$$I_1(\mathbf{Q}) \propto \frac{\hbar}{2} \sum_{\mathbf{Q},j} \frac{1}{\omega_{\mathbf{Q},j}} \coth\left(\frac{\hbar\omega_{\mathbf{Q},j}}{k_{\mathrm{B}}T}\right) |\mathbf{F}_j(\mathbf{Q})|^2.$$
 (8.2)

where,  $\hbar$  is the reduced Plank's constant, T is the temperature, and  $k_{\rm B}$  is the Boltzmann constant. Here, the summation over j runs from 1 to 6, corresponding to the six phonon branches arising from the two silicon atoms in the primitive cell. The term  $|\mathbf{F}_j(\mathbf{Q})|^2$  denotes the square magnitude of the one-phonon structure factor for mode j, and is given by:

$$|\mathbf{F}_{j}(\mathbf{Q})|^{2} = \sum_{s} \frac{f_{s}(\mathbf{Q})}{\sqrt{m_{s}}} \exp(-M_{s})(\mathbf{Q} \cdot \boldsymbol{\epsilon}_{\mathbf{Q},j,s}) \exp(-i\mathbf{K}_{\mathbf{Q}} \cdot \boldsymbol{\tau}(s)),$$
 (8.3)

where,  $f_s(\mathbf{Q})$  is the atomic scattering factor for electrons associated with atom s (in this case silicon),  $m_s$  is the atomic mass of silicon,  $M_s$  is the Debye-Waller factor for silicon,  $\mathbf{K}_{\mathbf{Q}}$  is the reciprocal lattice vector  $\mathbf{Q}$  folded into the first Brillouin zone,, and  $\tau(s)$  is the atomic basis vector for atom s. The basis vectors used for silicon are  $\tau(1)=(0,0,0)$  for the first atom and  $\tau(2)=(1.36\text{\AA},1.36\text{\AA},1.36\text{\AA})$  for the second atom.

The atomic scattering factors  $f(\mathbf{Q})$  for silicon were computed using the Kirkland empirical parameterisation [130], which provides an analytic expression for the electron scattering amplitude as a function of scattering vector. Since the scattering amplitude depends on the relativistic electron wavelength, and consequently on the accelerating voltage of the electron beam, a scaling factor was applied to adjust for the specific

experimental conditions. This scaling factor, e=1.3914, arises from the ratio of the relativistic electron mass m at 200 kV accelerating voltage to the rest mass  $m_0$ , effectively correcting the scattering amplitude to reflect the increased electron momentum. Thus, the Kirkland formula for the atomic scattering factor was multiplied by this factor e to obtain  $f(\mathbf{Q})$  values appropriate for the 200 keV electron beam used in the experiments. While the Kirkland formula itself is detailed in Chapter 2, this relativistic correction factor is an additional empirical scaling applied in the current calculations to enhance accuracy as relativistic effects are significant at high accelerating voltage and must be accounted for to precisely model scattering behaviour.

The Debye-Waller factor  $M_s$ , which accounts for the attenuation of the scattering amplitude due to thermal vibrations in silicon, was calculated using the expression:

$$M_s = \frac{\mathbf{Q}^2}{12m_s} \sum_{\mathbf{k},j} |a_{\mathbf{k},j}|^2 |\boldsymbol{\epsilon}_{\mathbf{k},j,s}|^2, \tag{8.4}$$

Where,  $|a_{\mathbf{k},j}|^2$  is the square amplitudes of each phonon mode at a given wavevector  $\mathbf{k}$ , and is given by:

$$|a_{\mathbf{k},j}|^2 = \frac{\hbar}{\omega_{\mathbf{Q},j}} \coth\left(\frac{\hbar\omega_{\mathbf{Q},j}}{k_{\mathrm{B}}T}\right)$$
 (8.5)

The squared phonon eigenvector magnitudes in equation 8.4,  $|\epsilon_{\mathbf{k},j,s}|^2$ , were extracted directly from CASTEP. Due to the symmetry and mass equivalence of the two atoms, the eigenvector contributions are equally partitioned, with each atom contributing 0.5 to the total normalised eigenvector magnitude for each mode and wavevector, satisfying the normalisation condition:

$$\sum_{s=1}^{2} |\boldsymbol{\epsilon}_{\mathbf{k},j,s}|^2 = 1 \tag{8.6}$$

This framework combines the lattice dynamical information from CASTEP with scattering theory to compute theoretical first-order TDS intensities at reciprocal lattice vectors relevant to the experiment.

### 8.1.1 TDS intensity analysis at room temperature

TDS intensities were experimentally extracted from SADP of silicon acquired along the [100] zone axis at room temperature with  $t/\lambda$  ratio of 0.59. To quantify TDS intensity near the 022 reflections, line profiles were extracted along the  $\langle 110 \rangle$  crystallographic directions adjacent to these Bragg spots. Specifically, eight line profiles were extracted symmetrically around the 022 reflections. Each line profile traces the variation of scattered intensity as a function of scattering vector magnitude Q, centred near the 022 reflection. The decision to collect eight line profiles arises from the practical challenge of achieving perfect alignment to the [100] zone axis. Minor misalignments or slight deviations from the ideal zone axis can significantly influence the measured diffraction intensities and TDS features. By extracting multiple datasets with small variations, these minor deviations are effectively averaged out, thereby minimising systematic errors associated with slight zone axis misalignment. Figure 8.2 illustrates the [100] zone axis diffraction pattern, with arrows indicating the directions along which these line profiles were taken.

Alternative reflections located further from the central beam, such as 044, can be considered; however, the intensity of these reflections will be lower. To ensure quantitative reliability of the extracted TDS profiles, the 022 reflections situated close enough to the central beam were selected for better accuracy.

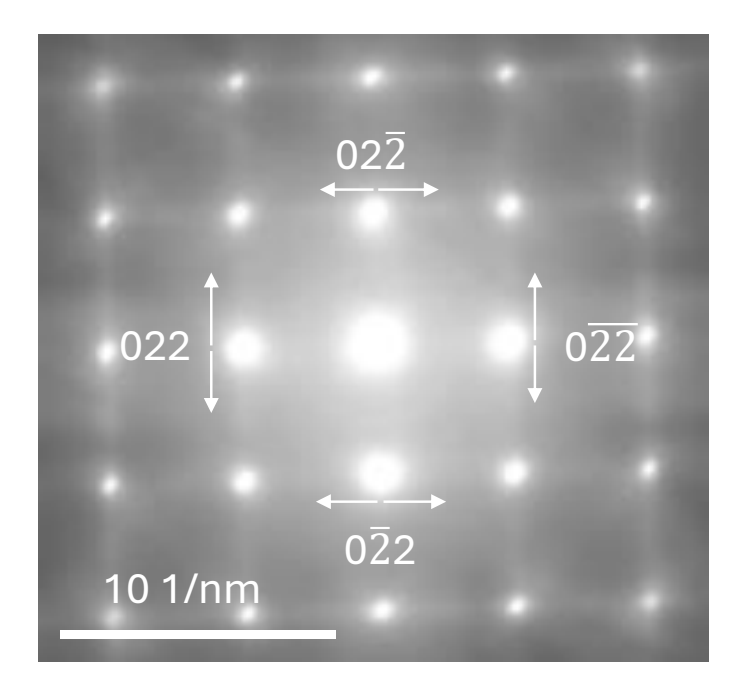


Figure 8.2: SADP of silicon acquired along the [100] zone axis at room temperature.

At each discrete scattering vector  $\mathbf{Q}$ , along these profiles, the experimental intensity values were averaged across the eight line profiles to obtain the mean intensity  $\mathbf{I}_{\exp}(\mathbf{Q}_i)$ . The standard deviation  $\sigma$  was also calculated at each point, providing an empirical estimate of the experimental uncertainty associated with intensity measurements. This variance reflects local fluctuations, thus enabling statistically meaningful error bars for subsequent analysis. Prior to comparison with theoretical data, both the mean experimental intensities and the corresponding theoretical first-order TDS intensities were normalised. Normalisation involved scaling each dataset such that their maximum intensity was unity, thereby preserving relative variations while removing absolute scale discrepancies caused by experimental conditions such as exposure time, detector sensitivity, and beam current. The theoretical first-order TDS intensity  $(\mathbf{I}_{\exp}(\mathbf{Q}_i))$  calculated at room temperature (300 K) and the mean experimental intensity  $(\mathbf{I}_{\exp}(\mathbf{Q}_i))$  were then plotted together as a function of the scattering vector magnitude Q (Figure 8.3).

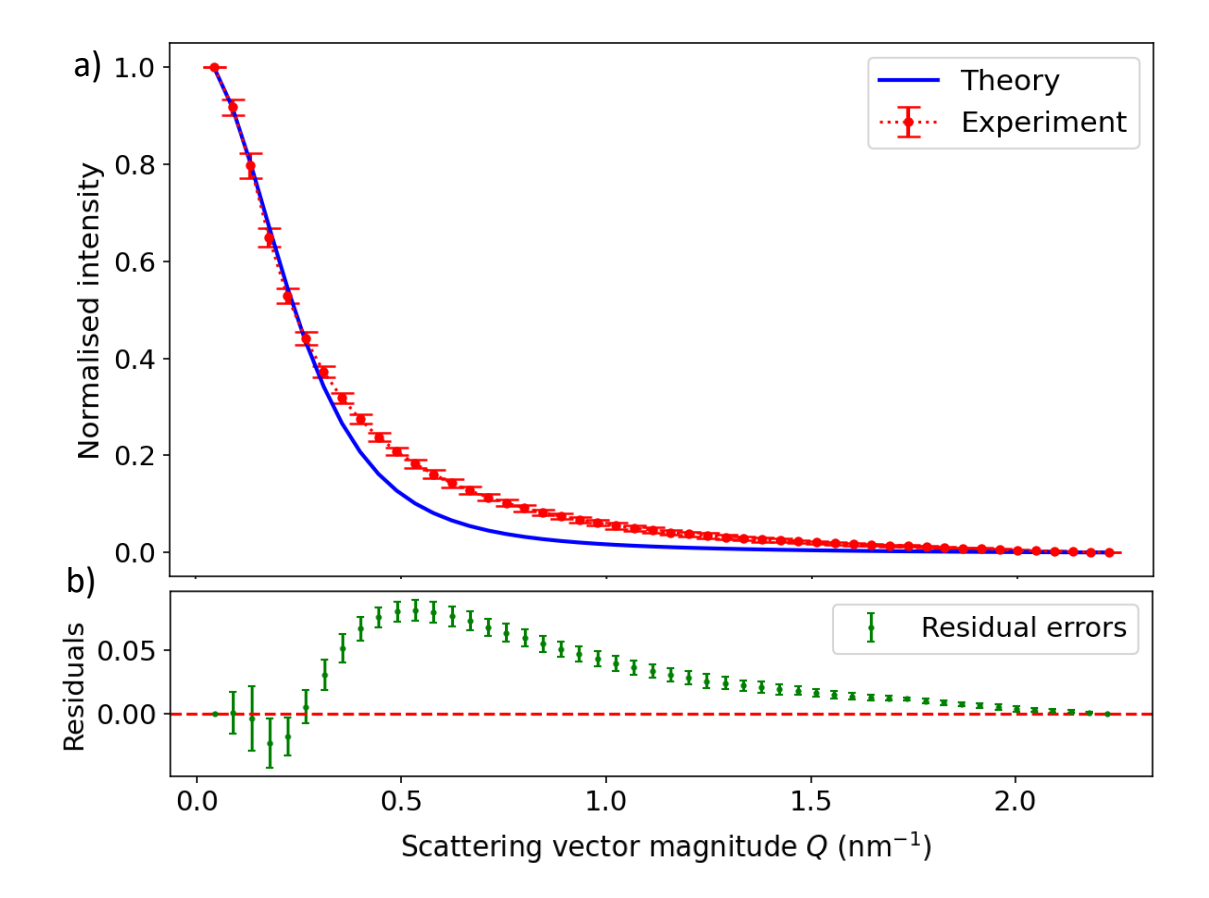


Figure 8.3: (a) Comparison of the theoretical first-order TDS intensity and mean experimental TDS intensity as a function of scattering vector magnitude Q with error bars of  $\sigma$ , and (b) Residuals between experimental and first-order TDS intensities.

The figure presents the mean experimental TDS intensity, plotted with error bars representing one standard deviation ( $\sigma$ ) calculated from the eight line profiles, alongside the theoretical first-order TDS intensity. The comparison shown in Figure 8.3a reveals that while the theoretical and experimental TDS intensities generally follow the same overall pattern as the scattering vector  $\mathbf{Q}$  varies, the experimental intensities are noticeably higher than the theory predicts between approximately 0.3 and 1.8 nm<sup>-1</sup>. This suggests that there are additional contributions to the scattering in the experiment that the current theoretical model does not capture.

To examine these discrepancies in more detail, a residual analysis was performed in which the difference between the mean experimental intensity and uncorrected theoretical intensity was computed at each scattering vector. The resulting residuals are shown in Figure 8.3b, plotted together with error bars corresponding to the experimental standard deviation derived from the eight line profiles. The residuals are systematically positive across most of the Q range, with a pronounced maximum between approximately 0.3 and 1.0 nm<sup>-1</sup>. This pattern indicates a consistent excess of experimental intensity relative to the theoretical predictions, and highlights that the model substantially underestimates the diffuse scattering in this region.

The reduced chi-square statistic, defined by

$$\chi_{\nu}^{2} = \frac{1}{N-p} \sum_{i}^{N} \frac{\left[\mathbf{I}_{\exp}(\mathbf{Q}_{i}) - \mathbf{I}_{1}(\mathbf{Q}_{i})\right]^{2}}{\sigma^{2}(\mathbf{Q}_{i})},$$
(8.7)

was calculated to evaluate the degree of agreement between theory and experiment. Here, N is the number of data points, p=0 since no fitting parameters were applied at this stage, and  $\sigma(\mathbf{Q}_i)$  is the experimental uncertainty at each  $\mathbf{Q}_i$ . This yielded a reduced chi-square value of approximately 36, highlighting a substantial deviation between the theoretical model and the measured data. This large value of  $\chi^2_{\nu}$  confirms that the theoretical model in its raw form does not adequately describe the experimental intensities. This discrepancy can be attributed to several factors that influence the experimental measurements but are not fully represented in the theoretical model.

To quantify and improve the agreement between the theoretical and experimental TDS intensities, a fitting procedure was performed to the theoretical intensity. Since absolute intensity scales between theory and experiment can differ due to variations in beam current, exposure time, and detector sensitivity, the theoretical TDS curve was scaled by an adjustable factor. Furthermore, to account for the influence of instrumental resolution, the theoretical intensity was convolved with a Gaussian point-spread function (PSF), which accounts for the imperfections of the detector. Additionally, to model the sharp elastic scattering signal near the Bragg peak, which is not included in the theoretical first-order TDS, a Dirac delta function  $\delta(\mathbf{Q} - \mathbf{G})$  centred at the Bragg

reflection  $\mathbf{G}$  was included in the model and similarly convolved with the same Gaussian PSF. This term simulates the Bragg reflection broadened by instrumental effects. The model for the fitted intensity  $I_{model}(\mathbf{Q})$  as a function of the scattering vector magnitude was thus expressed as:

$$I_{\text{model}}(\mathbf{Q}) = [A \times \delta(\mathbf{Q} - \mathbf{G}) + B \times \mathbf{I}_1(\mathbf{Q}_i)] \otimes G(Q_i) + C, \tag{8.8}$$

with

$$G(Q_i) = \frac{1}{\omega\sqrt{2\pi}} \exp\left(\frac{-|Q_i - \mathbf{G}|^2}{2\omega^2}\right), \tag{8.9}$$

where, A and B are scale factors applied to match experimental conditions,  $G(Q_i)$  is the Gaussian PSF with standard deviation  $\omega$ , and C is a constant offset accounting for residual background signal, such as dark subtraction errors in the detector. The PSF is area-normalised, such that  $\int G(Q_i) dQ_i = 1$ , conserving total intensity during convolution.

To improve the agreement between theory and experiment, the four fitting parameters A, B, C and  $\omega$  were adjusted. This optimisation was performed to minimise the reduced chi-square value, which ultimately converged to approximately 11.7. Although this represents a notable improvement over the uncorrected case, it still indicates a significant residual mismatch between the theoretical and experimental intensity distributions.

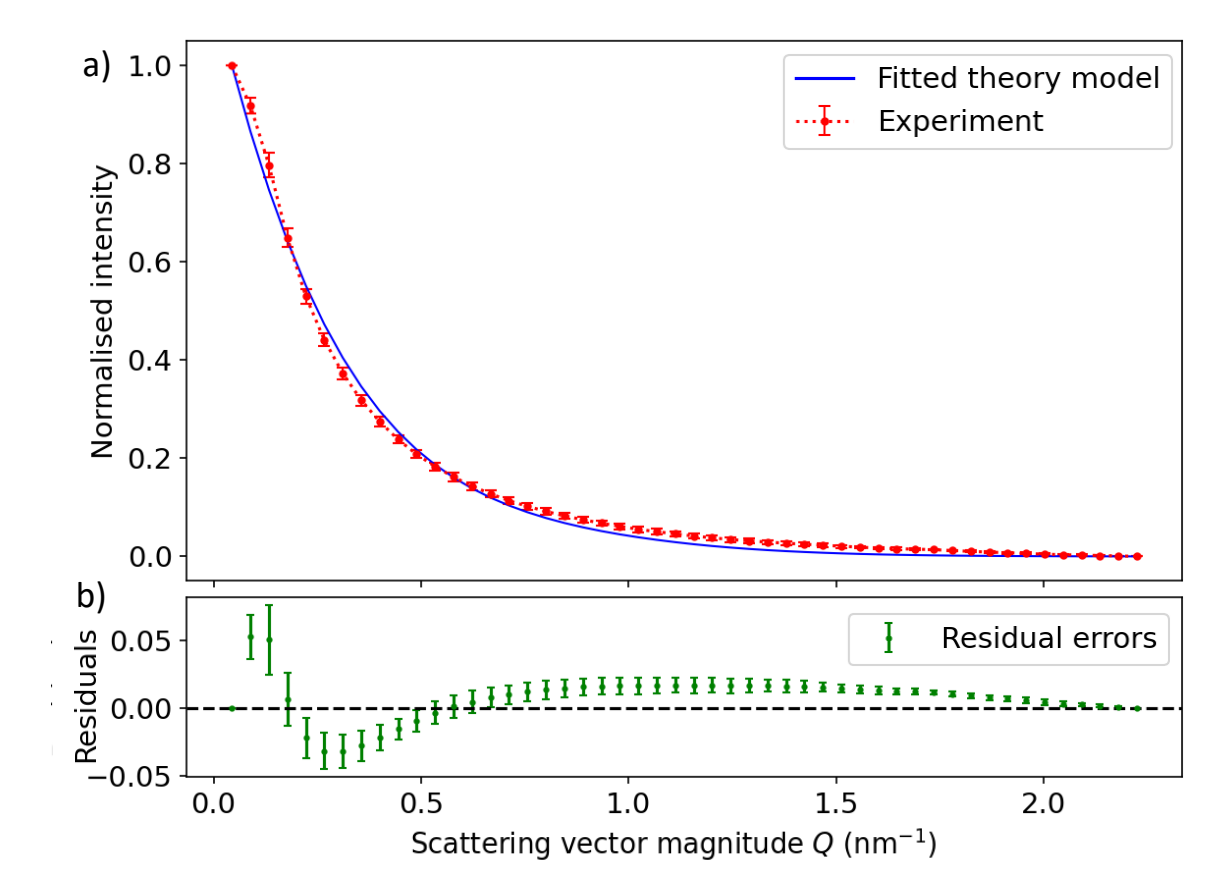


Figure 8.4: (a) Comparison of the optimised theoretical first-order TDS intensity and mean experimental TDS intensity (Equation 8.8) as a function of scattering vector magnitude Q with error bars of  $\sigma$ , and (b) Residuals between experimental and first-order TDS intensities.

Several factors likely contribute to this discrepancy. Firstly, the theoretical intensity model is based solely on the first-order thermal diffuse scattering approximation and does not incorporate higher-order phonon contributions, which can add diffuse intensity in the experimental intensity. Secondly, the theoretical model is based on a kinematic approximation which assumes electrons scatter only once. But electrons strongly interact with the crystal and undergo multiple scattering events. These complex interactions can redistribute intensity in ways that increase the diffuse signal. Because dynamical scattering is not accounted for in the current theory, the predicted intensities tend to underestimate the experimentally observed values. Thirdly, the Gaussian point-spread function used here assumes a symmetric and idealised form of instrumental broadening, but in practice, the actual broadening may be asymmetric, or affected by specimen-

specific features such as slight surface amorphisation, as evidenced by the diffuse ring around the central beam in Figure 8.2. Finally, while the constant offset term C accounts for background noise, it cannot compensate for intensity arising from inelastic scattering such as plasmons. As a result, the fitted model captures the general shape of the diffuse signal but does not reproduce its full complexity, explaining why the reduced chi-square remains high despite parameter optimisation.

As an alternative to the Gaussian PSF convolution model, a second fitting strategy was implemented in which the theoretical first-order TDS intensity was scaled and directly augmented by an exponential decay function of the form  $A e^{(-bQ^2)}$ . This exponential term accounts for additional diffuse background and/or broadening arising from instrument-related effects such as the detector point spread function. Unlike the PSF convolution method, which spreads the entire TDS profile according to a Gaussian function, this exponential term decreases the baseline intensity more smoothly and broadly in regions away from the Bragg peak, and thus provides a more flexible mechanism for matching the diffuse tails observed in the experimental data. The resulting model was expressed as:

$$I_{\text{model}}(\mathbf{Q}) = S \times I_1(\mathbf{Q}) + A \exp(-bQ^2) + C, \tag{8.10}$$

where, S is a scale factor applied to the theoretical intensity, A and b define the amplitude and decay of the exponential broadening term, and C is a constant background offset.

The resulting comparison between the optimised model and the experimental TDS intensity is shown in Figure 8.5a. Optimisation of this model produced a reduced chi-square value of approximately 1.5, representing a substantial improvement over the previous model incorporating the delta function and PSF convolution (which yielded  $\approx 11.7$ ). This result indicates that the exponential decay function provides a better empirical match to the experimental diffuse intensity distribution, effectively compensating for background contributions and instrumental broadening not captured in the theoretical model alone.

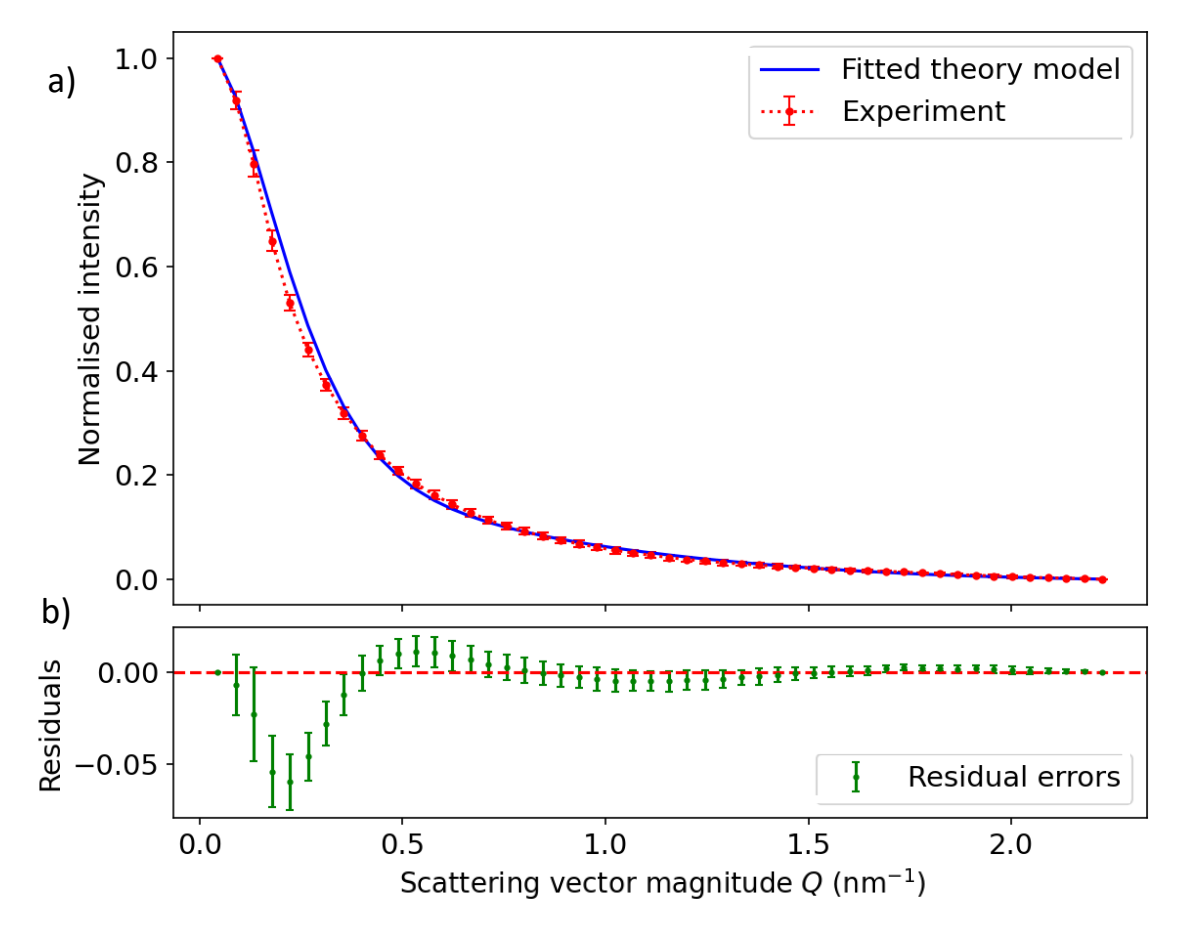


Figure 8.5: a) Comparison of the experimental TDS intensity with the optimised model (Equation 8.10) incorporating a scaled theoretical TDS curve and an exponential background of the form  $\exp(-bQ^2)$ , and b) Residuals between experimental and first-order TDS intensities.

### 8.1.2 TDS Intensity analysis at cryogenic temperature

To investigate the temperature dependence of thermal diffuse scattering, a follow-up experimental and theoretical analysis was conducted at cryogenic conditions. The goal was to evaluate how phonon population changes at lower temperature influence the TDS signal, and to compare this with corresponding theoretical calculations.[100] SADP pattern of silicon was acquired at approximately 123 K, and the same data extraction and analysis described for the room temperature case was applied to this low-temperature dataset. The phonon frequencies and eigenvectors used to compute the theoretical TDS intensity were kept unchanged, as these depend on the crystal structure and in-

teratomic force constants, which vary only slightly with temperature in the harmonic approximation. However, the temperature T in the first-order TDS expression was updated from 300 K to 123 K. Figure 8.6 shows the normalised theoretical TDS intensities calculated at 300 K and 123 K. Since the temperature enters the model through the thermal occupation factor  $\coth\left(\frac{\hbar\omega}{k_{\rm B}T}\right)$ , cooling the sample effectively reduces the population of thermally excited phonons, particularly the intermediate-frequency acoustic modes that contribute most significantly to diffuse scattering at intermediate scattering vectors. As these modes are increasingly depopulated at lower temperatures, the corresponding TDS intensity diminishes markedly with Q. This explains why the cryogenic curve in Figure 8.6 is noticeably narrower than the room temperature counterpart: the suppression of acoustic phonon contributions at 123 K leads to a sharper decline in intensity with increasing Q, reflecting the reduced diffuse scattering at intermediate Q.

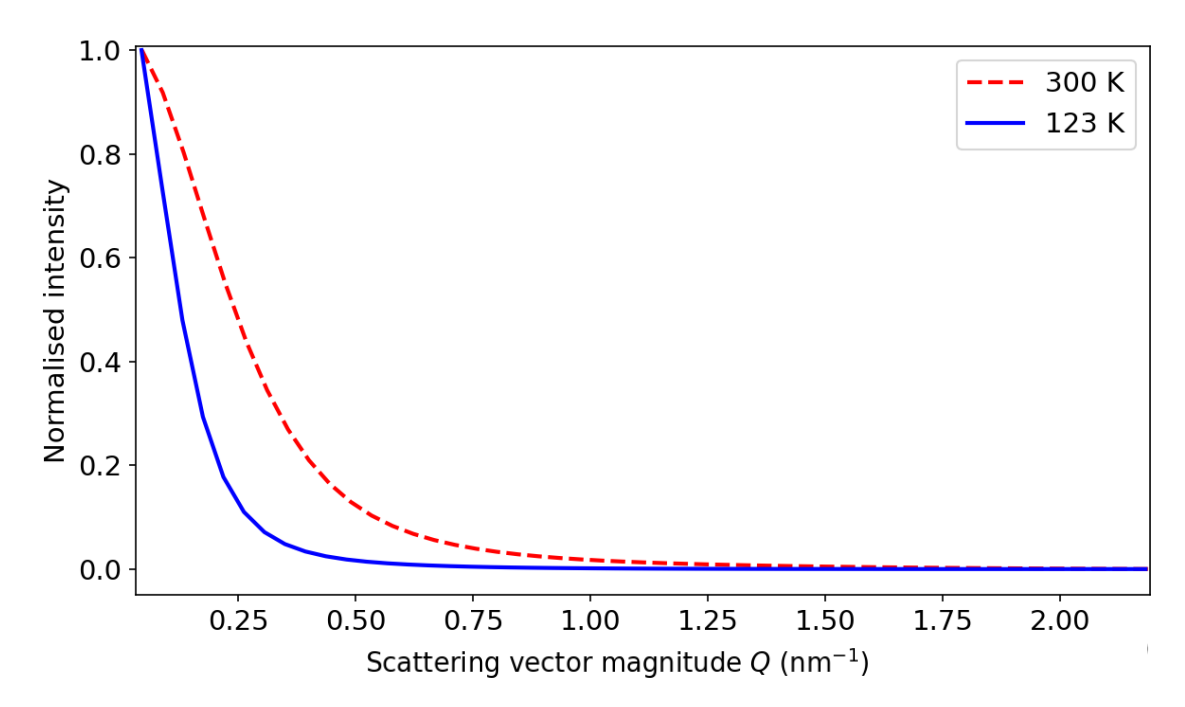


Figure 8.6: Comparison of the theoretical first-order TDS intensities computed at 300K and 123K.

To investigate the experimental impact of temperature on thermal diffuse scattering (TDS), the same line profile extraction procedure described in the previous section was applied to data acquired at cryogenic temperature (123 K). The resulting profiles for both room temperature (300 K) and cryogenic conditions are compared in Figure 8.7.

Both datasets were normalised such that their maximum intensity is unity, allowing their relative profiles to be directly compared.

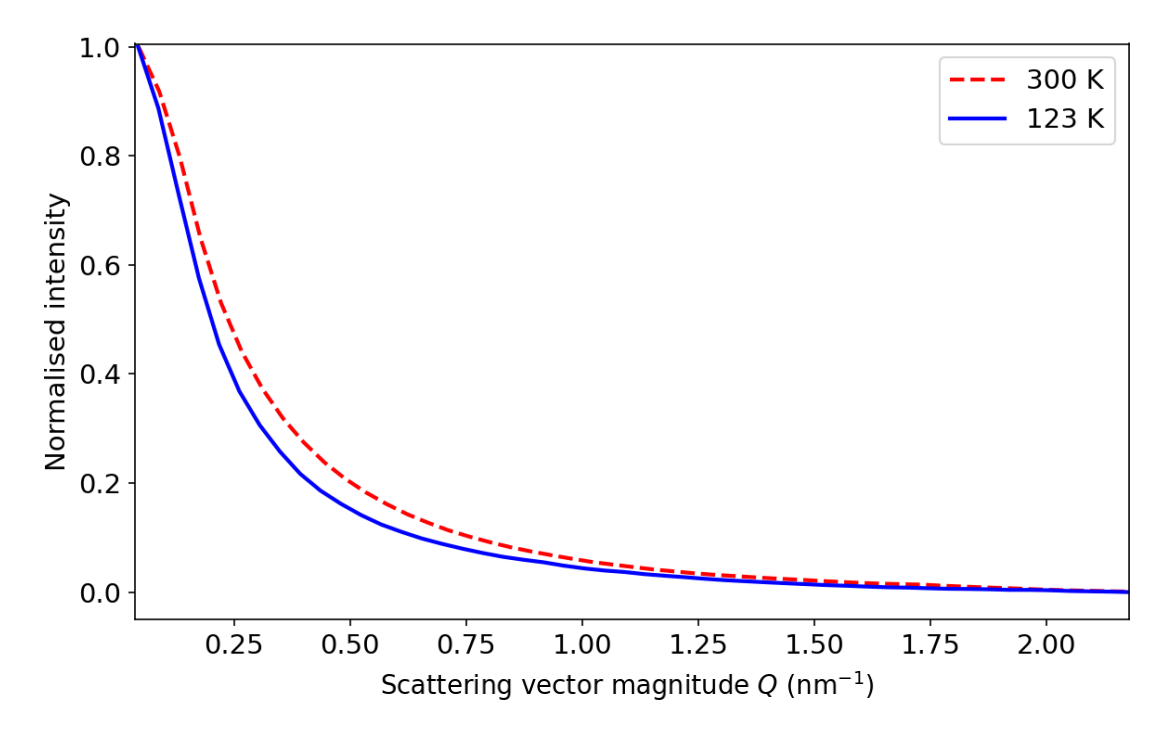


Figure 8.7: Comparison of the experimental intensities computed at 300K and 123K.

As shown in the Figure 8.7, the diffuse scattering signal at 123 K is consistently lower than that observed at 300 K across the entire range of scattering vector  $\mathbf{Q}$ . This reduction in intensity is a direct consequence of the diminished phonon population at lower temperatures, particularly the acoustic branches that dominate scattering at intermediate Q. The difference between the two curves is most evident in the range  $Q \approx 0.2$  - 1.5 nm<sup>-1</sup>, where TDS is strongest due to contributions from thermally populated vibrational modes. The experimental results closely mirror the trends predicted by the theoretical model, with both datasets exhibiting a clear suppression of diffuse scattering intensity at cryogenic temperatures. In particular, the steeper decay and reduced intensity of the 123 K curves in both theory and experiment confirm that the observed temperature dependence arises from the diminished population of acoustic phonon modes.

To quantitatively assess the agreement between the theoretical predictions and the

experimental diffuse scattering intensities measured at 123 K, the reduced chi-square statistic was first computed using the unmodified theoretical TDS intensity calculated at 123 K. Both datasets were normalised, and no scaling or instrumental corrections were applied at this stage. Figure 8.8a presents a direct comparison between the theoretical curve and the mean experimental intensity profile, with error bars indicating one standard deviation derived from the eight extracted line profiles. The corresponding residuals are shown in Figure 8.8b.

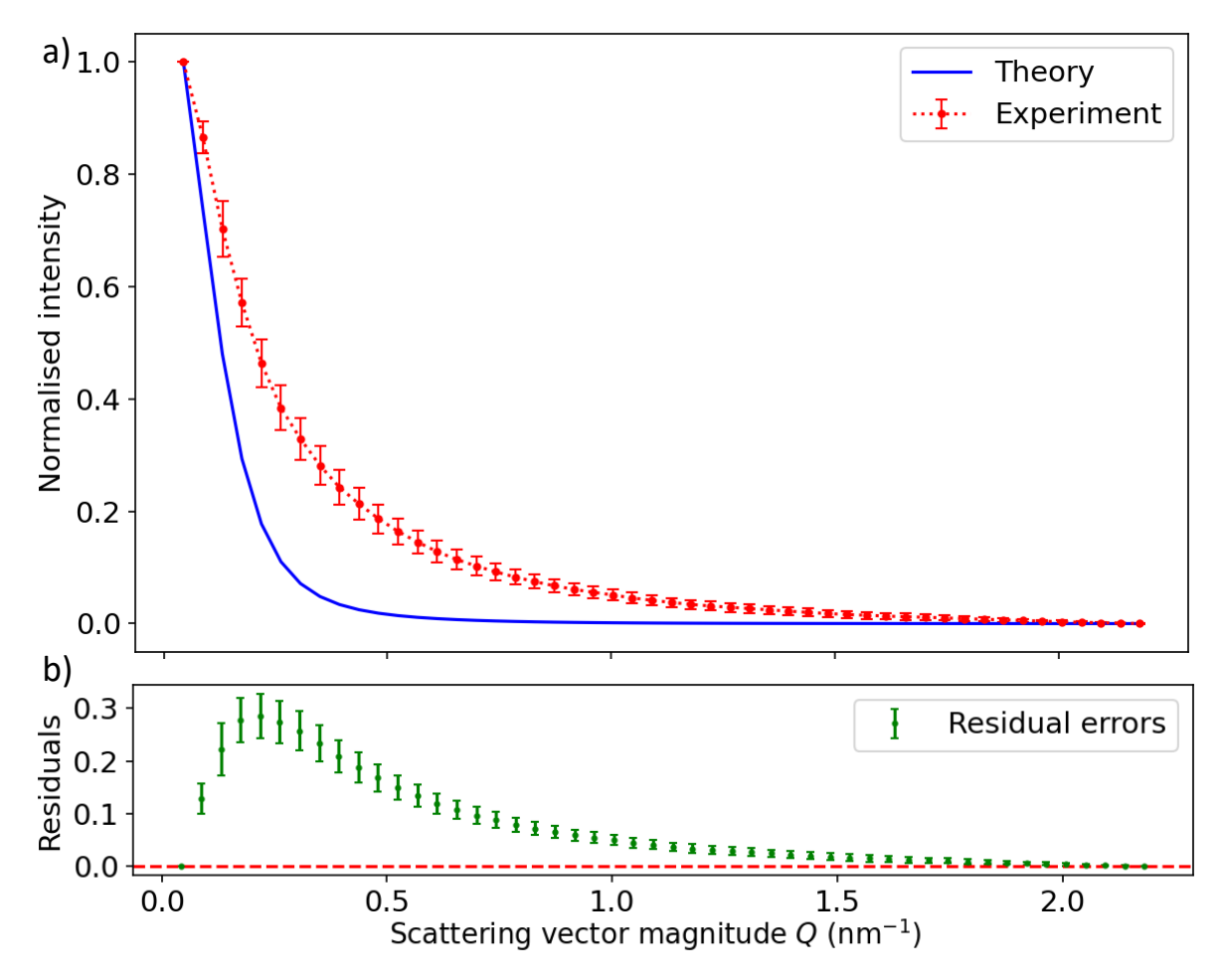


Figure 8.8: a) Comparison of the theoretical first-order TDS intensity and mean experimental TDS intensity as a function of scattering vector magnitude Q with error bars of  $\sigma$  at 123 K, and b) Residuals between experimental and first-order TDS intensities.

This analysis yielded a reduced chi-square value of approximately 20. While this is notably lower than the corresponding value at room temperature (approximately 36), the improvement does not necessarily indicate that the model performs more accurately

under cryogenic conditions. Instead, the reduction is primarily attributed to increased experimental uncertainty in the 123 K dataset, as reflected in the larger standard deviations calculated across the eight extracted line profiles. This elevated uncertainty arises from the fact that the diffraction pattern was not perfectly aligned with the [100] zone axis, leading to enhanced profile-to-profile variation during averaging. As a result, the error bars in the cryogenic dataset are broader, which in turn reduces the statistical weight of residuals when computing the reduced chi-square. It is also worth noting that, despite the lower chi-square value, the absolute residuals in the cryogenic dataset are significantly higher, reaching values up to approximately 0.22, in contrast to a maximum of around 0.08 in the room temperature case. This highlights that reduced chi-square values must be interpreted cautiously, taking into account both residual magnitude, its profile, and experimental error.

To improve the model fit and account for instrumental broadening, the theoretical TDS intensity was subsequently scaled and convolved with a Gaussian PSF, together with a Dirac delta function to represent the elastic scattering contribution broadened by the same PSF. The functional form of this model is identical to that described previously for the room-temperature data (Equation 8.8). Optimisation of the scale factors and PSF width was carried out following the same procedure as in the room-temperature analysis, by minimising the reduced chi-square statistic between the model and experimental data.

This approach reduced the chi-square value to approximately 6. Although this represents a numerical improvement, the residuals remain substantial throughout the Q range, as illustrated in Figure 8.9. The figure shows both the fitted model compared with the experimental data and the corresponding residuals plotted as a function of scattering vector. The comparison plot highlights that, while the PSF-convolved model reproduces the overall decay of the measured intensity, it does not fully capture the finer details of thermal diffuse scattering behaviour.

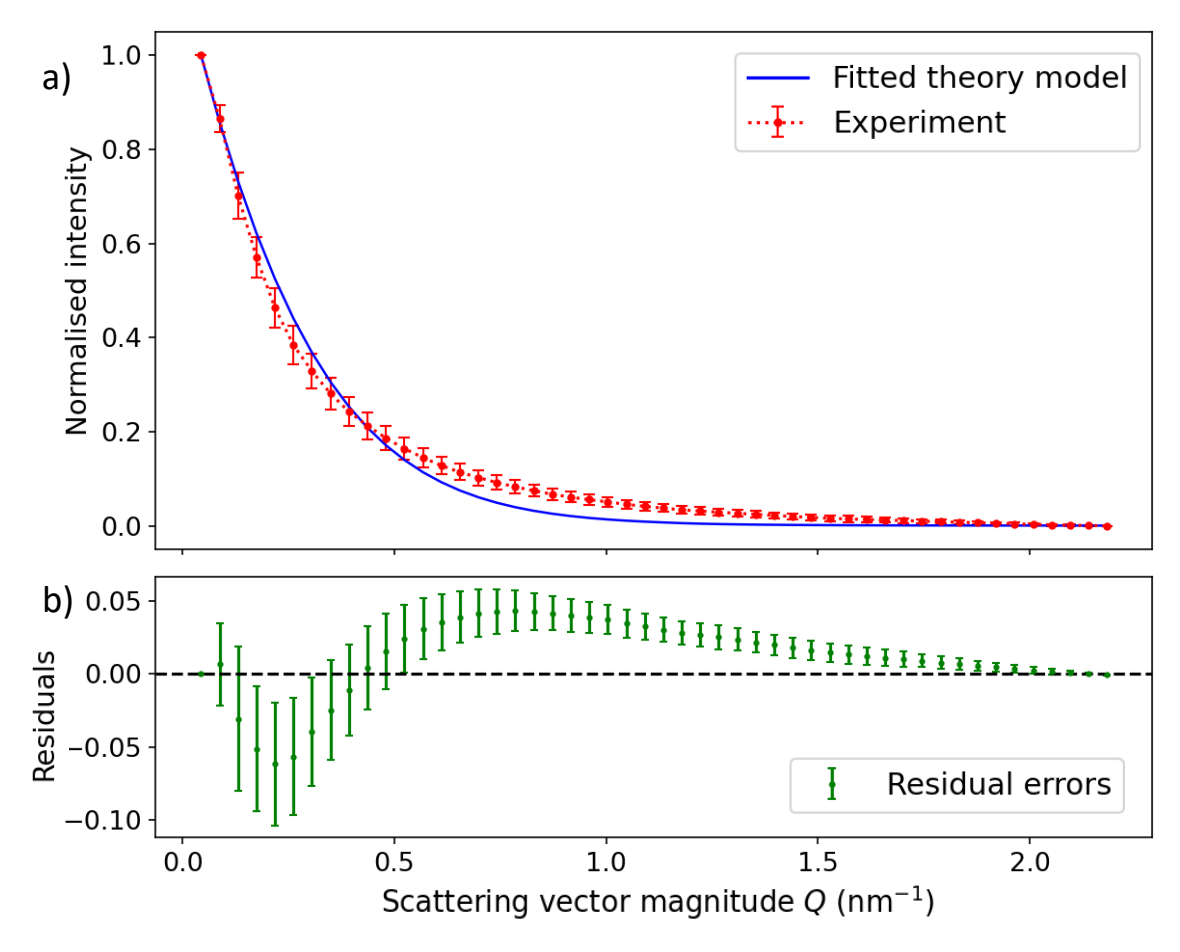


Figure 8.9: (a) Comparison of the optimised theoretical first-order TDS intensity (Equation 8.8) and mean experimental TDS intensity as a function of scattering vector magnitude Q with error bars of  $\sigma$  at 123 K, and (b) Residuals between experimental and first-order TDS intensities.

To further improve the agreement between theory and experiment, a second fitting strategy was implemented in which the theoretical first-order TDS intensity was scaled and augmented by an exponential decay function (Equation 8.10). The same fitting procedure used for the room-temperature dataset was applied here. Parameter optimisation yielded a reduced chi-square value of approximately 1.7, representing a significant improvement over both the uncorrected model ( $\chi^2_{\nu} \approx 20$ ) and the PSF-convolved model ( $\chi^2_{\nu} \approx 6$ ). The resulting comparison between the fitted model and experimental data is shown in Figure 8.10, along with the corresponding residuals.

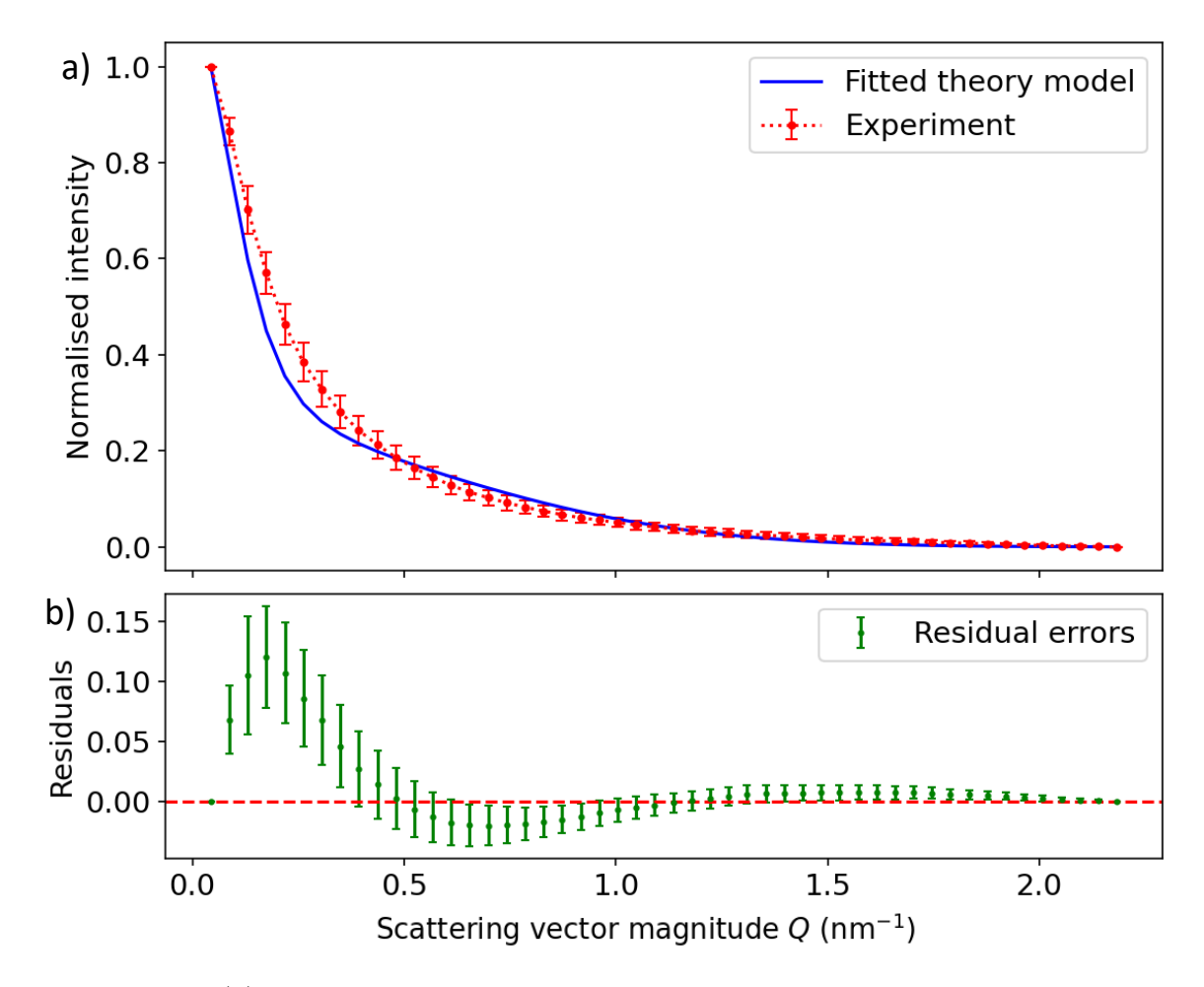


Figure 8.10: (a) Comparison of the optimised theoretical first-order TDS intensity (Equation 8.10) and mean experimental TDS intensity as a function of scattering vector magnitude Q with error bars of  $\sigma$  at 123 K, and (b) Residuals between experimental and first-order TDS intensities.

Although the exponential model significantly reduces the residual scatter and achieves a lower chi-square statistic, it does not perfectly reproduce the experimental intensity distribution. In particular, the model systematically underestimates the intensity at low scattering vectors ( $Q < 0.4 \text{ nm}^{-1}$ ), where the experimental signal remains elevated. This discrepancy may reflect subtle physical effects not captured by the exponential background, such as higher-order phonon scattering or residual dynamical interactions that disproportionately influence low- Q intensity. Another likely contributing factor is the slight misalignment of the diffraction pattern from the ideal [100] zone axis during data acquisition. As discussed previously, this misalignment introduced variability across line profiles and may have led to artificially elevated low-angle scattering in the

experimental average. It is therefore plausible that a more precise zone axis alignment would have resulted in a closer match between the fitted model and experimental data. Despite this limitation, the exponential model provides the best overall agreement with the experimental data among the models tested, and its relatively low chi-square value demonstrates that it captures the majority of the diffuse scattering behaviour observed at cryogenic temperature.

### 8.1.3 Conclusion

This chapter presented a comparative analysis of theoretical and experimental TDS in silicon at room temperature (300 K) and cryogenic temperature (123 K). Theoretical TDS intensities were computed from phonon dispersion curves along  $\Gamma$ -K obtained via DFT and compared to experimental profiles extracted along 000 \rightarrow 022 from [100] electron diffraction pattern of silicon. While the uncorrected theoretical model captured the general decay of intensity with increasing scattering vector, it consistently underestimated experimental values, particularly at intermediate Q due to the model's limitation to the first-order TDS and the instrumental errors in the experimental data. Fitting the model using a Gaussian point spread function and then an exponential background improved the agreement significantly. The exponential model yielded the best fit at both temperatures, lowering the reduced chi-square to approximately 1.5 at room temperature and 1.7 at 123 K. However, at cryogenic temperature, improved chi-square values were partially due to increased experimental uncertainty from slight zone axis misalignment. Nonetheless, the study confirms that empirical fitting can effectively bridge the gap between first-order TDS theory and experimental measurements, laying a foundation for integrating phonon simulations with experimental TDS in more complex systems.

## **Outlook**

The investigations presented in this thesis have laid a robust foundation for understanding the influence of degenerate boron doping on the vibrational and scattering properties of silicon using a combination of density functional theory (DFT) and advanced electron microscopy techniques. These results do not represent an endpoint but rather the beginning of a broader research trajectory that links atomic-scale phenomena with materials performance. The insights obtained here open a range of opportunities for deepening the theoretical framework, expanding the methodological reach, and applying the approach to other technologically vital materials systems.

The first strand of future work arises from the vibrational analysis of boron-related defects. While this study successfully established the vibrational properties of boron defects in silicon through both experimental EELS and density functional theory simulations, the natural next step is to undertake the computation of Raman spectra for the range of defect configurations already considered. In particular, simulations of the Raman active vibrational modes for the substitutional acceptor defects, the interstitial boron atoms, and the various interstitial cluster configurations can be carried out. By applying DFT, the susceptibility tensor associated with each vibrational mode can be computed and used to obtain the Raman intensity. This analysis would clarify which specific phonon modes are expected to be strongly Raman-active and would allow the construction of simulated Raman spectra for each configuration. These simulated spec-

tra could then serve as a benchmark for future theoretical or experimental studies involving other defect types or more complex doping profiles.

The second major direction builds upon the diffuse scattering analysis comparing elemental and boron-doped silicon through selected area diffraction patterns and multislice simulations. An essential progression of this work is to incorporate the effects of correlated phonon displacements into the multislice calculations. The methodology employed in this thesis relied predominantly on the frozen phonon approximation, wherein the thermal motion of atoms is modelled as an ensemble of uncorrelated displacements sampled from Gaussian distributions defined by the Debye-Waller factor. This approximation, though often sufficient for bulk materials, neglects the reality that phonon modes, particularly in defect systems, are spatially correlated. Extending the multislice approach to incorporate such correlations will require implementing methods that couple the thermal diffuse scattering contribution with the lattice dynamical matrix derived from DFT. Notably, this would involve calculating the phonon eigenvectors and frequencies, then constructing displacement fields that are consistent with these modes, rather than sampling independent Gaussian displacements per atom. Such an approach will improve the realism of diffuse scattering simulations and more accurately capture the temperature dependence of the TDS.

In parallel, the scope of point defect investigations should be broadened beyond boron doped silicon. A compelling direction is to apply similar simulation methodologies to oxygen-related point defects in complex oxides, especially those with functional properties such as superconductivity or ionic conductivity. For example, oxygen vacancies and interstitials in superconducting cuprates, or in Brownmillerite-type structures, can have profound effects on lattice dynamics and local strain fields. Extending the diffuse scattering analysis to these systems will allow researchers to probe defect induced distortions and lattice softening in technologically important materials, while leveraging the techniques refined in this thesis.

The comparative study of first-order TDS intensities and experimental measurements presented in the third result chapter yielded promising initial agreement but was necessarily constrained by the use of a kinematical scattering approximation and the exclusion of higher-order TDS terms. So the third research avenue for future work will therefore be to incorporate dynamical scattering effects into the TDS simulation framework. Dynamical diffraction effects, arising from multiple elastic and inelastic scattering events within the specimen, are known to distort both the angular dependence and the magnitude of TDS intensities. Accurately capturing these effects requires implementation of dynamical diffraction formalisms, potentially via the multislice approach extended to inelastic phonon and plasmon scattering. Another promising avenue for incorporating plasmon contributions into theoretical TDS simulations involves the use of a combined Bloch wave-Monte Carlo framework. This method allows for the explicit treatment of delocalised inelastic scattering events such as plasmon excitation, where electron wavefunction evolution is computed following probabilistically determined scattering events within the crystal. The framework accounts for changes in trajectory, scattering angle, and energy loss while maintaining consistency with the underlying dynamical diffraction conditions. Incorporating phonon and plasmon scattering in the current model would allow a more faithful reproduction of the experimental observations.

Beyond the inclusion of dynamical scattering, future work should seek to account for higher-order TDS contributions. These arise from processes in which two or more phonons are excited simultaneously, leading to intensity components beyond the first-order term. Though the computational cost of including such terms is formidable, given the need to sum the entire first Brillouin zone, it is anticipated that these contributions become increasingly important important with specimen thickness and may partially explain discrepancies between modelled and experimental profiles observed in this study.

Finally, a further prospective avenue is the extension of TDS studies to defective systems incorporating point defects, such as interstitial boron clusters and substitutional acceptors. A promising approach for simulating the diffuse scattering contributions of such defects is the incorporation of Kanzaki forces, lattice force fields induced by point defects, directly into the expression for the scattered intensity. The Kanzaki formalism enables a rigorous treatment of lattice relaxation fields surrounding defects and can therefore capture defect-induced diffuse scattering in defect systems.

# **Bibliography**

- [1] L. Hoddeson, E. Braun, J. Teichmann and S. Weart, Out of the crystal maze: chapters from the history of solid state physics. Oxford University Press, 1992.
- [2] I. M. Ross, 'The invention of the transistor,' Proceedings of the IEEE, vol. 86, no. 1, pp. 7–28, 1998.
- [3] P. Eckstein, 'Jack kilby (1923-2005),' *IEEE Annals of the History of Computing*, vol. 29, no. 01, pp. 90–95, 2007.
- [4] M. Novikov, 'Oleg vladimirovich losev: Pioneer of semiconductor electronics (celebrating one hundred years since his birth),' *Physics of the Solid State*, vol. 46, no. 1, pp. 1–4, 2004.
- [5] C. E. Fritts, 'On the fritts selenium cells and batteries,' *Journal of the Franklin Institute*, vol. 119, no. 3, pp. 221–232, 1885.
- [6] F. Michael, Experimental Researches in Electricity. Fourth Series. The Royal Society, 1833, vol. 123, pp. 507–522.
- [7] W. Mönch, '125 years of metal-semiconductor contacts: Where do we stand?' In Advances in Solid State Physics 39, Springer, 2007, pp. 13–24.
- [8] M. J. Kelly, Low-dimensional semiconductors: materials, physics, technology, devices. Clarendon Press, 1995, vol. 3.
- [9] T. Kimoto and J. A. Cooper, Fundamentals of silicon carbide technology: growth, characterization, devices and applications. John Wiley & Sons, 2014.

- [10] K. Biswas and A. Sarkar, Advanced Nanoscale MOSFET Architectures: Current Trends and Future Perspectives, pp. 301–310, 2024.
- [11] J. M Fiore, Semiconductor Devices: Theory and Application. dissidents, 2017.
- [12] D. K. Ferry, Semiconductors: Bonds and bands. IoP Publishing, 2019.
- [13] R. J. Tilley, Defects in solids. John Wiley & Sons, 2008.
- [14] W. D. Callister et al., Materials science and engineering: an introduction. John wiley & sons New York, 2007, vol. 7.
- [15] D. Hull and D. J. Bacon, Introduction to dislocations. Elsevier, 2011, vol. 37.
- [16] M. D. McCluskey and A. Janotti, 'Defects in semiconductors,' Journal of Applied Physics, vol. 127, no. 19, 2020.
- [17] G. Li, Q. Wang, Z. Cui and R. Guo, 'Competition between intrinsic and extrinsic phonon scatterings in cubic bp and bas with point defects,' *Physical Review B*, vol. 107, no. 18, p. 184118, 2023.
- [18] C. A. Polanco and L. Lindsay, 'Ab initio phonon point defect scattering and thermal transport in graphene,' *Physical Review B*, vol. 97, no. 1, p. 014303, 2018.
- [19] V. Lordi, P. Erhart and D. Åberg, 'Charge carrier scattering by defects in semiconductors,' *Physical Review B—Condensed Matter and Materials Physics*, vol. 81, no. 23, p. 235 204, 2010.
- [20] D. Vasileska, G. Formicone and D. K. Ferry, 'Doping dependence of the mobility enhancement in surface-channel strained-si layers,' *Nanotechnology*, vol. 10, no. 2, p. 147, 1999.
- [21] E. Astrova, V. Voronkov, V. Kozlov and A. Lebedev, 'Process induced deep-level defects in high purity silicon,' *Semiconductor science and technology*, vol. 13, no. 5, p. 488, 1998.
- [22] V. Ivanov et al., 'Database of semiconductor point-defect properties for applications in quantum technologies,' arXiv preprint arXiv:2303.16283, 2023.

- [23] W. Wan, C. Tang, A. Qiu and Y. Xiang, 'The size effects of point defect on the mechanical properties of monocrystalline silicon: A molecular dynamics study,' *Materials*, vol. 14, no. 11, p. 3011, 2021.
- [24] B. Raghothamachar, G. Dhanaraj, J. Bai and M. Dudley, 'Defect analysis in crystals using x-ray topography,' *Microscopy research and technique*, vol. 69, no. 5, pp. 343–358, 2006.
- [25] P. Voyles, D. Muller, J. Grazul, P. Citrin and H.-J. Gossmann, 'Atomic-scale imaging of individual dopant atoms and clusters in highly n-type bulk si,' *Nature*, vol. 416, no. 6883, pp. 826–829, 2002.
- [26] A. A. Bunaciu, E. G. UdriŞTioiu and H. Y. Aboul-Enein, 'X-ray diffraction: Instrumentation and applications,' *Critical reviews in analytical chemistry*, vol. 45, no. 4, pp. 289–299, 2015.
- [27] A. George, S. K. Sharma, S. Chawla, M. Malik and M. Qureshi, 'Detailed of x-ray diffraction and photoluminescence studies of ce doped zno nanocrystals,' Journal of Alloys and Compounds, vol. 509, no. 20, pp. 5942–5946, 2011.
- [28] E. Zschech, W. Yun and G. Schneider, 'High-resolution x-ray imaging—a power-ful nondestructive technique for applications in semiconductor industry,' *Applied Physics A*, vol. 92, no. 3, pp. 423–429, 2008.
- [29] S. Dolabella, A. Borzi, A. Dommann and A. Neels, 'Lattice strain and defects analysis in nanostructured semiconductor materials and devices by high-resolution x-ray diffraction: Theoretical and practical aspects,' Small Methods, vol. 6, no. 2, p. 2100932, 2022.
- [30] S. Mu and D. Stowe, Correlative x-ray microanalysis of a boron steel sample using micro-xrf and sem-eds, 2024.
- [31] C. Shull and E. Wollan, 'X-ray, electron, and neutron diffraction,' *Science*, vol. 108, no. 2795, pp. 69–75, 1948.

- [32] B. Haberl, M. Guthrie and R. Boehler, 'Advancing neutron diffraction for accurate structural measurement of light elements at megabar pressures,' *Scientific Reports*, vol. 13, no. 1, p. 4741, 2023.
- [33] D. S. Sivia, Elementary scattering theory: for X-ray and neutron users. Oxford University Press, 2011.
- [34] P. Hohenberg and W. Kohn, 'Density functional theory (dft),' Phys. Rev, vol. 136, no. 1964, B864, 1964.
- [35] W. Kohn, 'Electronic structure of matter-wave functions and density functionals,' Rev. Mod. Phys., vol. 71, no. 5, pp. 1253–1266, 1999.
- [36] W. Kohn and L. J. Sham, 'Self-consistent equations including exchange and correlation effects,' *Physical review*, vol. 140, no. 4A, A1133, 1965.
- [37] W. Kohn, A. D. Becke and R. G. Parr, 'Density functional theory of electronic structure,' *The journal of physical chemistry*, vol. 100, no. 31, pp. 12974–12980, 1996.
- [38] M. McCluskey, 'Local vibrational modes of impurities in semiconductors,' *Journal* of Applied Physics, vol. 87, no. 8, pp. 3593–3617, 2000.
- [39] R. Gurunathan, R. Hanus, M. Dylla, A. Katre and G. J. Snyder, 'Analytical models of phonon–point-defect scattering,' *Physical Review Applied*, vol. 13, no. 3, p. 034 011, 2020.
- [40] D. Perovic, C. Rossouw and A. Howie, 'Imaging elastic strains in high-angle annular dark field scanning transmission electron microscopy,' *Ultramicroscopy*, vol. 52, no. 3-4, pp. 353–359, 1993.
- [41] T. Lovejoy, G. Corbin, N. Dellby, M. Hoffman and O. Krivanek, 'Advances in ultra-high energy resolution stem-eels,' *Microscopy and Microanalysis*, vol. 24, no. S1, pp. 446–447, 2018.
- [42] M. J. Lagos, I. C. Bicket, S. S. Mousavi M and G. A. Botton, 'Advances in ultrahigh-energy resolution eels: Phonons, infrared plasmons and strongly coupled modes,' *Microscopy*, vol. 71, no. Supplement\_1, pp. i174–i199, 2022.

- [43] R. Egoavil, N. Gauquelin, G. Martinez, S. Van Aert, G. Van Tendeloo and J. Verbeeck, 'Atomic resolution mapping of phonon excitations in stem-eels experiments,' *Ultramicroscopy*, vol. 147, pp. 1–7, 2014.
- [44] V. Kumar and J. P. Camden, 'Imaging vibrational excitations in the electron microscope,' The Journal of Physical Chemistry C, vol. 126, no. 40, pp. 16919– 16927, 2022.
- [45] R. Xu and T. C. Chiang, 'Determination of phonon dispersion relations by x-ray thermal diffuse scattering,' *Zeitschrift für Kristallographie-Crystalline Materials*, vol. 220, no. 12, pp. 1009–1016, 2005.
- [46] C. Kittel, Introduction to Solid State Physics. New York: John Wiley and Sons, 8th ed, 2005. DOI: 10.1119/1.1934457.
- [47] Y. Peter and M. Cardona, Fundamentals of semiconductors: physics and materials properties. Springer Science & Business Media, 2010.
- [48] K. E. Petersen, 'Silicon as a mechanical material,' *Proceedings of the IEEE*, vol. 70, no. 5, pp. 420–457, 1982.
- [49] I. T. Witting et al., 'The thermoelectric properties of bismuth telluride,' Advanced Electronic Materials, vol. 5, no. 6, p. 1800 904, 2019.
- [50] S. Zhuiykov, Nanostructured Semiconductor Oxides for the Next Generation of Electronics and Functional Devices. Woodhead Publishing, 2014, pp. 1–49. DOI: https://doi.org/10.1533/9781782422242.1.
- [51] M. Rahman, 'A review on semiconductors including applications and temperature effects in semiconductors,' American Academic Scientific Research Journal for Engineering, Technology, and Sciences, vol. 7, no. 1, pp. 50–70, 2014.
- [52] S. Hunklinger and C. Enss, Solid state physics. Walter de Gruyter GmbH & Co KG, 2022.
- [53] Y.-F. Tsay and B. Bendow, 'Band structure of semiconductors under high stress,' *Physical Review B*, vol. 16, no. 6, p. 2663, 1977.
- [54] L.-f. Lou, Introduction to phonons and electrons. World Scientific, 2003.

- [55] M. G. Cottam, Dynamical Properties in Nanostructured and Low Dimensional Materials. IoP Publishing, 2022.
- [56] S. Fonash, Solar cell device physics. Elsevier, 2012.
- [57] P. Hofmann, Solid state physics: an introduction. John Wiley & Sons, 2022.
- [58] S. M. Sze, Y. Li and K. K. Ng, *Physics of semiconductor devices*. John wiley & sons, 2021.
- [59] M. Huang, M. Chen and T. Zheng, 'Direction-dependent functions of physical properties for crystals and polycrystals,' Acta Mechanica Sinica, vol. 25, no. 5, pp. 639–649, 2009.
- [60] B. G. Streetman, S. Banerjee et al., Solid state electronic devices. Prentice hall New Jersey, 2000, vol. 4.
- [61] K. Morrison, Characterisation methods in solid state and materials science. IOP Publishing, 2019.
- [62] D. Schmool, Solid State Physics: From the Material Properties of Solids to Nanotechnologies. Mercury Learning and Information, 2016.
- [63] M. L. Leek, Crystalline Solid State Physics: An Interactive Guide. IOP Publishing, 2023.
- [64] R. Peierls, More surprises in theoretical physics. Princeton University Press, 1991.
- [65] D. S. Sholl and J. A. Steckel, Density functional theory: a practical introduction. John Wiley & Sons, 2022.
- [66] J. H. Davies, The physics of low-dimensional semiconductors: an introduction. Cambridge university press, 1998.
- [67] A. F. J. Levi, Essential semiconductor laser device physics. Morgan & Claypool Publishers, 2018.
- [68] C. Bradley and A. Cracknell, The mathematical theory of symmetry in solids: representation theory for point groups and space groups. Oxford University Press, 2009.

- [69] J. Singh, Electronic and optoelectronic properties of semiconductor structures. Cambridge University Press, 2007.
- [70] T. Ihn, Semiconductor Nanostructures: Quantum states and electronic transport.OUP Oxford, 2009.
- [71] L. Alcácer, Electronic structure of organic semiconductors: polymers and small molecules. Morgan & Claypool Publishers, 2018.
- [72] S. B. Roy, Mott insulators: physics and applications. IOP publishing, 2019.
- [73] Z. Guo and L. Tan, Fundamentals and applications of nanomaterials. Artech House, 2009.
- [74] J. H. Simmons and K. S. Potter, Optical materials. Elsevier, 1999.
- [75] S. J. Clark, M. D. Segall, C. J. Pickard, P. J. Hasnip, K. Probert M. J. and Refson and M. C. Payne, 'Determination of phonon dispersion relations by x-ray thermal diffuse scattering,' "First principles methods using CASTEP", vol. 220, no. (5-6), pp. 567–570, 2005.
- [76] E. Kaxiras, Atomic and electronic structure of solids. 2003.
- [77] P. Misra, *Physics of condensed matter*. Academic Press, 2011.
- [78] B. Fultz, 'Vibrational thermodynamics of materials,' *Progress in Materials Science*, vol. 55, no. 4, pp. 247–352, 2010.
- [79] N. Shulumba, 'Vibrations in solids: From first principles lattice dynamics to high temperature phase stability,' Ph.D. dissertation, Linköping University Electronic Press, 2015.
- [80] J. Tidholm, Lattice dynamics: From fundamental research to practical applications. Linköping University Electronic Press, 2020, vol. 2103.
- [81] M. T. Dove, Introduction to lattice dynamics. Cambridge university press, 1993.
- [82] A. T. Maradudin and S. H. Vosko, 'Symmetry properties of the normal vibrations of a crystal,' *Reviews of Modern Physics*, vol. 40, no. 1, p. 1, 1968.
- [83] J. Wolfe, 'Imaging phonons: Acoustic wave propagation in solids. cambridge university press,' 1998.

- [84] R. Xu and T. C. Chiang, 'Determination of phonon dispersion relations by x-ray thermal diffuse scattering,' *Zeitschrift für Kristallographie-Crystalline Materials*, vol. 220, no. 12, pp. 1009–1016, 2005.
- [85] N. W. Ashcroft and N. D. Mermin, Solid state physics, 2022.
- [86] I. G. Kuleyev, I. I. Kuleyev, S. M. Bakharev and V. V. Ustinov, Phonon Focusing and Phonon Transport: In Single-Crystal Nanostructures. Walter de Gruyter GmbH & Co KG, 2020.
- [87] L. Tilly, 'Defects in semiconductors,' Lund Univ.(Sweden). Dept. of Solid State Physics, Tech. Rep., 1993.
- [88] C. Winrich, Semiconductors and modern electronics. Morgan & Claypool Publishers, 2019.
- [89] G. Domingo, Semiconductor basics: a qualitative, non-mathematical explanation of how semiconductors work and how they are used. John Wiley & Sons, 2020.
- [90] L. Keldysh, 'Deep levels in semiconductors,' in SELECTED PAPERS OF LE-ONID V KELDYSH, World Scientific, 2024, pp. 33–40.
- [91] J. R. Hook and H. E. Hall, Solid state physics. John Wiley & Sons, 2013.
- [92] S. M. Sze, Semiconductor devices: physics and technology. John wiley & sons, 2008.
- [93] V. I. Fistul, Heavily doped semiconductors. Springer Science & Business Media, 2012, vol. 1.
- [94] J.-P. Colinge and C. A. Colinge, *Physics of semiconductor devices*. Springer Science & Business Media, 2005.
- [95] A. Rockett, *The materials science of semiconductors*. Springer Science & Business Media, 2007.
- [96] J. Matthew, 'Point defects in solids. vol. 1. general & ionic crystals,' Acta Crystallographica Section A: Crystal Physics, Diffraction, Theoretical and General Crystallography, pp. 219–219, 1973.

- [97] C. Freysoldt et al., 'First-principles calculations for point defects in solids,' Reviews of modern physics, vol. 86, no. 1, pp. 253–305, 2014.
- [98] P. Mooney, L. Cheng, M. Süli, J. Gerson and J. Corbett, 'Defect energy levels in boron-doped silicon irradiated with 1-mev electrons,' *Physical Review B*, vol. 15, no. 8, p. 3836, 1977.
- [99] W. Cai and W. D. Nix, *Imperfections in crystalline solids*. Cambridge University Press, 2016.
- [100] H. Kanzaki, 'Point defects in face-centred cubic lattice—i distortion around defects,' *Journal of Physics and Chemistry of Solids*, vol. 2, no. 1, pp. 24–36, 1957.
- [101] P. Flinn and A. Maradudin, 'Distortion of crystals by point defects,' *Annals of Physics*, vol. 18, no. 1, pp. 81–109, 1962.
- [102] B. Gurrutxaga-Lerma and J. Verschueren, 'Generalized kanzaki force field of extended defects in crystals with applications to the modeling of edge dislocations,'

  Physical Review Materials, vol. 3, no. 11, p. 113801, 2019.
- [103] N. Papanikolaou, R. Zeller, P. Dederichs and N. Stefanou, 'Lattice distortion in cu-based dilute alloys: A first-principles study by the kkr green-function method,' *Physical Review B*, vol. 55, no. 7, p. 4157, 1997.
- [104] J. Angress, A. Goodwin and S. Smith, 'A study of vibrations of boron and phosphorus in silicon by infra-red absorption,' Proceedings of the Royal Society of London. Series A. Mathematical and Physical Sciences, vol. 287, no. 1408, pp. 64–88, 1965.
- [105] K. Khoo and J. R. Chelikowsky, 'First-principles study of vibrational modes and raman spectra in p-doped si nanocrystals,' *Physical Review B*, vol. 89, no. 19, p. 195 309, 2014.
- [106] J. Adey, R. Jones, D. Palmer, P. Briddon and S. Öberg, 'Theory of boron-vacancy complexes in silicon,' *Physical Review B—Condensed Matter and Materials Physics*, vol. 71, no. 16, p. 165 211, 2005.

- [107] N. Sclar, 'Resistivity and deep impurity levels in silicon at 300 k,' *Ieee Transactions On Electron Devices*, vol. 24, no. 6, pp. 709–712, 1977.
- [108] N. D. Arora, J. R. Hauser and D. J. Roulston, 'Electron and hole mobilities in silicon as a function of concentration and temperature,' *IEEE Transactions on* electron devices, vol. 29, no. 2, pp. 292–295, 1982.
- [109] D. M. Brown and R. Bray, 'Analysis of lattice and ionized impurity scattering in p-type germanium,' *Physical Review*, vol. 127, no. 5, p. 1593, 1962.
- [110] D. Long, 'Scattering of conduction electrons by lattice vibrations in silicon,' *Physical Review*, vol. 120, no. 6, p. 2024, 1960.
- [111] D. S. Sivia, Elementary scattering theory: for X-ray and neutron users. Oxford University Press, 2011.
- [112] L. De Broglie, 'The wave nature of the electron,' *Nobel lecture*, vol. 12, pp. 244–256, 1929.
- [113] J. M. Ziman, *Principles of the Theory of Solids*. Cambridge university press, 1979.
- [114] B. Cantor, The equations of materials. Oxford University Press, 2020.
- [115] A. M. Glazer, A journey into reciprocal space: a crystallographer's perspective. IOP Publishing, 2021.
- [116] C. MacDonald, An introduction to x-ray physics, optics, and applications. Princeton University Press, 2017.
- [117] O. H. Seeck and B. Murphy, X-ray diffraction: modern experimental techniques. CRC Press, 2015.
- [118] C. Hammond, *The basics of crystallography and diffraction*. Oxford University Press, USA, 2015, vol. 21.
- [119] D. Chakrabarty, D. Guha and A. Biswas, 'Solid state properties and catalytic behavior of the  $\alpha$ -and  $\beta$ -vanadium bronzes,' *Journal of Solid State Chemistry*, vol. 22, no. 3, pp. 263–271, 1977.

- [120] Y. Leng, Materials characterization: introduction to microscopic and spectroscopic methods. John Wiley & Sons, 2013.
- [121] E. Zolotoyabko, Basic concepts of X-ray diffraction. John Wiley & Sons, 2014.
- [122] C. Giacovazzo, Fundamentals of crystallography. Oxford university press, USA, 2002, vol. 7.
- [123] L. Maiwald, S. Lang, D. Jalas, H. Renner, A. Y. Petrov and M. Eich, 'Ewald sphere construction for structural colors,' *Optics express*, vol. 26, no. 9, pp. 11352–11365, 2018.
- [124] W. Zachariasen, 'A general theory of x-ray diffraction in crystals,' *Acta Crystal-lographica*, vol. 23, no. 4, pp. 558–564, 1967.
- [125] E. Lifshin, X-ray Characterization of Materials. John Wiley & Sons, 2008.
- [126] B. Warren, X-Ray Diffraction. Dover, 1990, vol. 208.
- [127] L. M. Peng, 'Electron atomic scattering factors and scattering potentials of crystals,' *Micron*, vol. 30, no. 6, pp. 625–648, 1999.
- [128] C. Humphreys, 'The scattering of fast electrons by crystals,' Reports on Progress in Physics, vol. 42, no. 11, p. 1825, 1979.
- [129] J. M. Cowley, Electron diffraction techniques. Oxford University Press, 1992, vol. 2.
- [130] E. J. Kirkland, Advanced computing in electron microscopy. Springer, 1998, vol. 12.
- [131] C. Giacovazzo, 'Phasing in crystallography: A modern perspective,' *Rendiconti Lincei*, vol. 24, pp. 71–76, 2013.
- [132] A. J. Blake, J. M. Cole, J. S. Evans, P. Main, S. Parsons and D. J. Watkin, Crystal structure analysis: principles and practice. OUP Oxford, 2009, vol. 13.
- [133] J. Stangl, C. Mocuta, V. Chamard and D. Carbone, *Nanobeam X-ray Scattering:*Probing matter at the nanoscale. John Wiley & Sons, 2013.

- [134] H. Lohstöter, H. Spalt and H. Peisl, 'X-ray scattering from the displacement field of point defects,' *Phys. Rev. Lett.*, vol. 29, pp. 224–226, 4 Jul. 1972. DOI: 10.1103/PhysRevLett.29.224. [Online]. Available: https://link.aps.org/doi/10.1103/PhysRevLett.29.224.
- [135] R. Celotta and T. B. (B. Lucatorto, Experimental methods in the physical sciences. Volume 34 (Experimental methods in the physical sciences; v. 34), eng. San Diego: Academic Press, 1999, ISBN: 1-281-74950-8.
- [136] J. Als-Nielsen and D. McMorrow, Elements of modern X-ray physics. John Wiley & Sons, 2011.
- [137] G. L. Squires, Introduction to the theory of thermal neutron scattering. Courier Corporation, 1996.
- [138] P. Blaise and O. Henri-Rousseau, *Quantum Oscillators*. John Wiley & Sons, 2011.
- [139] A. Girard et al., 'Structural, elastic and vibrational properties of celestite, srso4, from synchrotron x-ray diffraction, thermal diffuse scattering and raman scattering,' *Journal of Physics: Condensed Matter*, vol. 31, no. 5, p. 055703, 2018.
- [140] P. Kroon and A. Vos, 'Thermal diffuse scattering for molecular crystals: Errors in x-ray diffraction intensities and atomic parameters,' Acta Crystallographica Section A: Crystal Physics, Diffraction, Theoretical and General Crystallography, vol. 35, no. 4, pp. 675–684, 1979.
- [141] P. Dederichs, 'Diffuse scattering from defect clusters near bragg reflections,' *Physical Review B*, vol. 4, no. 4, p. 1041, 1971.
- [142] M. A. Krivoglaz, X-ray and neutron diffraction in nonideal crystals. Springer Science & Business Media, 2012.
- [143] H. Dosch, U. Schubert, H. Metzgert and J. Peisl, 'Diffuse x-ray scattering from interstitial nitrogen in niobium. ii. diffuse scattering due to heavily distorting point defects,' *Journal of Physics F: Metal Physics*, vol. 14, no. 11, p. 2467, 1984.

- [144] H. G. Haubold, 'Application of x-ray diffuse scattering to structure determinations of point-defects,' *Revue de Physique Appliquee*, vol. 11, no. 1, pp. 73–81, 1976.
- [145] H. Metzger and H. Peisl, 'Huang diffuse x-ray scattering from lattice strains in high-concentration ta-h alloys,' *Journal of Physics F: Metal Physics*, vol. 8, no. 3, p. 391, 1978.
- [146] H. Kanzaki, 'Point defects in face-centred cubic lattice-ii x-ray scattering effects,'

  Journal of Physics and Chemistry of Solids, vol. 2, no. 2, pp. 107–114, 1957.
- [147] P. Ehrhart and W. Schilling, 'Investigation of interstitials in electron-irradiated aluminum by diffuse-x-ray scattering experiments,' *Physical Review B*, vol. 8, no. 6, p. 2604, 1973.
- [148] P. Dederichs, 'The theory of diffuse x-ray scattering and its application to the study of point defects and their clusters,' *Journal of Physics F: Metal Physics*, vol. 3, no. 2, p. 471, 1973.
- [149] C. W. Tucker Jr and P. Senio, 'X-ray scattering effects due to localized static lattice defects,' *Physical Review*, vol. 99, no. 6, p. 1777, 1955.
- [150] R. Averback and P. Ehrhart, 'Diffuse x-ray scattering studies of defect reactions in electron-irradiated dilute nickel alloys. i. ni-si,' *Journal of Physics F: Metal Physics*, vol. 14, no. 6, p. 1347, 1984.
- [151] B. v. Guerard, D. Grasse and J. Peisl, 'Structure of defect cascades in fast-neutron-irradiated aluminum by diffuse x-ray scattering,' *Physical Review Letters*, vol. 44, no. 4, p. 262, 1980.
- [152] J. W. Flocken and J. R. Hardy, 'Calculations of the intensity of x-ray diffuse scattering produced by point defects in cubic metals,' *Physical Review B*, vol. 1, no. 6, p. 2472, 1970.
- [153] L. De Broglie, 'Recherches sur la théorie des quanta,' Ph.D. dissertation, Migration-université en cours d'affectation, 1924.

- [154] P. A. Penczek, 'Resolution measures in molecular electron microscopy,' in *Methods in enzymology*, vol. 482, Elsevier, 2010, pp. 73–100.
- [155] A. C. McLaren, Transmission electron microscopy of minerals and rocks. 1991.
- [156] E. Ruska, 'The development of the electron microscope and of electron microscopy,' *Reviews of modern physics*, vol. 59, no. 3, p. 627, 1987.
- [157] D. S. Rao, K. Muraleedharan and C. Humphreys, 'Tem specimen preparation techniques,' Microscopy: science, technology, applications and education, vol. 2, p. 1232, 2010.
- [158] R. Egerton, P. Li and M. Malac, 'Radiation damage in the tem and sem,' *Micron*, vol. 35, no. 6, pp. 399–409, 2004.
- [159] R. F. Egerton, 'Electron energy-loss spectroscopy in the tem,' Reports on Progress in Physics, vol. 72, no. 1, p. 016502, 2008.
- [160] R. Egerton and M. Watanabe, 'Spatial resolution in transmission electron microscopy,' *Micron*, vol. 160, p. 103 304, 2022.
- [161] S. H. Oh et al., 'Point defect configurations of supersaturated au atoms inside si nanowires,' *Nano letters*, vol. 8, no. 4, pp. 1016–1019, 2008.
- [162] S. B. Lee and H. N. Han, 'Faceting-roughening transition of a cu grain boundary under electron-beam irradiation at 300 kev,' Scientific Reports, vol. 11, no. 1, p. 15563, 2021.
- [163] J. H. Warner, E. R. Margine, M. Mukai, A. W. Robertson, F. Giustino and A. I. Kirkland, 'Dislocation-driven deformations in graphene,' Science, vol. 337, no. 6091, pp. 209–212, 2012.
- [164] P. Zhao et al., 'Revealing the structure/property relationships of semiconductor nanomaterials via transmission electron microscopy,' Advanced Functional Materials, p. 2408 935, 2024.
- [165] X. Zhong, X. Zhou, S. J. Haigh, P. J. Withers and M. G. Burke, 'Challenges in fib tem sample preparation: Damage issues and solutions,' *Microscopy and Microanalysis*, vol. 28, no. S1, pp. 60–62, 2022.

- [166] R. Egerton, 'Control of radiation damage in the tem,' *Ultramicroscopy*, vol. 127, pp. 100–108, 2013.
- [167] A. Roy, 'Electronic emission & electron guns,' In Pulsed Power Technology:

  Pulsed Electron Beams and their Applications, 2010.
- [168] D. Williams and C. Carter, Transmission electron microscopy: a textbook for materials science. Springer Science & Business Media, 1996, vol. 2.
- [169] Y. Li, Y. Sun and J. Yeow, 'Nanotube field electron emission: Principles, development, and applications,' *Nanotechnology*, vol. 26, no. 24, p. 242 001, 2015.
- [170] A. Crewe, D. Eggenberger, J. Wall and L. Welter, 'Electron gun using a field emission source,' *Review of Scientific Instruments*, vol. 39, no. 4, pp. 576–583, 1968.
- [171] J. I. Goldstein, D. E. Newbury, D. C. Joy, A. Romig Jr, C. E. Lyman et al., 'Scanning electron microscopy and x-ray microanalysis a text for biologists, materials scientists, and geologists libro electrónico,'
- [172] L. E. Franken, K. Grünewald, E. J. Boekema and M. C. Stuart, 'A technical introduction to transmission electron microscopy for soft-matter: Imaging, possibilities, choices, and technical developments,' *Small*, vol. 16, no. 14, p. 1 906 198, 2020.
- [173] H. H. Rose, 'Optics of high-performance electron microscopes,' Science and Technology of Advanced Materials, vol. 9, no. 1, p. 014107, 2008.
- [174] K. M. Krishnan, *Principles of materials characterization and metrology*. Oxford University Press, 2021.
- [175] J. M. Zuo and J. C. Spence, Advanced transmission electron microscopy. Springer, 2017.
- [176] P. Buseck, J. Cowley and L. Eyring, *High-resolution transmission electron mi*croscopy: and associated techniques. Oxford University Press, 1989.
- [177] R. F. Egerton et al., *Physical principles of electron microscopy*. Springer, 2005, vol. 56.

- [178] S. J. Pennycook and P. D. Nellist, Scanning transmission electron microscopy: imaging and analysis. Springer Science & Business Media, 2011.
- [179] A. Lupini et al., 'Chapter 2: Scanning transmission electron microscopyy,' in Aug. 2015, pp. 30–79, ISBN: 978-1-84973-805-7. DOI: 10.1039/9781782621867-00030.
- [180] A. Bleloch and A. Lupini, 'Imaging at the picoscale,' *Materials Today*, vol. 7, no. 12, pp. 42–48, 2004.
- [181] M. Varela et al., 'Materials characterization in the aberration-corrected scanning transmission electron microscope,' *Annu. Rev. Mater. Res.*, vol. 35, no. 1, pp. 539–569, 2005.
- [182] O. L. Krivanek, T. C. Lovejoy, N. Dellby and R. Carpenter, 'Monochromated stem with a 30 mev-wide, atom-sized electron probe,' *Microscopy*, vol. 62, no. 1, pp. 3–21, 2013.
- [183] M. Mukai et al., 'Development of a monochromator for aberration-corrected scanning transmission electron microscopy,' *Microscopy*, vol. 64, no. 3, pp. 151–158, 2015.
- [184] K. Rajagopalan, M. Kaliannan and S. Kulandaivel, 'Transmission electron microscope,' in Non-Destructive Material Characterization Methods, Elsevier, 2024, pp. 167–188.
- [185] G. P. Holmes-Hampton, W.-H. Tong and T. A. Rouault, 'Biochemical and biophysical methods for studying mitochondrial iron metabolism,' in *Methods in Enzymology*, vol. 547, Elsevier, 2014, pp. 275–307.
- [186] H. Ibach and D. L. Mills, *Electron energy loss spectroscopy and surface vibrations*. Academic press, 2013.
- [187] A. E. Sykes, 'Development of a dynamic environmental transmission electron microscope for the study of light-induced dynamics in nanoscale materials,' Ph.D. dissertation, University of Illinois at Urbana-Champaign, 2021.

- [188] H. Hirai, 'Electron energy-loss spectroscopy and its applications to characterization of carbon materials,' in *Carbon Alloys*, Elsevier, 2003, pp. 239–256.
- [189] Y.-U. Heo, 'Comparative study on the specimen thickness measurement using eels and ched methods,' *Applied Microscopy*, vol. 50, no. 1, p. 8, 2020.
- [190] C. V. Raman, 'A new radiation,' Indian Journal of physics, vol. 2, pp. 387–398, 1928.
- [191] S. Harmsen and S. S. Gambhir, 'Molecular imaging using raman scattering,' in Molecular Imaging, Elsevier, 2021, pp. 343–357.
- [192] D. Cialla-May, M. Schmitt and J. Popp, 'Theoretical principles of raman spectroscopy,' *Physical Sciences Reviews*, vol. 4, no. 6, 2019.
- [193] L. J. Jacob and H.-P. Deigner, 'Nanoparticles and nanosized structures in diagnostics and therapy,' in *Precision Medicine*, Elsevier, 2018, pp. 229–252.
- [194] D. Wolverson, 'Raman spectroscopy,' in *Characterization of Semiconductor Heterostructures and Nanostructures*, Elsevier, 2008, pp. 249–288.
- [195] P. Vandenabeele, Practical Raman spectroscopy: an introduction. John Wiley & Sons, 2013.
- [196] J. R. Ferraro, Introductory raman spectroscopy. Elsevier, 2003.
- [197] M. S. Amer, Raman spectroscopy, fullerenes and nanotechnology. Royal Society of Chemistry, 2010.
- [198] J. Mayer, L. A. Giannuzzi, T. Kamino and J. Michael, 'Tem sample preparation and fib-induced damage,' MRS bulletin, vol. 32, no. 5, pp. 400–407, 2007.
- [199] C. A. Volkert and A. M. Minor, 'Focused ion beam microscopy and micromachining,' MRS bulletin, vol. 32, no. 5, pp. 389–399, 2007.
- [200] A. Rigort and J. M. Plitzko, 'Cryo-focused-ion-beam applications in structural biology,' *Archives of biochemistry and biophysics*, vol. 581, pp. 122–130, 2015.
- [201] N. Yao, Focused ion beam systems: basics and applications. Cambridge University Press, 2007.

- [202] D. C. Cox, Introduction to Focused Ion Beam Nanometrology. Morgan & Claypool Publishers, 2015.
- [203] I. Ahmad and M. Maaza, Ion Beam Applications. BoD–Books on Demand, 2018.
- [204] A. Brunelle, D. Touboul and O. Laprévote, 'Biological tissue imaging with time-of-flight secondary ion mass spectrometry and cluster ion sources,' *Journal of mass spectrometry*, vol. 40, no. 8, pp. 985–999, 2005.
- [205] D. McPhail, 'Applications of secondary ion mass spectrometry (sims) in materials science,' *Journal of materials science*, vol. 41, pp. 873–903, 2006.
- [206] L. Van Vaeck, A. Adriaens and R. Gijbels, 'Static secondary ion mass spectrometry (s-sims) part 1: Methodology and structural interpretation,' Mass Spectrometry Reviews, vol. 18, no. 1, pp. 1–47, 1999.
- [207] S. Fearn, An introduction to time-of-flight secondary ion mass spectrometry (ToF-SIMS) and its application to materials science. Morgan & Claypool Publishers, 2015.
- [208] S. G. Boxer, M. L. Kraft and P. K. Weber, 'Advances in imaging secondary ion mass spectrometry for biological samples,' *Annual review of biophysics*, vol. 38, no. 1, pp. 53–74, 2009.
- [209] J. C. Vickerman and I. S. Gilmore, Surface analysis: the principal techniques. John Wiley & Sons, 2011.
- [210] E. Ramsden, Hall-effect sensors: theory and application. Elsevier, 2011.
- [211] D. Chattopadhyay and H. Queisser, 'Electron scattering by ionized impurities in semiconductors,' *Reviews of Modern Physics*, vol. 53, no. 4, p. 745, 1981.
- [212] A. A. Ali, G. Yanling and C. Zifan, 'Study of hall effect sensor and variety of temperature related sensitivity.,' *Journal of Engineering & Technological Sciences*, vol. 49, no. 3, 2017.
- [213] C. Yang, J. C. Meza, B. Lee and L.-W. Wang, 'Kssolv—a matlab toolbox for solving the kohn-sham equations,' *ACM Transactions on Mathematical Software* (TOMS), vol. 36, no. 2, pp. 1–35, 2009.

- [214] B. I. Sharma, 'Basic concepts of density functional theory: Electronic structure calculation,' in *Journal of Physics: Conference Series*, IOP Publishing, vol. 765, 2016, p. 012 004.
- [215] A. Görling, 'Density-functional theory beyond the hohenberg-kohn theorem,' *Physical Review A*, vol. 59, no. 5, p. 3359, 1999.
- [216] V. Sahni and V. Sahni, 'The hohenberg-kohn theorems and kohn-sham density functional theory,' Quantal Density Functional Theory, pp. 99–123, 2004.
- [217] W. Kohn and L. J. Sham, 'Self-consistent equations including exchange and correlation effects,' *Physical review*, vol. 140, no. 4A, A1133, 1965.
- [218] C.-R. Gerhorst et al., 'Phonons from density-functional perturbation theory using the all-electron full-potential linearized augmented plane-wave method fleur,' *Electronic structure*, vol. 6, no. 1, p. 017 001, 2024.
- [219] R. M. Martin, Electronic structure: basic theory and practical methods. Cambridge university press, 2020.
- [220] R. M. Dreizler and E. K. Gross, Density functional theory: an approach to the quantum many-body problem. Springer Science & Business Media, 2012.
- [221] F. Giustino, Materials modelling using density functional theory: properties and predictions. Oxford University Press, 2014.
- [222] M. C. Payne, M. P. Teter, D. C. Allan, T. Arias and a. J. Joannopoulos, 'Iterative minimization techniques for ab initio total-energy calculations: Molecular dynamics and conjugate gradients,' Reviews of modern physics, vol. 64, no. 4, p. 1045, 1992.
- [223] D. Hamann, M. Schlüter and C. Chiang, 'Norm-conserving pseudopotentials,' *Physical review letters*, vol. 43, no. 20, p. 1494, 1979.
- [224] G. Kresse and D. Joubert, 'From ultrasoft pseudopotentials to the projector augmented-wave method,' *Physical review b*, vol. 59, no. 3, p. 1758, 1999.
- [225] S. Wei and M. Chou, 'Phonon dispersions of silicon and germanium from first-principles calculations,' *Physical Review B*, vol. 50, no. 4, p. 2221, 1994.

- [226] S. Baroni, S. De Gironcoli, A. Dal Corso and P. Giannozzi, 'Phonons and related crystal properties from density-functional perturbation theory,' Reviews of modern Physics, vol. 73, no. 2, p. 515, 2001.
- [227] E. M. Kadilenko and R. Grinis, 'The power of hellmann-feynman theorem: Kohn-sham dft energy derivatives with respect to the parameters of exchange-correlation functional at linear cost,' 2024.
- [228] G. Ackland, M. Warren and S. Clark, 'Practical methods in ab initio lattice dynamics,' *Journal of Physics: Condensed Matter*, vol. 9, no. 37, p. 7861, 1997.
- [229] J. Spence, 'Direct inversion of dynamical electron diffraction patterns to structure factors,' *Acta Crystallographica Section A*, vol. 54, no. 1, pp. 7–18, 1998.
- [230] J. M. Cowley and A. F. Moodie, 'The scattering of electrons by atoms and crystals. i. a new theoretical approach,' Acta Crystallographica, vol. 10, no. 10, pp. 609–619, 1957.
- [231] C. Cai and J. Chen, 'An accurate multislice method for low-energy transmission electron microscopy,' *Micron*, vol. 43, no. 2-3, pp. 374–379, 2012.
- [232] J. M. Cowley, Diffraction physics. Elsevier, 1995.
- [233] B. G. Mendis, Electron beam-specimen interactions and simulation methods in microscopy. John Wiley & Sons, 2018.
- [234] I. Lobato and D. Van Dyck, 'Multem: A new multislice program to perform accurate and fast electron diffraction and imaging simulations using graphics processing units with cuda,' *Ultramicroscopy*, vol. 156, pp. 9–17, 2015.
- [235] J. Madsen and T. Susi, 'The abtem code: Transmission electron microscopy from first principles,' *Open Research Europe*, vol. 1, p. 24, 2021.
- [236] A. Gómez-Rodríguez, L. Beltrán-del-Río and R. Herrera-Becerra, 'Simulatem: Multislice simulations for general objects,' *Ultramicroscopy*, vol. 110, no. 2, pp. 95–104, 2010.
- [237] Y. Wang, Y. Sun and Z. Ding, 'An improved quantum algorithm of the multislice method,' arXiv preprint arXiv:2411.17482, 2024.

- [238] V. Grillo, L. Marrucci, E. Karimi, R. Zanella and E. Santamato, 'Quantum simulation of a spin polarization device in an electron microscope,' New Journal of Physics, vol. 15, no. 9, p. 093 026, 2013.
- [239] X. Jiang, W. Van den Broek and C. T. Koch, 'Inverse dynamical photon scattering (idps): An artificial neural network based algorithm for three-dimensional quantitative imaging in optical microscopy,' *Optics express*, vol. 24, no. 7, pp. 7006–7018, 2016.
- [240] Z. Herdegen, B. Diederichs and K. Müller-Caspary, 'Thermal vibrations in the inversion of dynamical electron scattering,' *Physical Review B*, vol. 110, no. 6, p. 064 102, 2024.
- [241] F. F. Krause, D. Bredemeier, M. Schowalter, T. Mehrtens, T. Grieb and A. Rosenauer, 'Using molecular dynamics for multislice tem simulation of thermal diffuse scattering in algan,' *Ultramicroscopy*, vol. 189, pp. 124–135, 2018.
- [242] P. M. Zeiger and J. Rusz, 'Frequency-resolved frozen phonon multislice method and its application to vibrational electron energy loss spectroscopy using parallel illumination,' *Physical Review B*, vol. 104, no. 10, p. 104 301, 2021.
- [243] A. Gusev and A. Bulanov, 'High-purity silicon isotopes 28 si, 29 si, and 30 si,'

  Inorganic Materials, vol. 44, pp. 1395–1408, 2008.
- [244] A. Simonian, A. Sproul, Z. Shi and E. Gauja, 'Observation of fano resonance in heavily doped p-type silicon at room temperature,' *Physical Review B*, vol. 52, no. 8, p. 5672, 1995.
- [245] M. Rüdiger, J. Greulich, A. Richter and M. Hermle, 'Parameterization of free carrier absorption in highly doped silicon for solar cells,' *IEEE Transactions on Electron Devices*, vol. 60, no. 7, pp. 2156–2163, 2013.
- [246] O. L. Krivanek et al., 'High-energy-resolution monochromator for aberration-corrected scanning transmission electron microscopy/electron energy-loss spectroscopy,' *Philosophical Transactions of the Royal Society A: Mathematical, Physical and Engineering Sciences*, vol. 367, no. 1903, pp. 3683–3697, 2009.

- [247] F. Chigondo, 'From metallurgical-grade to solar-grade silicon: An overview,' Silicon, vol. 10, pp. 789–798, 2018.
- [248] M. Hakala, M. J. Puska and R. M. Nieminen, 'First-principles calculations of interstitial boron in silicon,' *Physical Review B*, vol. 61, no. 12, p. 8155, 2000.
- [249] N. Hine, K. Frensch, W. Foulkes and M. Finnis, 'Supercell size scaling of density functional theory formation energies of charged defects,' *Physical Review B—Condensed Matter and Materials Physics*, vol. 79, no. 2, p. 024112, 2009.
- [250] A. Martin, S. Findlay and L. Allen, 'Model of phonon excitation by fast electrons in a crystal with correlated atomic motion,' *Physical Review B—Condensed Matter and Materials Physics*, vol. 80, no. 2, p. 024308, 2009.
- [251] T. Soma and H. Matsuo, 'Debye-waller factor of si and ge,' physica status solidi (b), vol. 111, no. 2, K93–K97, 1982.
- [252] D. A. Muller, B. Edwards, E. J. Kirkland and J. Silcox, 'Simulation of thermal diffuse scattering including a detailed phonon dispersion curve,' *Ultramicroscopy*, vol. 86, no. 3-4, pp. 371–380, 2001.
- [253] G. A. Slack, D. W. Oliver and F. Horn, 'Thermal conductivity of boron and some boron compounds,' *Physical Review B*, vol. 4, no. 6, p. 1714, 1971.
- [254] A. Kumar, E. Tiukalova, K. Venkatraman, A. Lupini, J. A. Hachtel and M. Chi, 'Calibrating cryogenic temperature of tem specimens using eels,' *Ultramic-roscopy*, vol. 265, p. 114 008, 2024.